



PREPARATION OF N-Si-P-GaSe HETEROJUNCTIONS BASED ON AN AMORPHOUS GaSe LAYER WITHOUT IMPURITIES AND STUDY OF THEIR ELECTRICAL PROPERTIES

Rahim Salim Madatov^a, A.S. Alekperov^b, F.N. Nurmammadova^c,

 Narmin A. Ismayilova^{d,e},  Sakin H. Jabarov^{a,*}

^a Institute of Radiation Problems, Ministry of Science and Education Republic of Azerbaijan, Baku, AZ-1143, Azerbaijan

^b Azerbaijan State Pedagogical University, Baku, AZ-1000, Azerbaijan

^c Baku Engineering University, Khirdalan, AZ-0101, Azerbaijan

^d Institute of Physics, Ministry of Science and Education Republic of Azerbaijan, Baku, AZ-1143, Azerbaijan

^e Western Caspian University, Baku AZ-1001, Azerbaijan

*Corresponding Author e-mail: sakin@jmr.ru

Received October 25, 2023; revised November 28, 2023; accepted December 11, 2023

The electrical and photoelectric properties of anisotype n-Si-p-GaSe heterojunctions obtained as a result of the deposition of a GaSe thin layer on a cold n-Si single crystal substrate by the thermal evaporation method were studied. It was determined that the height of the potential barrier in thermal annealing structures at $T = 200^\circ\text{C}$ during $t = 3$ hours occurs due to the decrease in the density of states of local levels located near the Fermi level in the amorphous layer. The mechanism of photosensitivity in an isotype heterostructures was analyzed and it was found that the photosensitivity of the heterojunction increases as a result of a decrease in the surface density of state at the contact boundary of the components, by thermal means. The spectral distribution of the quantum efficiency in the n-Si – p-GaSe heterojunction was studied and their perspective was determined.

Keywords: GaSe; Thin film; Heterojunction; Electrophysical properties

PACS: 73.40.Lq, 81.05.Gc, 61.82.fk

1. INTRODUCTION

Even though semiconductor materials have been studied for a long time, these studies are continued in this period with modern methods. The main reason for this is that they have different functional properties. Due to the change in functions under the influence of the size effect, extensive research is being carried out on these materials at the atomic level [1-7]. The study of heterojunctions in these materials is of particular importance [8-10]. Because the obtained results further increase their application areas. The study of physical processes in semiconductor structures is related to increasing the efficiency of photoconverters and reducing the cost of solar cells. The research conducted to increase the efficiency of solar cells is one of the important directions of solar energy. One of the promising solutions to this problem is the creation of thin-layer structures. GaSe crystal, which is of practical importance in small-sized electronic systems, occupies a special place among A_3B_6 type compounds. The high drift mobility ($\sim 7000 \text{ cm}^2/\text{V}\cdot\text{s}$) of electrons in ultra-thin GaSe nanosheets expands its application possibilities [11-14]. On the other hand, the width of the forbidden band gap of GaSe crystal nanolayers strongly depends on the thickness of the layer, and the variation of optical and photoelectric properties with control of thickness increases their application in optoelectronics [15-19]. To create effective photoconverter structures based on GaSe crystal, Si-based amorphous and single crystals as well as complex semiconductor compounds are used [16]. Spectral distribution of photosensitivity in a-Si:H – n-InSe and Si - GaN(O) structures obtained by a new technological method was investigated and the prospects of obtained heterojunctions were shown [17,18]. Since the creation of a potential barrier in disordered semiconductors in the aforementioned structures is based on the classical potential barrier model, the role of deep energy levels localized near the Fermi level in the formation of p-n junctions is not taken into account, so there is a need to conduct new research in this direction [19]. There exist several experimental and theoretical studies for the physical properties of GeS crystal but so far, its thin film properties are still not sufficiently studied.

The aim of the study is investigation of the important characteristics of the heterocontact (n-Si – p-GaSe) created based on Si single crystal and p-GaSe thin layer (amorphous and polycrystalline).

2. A METHOD FOR PRODUCING A HETEROCONTACT AND MEASUREMENT METHODOLOGY

During the creation of the photosensitive structure, a chemically cleaned (100) oriented n-Si (KEF-7,5) single crystal was taken as a substrate. As the second component, scraps of GaSe single crystal grown by the Bridgman method were used. GaSe scraps were deposited on a cold Si (thickness $\sim 50 \mu\text{m}$) substrate by thermal evaporation method in a vacuum ($\sim 10^{-6}$ mmHg). The thickness of the obtained thin layers was $\sim 0.8\text{-}2 \mu\text{m}$. To determine the crystallization temperature of the thin layer, it was thermally annealed in a vacuum at a temperature of $t = 200^\circ\text{C}$ for a period of $\tau = 2\text{-}3$ hours. The optical absorption coefficient, dark conductivity and stationary photoconductivity were measured in the thin film

with amorphous and crystalline structure [20]. The volt-farad characteristic (VFC), electrical and photoelectric properties of the prepared n-Si - p-GaSe structure were studied [19].

3. RESULTS AND DISCUSSION

Figure 1 shows the volt-farad characteristics of n-Si - p-GaSe structures on a cold substrate (1) and thermally annealed (2).

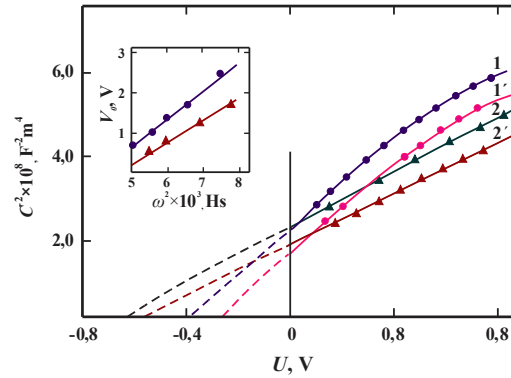


Figure 1. Voltage-Farad characteristics of the n-Si – p-GaSe structure

It can be seen from Figure 1 that the dependence of $C^2 \sim f(U)$ has a linear character in the thermally annealed sample (curve 2), while deviations from the linear dependence are observed in the sample with a cold base at high voltages. This shows that the distribution of impurity atoms in the region of bulk charges has a non-linear character (measurements were carried out at frequencies $f = 50\text{-}100$ kHz). The contact potential difference, p-n junction width, and electrostatic field intensity for both structures were calculated according to [19,21] and for the thermally annealed sample were ~ 0.5 V, $2 \cdot 10^{-4}$ cm, $3.2 \cdot 10^4$ V/cm, and for the sample with cold substrate were ~ 0.38 V, $3 \cdot 10^{-5}$ cm, $7.2 \cdot 10^2$ V/cm.

From the slope of the curves from VFC, the concentration of charge carriers was calculated according to [20] and was $2.3 \cdot 10^{15}$ cm^{-3} and $1.8 \cdot 10^{13}$ cm^{-3} , respectively. Based on the comparison of the parameters obtained during the calculation, it can be concluded that due to the weak interatomic bond in the GaSe layer obtained on a cold substrate, the nature of the distribution of ionized atoms in the range of bulk charges depends on the localized oxygen layer (dielectric layer) at the Si - α GaSe boundary during thermal evaporation. This fact is evident from the VFC extracted at different temperatures $C^2 \sim f(U)$. Figure 1 shows the VFC of the n-Si-p-GaSe structure at different temperatures. It can be seen from the figure that with increasing temperature, the dependence of $C^2 \sim f(U)$ in samples with a cold substrate (1) changes more sharply than in thermally annealed samples. The reason for this may be the high concentration of unstable defects.

Figure 2 shows the thermally annealed volt-ampere characteristics of the n-Si – p-GaSe structure at different temperatures.

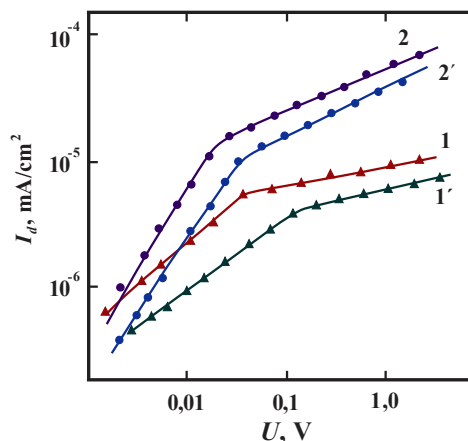


Figure 2. Current-voltage characteristics of the n-Si – p-GaSe structure (at different temperatures: $T = 100$ K (1' and 2'), $T = 300$ K (1 and 2), 1 and 1' GaSe obtained on a cold layer substrate, and 2 and 2' - a GaSe layer at a temperature of $T = 473$ K)

It can be seen from Figure 2 that at temperature $T = 300$ K and at low voltages, the dependence of $I \sim f(U)$ obeys the law $I \sim \exp(eU/\beta kT)$ ($\beta = 2\text{-}3$), and at high voltages obey the law $(0.3\text{-}0.4$ V) $I \sim AU^m$ ($m = 1.5\text{-}2$). At low temperature (100 K), due to the increase of the voltage drop in the crystal, the Volt-Ampere characteristics (VAC) shift towards the high voltage region, but the exponential regularities are preserved. The analysis of the obtained experimental results shows that the rectifier capacitance of the p-n junction obtained on a cold substance is lower than that of the annealed

layer since the layer obtained on the cold substance is in an amorphous state. Crystallization centers formed in the amorphous layer during thermal annealing led to improvement of the current rectification property. Figure 3 shows the VAC opposite direction of the n-Si – p-GaSe structure at different temperatures. It can be seen from the figure (curves 1, 2) that the current in the thermally annealed sample (curve 1) obeys the law of $I \sim U^m$.

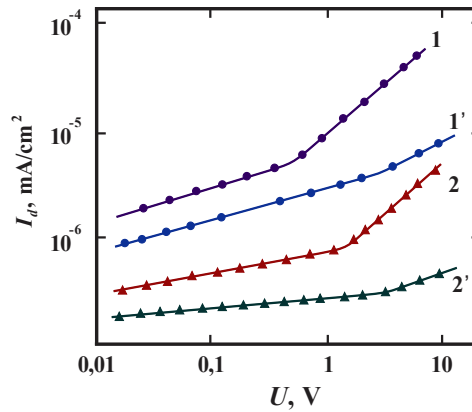


Figure 3. VAX of n-Si-p-GaSe structures in the opposite direction. $T = 100$ K (1', 2'), $T = 300$ K (1, 2), 1-1' GaSe layer obtained on a cold substrate, 2-2' – GaSe layer at $T = 473$ K

The slope of the dependence $I \sim f(U)$ consists of two parts. In the region of $U = 0-8$ V, the diode coefficient is $m \sim 1.1$, and in the high voltage region it is $m \sim 1.5$. In the amorphous layered structure (2), small deviations are observed at values of reverse voltage $U > 10$ V, and the diode coefficient is close to $m \sim 1$. This may be due to the high layer and small barrier capacity of the layer, as shown in [19,22].

The VAC analysis of the n-Si-p-GaSe structure shows that the current flow mechanism in anisotropic n-Si-p-GaSe structures depends on the value of the contact potential difference that forms the area of bulk charges. As shown in [23], due to the high density of state in the vicinity of Fermi level ($\sim 10^{18} \text{ cm}^{-3}$), the height of the potential barrier decreases as a result of the change of the potential and electric field distribution in the area of bulk charges. This leads to a deterioration in the quality factor of the p-n junction relative to the structure undergoing crystallization.

Figure 4 shows the spectral characteristics of n-Si – p-GaSe structures (1,2- heated substrate; 3,4 cold substrate, GaSe surface illuminated) $T = 300$ K.

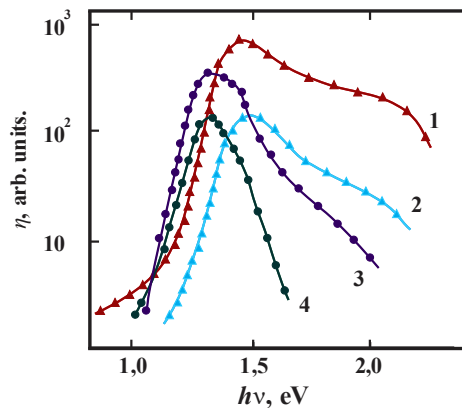


Figure 4. Spectral characteristics of n-Si/p-GaSe structures (1 – heated substrate; cold substrate, illuminated GaSe surface; 3 - heated cold substrate: cold substrate, surface illuminated from the Si side)

From curve 1 in Figure 4, it can be seen that the "window effect" observed in the spectral range of 1.0-3.0 eV during illumination from the wide-band surface of the heterojunction obtained on the heated substrate is related to the forbidden gap of the compounds. The width of the photosensitive region of the spectrum observed at the maximum photosensitivity $h\nu \sim 1.5$ eV was $\Delta S \sim 70-800$ meV. the sharp decrease in photocurrent at values of $h\nu > 2.6$ eV is due to the decrease in interband electron transitions. As can be seen from curve 2 in Figure 4 the photosensitivity of the heterojunction formed on the cold substrate decreases compared to curve 1 and reaches its maximum value at $h\nu = 1.5$ eV. The half-width of the spectrum decreases and becomes $\Delta S \sim 45-500$ meV. The shortening of photosensitivity and spectral range is due to high electroactive local defect density at the contact boundary [23].

The photosensitivity and spectral width decrease when the heterojunction formed on the heated substrate during illumination from the Si side (3rd curve in Figure 4). In this case, the energy corresponding to the maximum value of the photocurrent shifts to the lower energy region and becomes $h\nu = 1.2$ eV. When the heterojunction formed on the cold substrate and is illuminated from the Si side, the obtained spectrum shifts to the long-wave region (curve 4) and the the

short-wavelength border of photosensitivity corresponds to the band gap of the Si substrate. As can be seen from Figure 4, the red border of the spectral characteristics of n-Si – p-GaSe structures is determined by the forbidden gap of the substrate. Kinetic analysis of photocurrents in anisotropic n-Si – p-GaSe structures shows that the mechanism of photoconductivity depends on the distribution density of defects at the amorphous-crystalline boundary (HJ). Photosensitivity is reduced because photocarriers in the HJ, formed in a cold substrate illuminated from a wide bandgap, are trapped by local high-density levels formed at the interface. After thermal annealing (Fig. 4. curve 1) due to the orderly distribution of electroactive defects in the area of bulk charges, the height of the potential barrier for the main charge carriers increases (Fig. 1) and the photosensitivity of HJ increases several times. With the applying of an external voltage to HJ- (direct or opposite direction), the Fermi level position in the region of bulk charges changes, as well as the height of the potential barrier, as a result of which the diffusion and drift velocities of charge carriers are change. This causes a redistribution of charged defects in the area of bulk charges. From the comparison of the volt-farad characteristics of n-Si-p-GaSe structures, it can be seen that the processes occurring at the boundary during the amorphous GaSe - Si contact depend on the distribution of the electroactive density of states localized in the vicinity of the Fermi level. Considering that broken bonds in amorphous layers are sensitive to external influences (temperature, electric field, ionizing rays), their recovery process is accelerated during thermal annealing and due to the redistribution of electroactive local levels, occurs equilibrium in the area of bulk charges. This leads to an increase in the height of the potential barrier in the structure.

To clarify the current flow mechanism, the zone diagram of the studied heterojunction was built according to Anderson's model (Figure 5).

Since there is no information about the electron affinity parameter for the GaSe layer, the main parameters of the zone diagram –breakdown (ΔE_c and ΔE_v) were calculated according to the experimental values of the diffusion potential (V_{d1} and V_{d2}) taking into account the Fermi level of the components and the energy values of the forbidden gap. For the calculation, the electron affinity $\chi_n = \chi_p = 3.6$ eV for the GaSe crystal was used [22,23]. Based on the results of the mentioned literature, the breakdowns of the energy zones for the nSi-aGaSe heterojunction were calculated for conduction and valence bands $\Delta E_c \sim 1.55$ eV, $\Delta E_v \sim 0.15$ eV respectively. The high density of state at the contact boundary of the HJ, formed based on the used model, is due to the incompatibility of the structural parameters of the components. Since partial crystallization is observed in the a-GaSe layer during thermal annealing, the photosensitivity of the structure increases due to a decrease in the density of states of the surface. The obtained results correspond to the values given for InSe – GaSe and Si – GaSe in [15,17].

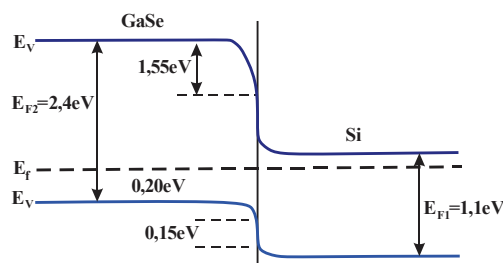


Figure 5. Band energy diagram of the n-Si-p-GaSe heterojunction

4. CONCLUSIONS

Thus, based on VFC, the influence of the charge density distribution on the electrostatic parameters in the region of bulk charges in a heterostructure formed based on amorphous GeSe and crystalline n-Si was determined. It was found that an increase in the contact potential difference in the dependence of $C^2 \sim f(V)$ for thermally annealed n-Si – p-GaSe sample is due to reduce the density of states near the Fermi level (from $\sim 10^{19}$ eV $^{-1}$ cm $^{-1}$ to 10^{16} eV $^{-1}$ cm $^{-1}$) in the amorphous GaSe layer. In an amorphous GaSe layer, the distribution of potential and electric field intensity in the region of bulk charges changes due to the presence of the density of states of charged local levels located in the vicinity of the Fermi level. As a result of a decrease in the density of states at the contact boundary during thermal annealing, the intensity in the bulk charge region decreases, and the width of the region of bulk charges and the height of the potential barrier increase from 0.4 to 0.8. eV.

ORCID

©Narmin A. Ismayilova, <https://orcid.org/0000-0002-5388-4175>; ©Sakin H. Jabarov, <https://orcid.org/0000-0002-3153-5804>

REFERENCES

- [1] S.H. Jabarov, N.A. Ismayilova, D.P. Kozlenko, T.G. Mammadov, N.T. Mamedov, H.S. Orudzhev, S.E. Kichanov, et al., "Structural and elastic properties of TlInSe₂ at high pressure," *Solid State Sciences*, **111**, 106343 (2021). <https://doi.org/10.1016/j.solidstatesciences.2020.106343>
- [2] Y.I. Aliyev, Y.G. Asadov, T.M. Ilyasli, F.M. Mammadov, T.G. Naghiyev, Z.A. Ismayilova, M.N. Mirzayev, and S.H. Jabarov, "Structural aspects of thermal properties of AgCuS compound," *Modern Physics Letters B*, **34**(05), 2050066 (2020). <https://doi.org/10.1142/S0217984920500669>

- [3] A.S. Alekperov, S.H. Jabarov, M.N. Mirzayev, E.B. Asgerov, N.A. Ismayilova, Y.I. Aliyev, T.T. Thabethe, and N.T. Dang, "Effect of gamma irradiation on the microstructure of the layered $\text{Ge}_{0.995}\text{Nd}_{0.005}\text{S}$," *Modern Physics Letters B*, **33**(09), 1950104 (2019). <https://doi.org/10.1142/S0217984919501045>
- [4] N.N. Mursakulov, N.N. Abdulzade, S.H. Jabarov, and Ch.E. Sabzalieva, "Investigation of $\text{CuIn}_{1-x}\text{Ga}_x\text{Se}_2$ thin films for solar cells obtained by the magnetron sputtering method from two magnetrons shifted to each other," *New Materials, Compounds and Applications*, **6**(2), 140-147 (2022). http://jomardpublishing.com/UploadFiles/Files/journals/NMCA/v6n2/Mursakulov_et_al.pdf
- [5] S.H. Jabarov, "First principles study of structural phase transition in Ag_2S under high pressure," *Integrated Ferroelectrics*, **230**, 23-28 (2022). <https://doi.org/10.1080/10584587.2022.2102794>
- [6] Y.I. Aliyev, F.G. Asadov, T.M. Ilyashi, A.O. Dashdemirov, R.E. Huseynov, and S.H. Jabarov, "Vibrational properties of YbAs_2S_4 and YbAs_2Se_4 compounds: by infrared spectroscopy," *Ferroelectrics*, **599**, 78-82 (2022). <https://doi.org/10.1080/00150193.2022.2113641>
- [7] B.G. Tagiyev, O.B. Tagiyev, A.I. Mammadov, V.X. Quang, T.G. Naghiyev, S.H. Jabarov, M.S. Leonenya, et al., "Structural and luminescence properties of $\text{Ca}_x\text{Ba}_{1-x}\text{Ga}_2\text{S}_4$: Eu^{2+} chalcogenide semiconductor solid solutions," *Physica B: Condensed Matter*, **478**, 58-62 (2015). <https://doi.org/10.1016/j.physb.2015.08.061>
- [8] Sh.B. Utamuradova, Sh.Kh. Daliev, D.A. Rakhmanov, A.S. Doroshkevich, V.A. Kinev, O.Yu. Ponomareva, M.N. Mirzayev, et al., "IR – spectroscopy of n-Si<Pt> irradiated with protons," *Advanced Physical Research*, **5**(2), 73-80 (2023). http://jomardpublishing.com/UploadFiles/Files/journals/APR/V5N2/Utamuradova_et_al.pdf
- [9] A.S. Alekperov, A.O. Dashdemirov, N.A. Ismayilova, and S.H. Jabarov, "Fabrication of a Ge–GeS: Nd heterojunction and investigation of the spectral characteristics, *Semiconductors*," **54**, 1406-1409 (2020). <https://doi.org/10.1134/S1063782620110044>
- [10] Sh.B. Utamuradova, D.A. Rakhmanov, A.S. Doroshkevich, I.G. Genov, Z. Slavkova, and M.N. Ilyina, "Impedance spectroscopy of p-Si<Pt>, p-Si<Cr> irradiated with protons," *Advanced Physical Research*, **5**(1), 5-11 (2023). http://jomardpublishing.com/UploadFiles/Files/journals/APR/V5N1/Utamuradova_et_al.pdf
- [11] G.A. Akhundov, N.A. Gasanova, and M.A. Nazametdinova, "Optical absorption, reflection and dispersion of GaS and GaSe layer crystals," *Physica Status Solidi b*, **15**, k109- k102 (1966). <https://doi.org/10.1002/PSSB.19660150249>
- [12] A.G. Kazim-zade, A. Mokhtari, I. Hympanova, V.M. Salmanov, Yu. Asadov, and A.A. Agaeva, "Influence of stacking disorder on the optical properties of layered crystals GaSe," *Acta Physica Universitatis Comenianae*, **XLVI-XLVII**, 101-108 (2005-2006). https://dai.fmph.uniba.sk/~lucan/apuc/_vol46-47/Apuc12.pdf
- [13] P.A. Hu, Z.Z. Wen, L.F. Wang, P.H. Tan, and K. Xiao, "Synthesis of few-layer GaSe nanosheets for high performance photodetectors," *ACS Nano*, **6**, 5988–5994 (2012). <https://doi.org/10.1021/nm300889c>
- [14] T. Kushida, F. Minami, Y. Oka, Y. Nakazaki, and Y. Tanaka, "Edge emission in GaSe and GaS," *Nuovo Cimento B*, **39**, 650-654 (1977). <https://doi.org/10.1007/BF02725806>
- [15] A.G. Kyazym-zade, M. Karabulur, A.Kh. Dincher, V.M. Salmanov, M.A. Dzhaferov, A.M. Guseinov, and R.M. Mamedov, "Structure, optical, and luminescent properties of GaSe nanoparticles," *Nanotechnologies in Russia*, **10**, 794-801 (2015).
- [16] Yu.A. Nikolaev, V.Yu. Rud', Yu.V. Rud', and E.I. Terukov, "Photoelectric phenomena in a-Si:H/p-CuInSe₂ heterostructures," *Semiconductors*, **34**, 658-661 (2000). <https://doi.org/10.1134/1.1188049>
- [17] V.N. Brudnyi, S.Yu. Sarkisov, and A.V. Kosobutsky, "On the charge neutrality level and the electronic properties of interphase boundaries in the layered ϵ -GaSe semiconductor," *Semiconductors*, **49**, 1307-1310 (2015). <https://doi.org/10.1134/S1063782615100061>
- [18] S.E. Aleksandrov, T.A. Gavrikova, and V.A. Zykov, "Photoelectric properties of isotype and anisotype Si/GaN:O heterojunctions," *Semiconductors*, **34**, 1295-1300 (2000). <https://doi.org/10.1134/1.1325426>
- [19] L.S. Berman, *Capacitive methods for the study of semiconductors*, (Nauka, Leningrad, 1972). (in Russian)
- [20] J Martinez-Pastor, A. Segura, J.L. Valdes, and A. Chevy, "Electrical and photovoltaic properties of indium - tin - oxide/p - InSe/Au solar cells," *Journal of Applied Physics*, **62**(4), 1477-1483 (1987). <https://doi.org/10.1063/1.339627>
- [21] A. Milns, and D. Feucht, *Heterojunctions and metal-semiconductor transitions*, (Mir, Moscow, 1975). (in Russian)
- [22] R.R. Daniels, G. Margaritondo, C. Quaresima, P. Perfetti, and F. Levy, "Summary Abstract: GaSe - Ge and GaSe - Si: two possible examples of schottky-like behavior of heterojunction interfaces," *Journal of Vacuum Science Technology A*, **3**(3), 979-980 (1985). <https://doi.org/10.1116/1.573369>
- [23] N.V. Vishnyakov, S.P. Vikhrov, V.G. Mishustin, A.P. Avachev, I.G. Utochkin, and A.A. Popov, "Formation of potential barriers in undoped disordered semiconductors," *Semiconductors*, **39**, 1147-1152 (2005). <https://doi.org/10.1134/1.2085261>

ОТРИМАННЯ ГЕТЕРОПЕРЕХОДІВ N-Si-P-GaSe НА ОСНОВІ АМОРФНОГО GaSe ШАРУ БЕЗ ДОМІШОК ТА ДОСЛІДЖЕННЯ ЇХ ЕЛЕКТРИЧНИХ ВЛАСТИВОСТЕЙ

Рахім Салім Мадатов^а, А.С. Алекперов^б, Ф.Н. Нурмаммадова^с, Нармін А. Ісмаїлова^{д,е}, Сакін Х. Джабаров^а

^аІнститут радіаційних проблем Міністерства науки і освіти Азербайджанської Республіки, Баку, AZ-1143, Азербайджан

^бАзербайджанський державний педагогічний університет, Баку, AZ-1000, Азербайджан

^сБакинський інженерний університет, Хирдалан, AZ-0101, Азербайджан



^дІнститут фізики Міністерства науки і освіти Азербайджанської Республіки, Баку, AZ-1143, Азербайджан

^еЗахідно-Каспійський університет, Баку AZ-1001, Азербайджан

Досліджено електричні та фотоелектричні властивості анізотипних гетеропереходів n-Si-p-GaSe, отриманих в результаті осадження тонкого шару GaSe на холодну монокристалну підкладку n-Si методом термічного випаровування. Визначено, що підвищення висоти потенційного бар'єру в структурах термічного відпау при $T = 200\text{ }^\circ\text{C}$ протягом $t = 3$ годин відбувається за рахунок зменшення густини станів локальних рівнів, розташованих поблизу рівня Фермі в аморфному шарі. Проаналізовано механізм fotocутливості в ізотипних гетероструктурах і встановлено, що fotocутливість гетеропереходу підвищується в результаті зменшення поверхневої щільності стану на межі контакту компонентів термічним шляхом. Досліджено спектральний розподіл квантової ефективності в гетеропереході n Si – p GaSe та визначено їх перспективу.

Ключові слова: GaSe; тонка плівка; гетероперехід; електрофізичні властивості

INFLUENCE OF DOPING CONDITIONS ON THE PROPERTIES OF NICKEL ATOMIC CLUSTERS

 **Kanatbay A. Ismailov^b, Zlikha M. Saparniyazova^b, Gulchekhira T. Kudeshova^b,
Gulbadan A. Seytimbetova^b,  Fayzulla A. Saparov^{a*}**

^a *Institute of Semiconductor Physics and Microelectronics at the National University of Uzbekistan
20 Yangi Almazar st., Tashkent, 100057, Uzbekistan*

^b *Karakalpak State University. 1 Ch. Abdirov st., Nukus, Karakalpakstan, 230100, Uzbekistan*

**Corresponding Author e-mail: sfa@inbox.ru*

Received October 23, 2023; revised January 22, 2024; accepted January 25, 2024

It is shown that the dynamics of changes in the state of nickel clusters depends on the temperature of the diffusion maximum and the cooling rate. It was found that with increasing annealing temperature and cooling rate, an increase in density and a decrease in cluster size are observed. In this case, the main attention was paid to the determination of the laws governing the change in the density, size, and structure of clusters from temperature and cooling. The process and dynamics of the interaction of clusters depends on the diffusion coefficient of impurity atoms in the lattice and the level of supersaturation of the solid solution. It has been established that with a change in the annealing temperature from $T = 1100^{\circ}\text{C}$ to 1250°C , the cluster density increases by almost 1-1.5 orders of magnitude, and their size decreases by a factor of 5–6. It seems to us that to obtain clusters with stable parameters, the optimal cooling rate is 200–300°C.

Keywords: Silicon; Impurity cluster; Doping; Diffusion; Cooling rate; Nanostructure; Diffusion coefficient; Cluster density

PACS: 78.30.Am

INTRODUCTION

The study of the influence of doping conditions on the properties of nickel atom clusters is of great scientific and practical interest. Since the study of the properties of clusters, their stability and degradation processes in them, makes it possible to create the necessary micro- and nanostructures of cluster-silicon, cluster-silicon-cluster, etc. [1; 2].

The formation of a cluster leads the system to a more equilibrium state with minimal internal energy [1, 10]. Therefore, for the formation of clusters of impurity atoms, the following conditions must be fulfilled:

- Impurity atoms must have a high diffusion coefficient and sufficient solubility in the studied semiconductor materials.

- They must not form silicides or other solid solutions.

- Bond energy of impurity atoms in a cluster should be sufficient so that such clusters do not decay when exposed to external influences or with time.

Let us analyze which impurity atoms in semiconductors and under what conditions can satisfy the above conditions.

Almost all the elements of the transition group in silicon have sufficiently large diffusion coefficients ($D \sim 10^{-5} \div 10^{-8} \text{ cm}^2/\text{s}$), but they have a low solubility ($N \sim 10^{15} \div 10^{18} \text{ cm}^{-3}$).

It should also be noted that these elements create several deep levels in the band gap, but the majority of the introduced atoms are in the electrically neutral state (90-99.99%). Under conditions of high-temperature diffusion doping, almost all elements of transition groups form silicide with silicon atoms with different compositions [3], therefore, it can be assumed that doping of silicon with elements of transition groups using high-temperature diffusion does not allow the formation of atomic clusters.

In this regard, we are studying and developing a new method of doping silicon with nickel atoms, the so-called low-temperature and step doping.

The essence of this doping method is to carry out diffusion of the impurity with a gradual and phased increase in the diffusion temperature from room temperature to a certain value, with a certain speed and holding the samples for a certain time at each diffusion stage [4,11].

The question is, what might be the result of such doping technique? It gives the following:

1. At low temperatures, the concentration of equilibrium vacancies is negligible and there is practically no capture of impurity atoms by vacancies.

2. In the region of low temperatures, the impurity is forced to diffuse only along the interstitial locations, which provides not only a high diffusion coefficient, but also significantly increases the probability of the interaction of impurity atoms with each other.

3. Under conditions of low-temperature alloying, the formation of silicides and other hard alloys is almost completely absent, since the concentration of impurity atoms will be insufficient for the formation of silicide [1, 5].

4. For impurities diffusing from the gas phase (Mn, Zn, S, Se, Te) erosion of the surface of the sample is excluded [6, 7].

Thus, we can say that the new doping method can create optimal conditions for the formation of clusters of impurity atoms. This allows us to create sensitive detectors and use them as implants in humans in the future.

MATERIALS AND METHODS

To study the effect of the maximum diffusion temperature on the state of clusters, samples were made based on n-type silicon with $c \approx 40 \Omega \cdot \text{cm}$, with an oxygen concentration of $N \sim 7 \cdot 10^{17} \text{ cm}^{-3}$. The maximum temperatures were $T = 1100^\circ\text{C}$, 1150°C , 1200°C and 1250°C , other doping conditions and cooling conditions were the same.

In this case, the main attention was paid to determining the laws of changes in the density, size, and structure of clusters as a function of temperature. The cluster size was determined by comparing with a calibration standard with a width of $75 \mu\text{m}$ with a maximum increase of INFRAM-I, the average density was determined by counting the number of clusters in a certain area. In this case, the standard error of the measurements was 10–12%.

RESULTS AND DISCUSSION

In Figure 1 it is shown the dynamics of changes in the state of nickel clusters depending on the temperature of the diffusion maximum. As can be seen from the figure, with an increase in the annealing temperature, an increase in density and a decrease in cluster sizes are observed.

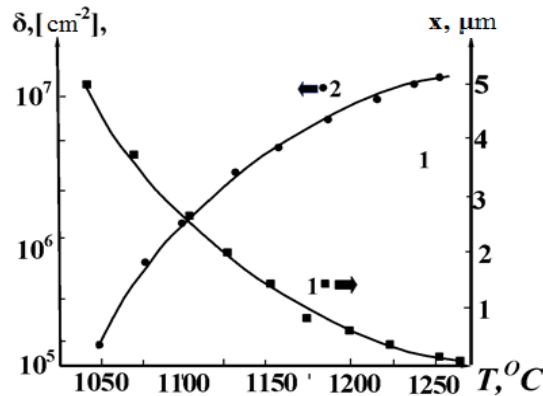


Figure 1. Change in the parameters of nickel clusters depending on temperature at the end of diffusion

Thus, it was found that with annealing temperature changing from $T = 1100^\circ\text{C}$ to 1250°C , the cluster density increases by almost 1-1.5 orders of magnitude, and their size decreases by 5–6 times. To study the effect of the cooling rate, 3 parties of samples were prepared in three ampoules with the same geometric parameters. They were alloyed at $T = 1200^\circ\text{C}$; the first party of samples was cooled by dropping the ampoule directly into the oil ($T = 25^\circ\text{C}$) [3,12,18]. The calculation shows that in this case, the cooling rate is about $v = 300^\circ\text{C/s}$. The second party of samples was cooled on a massive metal plate. In this case, the cooling rate is $\sim 100^\circ\text{C/s}$. The third one of samples was left in the furnace, after it was turned off, and which was cooled for a very long time for approximately 160-180 minutes to a temperature of $T = 200^\circ\text{C}$. The state of clusters in samples cooled at different rates is shown in Figure 2.

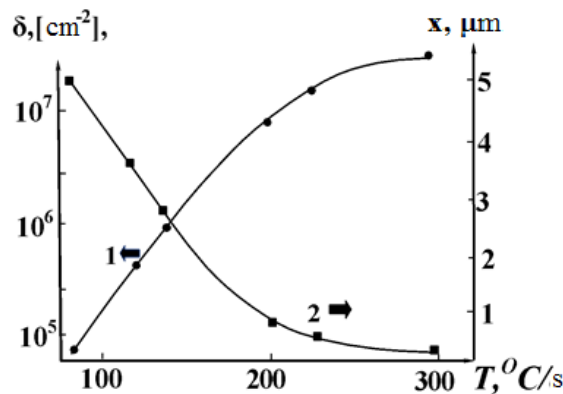


Figure 2. The effect of cooling rate on the parameters of nickel clusters

As can be seen in the samples cooled at a rate of $\vartheta_1 = 200^\circ\text{C/s}$, a significant decrease in the cluster size and a noticeable increase in their density are observed. At the maximum cooling rate, the INFRAM-I microscope did not allow observing the presence of any clusters not only on the surface, but throughout the volume. At the same time, in samples cooled in the furnace, a noticeable increase in cluster sizes is observed. Thus, it turned out that by changing the doping

conditions, one can control the density and size of clusters. It seems to us that to obtain clusters with reproducible parameters, the optimal cooling rate is 200–300°C/s. By changing the diffusion temperature (1100–1250°C), one can obtain the necessary density and size of clusters.

The physical nature of the interaction of clusters of impurity atoms in semiconductors does consist in the tendency of the system to a state with minimum free energy [8], i.e., to the gradual restoration of the equilibrium state of the system. Under ordinary conditions ($T \sim 300$ K), the introduced impurity atoms in the lattice, regardless of the doping method, create a locally deformation or electric potential. The magnitude of this potential is mainly determined by the size, electronic structure, charge state and concentration of impurity atoms. Consequently, we can assume that semiconductor materials supersaturated with impurity atoms are in a nonequilibrium state. Therefore, under the presence of appropriate thermodynamic conditions, the interaction of clusters of impurity atoms occurs, i.e., the process of restoring the equilibrium state of the system occurs due to the formation of stable complexes i.e. clusters. The process and dynamics of cluster interaction depends on the diffusion coefficient of impurity atoms in the lattice under the conditions under consideration, and the level of saturation of the solid solution. It follows that the interaction of clusters of impurity atoms with a small diffusion coefficient (i.e., an impurity forming a substitutional solid solution) occurs very slowly, almost not noticeably. However, for such impurity atoms with a high concentration ($N \sim 10^{21} \div 10^{22} \text{ cm}^{-3}$), the cluster interaction process is significantly accelerated [4]. In this regard, impurity atoms having a sufficiently large diffusion coefficient are of interest, i.e., impurities forming solid interstitial solutions. Thus, it can be argued that from the point of view of thermodynamics, cluster formation of impurity atoms is a natural process. But the speed of this process, as mentioned above, is mainly determined by the diffusion coefficient and the level of saturation of the solid solution.

The kinetics of the formation of clusters of impurity atoms in the crystal lattice of a semiconductor can be described by the following model. In the process, after diffusion thermal annealing, impurity atoms are in an extremely nonequilibrium state and must go to their centers of equilibrium (nuclei) of future clusters in their equilibrium positions. This process provides the system with the acquisition of minimum free energy. The kinetics of the process is determined by the following factors:

1. The coefficient of supersaturation K , which is determined by the ratio of the solubility of impurity atoms at diffusion temperature to solubility at thermal annealing temperature. The larger the K value, the more the system is in a nonequilibrium state. Therefore, we can assume that K is the main driving factor in the formation of clusters.

2. The formation of impurity atom clusters at the lattice sites is limited not only by the diffusion coefficient, but also by the formation of a sufficiently large concentration of vacancies. When impurity atoms are in internodes, the process is significantly accelerated due to the large diffusion coefficient and the possibility of cluster formation in internodes with certain states and structures, which does not require significant rearrangement of the crystal lattice and energy. The diffusion coefficient of impurity atoms at the thermal annealing temperature is determined by the ratio.

$$D_t = D_0 \exp\left(-\frac{E_g}{kT_t}\right)$$

where E_g is the diffusion activation energy; k is the Boltzmann constant. It can be seen from this relation that, with increasing temperature, the diffusion coefficient increases, but the coefficient K decreases accordingly.

3. The nuclei of clusters can be all kinds of defects - dislocations, vacancies, impurity atoms, etc. An analysis of experimental works [9, 10] shows that the density of clusters does not depend on the density of dislocations and exceeds their density by several orders of magnitude. Therefore, we can assume that the contribution of dislocations to the quality of the nucleus of clusters is not basic. Calculations show that the concentration of equilibrium vacancies in silicon, which are determined by the ratio:

$$N_v = N_0 \exp\left(-\frac{E_g}{kT}\right) = 5 \cdot 10^{22} \exp\left(-\frac{E_g}{kT}\right)$$

and the low-temperature annealing region is much lower than the concentration of impurity atom clusters in the lattice, which allows us to conclude that although vacancies can be cluster nuclei, their contribution is negligible. Therefore, we assume that the nuclei of the clusters are impurity atoms that are in equilibrium at the annealing temperature. In this regard, in a simplified model, we can assume that the concentration of impurity atoms that are in equilibrium at the annealing temperature can serve as the concentration of clusters.

4. The number of atoms in the clusters is mainly determined by the value of the supersaturation coefficient K . Therefore, it can be assumed that, by controlling the value of K , one can obtain both molecules consisting of several atoms and nanoclusters and clusters with sizes from 0.1 to 10 μm . The number of atoms in the clusters will be equal

$$N_v = \frac{N_0 - N_t}{N_t} = \frac{N_0}{N_t} - 1$$

Based on the results of studies with an INFRAM-I microscope, it was found that the cluster size varies within 0.1–3 μm . It seems to us that this is the size of the deformed region of the silicon lattice in which the clusters are located. Therefore, it can be assumed that the true cluster size is 0.05–1.5 μm .

Regarding the concentration and distribution of clusters in the lattice one can assume that if we take into account that for each elementary face-centered cubic lattice created by nickel atoms inside a silicon crystal, $n=4$ ($n = A/8 + C/2$), and determining the average volume of each cluster ($\sim 10^7 \text{ \AA}$) and the volume of the elementary lattice of nickel atoms ($\sim 20 \text{ \AA}$), then we can calculate on average how many unit cells are in each cluster. As the calculation shows, the average number of unit cells in each cluster is $\sim 10^5$, and the number of nickel atoms in each cluster is $N \sim 4 \cdot 10^5$ atoms. If we assume that almost all nickel atoms participate in cluster formation, then the cluster concentration is $N = N_i/n \sim 10^{12} \text{ cm}^{-3}$, (where N_{Ni} is the concentration of nickel atoms in silicon $\sim 10^{18} \text{ cm}^{-3}$).

Now we determine the concentration of clusters based on experimental data. The cluster density determined on the basis of INFRAM-I results is $\sim (4 \div 5) 10^6 \text{ cm}^{-2}$, the average diameter of each cluster is $\sim 0.5 \text{ \mu m}$, therefore there should be about 1011 clusters in one 1 cm^{-3} . This experimental data is quite close to the calculated data. Thus, it can be undoubtedly stated that the nickel atoms in silicon (at $T=1200^\circ\text{C}$) create clusters with a concentration of $\sim 10^{12} \text{ cm}^{-3}$. The results of microprobe analysis on the Jeol JXA-8800R and the electrical properties of the clusters showed that the clusters of nickel atoms have a conductivity close to metallic. Then it can be assumed that each cluster-silicon structure is a Schottky barrier, i.e., Schottky diode. The features of such a Schottky diode, unlike ordinary Schottky diodes, are, firstly, the absence of surface states in the metal-semiconductor contact region, this is an ideal Schottky barrier, secondly, "buried" Schottky diodes can be created, and thirdly, a cluster-silicon structure can be created - cluster or silicon-cluster-silicon with an ideal contact region; in the fourth, it is possible to control the area of such structures with a radius of $\sim 0.05 \div 1 \text{ \mu m}$.

CONCLUSION

By studying the various external influences and comparing the works of other authors, we made a conclusion that the sensitivity of the resulting samples demonstrates hundred times more magnitude to radial pressure in compare to results demonstrated by other authors [13-21]. And they demonstrate the results that met the parameters we needed. Based on the above, it can be assumed that the experimentally observed non-monotonicity of the dependences $\rho=f(P)$ is a consequence of two conflicting processes: the first is a decrease in the band gap and the associated change in the ionization energy of deep Ni levels, which leads to an increase in conductivity and the second is the decay of precipitates impurities with an increase in the concentration of electrically active centers, which, under the influence of pressure, are displaced from the volume of the semiconductor and change the spectrum of the surface charge distribution at the metal-semiconductor interface. Mechanical stresses that stimulate the gettering of defects from the bulk of the semiconductor, or impurities localized in the metal-semiconductor transition layer and interacting with surface states, may be responsible for changes in the properties of the interface under the influence of pressure [15, 16]. All these features show very interesting new functionalities of silicon with clusters of nickel atoms. For example, the abilities to create almost perfect Schottky barriers with gigantic frequency properties and to create photodetectors with a response time of the order of several picoseconds, as well as possibility to create integrated circuits with an ultrahigh degree of integration, etc.

Acknowledgment

The authors are grateful to the Director of the Research Institute of Semiconductor Physics and Microelectronics, Doctor of Physical and Mathematical Sciences, Prof. Sh.B. Utamuradova for assistance in conducting experiments and discussing the results.

ORCID

© Fayzulla A. Saparov, <https://orcid.org/0009-0001-4291-1334>; © Kanatbay A. Ismailov, <https://orcid.org/0000-0003-2867-0826>

REFERENCES

- [1] Z. Saparniyazova, T. Ismaylov, G. Abdireymova, G. Turmanova, and T.Kh. Hakimov, "Influence of γ - radiation on the properties of silicon with clusters impurity atoms of manganese and nickel," E3S Web of Conferences, **289**, 07020 (2021).
- [2] B.I. Boltaks, *Diffusion in semiconductors*, (State publishing house of physical and mathematical literature, Moscow, 1971). (in Russian)
- [3] S.I. Vlasov, and F.A. Saparov, "Effect of pressure on the electric properties of passivating coatings based on lead borosilicate glasses," Surface Engineering and Applied Electrochemistry, **47**(4), 338-339 (2011). <http://dx.doi.org/10.3103%2FS1068375511040156>
- [4] Z.M. Saparniyazova, K.A. Ismailov, A.K. Uteniyazov, and Kh.U. Kamalov, "Effect of the diffusion temperature on interaction of clusters with impurity atoms in silicon," Semiconductor Physics, Quantum Electronics and Optoelectronics, **24**(1), 22-25 (2021). <https://doi.org/10.15407/spqeo24.01.022>
- [5] K.M. Iliyev, Z.M. Saparniyazova, K.A. Ismailov, O.E. Sattarov, and S. Nigmonkhadzhaev, "Interaction of radiation defects with nickel atom clusters in silicon," Surf. Engin. Appl. Electrochem. **47**(5), 385-387 (2011). <https://doi.org/10.3103/S1068375511050103>
- [6] Kh.S. Daliev, Sh.B. Utamuradova, O.A. Bozorova, and Sh.Kh. Daliev, "Joint effect of Ni and Gf impurity atoms on the silicon solar cell photosensitivity," Applied Solar Energy, **41**(1), 80-81 (2005). <https://www.researchgate.net/publication/294234192>
- [7] Sh.B. Utamuradova, Kh.S. Daliev, E.K. Kalandarov, and Sh.Kh. Daliev, "Features of the behavior of lanthanum and hafnium atoms in silicon," Technical Physics Letters, **32**(6), 469-470 (2006). <https://doi.org/10.1134/S1063785006060034>
- [8] Sh.Kh. Daliev, and F.A. Saparov, "On the properties of the Si-SiO₂ transition layer in multilayer silicon structures", East European Journal of Physics, (4), 206-209 (2023), <https://doi.org/10.26565/2312-4334-2023-4-25>.

- [9] Sh.B. Utamuradova, Sh.Kh. Daliev, D.A. Rakhmanov, A.S. Doroshkevich, V.A. Kinev, O.Yu. Ponamareva, et al., *Advanced Physical research*, **5**(2), 73-80 (2023). http://jomardpublishing.com/UploadFiles/Files/journals/APR/V5N2/Utamuradova_et_al.pdf
- [10] S.B. Utamuradova, S.Kh. Daliev, E.M. Naurzalieva, and X.Yu. Utemuratova, "Investigation of defect formation in silicon doped with silver and gadolinium impurities by raman scattering spectroscopy", *East European Journal of Physics*, (3), 430–433 (2023). <https://doi.org/10.26565/2312-4334-2023-3-47>
- [11] A. Muratov, Z. Saparniyazova, I.I. Bakhdirov, and A. Bijanov, "Analysis of electricity loss calculation methods in distribution networks," *E3S Web of Conferences*, **289**, 07017 (2021).
- [12] S.I. Vlasov, F.A. Saparov, and K.A. Ismailov, "Effect of pressure on the characteristics of Schottky barrier diodes made of overcompensated semiconductor," *Semiconductor physics, quantum electronics & optoelectronics*, **13**(4), 363-365 (2010). http://journal-spqeo.org.ua/n4_2010/v13n4-2010-p363-365.pdf
- [13] Sh.B. Utamuradova, A.V. Stanchik, and D.A. Rakhmanov, "X-ray structural investigations of n-Si<P> irradiated with protons", *East European Journal of Physics*, (2), 201-205 (2023). <https://doi.org/10.26565/2312-4334-2023-2-21>
- [14] Abdurakhmanov K.P., Kulikov G.S., Lebedev A.A., Utamuradova Sh. B., and Yusupova S.A. "Influence of Oxygen and Carbon on the behavior of manganese in n-type Si", *Soviet physics semiconductors-USSR*, **25**(6), 648-650 (1991). <https://istina.msu.ru/journals/419406/> (in Russian)
- [15] Sh.Kh. Daliev, Y.A. Saydimov, F.A. Saparov, and F.B. Umarov, "Influence of pressure on characteristics metal-semiconductor interface boundaries", in: *Proceedings of the 1st International Scientific and Practical Internet Conference, "Importance of Soft Skills for Life and Scientific Success,"* (FOP Marenichenko, V.V., Dnipro, Ukraine, 2022). pp.41-45. https://ibn.idsi.md/sites/default/files/imag_file/Importance%20of%20Soft%20Skills%20for%20Life%20and%20Scientific%20Success_2022-1.pdf
- [16] D.M. Esbergenov, E.M. Naurzalieva, and S.A. Tursinbaev, "Enhancing the perfection of a silicon crystal doped with nickel and zinc impurities", *East European Journal of Physics*, (4), 172-176 (2023), <https://doi.org/10.26565/2312-4334-2023-4-19>
- [17] Sh.B. Utamuradova, K.S. Daliev, Sh.Kh. Daliev, and U.K. Erugliev, Capacitive spectroscopy of deep levels in silicon with samarium impurity, *East European Journal of Physics*, (4), 303 (2023), <https://doi.org/10.26565/2312-4334-2023-4-39>
- [18] Kh.S. Daliev, Sh.B. Utamuradova, O.A. Bozorova, and Sh.Kh. Daliev, "Joint influence of impurity atoms of nickel and hafnium on photosensitivity of silicon solar cells," *Geliotekhnika*, (1), 85–87 (2005).
- [19] S.B. Utamuradova, Z.T. Azamatov, M.A. Yuldoshev, N.N. Bazarbayev, and A.B. Bakhromov, "Investigations of nonlinear optical properties of lithium niobate crystals," *East European Journal of Physics*, (4), 147 (2023). <https://doi.org/10.26565/2312-4334-2023-4-15>
- [20] A.Yu. Leyderman, R.A. Ayukhanov, R.M. Turmanova, A.K. Uteniyazov, and E.S. Esenbaeva, "Non-recombination injection mode," *Semiconductor Physics, Quantum Electronics and Optoelectronics*, **24**(3), 248-254 (2021). <https://doi.org/10.15407/spqeo.24.03.248>
- [21] N.A. Turgunov, E.Kh. Berkinov, and R.M. Turmanova, "The effect of thermal annealing on the electrophysical properties of samples n-Si<Ni, Cu>," *East European Journal of Physics*, (3), 287 (2023). <https://doi.org/10.26565/2312-4334-2023-3-26>

ВПЛИВ УМОВ ЛЕГУВАННЯ НА ВЛАСТИВОСТІ КЛАСТЕРІВ АТОМІВ НІКЕЛЮ

Канатбай А. Ісмаїлов^b, Зліха М. Сапарніязова^b, Гульчехра Т. Кудешова^b,
Гульбадан А. Сейтімбетова^b, Файзулла А. Сапаров^a

^a Інститут фізики напівпровідників і мікроелектроніки при Національному університеті Узбекистану
100057, Ташкент, вул. Янгі Алмазар, 20, Узбекистан

^b Каракалпакський державний університет. вул. Ч. Абдірова 1, Нукус, Каракалпакстан, 230100, Узбекистан

Показано, що динаміка зміни стану кластерів нікелю залежить від максимальної температури дифузії та швидкості охолодження. Встановлено, що зі збільшенням температури відпалу та швидкості охолодження спостерігається збільшення щільності та зменшення розміру кластерів. При цьому основна увага приділялася визначенню закономірностей зміни щільності, розмірів і структури кластерів від температури та охолодження. Процес і динаміка взаємодії кластерів залежить від коефіцієнта дифузії домішкових атомів у ґратці та рівня перенасичення твердого розчину. Встановлено, що при зміні температури відпалу від $T = 1100^{\circ}\text{C}$ до 1250°C щільність кластерів зростає майже на 1-1,5 порядків, а їх розмір зменшується в 5-6 разів. Вірогідно, що для отримання кластерів з відтворюваними параметрами оптимальна швидкість охолодження становить $200\text{--}300^{\circ}\text{C}$.

Ключові слова: кремній; кластер домішок; допінг; дифузія; швидкість охолодження; наноструктура; коефіцієнт дифузії; щільність кластерів

EFFECT OF ELECTRON TRANSPORT LAYERS, INTERFACE DEFECT DENSITY AND WORKING TEMPERATURE ON PEROVSKITE SOLAR CELLS USING SCAPS 1-D SOFTWARE

 **Abubakar S. Yusuf^{a,b,*}, A.M. Ramalan^c, A.A. Abubakar^a, I.K. Mohammed^a**

^a Department of Physics, Federal University of Technology, P.M.B. 65, Minna, Nigeria

^b Department of Physics and Astronomy, Auckland University of Technology, New Zealand

^c Department of Physics, University of Abuja, P.M.B. 117, Abuja, Nigeria

*Corresponding Author e-mail: ayusuf@futminna.edu.ng, abubakar.yusuf@autuni.ac.nz

Received November 29, 2023; revised December 17, 2023; accepted December 30, 2023

Perovskite solar cells have garnered significant attention from solar cell researchers due to their potential for achieving high efficiency, primarily attributed to their exceptional Electron Transport layer (ETL). One of the key elements of perovskite solar cells for transporting electrons to generate current is the ETL material. Moreover, there is a promising avenue for enhancing stability and reducing fabrication costs by substituting the transport layer. In this study, TiO₂ and SnO₂ were used as ETL materials in the architecture of perovskite solar cells for a comparative analysis between two devices featuring distinct structures: TiO₂/CH₃NH₃PbI₃/Spiro-OMeTAD and SnO₂/CH₃NH₃PbI₃/Spiro-OMeTAD. To evaluate the performance of each electron transport layer (ETL), the SCAPS 1D tool was employed. The investigation involved varying the thickness of the electron transport layers, interface defect density and working temperature, allowing for a comprehensive assessment of key parameters such as voltage at open circuit (V_{oc}), short circuit current density (J_{sc}), fill factor (FF), and overall efficiency (PCE%). Remarkably, when employing SnO₂ as the ETL, the achieved efficiency stands at 10.10%. In contrast, utilizing TiO₂ as the ETL yields a slightly higher efficiency of 12.84%. These findings underline the nuanced influence of transport layer materials on the overall performance of perovskite solar cells.

Keywords: Perovskite; Solar cell; SCAP-1D

PACS: 02.60.Cb, 61.72.-y, 42.79.Ek, 84.60.Jt

INTRODUCTION

Global worries about the depletion of fossil fuels have led to an increasing demand for renewable energy sources considering recent technological advancements. Permanent resources may be provided by renewable energy; all that is needed for researchers to take use of these natural resources is to broaden their study scope. Solar energy is among the most promising renewable energy sources [1]. As a result, creating a new solar cell technology with higher power conversion efficiency (PCE) and lower processing costs will take a great deal of work. These days, organic and inorganic halide perovskite solar cells are simple to fabricate in a variety of locations, meet the aforementioned properties, and offer intrinsic benefits such as a high absorption coefficient, long carrier-diffusion length, and high carrier mobility [2]. They are thus very desirable for the next solar cell technologies. However, Kojima et al. from Tsutomu Miyasaka's Tokyo-based company built the first perovskite solar cell with a PCE of 2.2% in 2006 [3] and after a few years, they enhanced it to 3.8% [4]. Therefore, in less than one decade, perovskite-based solar cells jumped to a PCE of 25.2% in 2019 [5]. Enhancement of the device structure and perovskite material is the key to improving the performance of perovskite-based solar cells. The use of perovskite solar cells using methylammonium lead tri-iodide-based perovskite material is the subject of many investigations (MAPbI₃). This later is composed of ABX₃ structure, where A represents methylammonium (MA, CH₃NH₃), B is lead (Pb) and X represents a halide material anion, iodide (I). Despite the high performance provided by lead halide perovskite material, the factor of instability and toxicity may hamper its commercial production [6-8]. The better way to improve these factors, More recently, several mixed halide perovskite materials have been widely implemented as absorber layers in PSCs to further enhance the efficiency and stability [9], Ito et al. examined PSC with mixed Sn-Ge perovskite absorber layer (FA_{0.75}MA_{0.25}Sn_{0.95}Ge_{0.05}I₃) and reported PCE of 4.48% with improved stability in air due to the added Ge [10]. Afterwards, Ng et al. fabricated another mixed Sn-Ge perovskite cell and achieved PCE of 7.9%, short-circuit current density (J_{sc}) of 25.5 mA/cm², open-circuit voltage (V_{oc}) of 0.45 V and fill factor (FF) of 0.69 [11]. This far lower PCE of Sn-Ge-based PSCs in comparison with that of Pb-based PSCs is mainly attributed to their low open-circuit voltage which is due to the undesirable oxidation of Sn and consequently increased defect density [12]. In 2020, Minamoto et al. theoretically analysed mixed Sn-Ge perovskite solar cell with an inverted p-i-n planar structure and revealed that V_{oc} is strongly affected by built-in potential (V_{bi}) across the perovskite absorber layer, where V_{bi} is dominantly determined by the conduction band minimum (CBM) of the electron transport layer (ETL) and/or work function of back contact [9]. They showed that by optimizing the conduction band offset of perovskite and ETL as well as choosing suitable back contact, an improved V_{oc} of 0.93 V (PCE of 19.4%) can be achieved [9, 13]. According to the properties of Pb-, Sn-, Ge- and SnGe- based perovskites, we think that an appropriate combination of these layers as absorber layers in PSCs may lead to better performance in a wider range of solar spectrum. In this line of thought, Farhadi et al. [13] very recently have simulated and investigated a perovskite solar cell with a double absorber layer (MASnI₃/MAPbI₃) and achieved a high PCE of 30.88%.

In this study, using SCAPS-1D simulation tool [14], we propose and simulate a novel PSC structure with double ETLs layers consisting of TiO_2 and SnO_2 , $\text{TiO}_2/\text{SnO}_2$, and $\text{TiO}_2/\text{SnO}_2/\text{MAPbI}_3$ to take advantage of different ETLs important properties. Furthermore, we compare the output performance of the proposed cell with single and double ETL layers PSCs to show the efficiency improvement in double ETL layers PSC. Moreover, we concentrate on the effect of carrier transport materials, thickness of ETLs layers, interface defect density and working temperature on the efficiency of the proposed single and double ETL layers PSC. The improved performance of the proposed double ETL layers PSC can pave the path for further studies to fabricate experimentally and make benefit out of using double ETL layers layer in perovskite solar cells. Figure 1 and 2 display the perovskite solar cell layers using SCAPS-1D and SCAPS-1D define panel with each layers name.

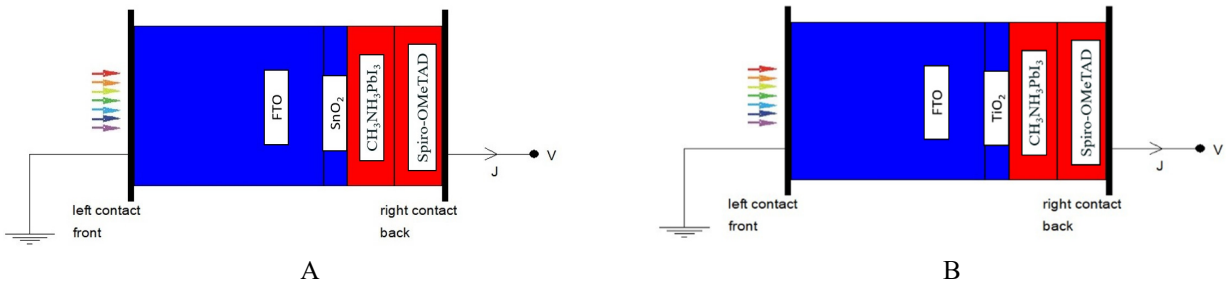


Figure 1. Perovskite solar cell layer with SCAPS-1D

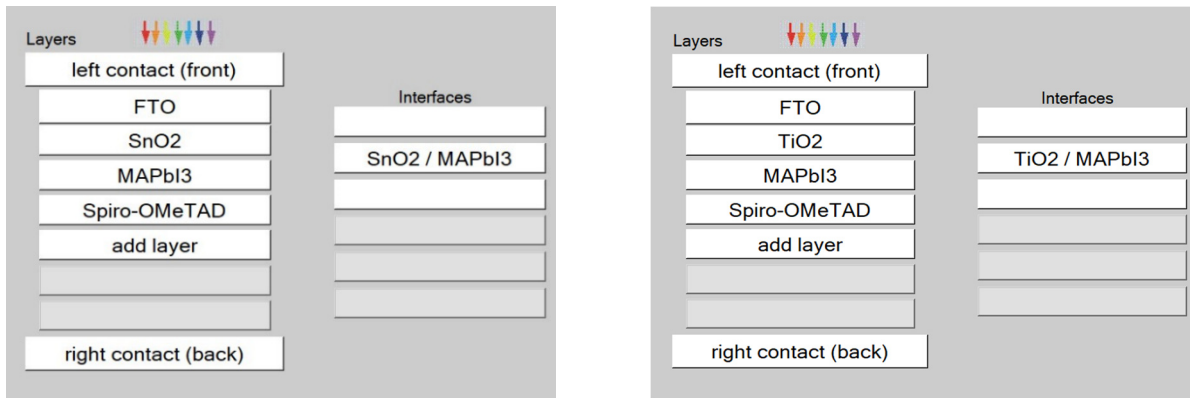


Figure 2. SCAPS-1D define panel with layers name

2. SCAPS-1D SIMULATION

A one-dimensional solar cell simulation tool will be used to replicate PSC and has been used to research several solar cell types, including CZTS, CIGS, and others [15, 16]. In contrast to other software, SCAPS features a very user-friendly operation window and a variety of grading, fault and recombination model options [17]. It acts like a real-life counterpart once all parameters have been defined [18]. Up to seven (7) semiconductor layers can be used to identify the primary characteristics of SCAPS, including the materials and defective attributes. By resolving the semiconductor fundamental equations, this software can simulate and help with the analysis of the J-V characteristics curve, the ac characteristics (C-V and C-f), the device's spectral response (QE), the open circuit voltage, the fill factor (FF), the short-circuit current (J_{sc}), and the power conversion efficiency (PCE) (V_{oc}), the energy bands of the materials used in solar cells, and the concentration of various materials [19]. Figure 3 below shows the working procedure of a SCAPS-1D.

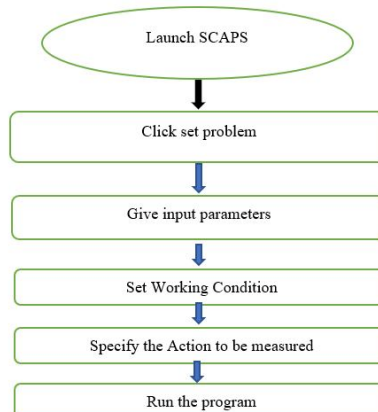


Figure 3. SCAPS working procedure

Numerical simulation was carried out using a software called The University of Gent created the Solar Cell Capacitance Simulator (SCAPS) [14] it was used to determine the influence of electron transport and perovskite active layers on solar cells parameters (Jsc, Voc, FF, and efficiency), various simulations were conducted to investigate the effects of ETLs with thicknesses ranging from 30 to 100 nm, the interface defect density (ETL/Perovskite absorber) varying from 10^{14} to 10^{19} , and the effect of temperature varying from 300 to 350K. The data used in the simulation and material parameters in SCAPS were implemented from theories and works of literature [20-25].

2.1. Numerical Simulation

The SCAPS-1D programme (solar cell capacitance simulator one dimension) was used to simulate solar cells by numerically resolving the one-dimensional Poisson and continuity equations that control semiconductor material under steady-state conditions [14]. The relationship between a p-n junction's electric field (E) and space charge density (ρ) is shown by the Poisson equation, which is represented by:

$$\frac{\partial^2 \phi}{\partial x^2} = \frac{\partial E}{\partial x} = -\frac{\rho}{\epsilon_s} = -\frac{q}{\epsilon_s} [p - n + N_D^+(x) - N_A^-(x) \pm N_t(x)] \quad (1)$$

Where N^+ , N , and N_t are the densities of ionized donors and acceptors, respectively, and where is the electrostatic potential, q is the elementary charge, s is the medium's static relative permittivity [26]. The following equations represent the electron and hole continuity in steady state:

$$\frac{\partial j_n}{\partial x} + G - R_n(n, p) = 0 \quad (2)$$

$$-\frac{\partial j_p}{\partial x} + G - R_p(n, p) = 0 \quad (3)$$

where R_n , R_p are the net rates of electron and hole recombination, G is the rate at which electron-hole pairs are created, and j_n , j_p are the current densities of electrons and holes. These equations provide the electron and hole current densities:

$$j_n = qu\mu_n E + qD_n \frac{\partial n}{\partial x} \quad (4)$$

$$j_p = qp\mu_p E + qD_p \frac{\partial p}{\partial x} \quad (5)$$

where q is the fundamental charge, n , p are the electron and hole mobilities, and D_n , D_p are the electron and hole diffusion coefficients. The SCAPS-1D program can simulate solar cells with up to seven layers and extract the fundamental properties of the cells, including their band diagram, generation and recombination rates, external quantum efficiency, cell current densities, J-V characteristic include power conversion efficiency, fill factor, open-circuit voltage, and short-circuit current.

To have a successful replication of the simulation carried out by [27], The simulation's parameters are taken from literature, experimental research, and theoretical study. The details for each layer are summarized in Table 1 [28-33].

Table 1. perovskite solar cell input parameters [27].

Parameters	ITO [30, 31]	TiO ₂ [29, 32]	SnO ₂ [33]	MAPbI ₃ (CH ₃ NH ₃ PbI ₃) [34]	Spiro-OmeTAD [29]
Thickness (nm)	300	30	30	100	100
Band gap (eV)	3.6	3.26	3.5	1.51	2.9
Electron affinity (eV)	4.2	4.2	4.0	4.0	2.2
Dielectric permittivity	10	10	9.0	6.6	3
CB effective density of states (cm ⁻³)	2.10 ¹⁸	2.2.10 ¹⁸	2.2.10 ¹⁷	1.2.10 ¹⁹	2.2.10 ¹⁸
VB effective density of states (cm ⁻³)	1.8.10 ¹⁹	1.8.10 ¹⁸	2.2.10 ¹⁷	2.9.10 ¹⁸	1.8.10 ¹⁸
Thermal velocity of electrons (cm/s)	10 ⁷	10 ⁷	10 ⁷	10 ⁷	10 ⁷
Thermal velocity of holes (cm/s)	10 ⁷	10 ⁷	10 ⁷	10 ⁷	10 ⁷
Electron mobility (cm ² /Vs)	50	20	20	2.7	10 ⁻⁴
Hole mobility (cm ² /Vs)	75	10	10	1.8	10 ⁻⁴
Shallow donor density N_D (cm ⁻³)	10 ¹⁹	10 ¹⁷	10 ¹⁵	0	0
Shallow acceptor density N_A (cm ⁻³)	0	0	0	1.3.10 ¹⁶	10 ¹⁸
Defect density N_t (cm ⁻³)	10 ¹⁵	10 ¹⁵	10 ¹⁸	4.10 ¹³	10 ¹⁵

3. RESULT AND DISCUSSION OF THE SIMULATION

3.1. Effect of the ETL (TiO₂) Thickness

Figure 4a show the $J-V$ performance of the device with varying TiO₂ thickness from 30 to 100 nm under illumination and in the dark. **Figure 4b** displays the QE for different TiO₂ thicknesses versus wavelength. Our study's findings demonstrate that when TiO₂ thickness increases, all photovoltaic parameters rise as well. This is explained by the TiO₂ layer's fractional absorption of incoming light and its greater transmittance, which prevents solar irradiance from reaching the perovskite skeleton [35]. Ranging the thickness from 30 to 100 nm causes the QE versus wavelength curve

to have a spectrum overlap, which is explained by a constant optical absorption efficiency within the chosen thickness values. The ideal thickness of TiO₂ is 100 nm, demonstrating a PCE of 12.89%, FF of 84.29%, J_{sc} of 12.13 mA/cm², and V_{oc} of 1.26 V.

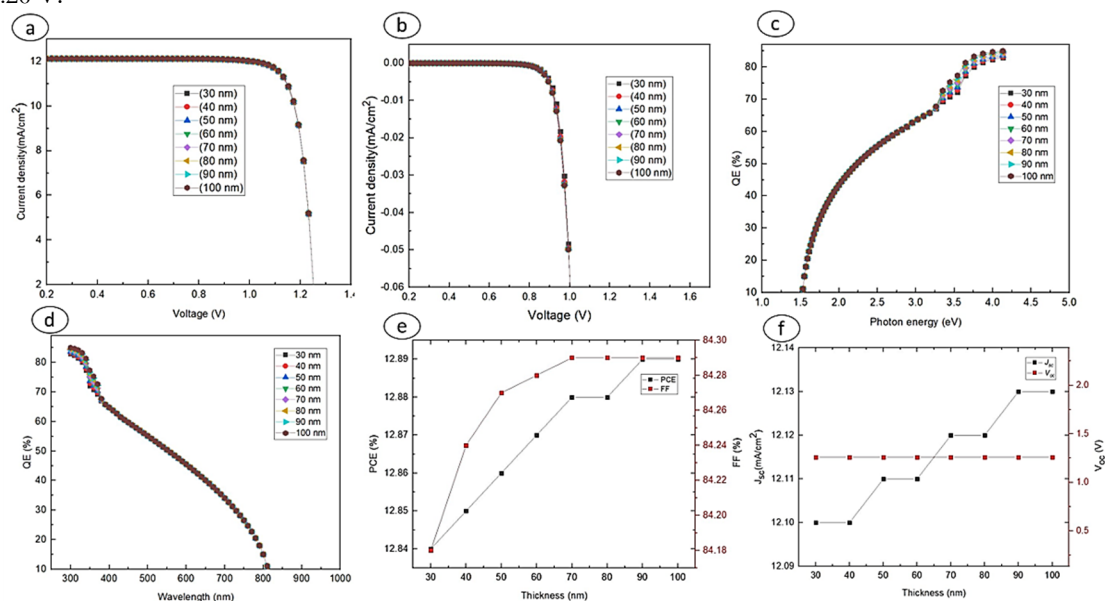


Figure 4. a - $J-V$ curve with varied ETM thickness under illumination; b - $J-V$ plot with varied ETM thickness in the dark; c - QE curve with respect to photon energy; d - QE curve with respect to wavelength; e - PCE and FF with respect to thickness, and f - J_{sc} and V_{oc} with respect to varied ETM thickness

3.2. Effect of the ETL (SnO₂) Thickness

Figure 5a show the $J-V$ performance of the device with varying SnO₂ thickness from 30 to 100 nm under illumination and in the dark. Figure 5b shows the QE against wavelength for varying SnO₂ thicknesses. The findings of our study demonstrate that as SnO₂ thickness increases, all photovoltaic parameters drop. This is explained by the SnO₂ layer's fractional absorption of incoming light and its reduced transmittance, which inhibits solar irradiance on the perovskite skeleton [35]. Ranging the thickness from 30 to 100 nm leads to a spectrum overlap in the QE versus wavelength graph. This is explained by the optical absorption efficiency being constant throughout the chosen thickness ranges. The optimum SnO₂ thickness is 30 nm, demonstrating a PCE of 10.10%, FF of 69.40%, J_{sc} of 12.07 mA/cm², and V_{oc} of 1.20 V.

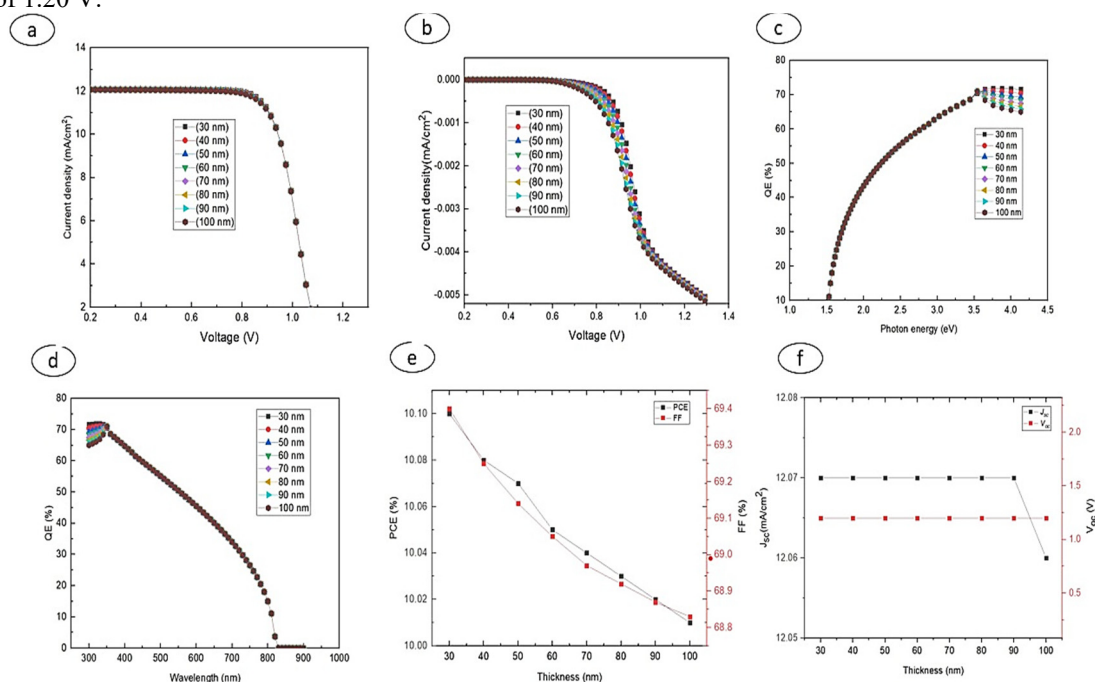


Figure 5. a - $J-V$ curve with varied ETL thickness under illumination; b - $J-V$ plot with varied ETL thickness in the dark; c - QE curve with respect to photon energy; d - QE curve with respect to wavelength; e - PCE and FF with respect to thickness, and f - J_{sc} and V_{oc} with respect to varied ETL thickness

3.3 Effect of the ETL (TiO₂/SnO₂) Thickness

First, we may clarify the stability in FF; FF indicates the caliber of the solar cell and is connected to the characteristics of the active layer. Because V_{oc} and E_g have a relationship, the perovskite layer band gap remains unchanged, which accounts for V_{oc} stability. The increase in light absorption in the TiO₂/SnO₂ layer with increasing layer thickness is the second factor contributing to the decline in J_{sc} . More proof can be drawn from examining the quantum efficiency curve, which indicates that this has an impact on the number of photons transmitted to the active layer (in this case, Perovskite), which then leads to a reduction in the photo-generated carriers in these layers. The quantum efficiency at short wavelengths increases with increasing TiO₂/SnO₂ thickness (300-380 nm). The short wavelengths are known to be absorbed close to the solar cell's surface and away from the effective region. As a result, fewer carriers are produced to produce the desired effects, which reduces the short-circuit current. where the relationship between the quantum efficiency and the short circuit current density is direct. Solar cell's power conversion efficiency (PCE) also drops as the J_{sc} falls [36]. The optimum TiO₂/SnO₂ thickness is 30 nm, demonstrating a PCE of 12.68%, FF of 83.48%, J_{sc} of 12.09 mA/cm², and V_{oc} of 1.25 V.

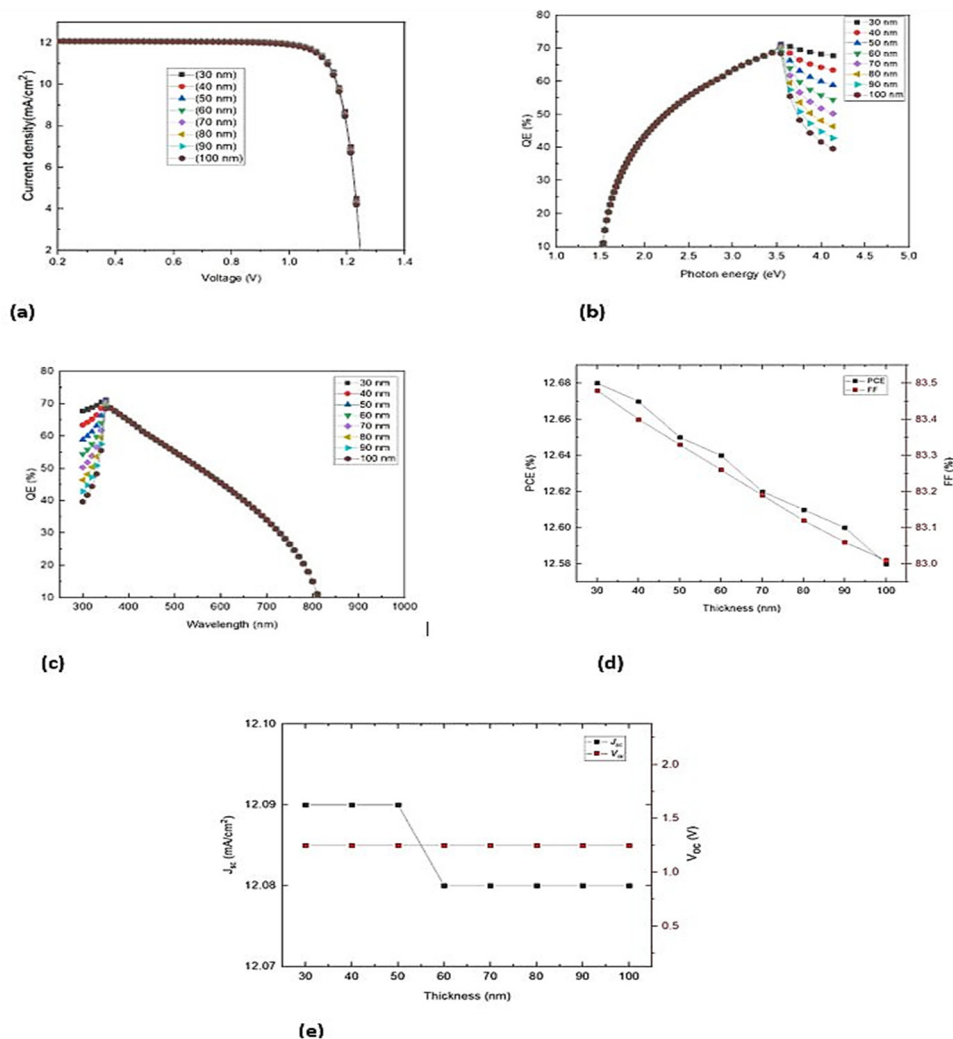


Figure 6. a $J-V$ curve with varied ETM thickness under illumination. b QE curve concerning photon energy. c QE curve concerning wavelength. d PCE and FF concerning thickness and e J_{sc} and V_{oc} concerning varied ETM thickness

3.4 Effect of Interface defect density TiO₂/MAPbI₃

Due to the discontinuity in structure of solar cells, there is a high likelihood of introducing localised defect states between two-layer interfaces. Minority carrier recombination velocities are the best way to quantify the impact of defect interface density [37]. To investigate how the interface flaw affects the TiO₂/MAPbI₃ interface of PSCs, the N_t was varied from 10^{14} to 10^{19} cm⁻² while keeping other parameters unchanged. **Figure 7a** shows the $J-V$ curve with varied interface defects, while **Figure 7b** shows the PCE and FF concerning the interface defect, and **Figure 7c** depicts the J_{sc} and V_{oc} in relation to the defect density at the contact. Based on the findings, the photovoltaic parameters (PCE, FF, J_{sc} , and V_{oc}) decreased with increasing the defect density from 10^{14} to 10^{19} cm⁻². Consequently, while creating PSCs with a high PCE, the interface modification and film morphology to control N_t must be carefully managed. The optimum TiO₂/MAPbI₃ interface defect density is 10^{14} cm⁻², demonstrating a PCE of 10.19 %, FF of 82.19 %, J_{sc} of 12.10 mA/cm², and V_{oc} of 1.02 V.

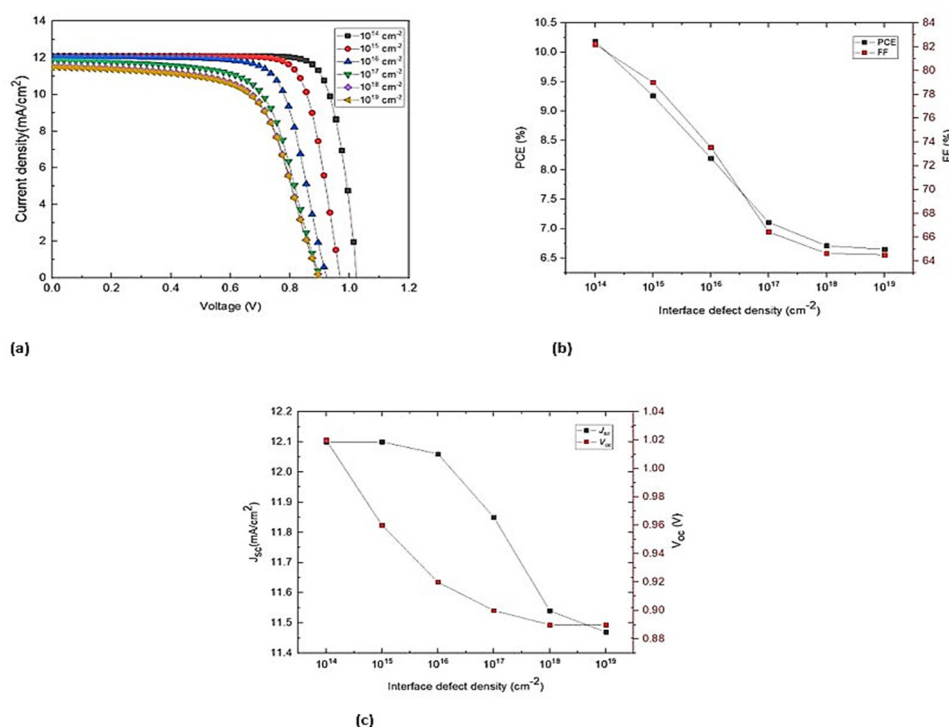


Figure 7. **a** $J-V$ curve with varied interface defect density. **b** The correlations of PCE and FF with interface defect and **c** J_{sc} and V_{oc} with interface defect density

3.5. Effect of Interface defect density on SnO₂/MAPbI₃

It is common for localized defect states to be introduced between two-layer interfaces because of the structural discontinuity in solar cells. Minority carrier recombination velocities provide the most accurate way to articulate the impact of defect interface density [37]. To investigate the impact the interface flaw has on the SnO₂/MAPbI₃ interface of PSCs, the N_t was varied from 10^{14} to 10^{19} cm⁻² while keeping other parameters unchanged.

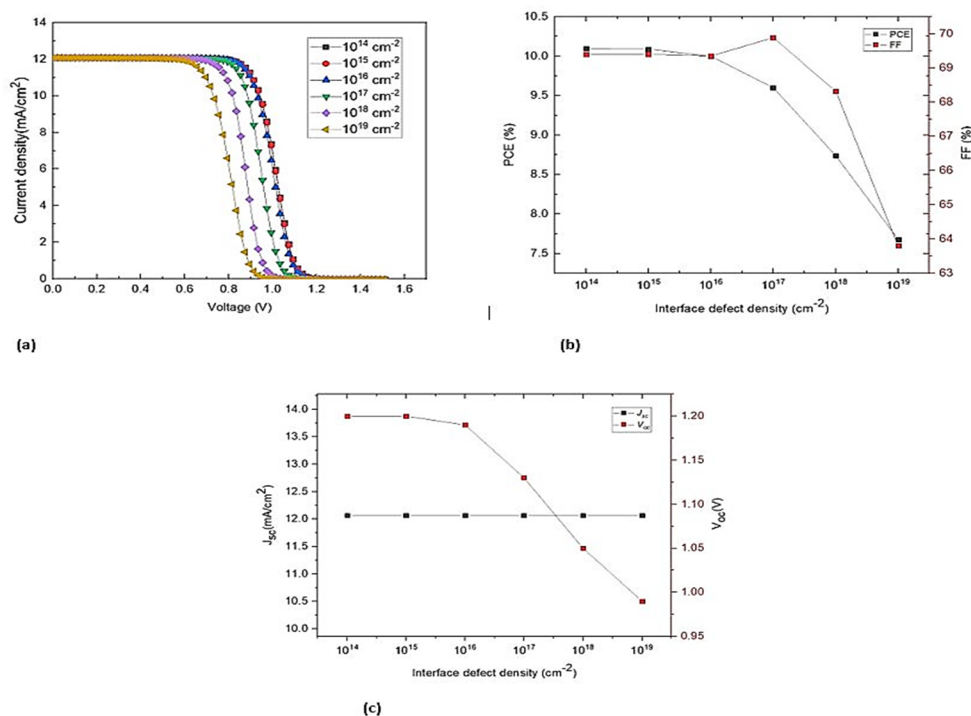


Figure 8. **a** $J-V$ curve with varied interface defect density. **b** The correlations of PCE and FF with interface defect and **c** J_{sc} and V_{oc} with interface defect density.

Figure 8a shows the $J-V$ curve with varied interface defects, while **Figure 8b** shows the PCE and FF concerning the interface defect, and **Figure 8c** depicts the J_{sc} and V_{oc} concerning the interface defect density. From the results

obtained, the photovoltaic parameters (PCE, FF, and V_{oc}) decreased with increasing the defect density from 10^{14} to 10^{19} cm^{-2} while J_{sc} remained unaltered. Consequently, while creating PSCs with a high PCE, the interface modification and film morphology to control N_t must be carefully managed. The optimum $\text{SnO}_2/\text{MAPbI}_3$ interface defect density is 10^{14} cm^{-2} demonstrating a PCE of 10.10 %, FF of 69.40 %, J_{sc} of 12.07 mA/cm^2 , and V_{oc} of 1.20 V.

3.6 Effect of Temperature on ETL (TiO_2)

An essential aspect in determining a solar cell device's output is its temperature. We used simulation to expose our gadget to temperatures between 300 and 350 K to examine its impact on its performance. When light is absorbed, PSC's temperature may rise and commonly rises beyond 300 K. [38]. **Figure 9. a–c** displays the temperature-dependent current density, PCE and FF, J_{sc} and V_{oc} .

In the current study, PCE, J_{sc} , V_{oc} , and FF all drop as temperature rises. This might be the result of the electron reaching an unstable state at a higher temperature after absorbing enough photons, which increases the rate of recombination and lowers the PCE, J_{sc} , V_{oc} , and FF [39]. The optimum TiO_2 temperature is 300 K, demonstrating a PCE of 10.10 %, FF of 69.40 %, J_{sc} of 12.07 mA/cm^2 , and V_{oc} of 1.20 V.

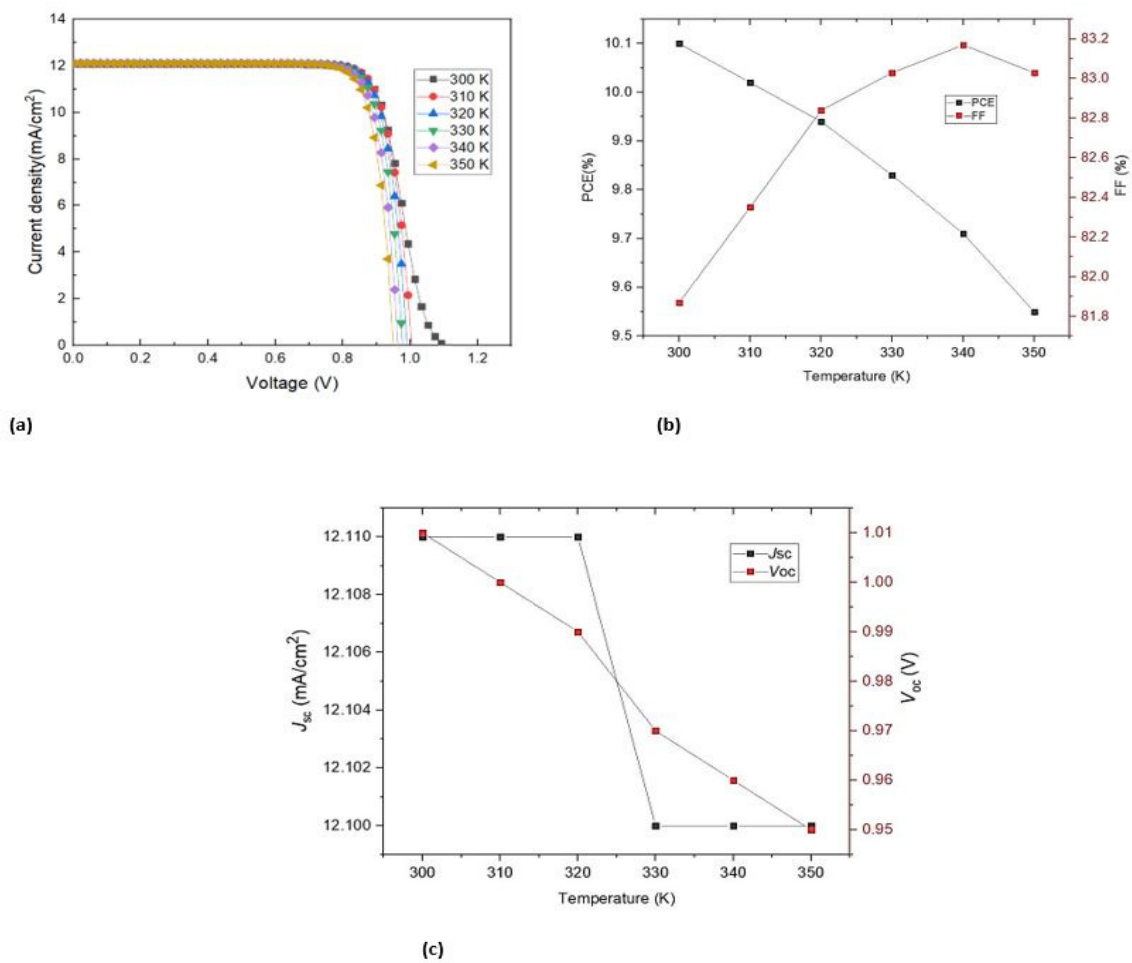


Figure 9. a J - V curve as a function of temperature. **b** Correlation of PCE and FF with temperature. **c** Correlation of J_{sc} and V_{oc} with temperature.

3.7 Effect of Temperature on ETL (SnO_2)

For solar cell devices output, temperature is a crucial determining element. Utilizing simulation, we subjected the device to temperatures between 300 and 350 K to examine its impact on the performance of our technology. When light is absorbed, PSC's temperature may rise and commonly rises beyond 300 K [38]. **Figure 10. a–c** shows the current density, PCE and FF, and J_{sc} and V_{oc} in relation to temperature. The current study shows that a rise in temperature causes a fall in PCE, J_{sc} , V_{oc} , and FF. This might be as a result of the electron reaching an unstable state and absorbing enough photons at a higher temperature, which increases the rate of recombination and lowers the PCE., J_{sc} , and V_{oc} [39]. The optimum SnO_2 temperature is 300 K, demonstrating a PCE of 8.52 %, FF of 67.22 %, J_{sc} of 12.07 mA/cm^2 , and V_{oc} of 1.04 V.

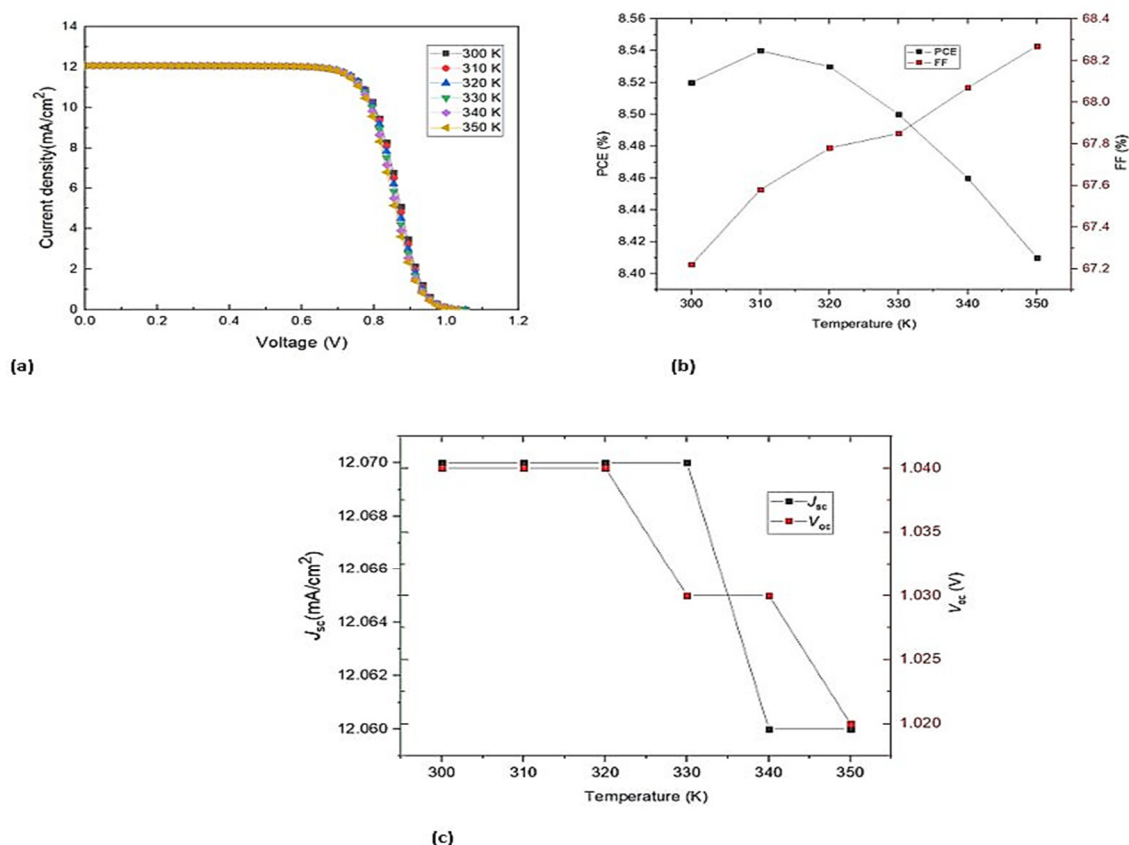


Figure 10. a - J - V curve as a function of temperature; b - Correlation of PCE and FF with temperature; c - Correlation of J_{sc} and V_{oc} with temperature.

4. SUMMARY OF THE SIMULATION RESULTS

In this work, the perovskite solar cell structure $\text{TiO}_2/\text{CH}_3\text{NH}_3\text{PbI}_3/\text{Spiro-OMeTAD}$ and $\text{SnO}_2/\text{CH}_3\text{NH}_3\text{PbI}_3/\text{Spiro-OMeTAD}$ is numerically modeled by carefully varying the effect of ETLs thickness, interface defect density and working temperature on charge carriers of the electron transport and perovskite active layers on the solar cells, we can conclude from the results obtained above that the thickness and temperature did not significantly enhance the device power conversion efficiency. But instead, the interface defect density had a significant enhancement on the device power conversion efficiency for both $\text{TiO}_2/\text{MAPbI}_3$ and $\text{SnO}_2/\text{MAPbI}_3$ which was found out to be at 10^{14}cm^{-2} with optimum values of PCE of 10.19 %, FF of 82.19 %, J_{sc} of 12.10 mA/cm², and V_{oc} of 1.02 V and PCE of 10.10 %, FF of 69.40 %, J_{sc} of 12.07 mA/cm², and V_{oc} of 1.20 V respectively. It could be concluded that the electron transport and perovskite active materials can transmit and absorb the light intensity of the photons and exhibit that by optimizing the interface defect density parameter, the device power conversion efficiency could be increased to a higher efficiency.

Funding

This work was funded by the Tertiary education trust fund (Tetfund) Nigeria.

Declaration of Competing Interest

The authors declare that they have no known competing financial interests or personal relationships that could have influenced the work reported in this study.

Data Availability

Data will be made available on request.

Acknowledgements

We express our heartfelt gratitude to Tetfund Nigeria for supporting this study.

©Abubakar Sadiq Yusuf, <https://orcid.org/0000-0001-8181-9728>

REFERENCES

- [1] P. Kumar, S. Kumar, A.A. Adelodun, and K.-H. Kim, "Solar energy: Potential and future prospects," *Renewable and Sustainable Energy Reviews*, **82**, 894-900 (2018). <https://doi.org/10.1016/j.rser.2017.09.094>
- [2] I. Kemerchou, F. Rogti, B. Benhaoua, A. Hima, and A. Khechekhouche, "Characterization of organic/inorganic perovskite material $\text{CH}_3\text{NH}_3\text{PbI}_3$ prepared by spray pyrolysis with moving nozzle method," *Recueil De Mécanique*, **4**(1), 342–348 (2019). <https://doi.org/10.5281/zenodo.3447388>
- [3] A. Kojima, K. Teshima, T. Miyasaka, and Y. Shirai, "Novel photoelectrochemical cell with mesoscopic electrodes sensitized by lead-halide compounds," *ECS Meeting Abstracts*, **MA2006-02**, 397 (2006). <https://doi.org/10.1149/MA2006-02/7/397>

- [4] A. Kojima, K. Teshima, Y. Shirai, and T. Miyasaka, "Organometal halide perovskites as visible-light sensitizers for photovoltaic cells," *Journal of the American Chemical Society*, **131**(17), 6050-6051 (2009). <https://doi.org/10.1021/ja809598r>
- [5] NREL, *National renewable energy laboratory: best research-cell efficiency chart*, (2021). <https://www.nrel.gov/pv/cell-efficiency.html>
- [6] M.K. Assadi, S. Bakhoda, R. Saidur, and H. Hanaei, "Recent progress in perovskite solar cells," *Renewable and Sustainable Energy Reviews*, **81**, 2812-2822 (2018). <https://doi.org/10.1016/j.rser.2017.06.088>
- [7] P. Cheng, and X. Zhan, "Stability of organic solar cells: challenges and strategies," *Chemical Society Reviews*, **45**(9), 2544-2582 (2016). <https://doi.org/10.1039/C5CS00593K>
- [8] L.P. Lekesi, L.F. Koao, S.V. Motloung, T.E. Motaung, and T. Malevu, "Developments on Perovskite Solar Cells (PSCs): A Critical Review," *Applied Sciences*, **12**(2), 672 (2022). <https://doi.org/10.3390/app12020672>
- [9] T. Minemoto, Y. Kawano, T. Nishimura, Q. Shen, K. Yoshino, S. Iikubo, S. Hayase, and J. Chantana, "Theoretical analysis of band alignment at back junction in Sn-Ge perovskite solar cells with inverted p-i-n structure," *Solar Energy Materials and Solar Cells*, **206**, 110268 (2020). <https://doi.org/10.1016/j.solmat.2019.110268>
- [10] N. Ito, M.A. Kamarudin, D. Hirotsu, Y. Zhang, Q. Shen, Y. Ogomi, S. Iikubo, et al., "Mixed Sn-Ge perovskite for enhanced perovskite solar cell performance in air," *The journal of physical chemistry letters*, **9**(7), 1682-1688 (2018). <https://doi.org/10.1021/acs.jpcclett.8b00275>
- [11] M. Ng, and J.E. Halpert, "Single crystals of mixed Br/Cl and Sn-doped formamidinium lead halide perovskites via inverse temperature crystallization," *RSC Adv*, **10**(7), 3832-3836 (2020). <https://doi.org/10.1039/D0RA00060D>
- [12] N.-G. Park, "Organometal perovskite light absorbers toward a 20% efficiency low-cost solid-state mesoscopic solar cell," *The Journal of Physical Chemistry Letters*, **4**(15), 2423-2429 (2013). <https://doi.org/10.1021/jz400892a>
- [13] B. Farhadi, M. Ciprian, F. Zabihi, and A. Liu, "Influence of contact electrode and light power on the efficiency of tandem perovskite solar cell: Numerical simulation," *Solar Energy*, **226**, 161-172 (2021). <https://doi.org/10.1016/j.solener.2021.08.043>
- [14] M. Burgelman, P. Nollet, and S. Degraeve, "Modelling polycrystalline semiconductor solar cells," *Thin solid films*, **361**, 527-532 (2000). [https://doi.org/10.1016/S0040-6090\(99\)00825-1](https://doi.org/10.1016/S0040-6090(99)00825-1)
- [15] Y.H. Khattak, *Doct. Thesis, Modeling of high power conversion efficiency thin film solar cells*, Universitat Politècnica de València, 2019. <https://doi.org/10.4995/Thesis/10251/118802>
- [16] M. Burgelman, K. Decock, A. Niemegeers, J. Verschraegen, and S. Degraeve, *SCAPS manual*, (University of Gent Department of Electronics and Information Systems (ELIS) Campus Ardoyen, Technologiepark 914, Grote Steenweg Noord 9052 Gent-Zwijnaarde 'Belgium', 2016).
- [17] A. Husainat, W. Ali, P. Cofie, J. Attia, and J. Fuller, "Simulation and analysis of methylammonium lead iodide (CH₃NH₃PbI₃) perovskite solar cell with Au contact using SCAPS 1D simulator," *American Journal of Optics and Photonics*, **7**(2), 33 (2019). <https://doi.org/10.11648/j.ajop.20190702.12>
- [18] B.M. Soucase, I.G. Pradas, and K.R. Adhikari, "Numerical simulations on perovskite photovoltaic devices," in: *Perovskite Materials - Synthesis, Characterisation, Properties, and Applications*, edited by L. Pan, and G. Zhu, **445**, (IntechOpen, 2016). <https://doi.org/10.5772/61751>
- [19] Hazeghi, F. and S.M.B. Ghorashi, "Simulation of perovskite solar cells by using CuSCN as an inorganic hole-transport material," *Materials Research Express*, **6**(9), 095527 (2019). <https://doi.org/10.1088/2053-1591/ab2f1b>
- [20] T. Pu, H. Shen, and Q. Tang, "Simulation of a charged Al₂O₃ film as an assisting passivation layer for a-Si passivated contact P-type silicon solar cells," *Silicon*, **14**(7), 3339-3348 (2022). <https://doi.org/10.1007/s12633-021-01105-4>
- [21] S.T. Jan, and M. Noman, "Influence of layer thickness, defect density, doping concentration, interface defects, work function, working temperature and reflecting coating on lead-free perovskite solar cell," *Solar Energy*, **237**, 29-43 (2022). <https://doi.org/10.1016/j.solener.2022.03.069>
- [22] R. Kotipalli, B. Vermang, J. Joel, R. Rajkumar, M. Edoff, and D. Flandre, "Investigating the electronic properties of Al₂O₃/Cu(In, Ga) Se₂ interface," *AIP Advances*, **5**(10), 107101 (2015). <https://doi.org/10.1063/1.4932512>
- [23] K. Tan, P. Lin, G. Wang, Y. Liu, Z. Xu, and Y. Lin, "Controllable design of solid-state perovskite solar cells by SCAPS device simulation," *Solid-State Electronics*, **126**, 75-80 (2016). <https://doi.org/10.1016/j.sse.2016.09.012>
- [24] H. Abedini-Ahangarkola, S. Soleimani-Amiri, and S.G. Rudi, "Modeling and numerical simulation of high efficiency perovskite solar cell with three active layers," *Solar Energy*, **236**, 724-732 (2022). <https://doi.org/10.1016/j.solener.2022.03.055>
- [25] J. Lontchi, M. Zhukova, M. Kovacic, J. Krc, W.-C. Chen, M. Edoff, S. Bose, et al., "Optimization of Back Contact Grid Size in Al₂O₃-Rear-Passivated Ultrathin CIGS PV Cells by 2-D Simulations," *IEEE Journal of Photovoltaics*, **10**(6), 1908-1917 (2020). <https://doi.org/10.1109/JPHOTOV.2020.3012631>
- [26] T. Minemoto, and M. Murata, "Impact of work function of back contact of perovskite solar cells without hole transport material analyzed by device simulation," *Current Applied Physics*, **14**(11), 1428-1433 (2014). <https://doi.org/10.1016/j.cap.2014.08.002>
- [27] D. Stanić, V. Kojić, T. Čižmar, K. Juraić, L. Bagladi, J. Mangalam, T. Rath, and A. Gajović, "Simulating the performance of a formamidinium based mixed cation lead halide perovskite solar cell," *Materials*, **14**(21), 6341 (2021). <https://doi.org/10.3390/ma14216341>
- [28] S. Abdelaziz, A. Zekry, A. Shaker, and M. Abouelatta, "Investigating the performance of formamidinium tin-based perovskite solar cell by SCAPS device simulation," *Optical Materials*, **101**, 109738 (2020). <https://doi.org/10.1016/j.optmat.2020.109738>
- [29] S. Bansal, and P. Aryal, "Evaluation of new materials for electron and hole transport layers in perovskite-based solar cells through SCAPS-1D simulations," in: *2016 IEEE 43rd Photovoltaic Specialists Conference (PVSC)*, (IEEE, 2016). pp.1-4. <https://doi.org/10.1109/PVSC.2016.7749702>
- [30] H.-J. Du, W.-C. Wang, and J.-Z. Zhu, "Device simulation of lead-free CH₃NH₃SnI₃ perovskite solar cells with high efficiency," *Chinese Physics B*, **25**(10), 108802 (2016). <https://doi.org/10.1088/1674-1056/25/10/108802>
- [31] D. Liu, and T.L. Kelly, "Perovskite solar cells with a planar heterojunction structure prepared using room-temperature solution processing techniques," *Nature photonics*, **8**(2), 133-138 (2014). <https://doi.org/10.1038/nphoton.2013.342>
- [32] M.D. Stamate, "On the dielectric properties of dc magnetron TiO₂ thin films," *Applied Surface Science*, **218**(1-4), 318-323 (2003). [https://doi.org/10.1016/S0169-4332\(03\)00624-X](https://doi.org/10.1016/S0169-4332(03)00624-X)

- [33] S. Karthick, S. Velumani, and J. Bouclé, "Experimental and SCAPS simulated formamidinium perovskite solar cells: A comparison of device performance," *Solar Energy*, **205**, 349-357 (2020). <https://doi.org/10.1016/j.solener.2020.05.041>
- [34] Y. Gan D. Zhao, B. Qin, X. Bi, Y. Liu, W. Ning, R. Yang, and Q. Jiang, "Numerical Simulation of High-Performance CsPbI₃/FAPbI₃ Heterojunction Perovskite Solar Cells," *Energies*, **15**(19), 7301 (2022). <https://doi.org/10.3390/en15197301>
- [35] E. Danladi, M.Y. Onimisi, S. Garba, R.U. Ugbe, J.A. Owolabi, O.O. Ige, G.J. Ibeh, and A.O. Muhammed, "Simulation and optimization of lead-based perovskite solar cells with cuprous oxide as a P-type inorganic layer," *Journal of the Nigerian Society of Physical Sciences*, 72-81 (2019). <https://doi.org/10.46481/jnsps.2019.13>
- [36] S.B. Zerarka Selssabil, M.Sc. thesis, "Study of electron transport effect on perovskite solar cells using simulation," University Mohamed Khider de Biskra, 2020.
- [37] M.S. Rahman, S. Miah, M.S.W. Marma, and T. Sabrina, "Simulation based investigation of inverted planar perovskite solar cell with all metal oxide inorganic transport layers," in: *2019 International Conference on Electrical, Computer and Communication Engineering (ECCE)*, (IEEE, 2019).
- [38] A.K. Das, R. Mandal, and D. Mandal, "Impact of HTM on lead-free perovskite solar cell with high efficiency," *Optical and Quantum Electronics*, **54**(7), 1-20 (2022). <https://doi.org/10.21203/rs.3.rs-1366687/v1>
- [39] U. Mehmood, A. Al-Ahmed, F.A. Al-Sulaiman, M.I. Malik, F. Shehzad, and A. Ul Haq Khan, "Effect of temperature on the photovoltaic performance and stability of solid-state dye-sensitized solar cells: A review," *Renewable and Sustainable Energy Reviews*, **79**, 946-959 (2017). <https://doi.org/10.1016/j.rser.2017.05.114>

ДОСЛІДЖЕННЯ ВПЛИВУ ЕЛЕКТРОННИХ ТРАНСПОРТНИХ ШАРІВ, ДЕФЕКТУ ЩІЛЬНОСТІ ІНТЕРФЕЙСУ ТА РОБОЧОЇ ТЕМПЕРАТУРИ НА ПЕРОВСКІТНІ СОНЯЧНІ БАТАРЕЇ З ДОПОМОГОЮ ПРОГРАМНОГО ЗАБЕЗПЕЧЕННЯ SCAPS 1-D

Абубакар С. Юсуф^{a,b}, А.М. Рамалан^c, А.А. Абубакар^a, І.К. Мохаммед^a

^a Кафедра фізики, Федеральний технологічний університет, Р.М.В. 65, Мінна, Нігерія

^b Кафедра фізики та астрономії, Оклендський технологічний університет, Нова Зеландія

^c Кафедра фізики, Університет Абуджі, Р.М.В. 117, Абуджа, Нігерія

Перовскітні сонячні панелі привернули значну увагу дослідників сонячних панелей через їх потенціал для досягнення високої ефективності, в першу чергу, пов'язаних з їх винятковим транспортним шаром електронів (ETL). Матеріал ETL є однією з важливих компонентів перовскітних сонячних панелей в проведенні електронів для створення струму. Більше того, існує перспективний проспект для підвищення стабільності та зниження витрат на їх виготовлення шляхом заміни транспортного шару. У цьому конкретному дослідженні TiO₂ та SnO₂ використовувались як матеріали ETL в архітектурі перовскітної сонячної панелі для порівняльного аналізу між пристроями, що містять різні структури: TiO₂/CH₃NH₃PbI₃/Spiro-OMeTAD та SnO₂/CH₃NH₃PbI₃/Spiro-OMeTAD. Для оцінки продуктивності кожного транспортного шару електронів (ETL) був використаний інструмент 1D SCAPS. Дослідження передбачало зміну товщини транспортних шарів електронів, щільності дефектів інтерфейсу та робочої температури, що дозволяє вичерпно оцінити пошук ключових параметрів таких як напруга на відкритому ланцюзі (VOC), щільність струму короткого замикання (JSC), коефіцієнт заповнення (FF) та загальна ефективність (PCE%). Примітно, що, використовуючи SnO₂ як ETL, досягнута ефективність становить 10,10 %. На відміну від цього, використання TiO₂ у якості ETL дає дещо більшу ефективність 12,84%. Ці знахідки підкреслюють нюанси впливу матеріалів транспортного шару на загальну продуктивність сонячних перовскітних батарей.

Ключові слова: перовскіт; сонячна панель; SCAP-1D

SYNTHESIS, CHARACTERIZATION AND FUNCTIONALIZATION OF P3HT-CNT NANOCOMPOSITE THIN FILMS WITH DOPED Ag₂O

Hayder Abdulmeer Abbas^{a*}, Wissem Cheikrohou Koubaa^b, Estabraq Talib Abdullah^c

^aMiddle Technical University, Technical Instructor Training Institute, Baghdad, Iraq

^bUniversity of Sfax, Faculty of Science of Sfax, Tunisia

^cUniversity of Baghdad College of Science, Department of Physics, Iraq

*Corresponding Author e-mail: hayder@mtu.edu.iq; Tel.: +964 771 407 3394

Received December 7, 2023; revised December 29, 2023; accepted January 11, 2023

This research focuses on the synthesis of carbon nanotube (CNT) and Poly(3-hexylthiophene) (P₃HT) (pristine polymer) with Ag doped (CNT/ P₃HT@Ag) nanocomposite thin films to be utilised in various practical applications. First, four samples of CNT solution and different ratios of the polymer (P₃HT) [0.1, 0.3, 0.5, and 0.7 wt.%] are prepared to form thin layer of P₃HT@CNT nanocomposites by dip-coating method of Ag. To investigate the absorption and conductivity properties for use in various practical applications, structure, morphology, optical, and photoluminescence properties of CNT/P₃HT @Ag nanocomposite are systematically evaluated in this study. In this regard, the UV/Vis/NIR spectrophotometer in the wavelength range of 350 to 700 nm is used to investigate the absorption, transmission spectrum, extinction coefficient (k) and refractive index of the samples prepared at room temperature. The XRD results indicate a slight increase in the crystallite size of the synthesized (CNT/ P₃HT@Ag) nanocomposite compared to CNT/P₃HT nanocomposite, which can be attributed to the better dispersion of the P₃HT and its favorable wrapping around the carbon nanotube structures. FESEM results show that the Ag nanoparticles are acting as a bridge between the CNT and P₃HT, creating a strong bond between the two materials that is strong enough to form thicker tubular structures. An appreciable increase in absorbance intensity (approximately 552 nm) is obtained by adding silver nanoparticles to the CNT/P₃HT matrix at 0.5% of P₃HT. Additionally, the prepared CNT/P₃HT@Ag thin films show greater transmittance – more than 42%, 45%, 49%, and 48% for P₃HT concentrations of 1%, 3%, 5%, and 7%, respectively. The preparation of the samples' extinction coefficient (k) and refractive index data show that the inclusion of silver nanoparticles to the CNT/P₃HT nanocomposite matrix has a significant improvement over the previous samples (CNT/P₃HT composite).

Keywords: Nanocomposite; Poly(3-hexylthiophene) (P₃HT); Carbon nanotube (CNT) solution; Dip-coating method; Photoluminescence properties; Transmission spectrum

PACS: 61.46.+w, 78.55.-m, 61.48.De, 11.30.Na

1. INTRODUCTION

Conjugated polymers have attracted a lot of attention lately because they may provide large, lightweight, and reasonably priced solutions. They are very adaptable because they work well with biodegradable and electronic/optoelectronic devices such organic solar cells, field effect transistors, and organic light emitting diodes [1]. That being said, most of these devices perform worse than more conventional mining methods. This is because conjugated polymers have a lot of imperfections poor mechanical qualities, and low stability [2]. In order to address these problems, the scientists investigated the application of inorganic nanoparticles/quantum dots and conductive polymers as nanocomposite materials in the creation of organic devices [3, 4].

Semiconductors with low processing costs, simple production processes, flexibility, and high operational power show promise for use in next optical devices. Due to the mid-conductor's comparatively high adsorption coefficient, these semiconductors allow for effective light absorption in thin films, paving the way for more sophisticated optoelectronic device applications [5].

The use of Poly(3-hexylthiophene) (P₃HT) as the active layer in different organic devices in conjunction with specific n-type semiconductors has been the subject of extensive research over the last several years. P₃HT is a highly desirable conjugated polymer due to its ability to easily dissolve in various solvents, making it an ideal candidate for processing as a soluble solid. With a high band gap of 1.9 eV, it is well-suited for absorbing powerful sunlight, which in turn promotes the absorption of solar light. Moreover, its high cavity mobility makes it particularly attractive for use in developing organic semiconductor devices [6]. Despite its advantageous solubility and high band gap, P₃HT's low conductivity, instability, and short transmission range, make it less suitable for electronic devices compared to inorganic materials [7]. To allow P₃HT to be used in electrical devices, these issues need to be addressed. In the polymer matrix, it should be noted that the arrangement of the chain is closely linked to the conductivity and optical properties of the conjugated π -conductors.

The mineral composition, which possesses higher momentum compared to its organic counterparts, has been extensively researched in order to enhance the physical properties of the material. Carbon-based nanomaterials such as multi-walled carbon nanotubes (MWCNT), graphene, and fullerenes are being thoroughly examined as potential filler materials that could lead to improved physical properties [8]. In this regard, carbon nanotubes (CNTs) are widely used in various semiconductor devices as electrodes, semiconductors, transparent electrodes, gas sensors, etc. due to their high

conductivity, high surface area, low mass density, and carrier mobility [9]. However, depositing a uniform thin layer of MWCNTs can be challenging, as they are chemically inert and insoluble in most solvents. Previous studies have shown that incorporating carbon-based nanomaterials can enhance the field-effect mobility. Nanocomposites based on nanoparticles indicated an improved performance in solar cells, LEDs, thermoelectric devices, and thin-film transistors (TFTs) [10-12].

Polymer composites are created by synthesizing polymers with nanoparticles, which helps to enhance their electronic and optical properties. CNTs are particularly promising materials for the fabrication of CNT/CNT composites because of their desirable characteristics, including high mechanical strength, high electrical conductivity, adjustable work performance, and soluble processing ability [13].

Photovoltaic cells and other electronic device applications are among the many applications for which polymer compositions containing carbon nanotubes offer tremendous potential. Additionally, achieving balanced injection and transfer for both types of carriers is crucial for the effective functioning of the system, and carbon nanotubes' high electron mobility plays a major part in this regard [6]. This performance can be improved even further by aligning the CNTs [14]. For example, the electric field at the polymer-CNT interface can promote de-oxidization and act as an electrical conduit to improve the charge and direction of light [15]. Due to their ease of processing, MWCNTs are more economical to create than their single-walled counterparts (SWCNTs) [16]. MWCNTs offer greater mechanical strength for composite-based systems and are more suitable for carrier transport than SWCNTs.

Rathore et al. [6] suggested the integration of P3HT with CNTs to form a CNT/polymer composite to overcome the issues of P3HT. They demonstrated that adding MWCNTs to the polymer matrix enhances the current density and modifies the absorption properties of the device.

Conducting polymers (CPs) have gained attention in the field of organic electronics due to their various advantages, such as ease of preparation in thin layers and the ability to adjust their band gap through chemical methods. CPs have been employed in various applications, including organic light emitting diodes (OLEDs), organic gas sensors (OGS), and organic solar cells (OSCs) [15, 16-20]. Among these CPs, P3HT is commonly used in OGSs and OSCs because it has a relatively narrow energy band of 1.93-1.95 eV, [21] allowing it to absorb a broad spectrum of solar energy.

As per the information provided, conjugated polymer materials have gained the interest of both scientists and engineers due to their ability to exhibit electrical and optical properties similar to semiconductors or metals, while also maintaining desirable mechanical properties and processing advantages of polymers. Soon after their discovery, these materials were recognized as potential candidates for use in electronic devices, including cost-effective alternatives for traditional LEDs, photovoltaic cells, and even disposable electronic devices. Poly(alkylthiophene), specifically poly(3-hexylthiophene) or P3HT, is significant because of its high chemical stability under various environmental conditions, high conductivity, and electronic gap that typically falls within the visible range of the electromagnetic spectrum [22-24].

Over the past few years, the preparation of thin films of P3HT, specifically rrP3HT, through solution processing has become increasingly important for various applications such as photovoltaic cells and field effect transistors. Researchers ascertained that the optoelectronic properties of P3HT films are affected by the microstructure and morphology of the prepared film. Generally, CNTs possess an appropriate structure that can interact with conjugated polymers via π - π electronic interactions. The conductive nanocomposites demonstrated that CNTs are an excellent choice for enhancing the optoelectronic properties of conjugated polymers. Specifically, fillers with an aspect ratio of 10^3 , such as SWNTs, can potentially result in a penetration threshold of less than 1% by weight. In this regard, Baibarac et al. [25] focused on composites containing MWNTs and conjugated polymers, particularly poly(phenylene vinylene) derivatives. They showed that there are interactions between the polymer and the outermost walls of the nanotube base plate.

Poly(3-hexylthiophene-2,5-diyl) (P3HT) is commonly employed as a light-absorbing material and as a hole transporting layer [26], as it exhibits a high level of molecular order through π - π stacking of neighboring molecules. When CNTs are introduced into P3HT-based organic photovoltaic devices, they have been found to enhance the dissociation rate of excitons and improve the efficiency of charge carrier collection.

Sa'aya et al. [27] and Nguyen [28] indicated that the process of producing films using conjugated polymers and CNTs would result in a greater degree of miscibility due to strong Van der Waals interactions between conjugated π bonds.

Up to the authors' knowledge, the structural characteristics of CNT/P3HT and Ag doped-CNT/P3HT nanocomposites have not been yet investigated in the open literature. Thus, this study comes to fill this gap. The main aim is to improve the conductivity and absorption of P3HT to be used in a variety of real-world applications. Accordingly, this study intends to synthesize CNT/P3HT and Ag doped-CNT/P3HT nanocomposites thin films. To systematically assure this presumption, the evaluation of the optical, photoluminescent, and structural characteristics of CNT/P3HT and Ag doped-CNT/P3HT (CNT/P3HT@Ag) nanocomposite thin films are carried out.

2. EXPERIMENTAL PART

2.1. Synthesis steps of P3HT@CNT

In this method, we first soak CNT in ODCB (dichlorobenzene). The amount of CNT is 1g/l, and with a quick calculation, the amount of 0.005 g is needed for 5ml of dichlorobenzene. A dark-colored solution was obtained. In another container, 5g per liter of P3HT was mixed in 5 ml of chloroform. With a quick calculation, this amount is equivalent to 0.025g of P3HT. An orange-colored solution was obtained. Then, the P3HT solution was slowly added to the CNT

solution in 5 steps. To achieve the best result, the dispersing process was achieved for several minutes after each addition. Finally, a dark red solution was obtained. The PET foils were cut and placed on a mild heater. Since the solution has high coloring power and high stickiness, it is slightly toxic and also volatile, and therefore, the foils were covered with a napkin. Then, the solution was spread evenly on the foil with the help of a spray so that an almost uniform surface can be obtained. Four samples were synthesized with CNT: P3HT ratio equal to 0.1, 0.3, 0.5, and 0.7.

2.2. Synthesis of silver oxide

Two grams of silver nitrate were dissolved in twenty-five milliliters of deionized water to create silver oxide. Next, 0.35 g of PVP was dissolved in 75 ml of deionized water to act as a polymerizing agent. It had been assured that the components would dissolve entirely. After adding the silver nitrate solution, the PVP solution was left aside for ten minutes. The solution also received a small addition of sodium hydroxide until its pH reached 10. For one hour, the solution was maintained in a bath that ranged from 70 °C to 80 °C until the last sediment formed. After that, the mixture was given to cool fully and the sediment settled for a whole day. The precipitate was dried after the solution had been filtered.

2.3. P3HT@CNT@Ag₂O

The percentage ratio of P3HT to CNT is variable and it was prepared with ratios of 0.1, 0.3, 0.5, and 0.7. To prepare the silver layers, a fixed amount of 0.8 mg was added to the above percentages in the final solution, and it was manually sprayed and dried on the PET substrate.

3. RESULTS AND DISCUSSION

3.1. X-ray diffraction analysis (XRD)

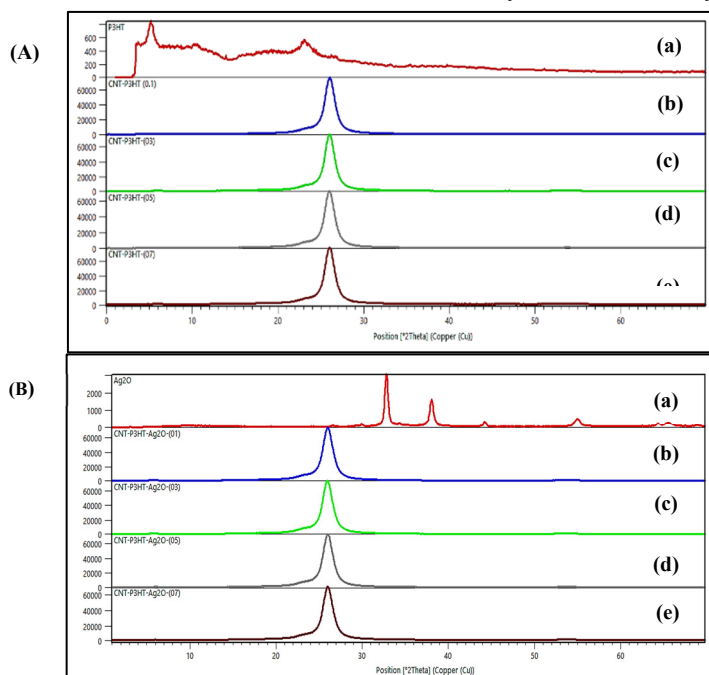


Figure 1. XRD patterns of (A) CNT/P₃HT and (B) CNT/P₃HT@ Ag thin films at different ratios (0.1, 0.3, 0.5, and 0.7 of P₃HT and 0.08 mg/L)

cause a slightly amplified in the intensity of the peak [302]. Afterward, peak [302] intensity decreases between 0.3 and 0.5 of P₃HT, which reveals that P₃HT is covering the surface of the CNT, leading to an improved crystallinity. This is especially true for the 0.5 amount of P₃HT, which had the lowest intensity of the [302] peak, indicating the highest level of crystallinity. Also, there is a slight shift in the position of the scattering peaks with the addition of P₃HT to the CNT lattice. The full width at half maximum (FWHM) indicates changes in crystal size values. This can be attributed to the physical wrapping of the polymer on the walls of the nanotubes [29]. Figure 1-B and Table 1 also indicate that the intensity of the [302] peak has been decreased due to adding silver nanoparticles in all cases. In this regard, the lowest peak intensity is at 0.3 P₃HT (Figure 1-B-c), which is also less intense than the previous case (the lowest [302] peak intensity at 0.5 P₃HT (Figure 1-A-d)). This suggests that silver nanoparticles are more effective at reducing [302] peak intensity when the P₃HT concentration in the sample is lower. These findings indicate that silver nanoparticles can therefore have a stronger effect on the [302] peak intensity at lower P₃HT concentrations.

The average crystallite size of the pure structure of P₃HT is about 11 nm, and it is about 6 nm for CNT/P₃HT nanocomposites. This indicates that P₃HT is acting as a template for the CNT to form a more ordered structure, reducing

Figure 1 displays the XRD results of the CNT/P₃HT nanocomposite thin films prepared using the dip coating process. In the diffraction spectrum obtained from P₃HT, the scattering peaks at $2\theta=5.29^\circ$ and 23.16° angles were observed, which result from first and higher-order reflections from the large distance large-length d-spacing for this material and are related to the in-plane interchain distance (Figure. 1A-a and Table 1). These reflections show that the polymer chains are arranged regularly and are caused by the material's long-range periodic organization. Higher-order peaks in the diffraction spectrum provide more evidence for this. Stated differently, the material's periodic arrangement produces a diffraction spectrum that displays reflections from the polymer chains as well as additional higher-order peaks that show how the polymer chains are organized. Additionally, the wide-angle peak of the amorphous halo (with less intensity at $2\theta = 23.16^\circ$) reveals the stacking distance between the thiophene rings [29].

Furthermore, it can be stated that by an increase of P₃HT value from 0.1 to 0.3 would

the size and increasing the crystallinity of the CNT. P₃HT at a 0.5 ratio in CNT/P₃HT nanocomposite reached the highest [302] peak, suggesting a crystalline structure. Also, the average crystallite size of synthesized silver nanoparticles is about 21 nm. By comparing the CNT/P₃HT nanocomposites containing silver nanoparticles (CNT/P₃HT @Ag) compared to their counterparts, a slight increase in the crystallite size can be observed, which can be attributed to the better dispersion of the P₃HT and its favorable wrapping around the carbon nanotube structures. This is because the silver nanoparticles interact with the surface of the carbon nanotubes, forming a stronger bond which aids to stabilize the nanocomposites and prevent the particles from agglomerating. Additionally, the P₃HT forms a protective layer around the particles, further preventing them from agglomerating. The result is a more evenly distributed particles with a larger average crystallite size [29, 30].

Table 1. Parameters obtained from XRD analysis

Sample:	Pos. [°2Th.]	Height [cts]	FWHM [°2Th.]	d-spacing [Å]
P ₃ HT	5.217	266	0.71	16.92623
CNT/P ₃ HT (0.1)	26.0593	50259	1.36	3.41664
CNT/P ₃ HT (0.3)	26.0131	50763	1.322	3.42261
CNT/P ₃ HT (0.5)	25.9973	43281	1.346	3.4264
CNT/P ₃ HT (0.7)	26.0179	48557	1.356	3.42198
CNT/P ₃ HT@Ag (0.1)	26.052	42846	1.296	3.41758
CNT/P ₃ HT@Ag (0.3)	25.991	41684	1.24	3.41758
CNT/P ₃ HT@Ag (0.5)	26.0409	42544	1.314	3.41901
CNT/P ₃ HT@Ag (0.7)	26.0495	42970	1.352	3.411790
Ag ₂ O	32.836	2084	0.401	2.72535

3.2. Field emission scanning electron microscopy (FESEM) analysis

The FESEM images in Figures 2 and 3 (a), (b), (c), and (d) indicate the morphology of CNT/P₃HT with different ratios of P₃HT (0.1, 0.3, 0.5, 0.7 wt.%) thin films and Ag-doped CNT/ P₃HT (CNT/P₃HT@Ag) nanocomposite thin films (the amount of silver oxide nanoparticles is constant and about 0.08 mg/L), respectively. The FESEM images show a view of CNT nanostructures with polymer wrappings. By comparing the shapes prepared from the samples (from Figure (2-a) to (2-d)), the number of disordered CNT observed has an increasing trend, which is well covered by the desired polymer (P₃HT).

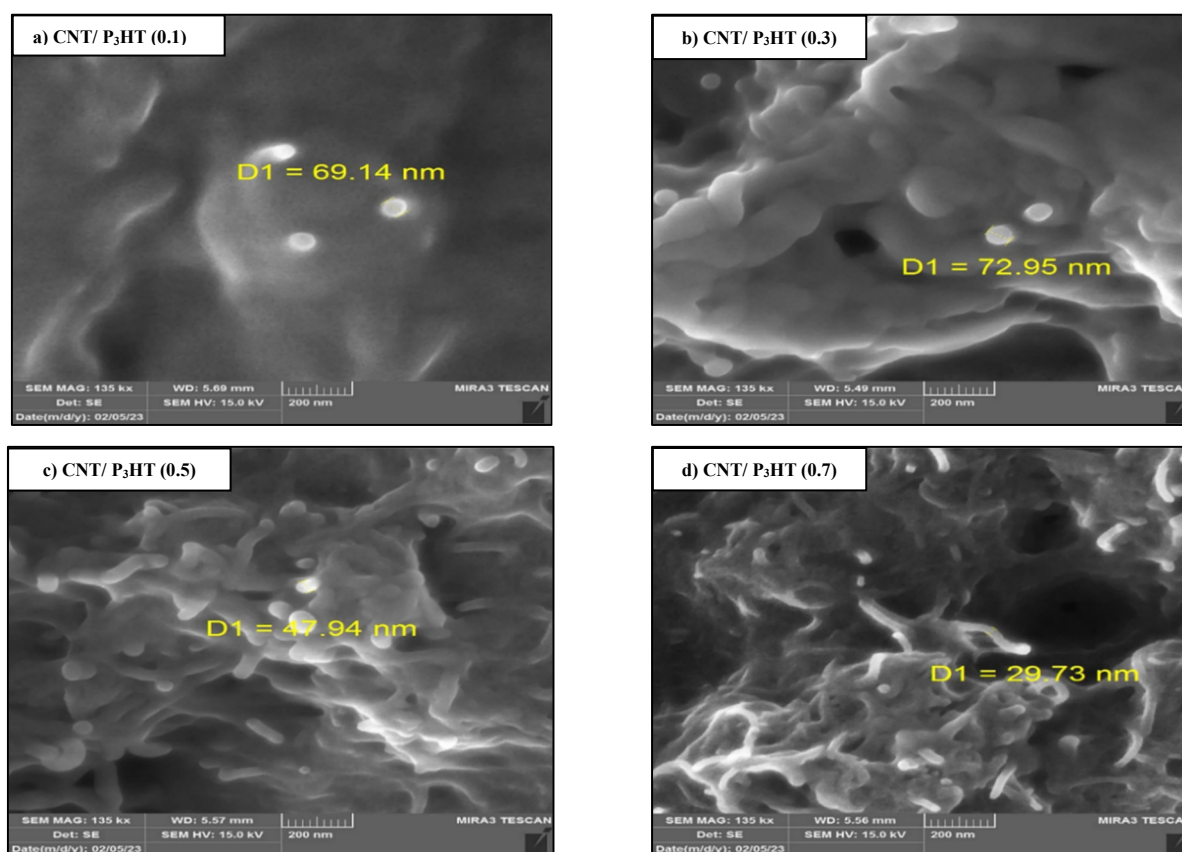


Figure 2. FESEM images of prepared thin films with different P₃HT concentrations: (a) CNT/P₃HT (0.1), (b) CNT/P₃HT (0.3), (c) CNT/P₃HT (0.5), and (d) CNT/P₃HT (0.7)

This is because the polymer matrix can fill in the gaps between CNTs and provide support, leading to an increase in the number of well-buried CNTs in the matrix. This is further evidenced by the FESEM images which show an increasing number of CNTs with tubular structures and well-covered by the polymer matrix. On the other hand, the performance of CNT is still not as impressive as expected due to some factors, including entanglement, misalignment, and metal impurities. These issues can affect the electrical and mechanical properties of CNTs, leading to weaker overall performance. As a result, CNTs cannot reach their full potential and their performance is limited. Based on studies conducted by Danish et al., it can be said that the mentioned issues can lead to a decrease in hole mobility and an increase in recombination pathways [31].

Clearly, Figures (2-a-d) assure that by increasing the amount of P₃HT in the CNT matrix, a more suitable distribution of carbon nanotubes can be achieved. There are, however, still certain regions where entangled nanotubes are visible. This may be due to insufficient amount for P₃HT to overcome the van der Waals forces towards the CNT surface, leading to better dispersion and wrapping. For CNT/P₃HT (0.5 of P₃HT) nanocomposite images in Figure 2-c, less entanglement and improved alignment of CNT can be observed. Also, this Figure shows a completely different surface morphology with an apparently larger CNT diameter. It appears that the exfoliation process has increased the diameter of the CNT due to the presence of newly exfoliated P₃HT chains [32].

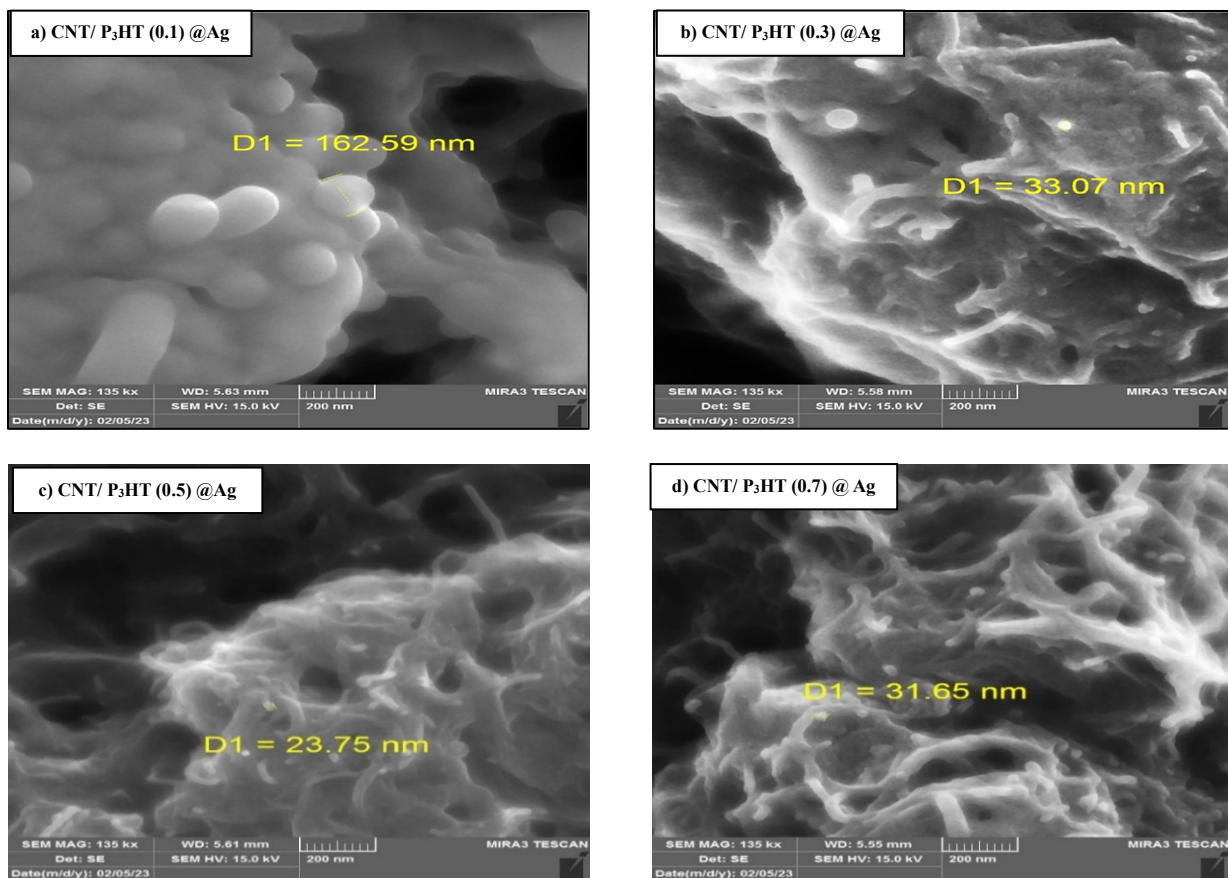


Figure 3. FESEM images of prepared CNT/P₃HT thin films after doping with silver oxide nanoparticles: (a) CNT/P₃HT (0.1)/Ag, (b) CNT/P₃HT (0.3)/Ag, (c) CNT/P₃HT (0.5)/Ag, and (d) CNT/P₃HT (0.7)/Ag [dopant amount: 0.08 mg/L]

The incorporation of silver nanoparticles into the CNT/P₃HT nanocomposite matrix, in smaller amounts of P₃HT (0.3 wt.%) (Figure 3-a-d), can demonstrate a better dispersion and less entanglement for nanotubes. In other words, silver nanoparticles in smaller amounts of P₃HT help the proper dispersion of carbon nanotubes. This is because silver nanoparticles have a strong affinity to the CNT/P₃HT nanocomposite matrix and can act as a bridge between the CNTs and P₃HT, helping to improve alignment and reduce entanglement. Furthermore, the silver nanoparticles reduce the overall viscosity of the nanocomposite matrix, resulting in better dispersion of the CNTs [33]. An average diameter size of the prepared nanocomposites (Figure 2-a-d) continued to decrease from 69 nm, 73 nm, 48 nm to 28 nm. This showed that the increase in the P₃HT concentration reinforces the effectiveness of P₃HT wrapping towards the CNT side-wall by increasing the diameter of CNT [33]. It is also clear from images (3-a-d) that by adding impurity (silver nanoparticles) into the pre-prepared CNT/P₃HT matrix, thicker tubular structures with rough surfaces and agglomerate-like mat structures were obtained, and this illustrates the wrapping of the polymer on the nanotubes to form a nanocomposite [34]. This suggests that the silver nanoparticles are acting as a bridge between the CNT and P₃HT, creating a strong bond between the two materials that is strong enough to form thicker tubular structures. Additionally, the rough surface of the

nanocomposite suggests that the silver nanoparticles are also acting as stabilizing agents to hold the nanotubes and polymer together.

The results of the Electron Diffraction X-ray (EDX) analysis of the CNT/P3HT composite thin films with varying P3HT concentrations (Figure 4-A) show that the carbon content of the composite increases and then decreases, followed by a notable decrease and enhancement in the weight of sulfur (S), indicating the formation of nanocomposites. The EDX analysis data shows that with increasing P3HT concentration, there is an initial raise in the carbon content of the nanocomposite thin films. This is likely due to the higher content of CNTs in the composite, which contains more carbon than P3HT. However, after a certain point, the carbon content decreases, indicating that the P3HT is beginning to dominate the composition of the composite. Additionally, the weight of sulfur (S) in the nanocomposite, is reduced and then enhanced, suggesting that there is a chemical interaction between the CNTs and P3HT in the nanocomposite [29].

Figure 4-B illustrates silver oxide nanoparticles doped successfully in a CNT/P3HT lattice. This figure demonstrates that adding silver nanoparticles to the pre-prepared nanocomposite lattice leads to the silver oxide nanoparticles forming chemical bonds with the CNTs and P3HT, further stabilizing the overall nanocomposite lattice. It also suggests that the CNTs and P3HT facilitate the nanoparticles' dispersal in the nanocomposite lattice. In this regard, Figure 3 obtained from SEM analysis of CNT/P3HT@Ag nanocomposite thin films confirms the accuracy of these results.

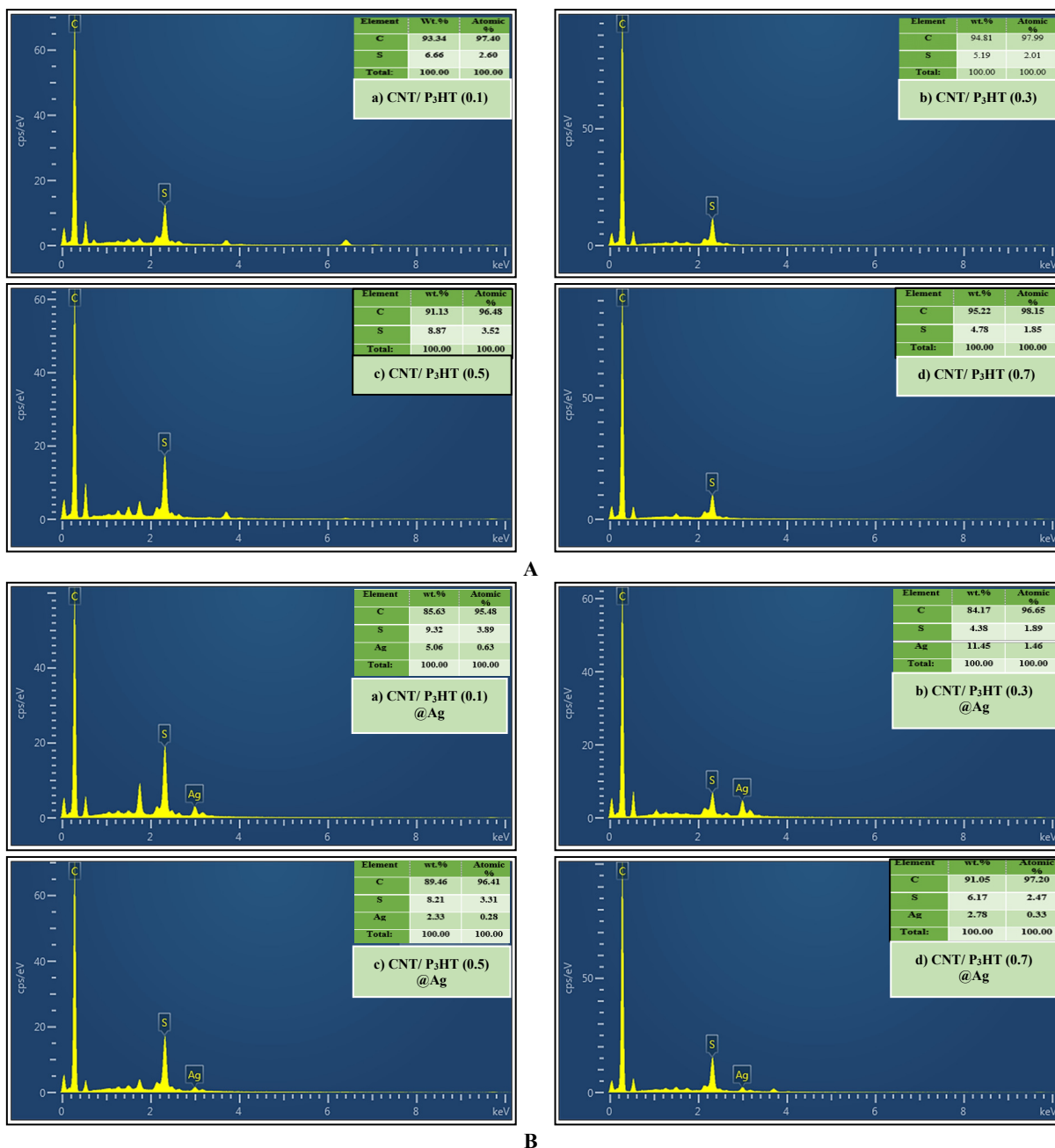


Figure 4. EDX images of (A) CNT/P₃HT thin films with different P₃HT concentrations: (a) CNT/P₃HT (0.1), (b) CNT/P₃HT (0.3), (c) CNT/P₃HT (0.5), and (d) CNT/P₃HT (0.7). EDX (B) CNT/P₃HT thin films after doping with silver oxide nanoparticles: (a) CNT/P₃HT (0.1)/Ag, (b) CNT/P₃HT (0.3)/Ag, (c) CNT/P₃HT (0.5)/Ag, and (d) CNT/P₃HT (0.7)/Ag [dopant amount: 0.08 mg/L]

3.3. Photoluminescence (PL) spectroscopy

Prior to deciding on an appropriate composite composition for uses like photoactive layers, it is important to examine the photoluminescence properties of the pristine polymer (P₃HT) and the CNT/P₃HT composite thin films. This study is important because the composite that exhibits the strongest quenching of photoluminescence also exhibits the largest charge separation that can be found in the photoactive layer. This is important because the composite film's charge separation potential increases with the strength of the photoluminescence quenching effect. This charge separation is essential to create the desired photoactive layer, which is necessary for the optimal performance of the application [35]. The PL spectrum of the CNT/P₃HT and CNT/P₃HT@Ag nanocomposites measured at an excitation wavelength of 440 nm is presented in Figure 5.

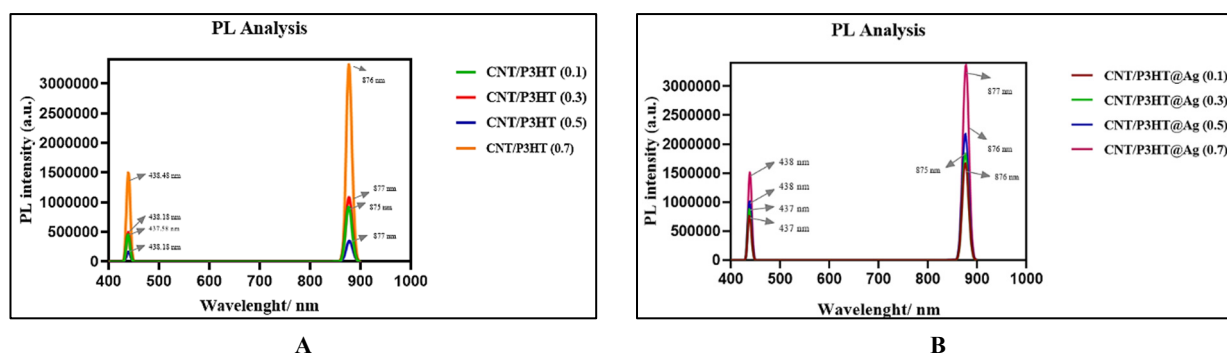


Figure 5. PL spectrum of the (A) prepared thin films with different P₃HT concentrations: (a) CNT/P₃HT (0.1), (b) CNT/P₃HT (0.3), (c) CNT/P₃HT (0.5), and (d) CNT/P₃HT (0.7). and (B) CNT/P₃HT thin films after doping with silver oxide nanoparticles: (a) CNT/P₃HT (0.1)/Ag, (b) CNT/P₃HT (0.3)/Ag, (c) CNT/P₃HT (0.5)/Ag, and (d) CNT/P₃HT (0.7)/Ag [dopant amount: 0.08 mg/L]. The excitation wavelength $\lambda = 440$ nm

Figure 5-A and 5-B illustrates the values of PL emission for CNT/P₃HT and CNT/P₃HT@Ag nanocomposite for different amounts of P₃HT (0.1, 0.3, 0.5, and 0.7) around 437, 438, 438, and 439 nm and for the CNT/P₃HT@Ag composites around 437, 437, 438, and 438 nm, respectively. Although CNTs are well-known fluorescence quenchers, the physical mixed system between P₃HT and CNTs causes photoluminescence quenching to be more noticeable for CNT/P₃HT. One other benefit of employing CNT/P₃HT in solar cells is this. However, P₃HT's emission peak intensity was greater than nanocomposites. This was explained as quenching brought on by the reduction of electron-hole recombination caused by charge transfer between the CNT and P₃HT. Strong luminous quenching of the as-prepared nanocomposites was seen at wavelengths of about 876 nm (attributed to the π - π^* bond in P₃HT). According to the reported studies [36, 37], CNTs are known as fluorescence quenchers. However, photoluminescence quenching is expected to be more pronounced for the prepared CNT/P₃HT nanocomposites due to the physical mixed system of P₃HT and CNTs. This phenomenon is an extra benefit for using these systems in photovoltaic applications such as photovoltaic cells [32].

According to these references [35, 38, 39], the emission peak intensity for pure P₃HT is around 581 nm, which is a larger amount compared to the prepared CNT/P₃HT nanocomposites. This behavior can be ascribed to quenching as a result of charge transfer between CNT and P₃HT reducing electron-hole recombination. On the other hand, strong light quenching of the prepared nanocomposites was observed at wavelengths around 876 nm (attributed to the π - π^* bond in P₃HT) [35]. In this regard, Kuila et al. [38] investigated the PL quenching of the CNT/P₃HT nanocomposite and corresponded it to the π - π interaction between the P₃HT and the carbon nanotubes (CNT) and presented additional deactivation (decaying) pathways for excited electrons [37, 39].

As a result, CNT/P₃HT@Ag (0.5 P₃HT) and CNT/P₃HT@Ag (0.1 and then 0.3 P₃HT) quench the PL intensity even more, reducing electron-hole recombination as a result of charge transfer between donor-acceptor materials. With these CNT/P₃HT (0.5 of P₃HT) and CNT/P₃HT@Ag (0.1 of P₃HT) samples, there is a high possibility of charge separation in the photoactive layer due to its strong PL quenching effect [30].

3.4. Ultraviolet-visible (UV-vis) spectroscopy

3.4.1 Absorption spectrum

UV/Vis/NIR spectrophotometer in the wavelength range of 350 to 700 nm was used to investigate the absorption and transmission spectrum of the samples prepared at room temperature. According to Figure 6(a), the absorption spectra of CNT/P₃HT at different ratios (0.1, 0.3, 0.5, and 0.7 wt.%) can be observed.

According to the reference [34], the absorption maximum (λ_{\max}) for P₃HT was observed at about 442-505 nm, which indicates extensive π -continuity and is in good agreement with reported values [29]. The CNT/P₃HT composites exhibited absorption bands at about 512-527 nm, which is attributed to the strong interactions between P₃HT and CNTs and suggesting a decrease in band gap [40]. The strong interactions between the two components lead to an increased conjugation of the polymer and the formation of an extended π -conjugated system, which gives rise to the absorption bands in the visible range. Additionally, the intensity of the absorption band raised with increasing P₃HT (0.5 wt.%) concentration, which is due to the enhanced number of P₃HT molecules in the nanocomposite. On the other hand, after

adding silver nanoparticles into the CNT/P₃HT nanocomposite matrix, increasing the percentage of P₃HT to about 0.3, an amplification in the absorption peak intensity is observed; Compared to the previous case, the increase in the amount of absorption intensity is ascertained in lower P₃HT amounts. This suggests that silver nanoparticles play a role in increasing the efficiency of the nanocomposite matrix by allowing for more efficient absorption of light at lower P₃HT percentages. This is due to the expansion of the surface area of the nanocomposite matrix provided by the silver nanoparticles, which allows for more efficient absorption of light [32]. Thus, All CNT/P₃HT samples with different ratios of P₃HT show improved adsorption efficiency. In addition, it is expected to improve electrical conductivity, thereby enhancing the performance of photovoltaic applications [30, 41].

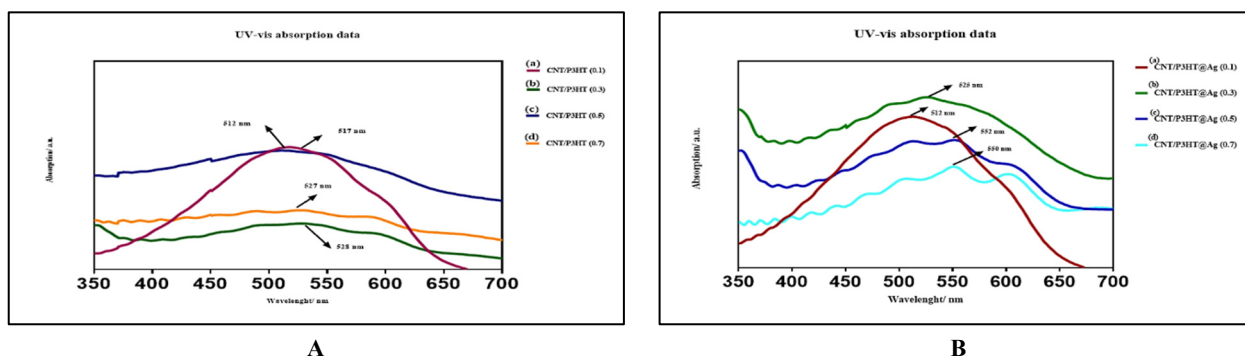


Figure 6. Schematic of absorption spectra of (A) prepared thin films with different P₃HT concentrations: (a) CNT/P₃HT (0.1), (b) CNT/P₃HT (0.3), (c) CNT/P₃HT (0.5), and (d) CNT/P₃HT (0.7). and (B) CNT/P₃HT thin films after doping with silver oxide nanoparticles: (a) CNT/P₃HT (0.1)/Ag, (b) CNT/P₃HT (0.3)/Ag, (c) CNT/P₃HT (0.5)/Ag, and (d) CNT/P₃HT (0.7)/Ag [dopant amount: 0.08 mg/L]

But in the case of nanocomposites reinforced with silver nanoparticles (CNT/P₃HT@Ag), as seen in Figure 6-B, a favorable boost in the maximum absorption intensity was observed for all prepared nanocomposite samples compared to pure P₃HT polymer. A significant improvement in absorbance intensity (around 552 nm) is observed when silver nanoparticles are added to the CNT/P₃HT matrix at 0.5% of P₃HT, which is a significant increase compared to the previous samples (CNT/P₃HT composite).

This shift towards longer wavelengths (red-shift of λ_{\max}) compared to the CNT/P₃HT nanocomposite matrix as well as the pure P₃HT can be attributed to the enhancement in the conjugation length of the P₃HT polymer due to the strong π - π interaction with CNTs, which subsequently leads to the increased organization of P₃HT chains on the nanotube surface. In the case of silver-reinforced nanocomposites (CNT/P₃HT@Ag), as mentioned earlier, due to the synergistic effect of these nanoparticles, a significant reinforcement in the absorption wavelength can be expected, which is consistent with the results previously obtained [34, 42]. This is because silver nanoparticles can act as a bridge between the P₃HT polymer and the carbon nanotubes, thereby forming a stronger bond that allows for a longer absorption wavelength. This is further reinforced by the fact that silver has a higher optical reflectance than carbon nanotubes, which also contributes to the increased absorption wavelength.

3.4.2. Transmission spectrum

Figure 7-A and 7-B shows the optical transmission spectrum for the as-prepared CNT/P₃HT and CNT/P₃HT@Ag nanocomposite thin films at different P₃HT ratios (0.1, 0.3, 0.5, and 0.7 wt.%) in the wavelength range of 350 to 1000 nm, which is in good agreement with the absorption spectrum data (Figures 7-A and B). Figure 7-A shows the amount of transmission in the visible region for these prepared CNT/P₃HT nanocomposites is more than 20%, 35%, 20%, and 32% for the concentrations of 1%, 3%, 5%, and 7% of P₃HT, which can indicate the good crystal quality of the samples.

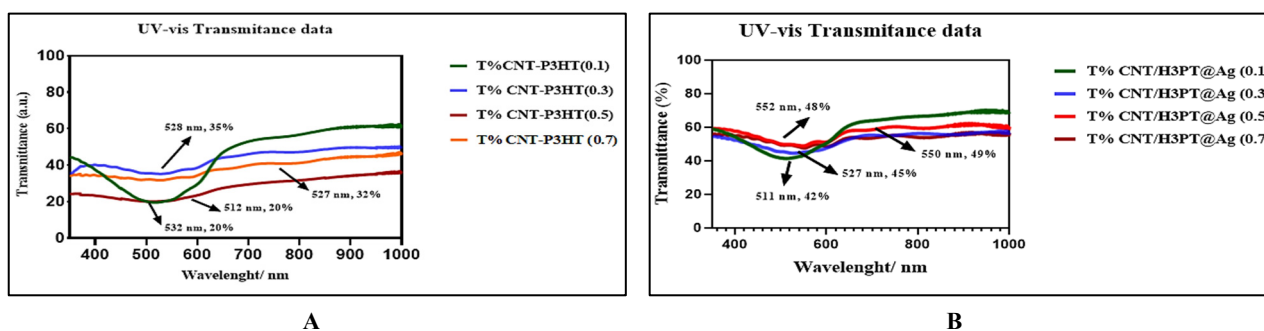


Figure 7: Schematic of optical transmission spectra of (A) prepared CNT/P₃HT thin films with different P₃HT concentrations: (0.1), (0.3), (0.5), and (0.7). and (B) CNT/P₃HT thin films after doping with silver oxide nanoparticles: CNT/P₃HT (0.1)/Ag, CNT/P₃HT (0.3)/Ag, CNT/P₃HT (0.5)/Ag, and CNT/P₃HT (0.7)/Ag [dopant amount: 0.08 mg/L]

Also, it is clear from Figure 7-B that the CNT/P₃HT nanocomposite samples have been reinforced with silver nanoparticles (CNT/P₃HT@Ag) with a better transmission spectrum for all P₃HT concentrations (0.1, 0.3, 0.5, and 0.7 wt.% of P₃HT). In other words, the amount of transmittance in the visible region for the as-prepared CNT/P₃HT@Ag thin films, in this case, is more than 42%, 45%, 49%, and 48% for the concentrations of 1%, 3%, 5%, and 7% of P₃HT, which can indicate the synergistic effect caused by the integration of silver nanoparticles in the CNT/P₃HT nanocomposite matrix. The silver nanoparticles enhance the light absorption and scattering of the nanocomposite matrix, which increases the amount of light transmitted in the visible region. This improves the light transmission results in higher transmittance values for the CNT/P₃HT@Ag thin films than for pure CNT/P₃HT thin films.

3.4.3. Absorption coefficient

By knowing the data of the transmission spectrum of the CNT/P₃HT and CNT/P₃HT@Ag nanocomposites at different P₃HT ratios (0.1, 0.3, 0.5, and 0.7 wt.%) (Figure 7), it is possible to calculate the absorption coefficient (8-A/B) of the as-prepared nanocomposites. The result of these calculations regarding the absorption coefficient spectrum of the samples as a function of wavelength. As can be seen from Figure 8-A, at long wavelengths (greater than 600 nm) there is very small absorption (all photons are transmitted), and at shorter wavelengths, i.e., at wavelengths between 510-528 nm, the absorption has the highest value (in the range of 0.0115-0.0164). It is expected that in this area, the transmission value in this range will decrease due to the transition of electrons from the valence band to the conduction band. This is in a reasonable agreement with the data obtained from the transmission spectrum (Figure 8-A). Specifically, the decrease in transmission value is due to the fact that when electrons transit from the valence band to the conduction band, their energy is absorbed. This energy is converted into heat, which reduces the ability of the material to transmit light. This decrease in the transmission is further evidenced by the transmission spectrum in Figure 8-A, which shows a decrease in intensity in the range of interest.

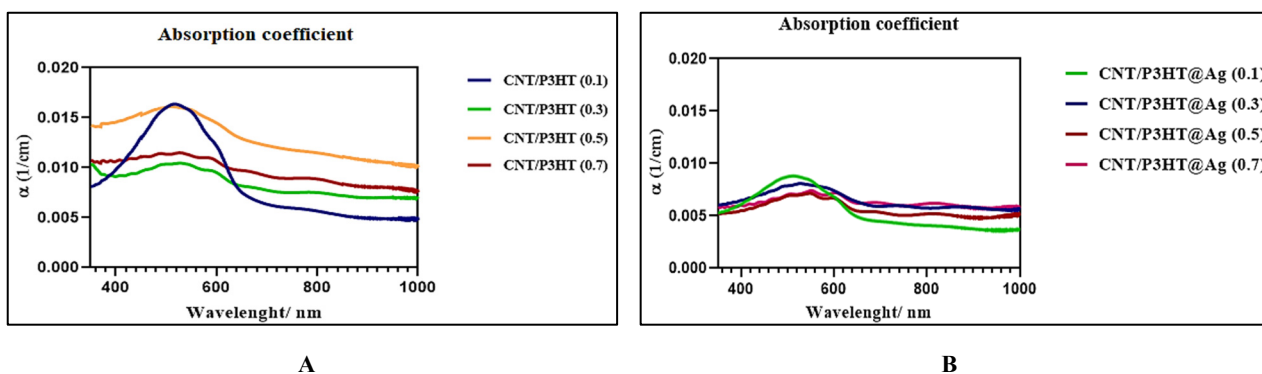


Figure 8. Schematic of absorption coefficient of (A) prepared thin films with different P₃HT concentrations: (0.1), (0.3), (0.5), and (0.7). and (B) CNT/P₃HT thin films after doping with silver oxide nanoparticles: CNT/P₃HT (0.1)/Ag, CNT/P₃HT (0.3)/Ag, CNT/P₃HT (0.5)/Ag, and CNT/P₃HT (0.7)/Ag [dopant amount: 0.08 mg/L]

Also, as can be seen from Figure 8-B, at long wavelengths (greater than 640 nm) there is very small absorption (most photons are transmitted), and at shorter wavelengths, i.e., at wavelengths between 512-600 nm, the absorption has the highest value (in the range of 0.0072-0.0088), which is in reasonable agreement with the data obtained from the transmission spectrum (Figure 7-B). The data related to the maximum absorption coefficient and the wavelength at which the absorption coefficient has its maximum value are presented in Table 2.

In addition, by comparing the absorption coefficient data for CNT/P₃HT and CNT/P₃HT@Ag nanocomposites, it can be seen that CNT/P₃HT nanocomposites have been reinforced with silver nanoparticles (CNT/P₃HT@Ag) as they have a lower absorption coefficient than their counterparts (CNT/P₃HT). However, it should be noted that the maximum absorption coefficient occurs for CNT/P₃HT@Ag nanocomposites at different wavelengths (shift towards larger wavelengths) compared to CNT/P₃HT thin films.

Table 2. Wavelength of peaks and their maximum absorption coefficient of as-prepared CNT/P₃HT and CNT/P₃HT/Ag nanocomposite thin films

Samples		Wavelength of peaks and their maximum absorption coefficient			
		P ₃ HT (0.1)	P ₃ HT (0.3)	P ₃ HT (0.5)	P ₃ HT (0.7)
CNT/P ₃ HT	λ(nm)	517	528	510	527
	α _{max}	0.016	0.0146	0.016	0.0115
CNT/P ₃ HT@Ag	λ (nm)	512	527	547	600
	α _{max}	0.0088	0.0081	0.0071	0.0072

3.4.4. Extinction coefficient (K)

With the help of the absorption coefficient and absorption data, the extinction coefficient (k) of CNT/P₃HT and CNT/P₃HT@Ag nanocomposites can be found. The changes in k in terms of λ are plotted in Figure 9 for these samples. According to these graphs (Figure 9- A-a to d), the extinction coefficient of CNT/P₃HT nanocomposites at different P₃HT ratios (0.1, 0.3, 0.5, and 0.7 wt.%) with increasing wavelength first has a peak in the areas (545 nm, 1005 nm, 1011 nm, and 993 nm) and then starts to decrease and is almost constant at long wavelengths. It should be noted that this rate of reduction is rapid only for CNT/P₃HT containing 0.1 wt.% of P₃HT, and it decreases slowly for the remaining three samples. The reason for the decrease in the extinction coefficient with the increase in wavelength is related to the decrease in absorption in the thin films, which corresponds to the optical transmission spectrum of the samples in Figure 7. Also, for the CNT/P₃HT nanocomposite reinforced with silver nanoparticles (CNT/P₃HT@Ag), a similar trend was observed. With the difference owing to the sample containing 0.1 of P₃HT, the decreasing trend compared to its counterpart (Figure 9-A), has a slower rate. According to these graphs (Figure 9-B), the extinction coefficient of CNT/P₃HT@Ag nanocomposites at different P₃HT ratios (0.1, 0.3, 0.5, and 0.7 wt.%) with increasing wavelength first has a peak in the areas (545-1005 nm) and then starts to decline with an almost constant and similar reduction rate and is almost constant at long wavelengths.

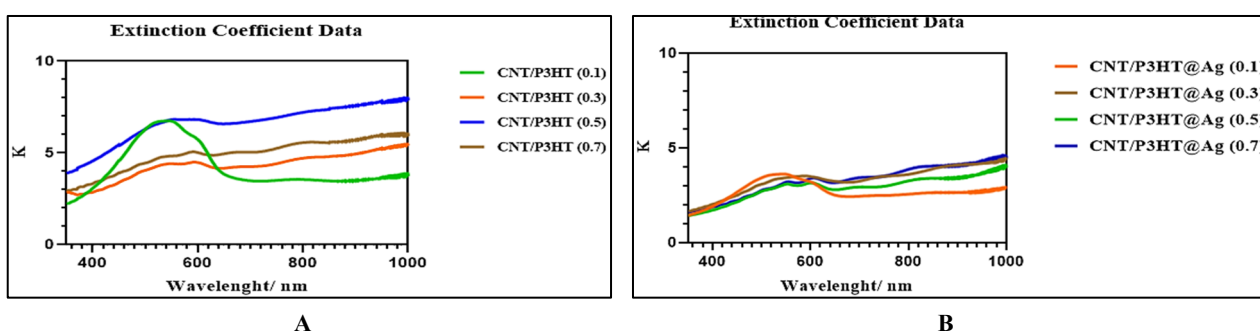


Figure 9. Variations in extinction coefficient according to wavelength for (A) CNT/P₃HT and (B) CNT/P₃HT@Ag nanocomposites with different P₃HT ratios

3.4.5. Refractive index (n)

Based on the data obtained from the optical analysis, the refractive index of CNT/P₃HT and CNT/P₃HT@Ag nanocomposites can be obtained. Figure 10-A/B shows the change in the refractive index according to the wavelength of the prepared samples. In other words, the refractive index of CNT/P₃HT and CNT/P₃HT@Ag nanocomposites decreases with increasing wavelengths. By comparing Figures 10-A and B, only the samples containing 0.1% of P₃HT have a significant decrease in the refractive index, which occurs at the wavelengths of 517 nm and 512 nm for CNT/P₃HT and CNT/P₃HT@Ag nanocomposites, respectively. But for the other three samples, a slight decrease in the refractive index can be observed. Finally, the refractive index reaches an almost constant value for all samples with increasing wavelengths. Also, Table 3 illustrates the wavelength of peaks and their minimum reflective index of as-prepared CNT/P₃HT and CNT/P₃HT@Ag nanocomposite thin films.

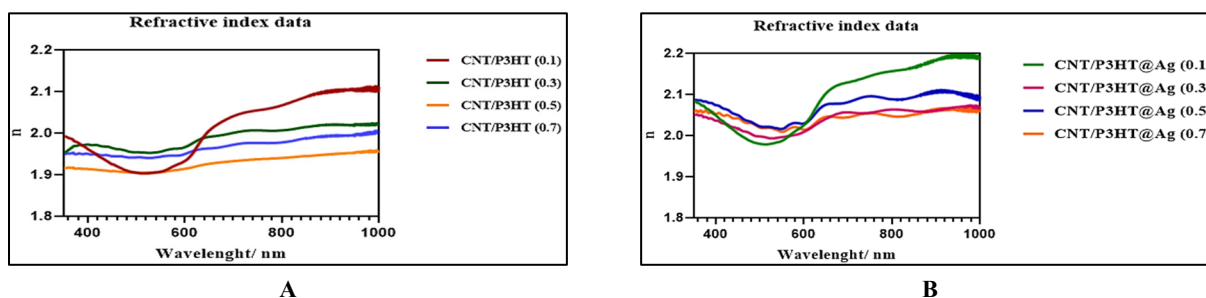


Figure 10. Variations in reflective index according to wavelength for (A) CNT/P₃HT and (B) CNT/P₃HT@Ag nanocomposites with different P₃HT ratios

Table 3. Wavelength of peaks and their minimum reflective index of as-prepared CNT/P₃HT and CNT/P₃HT/Ag nanocomposite thin films

Samples		Wavelength of peaks and their minimum reflective index			
		P ₃ HT (0.1)	P ₃ HT (0.3)	P ₃ HT (0.5)	P ₃ HT (0.7)
CNT/P ₃ HT	λ(nm)	517	526	512	490
	n _{min}	1.902	1.953	1.904	1.941
CNT/P ₃ HT@Ag	λ (nm)	512	527	547	550
	n _{min}	1.978	1.993	2.015	2.009

CONCLUSIONS

This study reported on the structure, morphology, optical, and photoluminescence properties of CNT/P3HT and Ag doped-CNT/P3HT (CNT/P3HT@Ag) nanocomposite thin films synthesised by dip-coating method. The study intended to enhance P3HT absorption and conductivity properties for use in various practical applications and systematically the effects on the structure, morphology, optical and photoluminescence were investigated. The XRD results exhibited the average crystallite size of synthesized silver nanoparticles is about 21 nm. By comparing the CNT/P3HT nanocomposites containing silver nanoparticles (CNT/P3HT @Ag) compared to their counterparts, a slight increase in the crystallite size was observed, which can be attributed to the better dispersion of the P3HT and its favorable wrapping around the carbon nanotube structures. The FESEM results showed that the silver nanoparticles are acting as a bridge between the CNT and P3HT, creating a strong bond between the two materials that is strong enough to form thicker tubular structures. The photoluminescence characteristics of both the pristine polymer (P₃HT) and the CNT/P₃HT composite thin films ascertained that adding silver nanoparticles to the CNT/P3HT matrix at 0.5% of P3HT results in a notable rise in absorbance intensity (about 552 nm), which is a considerable improvement over the prior samples (CNT/P3HT composite). Also, when silver nanoparticles are integrated into the CNT/P3HT nanocomposite matrix, the as-prepared CNT/P3HT@Ag thin films exhibit more transmittance—more than 42%, 45%, 49%, and 48% for P3HT concentrations of 1%, 3%, 5%, and 7%, respectively. Finally, the results of extinction coefficient (k) and refractive index of the samples prepared at room temperature have demonstrated that the addition of silver nanoparticles to the CNT/P3HT nanocomposite matrix has a synergistic impact.

Funding.

This research received no external funding.

Conflicts of Interest.

The authors declare no conflict of interest.

Data availability statement.

The data that support the findings of this study are available from the corresponding author upon reasonable request.

ORCID

Hayder Abdulmeer Abbas, <https://orcid.org/0009-0002-1029-2353>

Wissem Cheikrouhou Koubaa, <https://orcid.org/0000-0001-8907-0379>

Estabraq Talib Abdullah, <https://orcid.org/0000-0002-2893-3529>

REFERENCES

- [1] S. Shi, S. Ravi, and P. Silva, "High luminance organic light-emitting diodes with efficient multi-walled carbon nanotube hole injectors," *Carbon*, **50**, 4163-4170 (2012). <https://doi.org/10.1016/j.carbon.2012.04.065>
- [2] A.K. Singh, and R. Prakash, "Organic Schottky diode based on conducting polymer nanoclay composite," *RSC Advances*, **2**, 5277-5283 (2012). <https://doi.org/10.1039/C2RA20206A>
- [3] A. Bruno, T.D. Luccio, C. Borriella, F. Villani, S. Haque, and C. Minarini, "Exciton dynamics in hybrid polymer/qd blends," *Energy Procedia*, **44**, 167-175 (2014). <https://doi.org/10.1016/j.egypro.2013.12.024>
- [4] S. Lee, B.R. Lee, J. Kim, and M.H. Song, "Combination effect of polar solvent treatment on ZnO and polyuorene-based polymer blends for highly efficient blue based hybrid organic inorganic polymer light-emitting diodes," *Journal of Materials Chemistry C*, **2**, 8673-8677 (2014). <https://doi.org/10.1039/C4TC01726A>
- [5] J. Shi, J. Zhang, L. Yang, M. Qu, D.C. Qi, and K.H. Zhang, "Wide bandgap oxide semiconductors: from materials physics to optoelectronic devices," *Advanced materials*, **33**(50), 2006230 (2021). <https://doi.org/10.1002/adma.202006230>
- [6] P. Rathore, C.M.S. Negi, A.S. Verma, A. Singh, G. Chauhan, A.R. Inigo, and S.K. Gupta, "Investigation of the optical and electrical characteristics of solution-processed poly (3 hexylthiophene) (P3HT): multiwall carbon nanotube (MWCNT) composite-based devices," *Materials Research Express*, **4**(8), 085905 (2017). <https://doi.org/10.1088/2053-1591/aa7dac>
- [7] R. Meitzner, T. Faber, S. Alam, A. Amand, R. Roesch, M. Büttner, F. Herrmann-Westendorf, et al., "Impact of P3HT materials properties and layer architecture on OPV device stability," *Solar Energy Materials and Solar Cells*, **202**, 110151 (2019). <https://doi.org/10.1016/j.solmat.2019.110151>
- [8] N. Rao, R. Singh, and L. Bashambu, "Carbon-based nanomaterials: Synthesis and prospective applications," *Materials Today: Proceedings*, **44**, 608-614 (2021). <https://doi.org/10.1016/j.matpr.2020.10.593>
- [9] W. Aloui, A. Ltaief, and A. Bouazizi, 2013. Transparent and conductive multi walled carbon nanotubes flexible electrodes for optoelectronic applications. *Superlattices and Microstructures*, **64**, 581-589.
- [10] P.C. Mahakul, and P. Mahanandia, "Structural and electrical characteristics of solution processed P3HT-carbon nanotube composite," *IOP Conference Series: Materials Science and Engineering*, **178**(1), 012024 (2017). <https://doi.org/10.1088/1757-899X/178/1/012024>
- [11] Q.A. Yousif, K.M. Mahdi, and H.A., Alshamsi, "Enhanced photovoltaic performance of dye-sensitized solar cell based on ZnO nanoparticles and ZnO/graphene nanocomposites," *Journal of the Chinese Chemical Society*, **68**(9), 1637-1643 (2021). <https://doi.org/10.1002/jccs.202000382>
- [12] F. Ziaefar, A. Alizadeh, and Z. Shariatinia, "Dye sensitized solar cells fabricated based on nanocomposite photoanodes of TiO₂ and AlMo_{0.5}O₃ perovskite nanoparticles," *Solar Energy*, **218**, 435-444 (2021). <https://doi.org/10.1016/j.solener.2021.03.024>
- [13] H-J. Hwang, S-J. Joo, and H-S. Kim, "Copper nanoparticle/multiwalled carbon nanotube composite films with high electrical conductivity and fatigue resistance fabricated via flash light sintering," *ACS Applied Materials Interfaces*, **7**, 25413-25423 (2015). <https://doi.org/10.1021/acsami.5b08112>

- [14] B. King, and B. Panchapakesan, "Vacuum filtration-based formation of liquid crystal films of semiconducting carbon nanotubes and high-performance transistor devices," *Nanotechnology*, **25**, 175201 (2014). <https://doi.org/10.1088/0957-4484/25/17/175201>
- [15] M. Zhang, S. Höfle, J. Czolk, A. Mertens, and A. Colmann, "All-Solution Processed Transparent Organic Light Emitting Diodes," *Nanoscale*, **7**, 20009-20014 (2015). <https://doi.org/10.1039/C5NR05820A>
- [16] W. Zhou, X. Bai, E. Wang, and S. Xie, "Synthesis, structure, and properties of single-walled carbon nanotubes," *Advanced Materials*, **21**(45), 4565-4583 (2009). <https://doi.org/10.1002/adma.200901071>
- [17] D. Luo, Q.B. Chen, B. Liu, and Y. Qiu, "Emergence of Flexible White Organic Light-Emitting Diodes," *Polymers*, **11**, 384 (2019). <https://doi.org/10.3390/polym11020384>
- [18] G. Li, R. Zhu, and Y. Yang, "Polymer Solar Cells," *Nature Photonics*, **6**, 153-161 (2012). <https://doi.org/10.1038/nphoton.2012.11>
- [19] Y.Y. Gao, Z. Wang, G.T. Yue, X. Yu, X.S. Liu, G. Yang, F.R. Tan, et al., "Efficient Polymer Solar Cells with High Fill Factor Enabled by a Furo[3,4-c] Pyrrole-4,6-Dione-Based Copolymer," *Solar RRL*, **3**, 1900012 (2019). <https://doi.org/10.1002/solr.201900012>
- [20] Z.J. Zhang, J.H. Miao, Z.C. Ding, B. Kan, B.J. Lin, X.J. Wan, W. Ma, et al., "Efficient and Thermally Stable Organic Solar Cells Based on Small Molecule Donor and Polymer Acceptor," *Nature Communications*, **10**, 3271 (2019). <https://doi.org/10.1038/s41467-019-10984-6>
- [21] S. Ren, L.Y. Chang, S.K. Lim, J. Zhao, M., Smith, N. Zhao, V. Bulovic, et al., "Inorganic Organic Hybrid Solar Cell: Bridging Quantum Dots to Conjugate Polymer Nanowire," *Nano Letters*, **11**, 3998-4002 (2011). <https://doi.org/10.1021/nl202435t>
- [22] D. Chaudhary, S. Munjal, N. Khare, and V.D. Vankar, "Bipolar resistive switching and nonvolatile memory effect in poly (3-hexylthiophene)-carbon nanotube composite films," *Carbon*, **130**, 553-558 (2018). <https://doi.org/10.1016/j.carbon.2018.01.058>
- [23] M.D. Hampton, "Polythiophene nanowires for use in organic electronic applications," PhD diss, Cardiff University, 2012.
- [24] M. Tonga, "A Rational Ternary Design of P3HT/Insulating Polymers-CNTs/P3HT for the Enhanced Thermoelectric Performances," *Composite Interfaces*, **29**(2), 197-213 (2022). <https://doi.org/10.1080/09276440.2021.1913900>
- [25] M. Baibarac, G. Arzumanyan, M. Daescu, A. Udrescu, and K. Mamatkulov, "Anisotropic Photoluminescence of Poly (3-hexyl thiophene) and Their Composites with Single-Walled Carbon Nanotubes Highly Separated in Metallic and Semiconducting Tubes," *Molecules*, **26**(2), 294 (2021). <https://doi.org/10.3390/molecules26020294>
- [26] H. Zhu, M. Pan, M.B. Johansson, and E.M. Johansson, "High photon-to-current conversion in solar cells based on light-absorbing silver bismuth iodide," *ChemSusChem*, **10**(12), 2592-2596 (2017). <https://doi.org/10.1002/cssc.201700634>
- [27] N.S.N. Sa'aya, S.Z.N. Demon, N. Abdullah, A. Shatar, V.F.K. Ernest, and N.A. Halim, "Optical and Morphological Studies of Multiwalled Carbon Nanotube-incorporated Poly (3-hexylthiophene-2, 5-diyl) Nanocomposites," *Sensors & Materials*, **31**, 2997-3006 (2019). <https://doi.org/10.18494/SAM.2019.2513>
- [28] P.H.N. Nguyen, "Facile preparation, characterization of flexible organic solar cells using P3HT-MWCNTs composite photoactive layer," *Journal of Materials Science and Chemical Engineering*, **8**, 1-10 (2020). <https://doi.org/10.4236/msce.2020.810001>
- [29] M.R. Karim, "Synthesis and characterizations of poly (3-hexylthiophene) and modified carbon nanotube composites," *Journal of Nanomaterials*, **2012**, 34-38 (2012). <https://doi.org/10.1155/2012/174353>
- [30] S. Qotso, P. Mbule, and B. Mothudi, "Characterization of P3HT-CNT thin films for photovoltaic solar cell applications," in: *SAIP 2021 Proceedings*, <https://events.saip.org.za/event/206/contributions/7086/contribution.pdf>
- [31] D. Khan, et al., "Incorporation of carbon nanotubes in photoactive layer of organic solar cells," *Ain Shams Engineering Journal*, **12**(1), 897-900 (2021). <https://doi.org/10.1016/j.asej.2020.06.002>
- [32] B.K. Kuila, K. Park, and L. Dai, "Soluble P3HT-grafted carbon nanotubes: synthesis and photovoltaic application," *Macromolecules*, **43**(16), 6699-6705 (2010). <https://doi.org/10.1021/ma100917p>
- [33] N. Nurazzi, N. Abdullah, S.Z.N. Demon, N.A. Halim, and I.S. Mohamad, "The Influence of Reaction Time on Non-Covalent Functionalisation of P3HT/MWCNT Nanocomposites," *Polymers*, **13**(12), 1916 (2021). <https://doi.org/10.3390/polym13121916>
- [34] G. Keru, P.G. Ndungu, G.T. Mola, and V.O. Nyamori, "Bulk heterojunction solar cell with nitrogen-doped carbon nanotubes in the active layer: effect of nanocomposite synthesis technique on photovoltaic properties," *Materials*, **8**(5), 2415-2432 (2015). <https://doi.org/10.3390/ma8052415>
- [35] T.S.T. Khanh, N.P.H. Nam, and N.N. Dinh, "Facile preparation, characterization of flexible organic solar cells using P3HT-MWCNTs composite photoactive layer," *Journal of Materials Science and Chemical Engineering*, **8**, 1-10 2020. https://eprints.uet.vnu.edu.vn/eprints/id/eprint/4293/1/NPH%20Nam_MSCE_2020.pdf
- [36] P.J. Goutam, D.K. Singh, and P.K. Iyer, "Photoluminescence quenching of poly (3-hexylthiophene) by carbon nanotubes," *The Journal of Physical Chemistry C*, **116**(14), 8196-8201 (2012). <https://doi.org/10.1021/jp300115q>
- [37] D. Hernández-Martínez, et al., "Elaboration and characterization of P3HT-PEO-SWCNT fibers by electrospinning technique," *SN Applied Sciences*, **2**, 462-470 (2020). <https://doi.org/10.1007/s42452-020-2278-2>
- [38] B.K. Kuila, S. Malik, S.K. Batabyal, and A.K. Nandi, "In-situ synthesis of soluble poly (3-hexylthiophene)/multiwalled carbon nanotube composite: Morphology, structure, and conductivity," *Macromolecules*, **40**(2), 278-287 (2007). <https://doi.org/10.1021/ma061548e>
- [39] D. Meng, J. Sun, S. Jiang, Y. Zeng, Y. Li, S. Yan, J. Geng, and Y. Huang, "Grafting P3HT brushes on GO sheets: distinctive properties of the GO/P3HT composites due to different grafting approaches," *Journal of Materials Chemistry*, **22**(40), 21583-21591 (2012). <https://doi.org/10.1039/C2JM35317B>
- [40] V. Saini, Z. Li, S. Bourdo, E. Dervishi, Y. Xu, X. Ma, V.P. Kunets, "Electrical, optical, and morphological properties of P3HT-MWNT nanocomposites prepared by in situ polymerization." *The Journal of Physical Chemistry C*, **113**(19), 8023-8029 (2009). <https://doi.org/10.1021/jp809479a>
- [41] H. Tai, X. Li, Y. Jiang, G. Xie, and X. Du, "The enhanced formaldehyde-sensing properties of P3HT-ZnO hybrid thin film OTFT sensor and further insight into its stability," *Sensors*, **15**(1), 2086-2103 (2015). <https://doi.org/10.3390/s150102086>
- [42] J. Arranz-Andrés, and W.J. Blau, "Enhanced device performance using different carbon nanotube types in polymer photovoltaic devices," *Carbon*, **46**(15), 2067-2075 (2008). <https://doi.org/10.1016/j.carbon.2008.08.027>

**СИНТЕЗ, ХАРАКТЕРИСТИКА ТА ФУНКЦІОНАЛІЗАЦІЯ НАНОКОМПОЗИТНИХ ПЛІВОК РЗНТ-CNT
ЛЕГОВАНИХ Ag₂O**

Хайдер Абдулмір Аббас^a, Віссем Шейхроу Кубаа^b, Естабрак Таліб Абдуллах^c

^aСередній технічний університет, Інститут підготовки технічних інструкторів, Багдад, Ірак

^bУніверситет Сфакс, Факультет природничих наук, Сфакс, Туніс

^cНауковий коледж Багдадського університету, факультет фізики, Ірак

Дослідження зосереджено на синтезі вуглецевих нанотрубок (CNT) і полі(3-гексилтіофену) (РЗНТ) (первинного полімеру) з легованими Ag (CNT/РЗНТ@Ag) нанокompозитними тонкими плівками, для практичних застосувань. Були підготовлені чотири зразки розчину CNT з різним співвідношення полімеру (РЗНТ) [0,1, 0,3, 0,5 і 0,7 мас.%] для формування тонкого шару нанокompозитів РЗНТ@CNT методом покриття Ag. Для дослідження властивостей поглинання та провідності для використання в різних практичних застосуваннях, у цьому дослідженні систематично оцінювалися структура, морфологія, оптичні та фотолюмінесцентні властивості нанокompозиту CNT/РЗНТ@Ag. У зв'язку з цим використовувався спектрофотометр UV/Vis/NIR в діапазоні довжин хвиль від 350 до 700 нм для дослідження спектру поглинання, пропускання, коефіцієнта екстинкції (k) і показника заломлення зразків, виготовлених при кімнатній температурі. Результати XRD вказують на невелике збільшення розміру кристалітів синтезованого нанокompозиту (CNT/РЗНТ@Ag) порівняно з нанокompозитом CNT/РЗНТ, що можна пояснити кращою дисперсією РЗНТ та його сприятливим обгортанням навколо структур вуглецевих нанотрубок. Результати FESEM показують, що наночастинки Ag діють як місток між CNT і РЗНТ, створюючи зв'язок між двома матеріалами, який є достатньо міцним, щоб утворювати більш товсті трубчасті структури. Помітне збільшення інтенсивності поглинання (на приблизно 552 нм) досягається шляхом додавання наночастинок срібла до матриці CNT/РЗНТ при 0,5% РЗНТ. Крім того, підготовлені тонкі плівки CNT/РЗНТ@Ag демонструють більший коефіцієнт пропускання – понад 42%, 45%, 49% і 48% для концентрацій РЗНТ 1%, 3%, 5% і 7% відповідно. Підготовка даних про коефіцієнт екстинкції (k) і показник заломлення показує, що включення наночастинок срібла до нанокompозитної матриці CNT/РЗНТ має значне покращення порівняно з попередніми зразками (композит CNT/РЗНТ).

Ключові слова: нанокompозит; полі(3-гексилтіофен) (РЗНТ); розчин вуглецевих нанотрубок (CNT); метод занурення; фотолюмінесцентні властивості; спектр пропускання

STUDY OF STRUCTURAL AND ELECTRONIC PROPERTIES OF CsMgCl₃ COMPOUND

 Aman Kumar^{a*},  Harshit Gupta^b,  Dev Kumar^c,  Ritu Sharma^d,  Anuj Kumar^e,
Subodh Kumar Sharma^f, Aman Pal Singh^g

^aDepartment of Physics, Keral Verma Subharti College of Science, Swami Vivekanand Subharti University Meerut, India

^bDepartment of Electrical Engineering, Swami Vivekanand Subharti University Meerut, India

^cDepartment of Physics, C.C.S University Meerut, India

^dDepartment of Electronic and Communication Engineering, Subharti Polytechnic College, Swami Vivekanand Subharti University Meerut

^eMahamaya Government Degree college, Shearkot Bijnore, UP, India

^fDepartment of Physics, S. S. V. College, Hapur (C. C. S. University, Meerut U. P.), India

^gDepartment of Physics, M.M. College, Modinagar (C. C. S. University, Meerut U. P.), India

*Corresponding Author e-mail: 01amankumar@gmail.com

Received November 20, 2023; revised January 2, 2024; accepted January 8, 2024

In this report, we have investigated the CsMgCl₃ compound with the help of the WIEN2K software package. The structural and electronic properties are performed using the full potential augmented plane wave (FP-LAPW) method with the generalised gradient approximation (GGA) approximation as exchange correlation potentials. We used the Birch-Murnaghan equation (BME) to find the structural properties of the material. These include the lattice parameter, the bulk modulus, the first derivative of the bulk modulus, the minimum energy, and the volume. The structural properties match up with the experimental data. Electronic properties in terms of the band structure (BS) and total and partial density of state (T-DOS and P-DOS) profiles of CsMgCl₃ using GGA potentials exhibit an indirect wide energy band gap of 5.35 eV. All these properties show that the CsMgCl₃ compound is used as a perovskite in solar cells.

Keywords: GGA; Optoelectronic; Power generator; Band gap

PACS: 71.20. Lp; 71.20. Eh 71.20. _b

1. INTRODUCTION

The extraction of power from the most cost-effective sources, with the most efficient techniques, has garnered considerable attention among materials scientists. Hence, to ascertain the position of products in actual applications, it is imperative to define the operational characteristics of these gadgets. The utilisation of solar energy and the recovery of lost heat have significant promise. In recent times, there has been a significant surge in research pertaining to materials and compounds associated with photovoltaic technology and energy conversion applications. This surge can be attributed to the escalating impact of climate change and its detrimental consequences on the environment. According to this perspective, several halide perovskite compounds, both organic and inorganic in nature, have demonstrated significant promise as materials for photovoltaic applications such as solar cells. These compounds exhibit characteristics such as high-power conversion efficiency, high carrier mobility, and other desirable properties [1-8]. Collectively, these materials have been recognised for their exceptional capabilities in electrical, optoelectronic, and thermoelectric transportation applications [9–12]. The organic-inorganic hybrid halide perovskite CH₃NH₃PbI₃ has garnered significant attention from researchers because of its notable characteristics, such as extensive absorption, high mobility, and several advantageous thermoelectric and optoelectronic properties [11, 13-16]. However, certain limits have been noticed, including the fact that lead increases toxicity, which is not desirable from an environmental perspective [17]. Furthermore, it has been observed that the organic component undergoes decomposition, resulting in the release of detrimental chemicals [18]. To achieve the synthesis of lead-free perovskite compounds, alternative metal atoms such as Sn or Ge, with similar oxidation states, were substituted for the Pb atom. This substitution led to the development of certain pure inorganic and hybrid organic-inorganic compounds [19-21]. However, the substitutions indicate that lead-free compounds exhibit somewhat lower energy conversion efficiency and a lower figure of merit (ZT), which is a measure of the effectiveness of a thermoelectric material [22-23]. Consequently, there is a pressing need to conduct further research on alternative perovskite halides. Extensive research has been conducted on pure inorganic halide perovskite compounds due to the thermal decomposition of the organic component in hybrid perovskites at elevated temperatures [18]. Various studies have been conducted on compounds with diverse structural configurations, primarily focusing on their attributes through computational methods. The typical representation of their structure is ABX₃, wherein A and B are typically metals derived from main group elements, and X represents halides, specifically atoms of chlorine (Cl), bromine (Br), and iodine (I). Several lead-free halide perovskites have been identified, including CsGeX₃, CsSnX₃, TlGeX₃, TlSnI₃, CsMgBr₃, and others [24–28]. We have conducted research on hazardous inorganic perovskite compounds, specifically CsMgCl₃, which exhibit similarities to the compounds. CsMgI₃ has been omitted from consideration due to the findings of Ray et al, who determined that its cubic structure is not energetically possible as indicated by its positive formation energy [10]. Several experimental studies have been undertaken on CsMgX₃ compounds, focusing on their synthesis and structural analysis. These compounds have a

hexagonal lattice structure and are classified as non-perovskite compounds [29-31]. In a recent publication, Kaewmeechai et al., conducted a computational analysis on the structural and electrical characteristics of CsMgBr₃ in its three distinct phases [28]. However, it is important to note that there is a lack of comprehensive research conducted on the perovskite CsMgX₃ compounds. The past research findings indicate that halide perovskites belonging to the ABX₃ class can be found in cubic, tetragonal, and orthorhombic crystal systems. In light of the significant value associated with halide perovskites, there is a clear need to conduct a methodical and accurate examination of compounds belonging to the ABX₃ category. Such an inquiry holds great potential for enhancing our understanding in this field. Although there is a lack of comprehensive theoretical details about the potential optical applications of a computational approach, the existing body of experimental literature predominantly emphasises optical applications. In addition, there is a lack of research that elucidates the impact of halogen ion replacement on the optical and thermoelectric properties of CsMgCl₃. This study focuses only on the cubic phases of CsMgCl₃, examining their structural, and electronic properties using the GGA functional. These properties have not been previously investigated.

2. COMPUTATIONAL METHODOLOGIES

The simulations of CsMgCl₃ halide perovskites were conducted using the WIEN2K code, employing the self-consistent full-potential linearized augmented plane wave (FP-LAPW) approach. This method was integrated into the code [32-33]. The structural optimisation was performed using the PBE-GGA (Perdew-Burke-Ernzerhof generalised gradient approximation) exchange functional [34]. To accurately calculate the electronic characteristics, we employed the GGA exchange correlation functional [35], which yielded improved outcomes. The implementation of this technique necessitates the partitioning of the crystal structure into muffin-tin (MT) spheres that encompass the atomic sites and the interstitial regions located at the periphery of these spheres. In order to achieve Eigen-value convergence, a value of 8.0 is chosen for Rmt*Kmax, where Rmt represents the muffin tin radius. It is typically selected to be sufficiently big to prevent any overlap between the MT spheres. Kmax, on the other hand, refers to the maximum value of the reciprocal lattice vectors and is of utmost importance. The expansion of angular momentum is carried out by performing calculations using a k-mesh consisting of 15×15×15 k points, which allows for the integration of the irreducible Brillouin zone. The number of k-points in the Brillouin zone has been augmented to 2456, as the attributes under consideration exhibit a strong reliance on the higher density of k-points. The accompanying section fully presents all the equations involved in the computation of these properties.

3. RESULTS

3.1. Structural Properties

As previously stated, we have considered the cubic arrangement of the perovskite compounds under investigation and conducted structural optimisations. The fully relaxed structure is depicted in Figure 1. The Wyckoff positions for Cs and Mg atoms are designated as 1a (0, 0, 0) and 1b (0.5, 0.5, 0.5) respectively. Conversely, the halide ions (Cl) are situated in the 3c positions, namely (0, 0.5, 0.5), (0.5, 0, 0.5), and (0.5, 0.5, 0). The compounds with cubic structure are classified under the Pm3m space group.

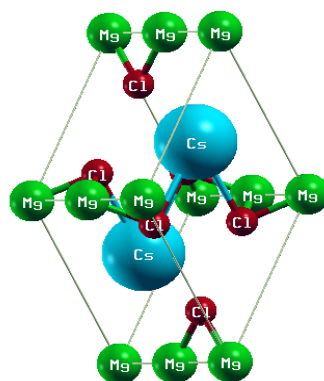


Figure 1. Unit cell structure of CsMgCl₃ generated by VESTA

The lattice parameters and other physical attributes, as presented in Table 1, were determined through volume optimisation using the Birch-Murnaghan equation of state, written as follows [36]:

$$E_{total} = E_0(V) + \frac{B_0 V_0}{B_0' (B_0' - 1)} \left[B_0 \left(1 - \frac{V_0}{V} \right) + \left(\frac{V_0}{V} \right)^{B_0'} - 1 \right]. \quad (1)$$

The equation was utilised to provide a graphical representation of the relationship between energy and volume, which is depicted in Figure 2. By analysing these plots, we can determine the minimal energy of the compounds in their ground state, as well as the corresponding optimum volumes. This analysis is conducted using the PBE-GGA method.

According to the data presented in Table 1, it is evident that the lattice constants for CsMgCl₃ is 7.29 Å, respectively. Notably, the latter value closely corresponds to a previously reported finding [28]. The observed bulk modulus and its pressure derivative for these compounds indicate that their values are not significantly like those of metals. This suggests that these compounds possess a modest level of compressibility.

Table 1. Calculated lattice constants (a_0), Min. cell volume (V_0), Ground state energy (E_0), Bulk modulus (B_0) and Pressure Derivative of bulk modulus (B_P), Band gap (E_g) and Fermi energy (E_F) of cubic CsMgCl₃.

Parameters	CsMgCl ₃	Experimental
Lattice parameter (Å)	7.292908648	5.178 [28]
Min. Volume (a. u) ³	1987.7230	-----
Bulk Modulus B (GPa)	26.3716	-----
Pressure derivative B _P (GPa)	5.9772	-----
Minimum energy E ₀ (Ryd)	-37501.898866	-----
Bandgap(eV)	5.35	6.35 [37]
Fermi energy (E _F)	0.02259	-----

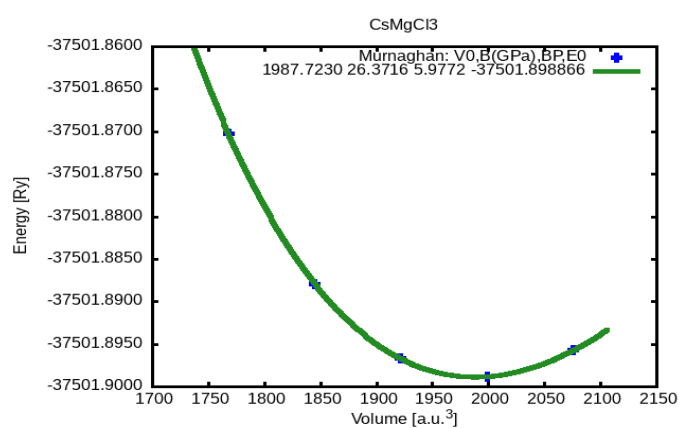


Figure 2. Variation of total energy with volume of CsMgCl₃ compound

3.2. Electronic Properties

To examine the electronic properties of these compounds, we have conducted calculations on their band structures using the PBE-GGA exchange correlation functionals. The results are presented in Figures 3(a-b).

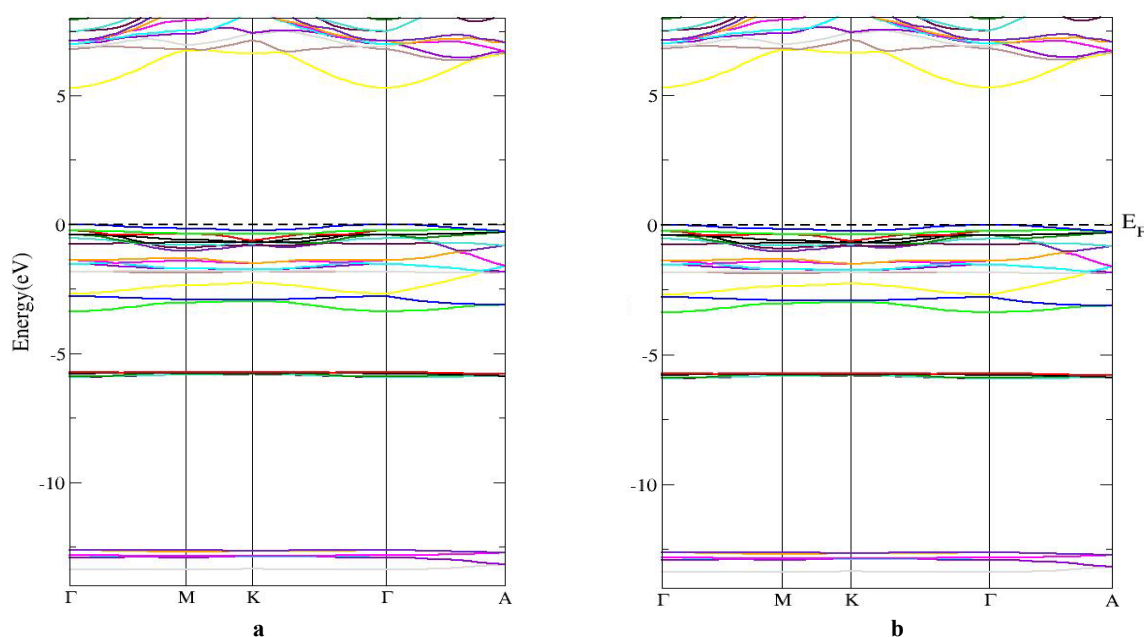


Figure 3. Electronic band structures of (a) CsMgCl₃ for spin up, (b) CsMgCl₃ for spin down, using GGA approach.

Various research in the field of density functional theory (DFT) have noted that the utilisation of exchange functionals can occasionally present challenges when attempting to accurately determine band gaps. The PBE-GGA functional has been found to significantly underestimate the band gaps of different materials and compounds due to a

self-interaction mistake. This issue could be addressed by utilising alternative methodologies, a highly effective approach that is extensively employed in DFT calculations for determining the electronic structure and various properties of compounds such as perovskites and Heusler alloys. In our investigation, we have calculated band gap for CsMgCl₃ compound by the utilisation of the generalised gradient approximation (GGA) technique with high symmetry k-points within the Brillouin zone is $\Gamma \rightarrow M \rightarrow K \rightarrow \Gamma \rightarrow A$, which is utilised for the computation of electronic structures. To begin with, the band structures of CsMgCl₃, as depicted in Figure 3(a-b), indicate that it exhibits characteristics of indirect wideband gap materials.

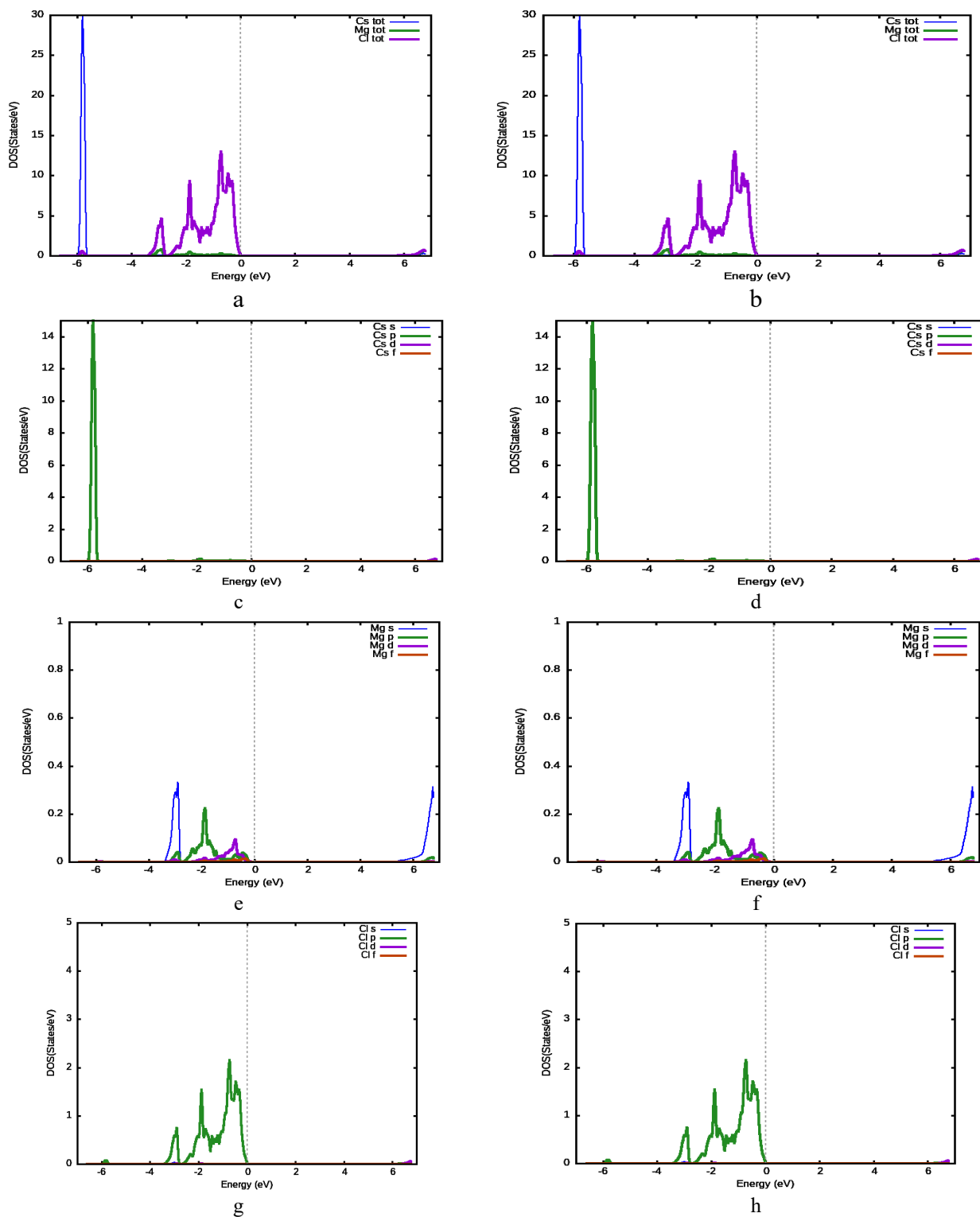


Figure 4. Total density of states of (a) CsMgCl₃ in spin-up, (b) CsMgCl₃ in spin-down and partial density of states of (c) Cs (s, p, d and f state) in spin-up, (d) Cs (s, p, d and f state) in spin-down, (e) Mg (s, p, d and f state) in spin-up, (f) Mg (s, p, d and f state) in spin-down, (g) Cl₃ (s, p, d and f state) in spin-up, (h) Cl₃ (s, p, d and f state) in spin-down

The conduction band minimum (CBM) is located at the Γ point, whereas the valence band maximum (VBM) is situated at the M point, resulting in the formation of an indirect gap. Nevertheless, a band gap of these compound found is 5.35 eV has been attained using GGA. It is important to note that the characteristics of the conduction and valence bands (CB and VB) are consistent in both cases. Additionally, it has been observed that the bands in the valence band (VB) are located at the Fermi level and exhibit a relatively low curvature at high-symmetry points. The presence of flat bands in a system suggests the existence of high effective masses, which can significantly influence the efficiency of transport properties. The findings of our study regarding the energy band gap of CsMgCl₃, as determined using the GGA potential, demonstrate a proximity to the experimental value of 8.5 eV. Furthermore, the bandgaps of our theoretical models exhibit a high level of concordance with the perovskite structures described. The electronic band profiles of these compounds demonstrate their characteristic as wide band gap semiconductors when analysed using the PBE-GGA potential. However, under ambient conditions, they exhibit insulating behaviour when assessed using the GGA method.

Another electronic property calculated such as the total density of states (TDOS) and partial density of states (PDOS) were calculated for these compounds using the GGA potential in order to gain a better understanding of the specific atoms and their orbitals that contribute to the band structure curves. This potential was chosen due to its ability to produce an enhanced band gap. The TDOS plot of CsMgCl₃, as illustrated in Figure 4(a-h), indicates that the primary contribution to the density of states (DOS) in the valence band (VB) arises from the halogen atom (Cl) located at the Fermi level edges. This halogen atom is also accountable for the presence of flat bands at the VB band boundaries. A notable increase in the energy levels of a Cs atom is observed at higher energy values, approximately 5 eV. This phenomenon is associated with the presence of degenerate bands in the valence band that exhibit a flat energy profile near this energy range. The appearance of states in the conduction band (CB) at higher energy levels, around 6.3 eV, can be attributed to the energy gap resulting from the lack of density of states (DOS) in the CB region at the Fermi level (E_F) up to approximately 6.3 eV. The study reveals a comparable contribution of the Cl and Cs atomic states in the CB system. The participation of the magnesium (Mg) atom is nearly negligible in the valence band (VB) and fairly evident in the conduction band (CB).

The relationship between specific orbitals of the atoms in the electronic structures of perovskite compounds is elucidated by the PDOS plot depicted in Figure 4 (c-h). The analysis of Fig. 4(a) and (b) reveals that the prominent peaks observed in the valence band (VB) can be attributed mostly to the density of states (DOS) originating from the p-orbitals of Cl atom in the vicinity of the Fermi energy (E_F). Additionally, a narrow peak corresponding to the energy states of p-orbitals of Cs atoms at higher energies is also observed. Additionally, we observe a negligible contribution from the s and p-orbitals of magnesium atoms. In the context of the chemical bond, the participation of halogen atoms experiences a significant decrease. Small peaks of states for magnesium (Mg) atoms, specifically in their s and p-orbitals, are observed at higher energy levels within the conduction band. The occurrence of density of states (DOS) in Cs atoms is attributed to the presence of its d-orbitals. Previous research has documented both theoretical and experimental studies pertaining to these specific halides [38-40].

CONCLUSION

The objective of this study is to investigate the structural, and electronic properties of Magnesium-based halides using the FP-LAPW technique. The findings on all parameters of Mg based halides indicate that these materials have the potential to be synthesised under normal atmospheric conditions. These include the lattice parameter, the bulk modulus, the first derivative of the bulk modulus, the minimum energy, and the volume. The structural properties match up with the experimental data. Electronic properties in terms of the band structure (BS) and total and partial density of state (T-DOS and P-DOS) profiles of CsMgCl₃ using GGA potentials exhibit an indirect wide energy band gap of 5.35 eV. All these properties show that the CsMgCl₃ compound is used as a perovskite in solar cells.

ORCID

© Aman Kumar, <https://orcid.org/0000-0002-8867-6595>; © Dev Kumar, <https://orcid.org/0009-0006-2726-4227>
 © Harshit Gupta, <https://orcid.org/0009-0007-3964-6895>; © Anuj Kumar, <https://orcid.org/0000-0003-3372-3718>
 © Ritu Sharma, <https://orcid.org/0009-0007-2725-4226>

REFERENCES

- [1] J.N. Burschka, S.J. Pellet, R. Moon, P. Humpry-Baker, M.K.N. Gao, and M. Gratzel, *Nature*, **499**, 316-319 (2013). <https://doi.org/10.1038/nature12340>
- [2] M. He, D. Zheng, M. Wang, C. Lin, and Z. Lin, *J. Mater. Chem. A*, **2**, 5994-6003 (2014). <https://doi.org/10.1039/C3TA14160H>
- [3] M. Grätzel, *Nat. Mater.* **13**, 838-842 (2014). <https://doi.org/10.1038/nmat4065>
- [4] Q.F. Dong, Y. Fang, Y. Shao, P. Mulligan, J. Qiu, L. Cao, and J. Huang, *Science*, **347**, 967-970 (2015). <https://doi.org/10.1126/science.aaa5760>
- [5] W. Lee, H. Li, A.B. Wong, D. Zhang, M. Lai, Y. Yu, Q. Kong, et al., *Proc. Natl. Acad. Sci. USA*, **114**, 8693 (2017). <https://doi.org/10.1073/pnas.1711744114>
- [6] R.E. Brandt, V. Stevanović, D.S. Ginley, and T. Buonassisi, *MRS Commun.* **5**, 265 (2015). <https://doi.org/10.1557/mrc.2015.26>
- [7] M. Saliba, T. Matsui, J.Y. Seo, K. Domanski, J.P. Correa-Baena, M.K. Nazeeeruddin, S.M. Zakeeruddin, et al., *Energy Environ. Sci.* **9**, 1989-1997 (2016). <https://doi.org/10.1039/C5EE03874J>
- [8] W. Zhang, G.E. Eperon, and H.J. Snaith, *Nat. Energy*, **1**, 16048 (2016). <https://doi.org/10.1038/nenergy.2016.48>
- [9] D.H. Fabini, J.G. Labram, A.J. Lehner, J.S. Bechtel, H.A. Evans, A.V. Ven, F. Wudl, et al., *Inorg. Chem.* **56**, 11-25 (2017). <https://doi.org/10.1021/acs.inorgchem.6b01539>

- [10] D. Ray, C. Clark, H.Q. Pham, J. Borycz, R.J. Holmes, E.S. Aydil, and L. Gagliardi, *J. Phys. Chem. C*, **122**, 7838-7848 (2018). <https://doi.org/10.1021/acs.jpcc.8b00226>
- [11] Y.P. He, and G. Galli, *Chem. Mater.* **26**, 5394-5400 (2014). <https://doi.org/10.1021/cm5026766>
- [12] M.A. Ali, N. Alam, S. Meena, S.A. Ali, A. Dar, G. Khan, Murtaza, et al., *Int. J. Quantum. Chem.* **120**, e26141 (2019). <https://doi.org/10.1002/qua.26141>
- [13] D. Shi, V. Adinolfi, R. Comin, M. Yuan, E. Alarousu, A. Buin, Y. Chen, et al., *Science*, **347**, 519-522 (2015). <https://doi.org/10.1126/science.aaa2725>
- [14] X. Mettan, R. Pisoni, P. Matus, A. Pisoni, J. Jacimovic, B. Nafradi, M. Spina, et al., *J. Phys. Chem. C*, **119**, 11506-11510 (2015). <https://doi.org/10.1021/acs.jpcc.5b03939>
- [15] G. Xing, N. Mathews, S. Sun, S.S. Lim, Y.M. Lam, M. Gratzel, S. Mhaisalkar, and T.C. Sum, *Science*, **342**, 344-347 (2013). <https://doi.org/10.1126/science.1243167>
- [16] C.C. Stoumpos, C.D. Malliakas, and M.G. Kanatzidis, *Inorg. Chem.* **52**, 9019-9038 (2013). <https://doi.org/10.1021/ic401215x>
- [17] A. Babayigit, A. Ethirajan, M. Muller, and B. Conings, *Nat. Mater.* **15**, 247-251 (2016). <https://doi.org/10.1038/nmat4572>
- [18] S.A. Chowdhury, K. Inzani, T. Pena, A. Dey, S.M. Wu, S.M. Griffin, and H. Askari, *J. of Engg. Mat. & Techno.* **144**, 011006 (2021). <http://dx.doi.org/10.1115/1.4051306>
- [19] T. Krishnamoorthy, H. Ding, C. Yan, W.L. Leong, T. Baikie, Z. Zhang, M. Sherburne, et al., *J. Mater. Chem. A*, **3**, 23829-23832 (2015). <https://doi.org/10.1039/C5TA05741H>
- [20] L.C. Tang, C.S. Chang, L.C. Tang, and J.Y. Huang, *J. Phys. Condens. Matter*, **12**, 9129-9143 (2017). <https://doi.org/10.1088/0953-8984/12/43/303>
- [21] F. Hao, C.C. Stoumpos, P. Guo, N. Zhou, T.J. Marks, R.P.H. Chang, and M.G. Kanatzidis, *J. Am. Chem. Soc.* **137**, 11445-11452 (2015). <https://doi.org/10.1021/jacs.5b06658>
- [22] S. Shao, J. Liu, G. Portale, H. Fang, G.R. Blake, G.H. TenBrink, L.J.A. Koster, et al., *Ad Energy Mat.* 1702019 (2017). <https://doi.org/10.1002/aenm.201702019>
- [23] Y. Takahashi, H. Hasegawa, Y. Takahashi, and T. Inabe, *J. Solid State Chem.* **205**, 39. (2013). <https://doi.org/10.1016/j.jssc.2013.07.008>
- [24] W. Ming, H. Shi, and M.H. Du, *J. Mater. Chem. A*, **4**, 13852-13858 (2016). <https://doi.org/10.1039/C6TA04685A>
- [25] L.Y. Huang, and W.R.L. Lambrecht, *Phys. Rev. B*, **88**, 165203 (2013). <https://doi.org/10.1103/PhysRevB.88.165203>
- [26] D.J. Singh, *J. Appl. Phys.* **112**, 083509 (2012). <https://doi.org/10.1063/1.4759240>
- [27] I. Chung, J.-H. Song, J. Im, J. Androulakis, C.D. Malliakas, H. Li, A.J. Freeman, et al., *J. Am. Chem. Soc.* **134**, 8579-8587 (2012). <https://doi.org/10.1021/ja301539s>
- [28] C. Kaewmeechai, Y. Laosiritaworn, and A.P. Jaroenjittichai, *J. Phys.: Conf. Ser.* **1380**, 012112 (2019). <https://doi.org/10.1088/1742-6596/1380/1/012112>
- [29] G.L. McPherson, A.M. McPherson, and J.L. Atwood, *J. Phys. Chem. Solids*, **41**, 495 (1980). [https://doi.org/10.1016/0022-3697\(80\)90180-8](https://doi.org/10.1016/0022-3697(80)90180-8)
- [30] A.P. Shpak, O.A. Glike, A.G. Dmitriev, P.A. Rodnyi, A.S. Voloshinovskii, and S.M. Pidzyrailo, *J. Electron. Spectrosc. Relat. Phenom.* **68**, 335-338 (1994). [https://doi.org/10.1016/0368-2048\(94\)02131-7](https://doi.org/10.1016/0368-2048(94)02131-7)
- [31] G.L. McPherson, T.J. Kistenmacher, and G.D. Stucky, *J. Chem. Phys.* **52**, 815-824 (1970). <https://doi.org/10.1063/1.1673061>
- [32] P. Blaha, K. Schwarz, P. Sorantin, and S.B. Trickey, *Comp. Phys. Commun.* **59**, 399-415 (1990). [https://doi.org/10.1016/0010-4655\(90\)90187-6](https://doi.org/10.1016/0010-4655(90)90187-6)
- [33] P. Blaha, K. Schwarz, G.K.H. Madsen, D. Kvasnicka, and J. Luitz, *wien2k, An Augment. Pl. Wave+ Local Orbitals Progr. Calc. Cryst. Prop.*, 2001.
- [34] J.P. Perdew, K. Burke, and M. Ernzerhof, *Phys. Rev. Lett.* **77**, 3865 (1996). <https://doi.org/10.1103/PhysRevLett.77.3865>
- [35] F. Tran, and P. Blaha, *Phys. Rev. Lett.* **102**, 226401 (2009). <https://doi.org/10.1103/PhysRevLett.102.226401>
- [36] F.D. Muranghan, *Proc. Natl. Acad. Sci. USA*, **30**, 5390 (1994).
- [37] G. Shwetha, V. Kanchana, and G. Vaitheeswaran, *J. of Solid State of Chem.* **227**, 110-116 (2015). <https://doi.org/10.1016/j.jssc.2015.03.024>
- [38] A. Kumar, A. Kumar, K. Kumar, R.P. Singh, R. Singh, and R. Kumar, *East European Journal of Physics*, (1), 109-117 (2023). <https://doi.org/10.26565/2312-4334-2023-1-13>
- [39] A. Kumar, R. Guatam, R.P. Singh, and A. Kumar, *International Journal of Advanced Science and Technology*, **29**(08), 1150-1158 (2020).
- [40] A. Kumar, R. Guatam, S. Chand, A. Kumar, and R.P. Singh, *Materials Physics & Mechanics*, **42**(1), 112-130 (2019). http://dx.doi.org/10.18720/MPM.4212019_10

ДОСЛІДЖЕННЯ СТРУКТУРНИХ ТА ЕЛЕКТРОНИХ ВЛАСТИВОСТЕЙ СПОЛУКИ CsMgCl₃

Аман Кумар^а, Харшіт Гупта^б, Дев Кумар^с, Ріту Шарма^д, Анудж Кумар^е, Субодх Кумар Шарма^ф, Аман Пал Сінгх^г

^аФакультет фізики, науковий коледж Керал Верма Субхарті, Університет Свамі Вівекананд Субхарті Меєрут, Індія

^бКафедра електротехніки, Університет Свамі Вівекананда Субхарті Меєрут, Індія

^сКафедра фізики, Університет CCS Меєрут, Індія

^дКафедра електронної та комунікаційної інженерії, політехнічний коледж, Університет Свамі Вівекананда Субхарті, Меєрут

^еГосударственный колледж Махамайя, Ширкот Биджнор, УР, Індія

^фФакультет фізики, Коледж S.S.V., Халур (Університет CCS, Меєрут, УР), Індія

^гКафедра фізики, М.М. Коледж, Модінагар (C. S. S. University, Meerut U. P.), Індія

У цій роботі ми досліджували сполуку CsMgCl₃ за допомогою програмного пакету WIEN2K. Структурні та електронні властивості визначалися з використанням методу повнопотенційних приєднаних плоских хвиль (FP-LAPW) з наближенням узагальненого градієнта (GGA) як обмінних кореляційних потенціалів. Ми використовували рівняння Берча-Мурнагана (BME) визначення структурних властивостей матеріалу. До них відносяться параметр решітки, модуль об'ємного стиску, перша похідна модуля об'ємного стиску, мінімальна енергія та об'єм. Структурні властивості відповідають експериментальним даним. Електронні властивості з точки зору зонної структури (BS), а також профілів повної та парціальної густини станів (T-DOS та P-DOS) CsMgCl₃ з використанням потенціалів GGA демонструють непряму широку енергетичну заборонену зону 5,35 еВ. Всі ці властивості показують, що з'єднання CsMgCl₃ може бути використаний як перовскітна структура в сонячних елементах.

Ключові слова: GGA; оптоелектроніка; генератор енергії; заборонена зона

NITROGEN ADSORPTION ON DOUBLE-WALLED CARBON NANOTUBE AT DIFFERENT TEMPERATURES: MECHANISTIC INSIGHTS FROM MOLECULAR DYNAMICS SIMULATIONS

 Utkir B. Uljayev*, Shakhnozaxon A. Muminova,  Ishmumin D. Yadgarov

Arifov Institute of Ion-Plasma and Laser Technologies, Academy of Sciences of Uzbekistan, Tashkent, 100125, Uzbekistan

**Corresponding Author e-mail: utkir.uljaev@outlook.com*

Received December 22, 2023; revised January 12, 2024; accepted January 24, 2024

Nitrogen-adsorbing carbon nanotubes have received considerable attention in the field of materials science due to their unique properties and potential applications. In particular, nitrogen-adsorbed double-walled carbon nanotubes (DWNTs) can exhibit a wide range of tunable electronic and optoelectronic properties. In this study, the effect of different temperatures (i.e., 300, 600, and 900 K) of DWNT on nitrogen adsorption is investigated through molecular dynamics simulations using the ReaxFF potential. The simulation results show a good nitrogen storage capacity of DWNT, particularly at 600 K, reaching a maximum gravimetric density of 12.4 wt%. This study contributes to a better understanding of the mechanisms governing nitrogen adsorption onto DWNTs at different temperatures.

Keywords: *Double-walled carbon nanotube, Nitrogen adsorption, Reactive molecular dynamics*

PACS: 61.46.-w, 02.70.Ns

INTRODUCTION

Carbon nanotubes (CNTs) have garnered broad interest across physics, chemistry, and materials science [1], showcasing promise in diverse applications including electronic devices [2], sensors [3], material reinforcement [4], adsorbents [5], and numerous other areas [7]. Among them, double-walled carbon nanotubes (DWNTs) have gained significant attention due to their improved stability and mechanical properties [8],[9]. The interactions of DWNTs with other atoms and molecules, particularly boron (B) [10], nitrogen (N) [11], calcium (Ca) [12], palladium (Pd) [13] and platinum (Pt) [14] have been intensively studied in recent years.

Among them, nitrogen (N) atoms adsorption (i.e., chemisorption) on carbon nanotubes has gained much attention in recent years due to its applications in various fields such as energy storage and catalysis [5], [6]. N atom chemisorption and doping on DWNTs are being explored as promising strategies to modify their electrical and chemical properties for various applications. Several studies have investigated the chemisorption mechanism of N atoms on the outer and inner walls of DWNTs, as well as the effect of N doping on their electronic and optical properties [15]. Chemisorption of N atoms on DWNTs depends on various factors, such as tube diameter and chirality, which in turn affect the strength and type of interaction with the adsorbate [11]. In this respect, understanding the chemisorption processes of N atoms on DWNTs is essential for the design of efficient nanomaterials for gas detection and separation [16], [17], [18]. Although nitrogen (N) atoms have been introduced into CNTs by various methods (e.g., CVD, ALD), controlling their amount in the structure is still one of the pressing problems [19], [20].

In this study, we investigate the chemisorption mechanisms of N atoms on DWNT at different temperatures using molecular dynamics (MD) simulations.

COMPUTATIONAL DETAILS

The process of nitrogen adsorption onto DWNTs is investigated using reactive MD simulations [21] using the LAMMPS package [22]. The ReaxFF potential is used to describe the interatomic interactions in the system [23]. This potential is chosen to describe the breaking and joining of bonds between atoms. A neat (5,5@10,10) nanotube was chosen as a DWNT model (DWNT(5,5)@(10,10)) in MD simulations (Fig.1). The diameter of DWNTs is 6.78 and 13.57 Å (Fig. 1) which is in the range of experimentally obtained nanotube diameters (6.3 Å–7.9 Å) and (13 Å–16 Å) [24]. Periodic boundary conditions are applied along the z-axis, which represents the length of the DWNT (28.12 Å), allowing the simulation of infinitely long DWNTs.

Initially, the energy of all model systems is minimized by the conjugated gradient method. Subsequently, the temperature and pressure of the systems are equilibrated to the desired values (300 K, 600, 900K and 0 Pa) in the NpT ensemble using a Berendsen thermostat and barostat [25] with coupling constants of 100 fs and 5000 fs, respectively. The chosen heating rate (i.e., 1 K/ps) corresponds to a previously reported range of values (0.1–10.0 K/ps) [26] and indicates that the deviations in the thermodynamic equilibrium of the model systems are insignificant during the temperature increase. In the case of the chemisorption of N atoms on DWNT, the system's temperature is kept at 300 K, 600 K and 900 K for 100 ps using a Bussi thermostat [27] with a coupling constant of 100 fs in the canonical NVT ensemble.

In the simulations, the pressure of N atoms in the system is calculated as $p = J\sqrt{2\pi MRT}/N_A$, [28] (1), where J is the impingement flux ($\text{nm}^{-2}\cdot\text{ns}^{-1}$), N_A is Avagadro's number, R is the universal gas constant, M is the molar mass of the N atom ($\text{kg}\cdot\text{mol}^{-1}$) and T is the temperature of the system (K). In this work, the impingement flux of the incident N atoms (i.e., 100 N) is $78.74 \text{ nm}^{-2}\cdot\text{ns}^{-1}$, and its corresponding pressure is approximately 1.94 MPa. The simulation is done under NVT conditions with N atoms added to the environment surrounding the surface of the nanotube at a 10 ps interval, and with a minimum distance of 10 Å (i.e., the cutoff radius of the interaction potential) between each N atoms and the model system.

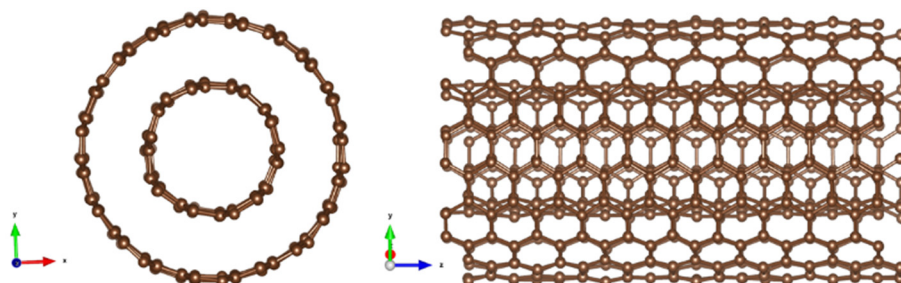


Figure 1. Top and side views of the DWNT(5,5)@(10,10) model system

The gravimetric density of nitrogen (N) atoms remaining on the surface of pure DWNTs under the influence of different temperatures (300 K, 600 K, 900 k) was calculated as follows:

$$wt\% = (1 + m_C N / m_N n)^{-1} \times 100\% \quad (1)$$

where m_C and N are the mass and number of carbon atoms in DWNT, m_N and n are the mass and number of adsorbed N atoms.

In all MD simulations, a time step of 0.1 fs is used. The simulations are repeated 5 times for each study case, and the final results are obtained by averaging the individual physical quantities.

RESULTS AND DISCUSSION

It can be seen from the results that N atoms adsorbed on the DWNT(5,5)@(10,10) surface for systems with different temperatures (i.e. 300, 600, 900 K) number adsorption N (%) atoms (or adsorption index, $(N_{\text{adsorption}}/N_{\text{total}}, \%)$) also varied. Specifically, with an increase in the number of adsorbed N atoms at a temperature of 300 K, the number of adsorbed N atoms was in the range of 2-48% (Fig.2a). Temperature of 600 K and 900 K, it is in the range of 2-77% and 10-61%, respectively.

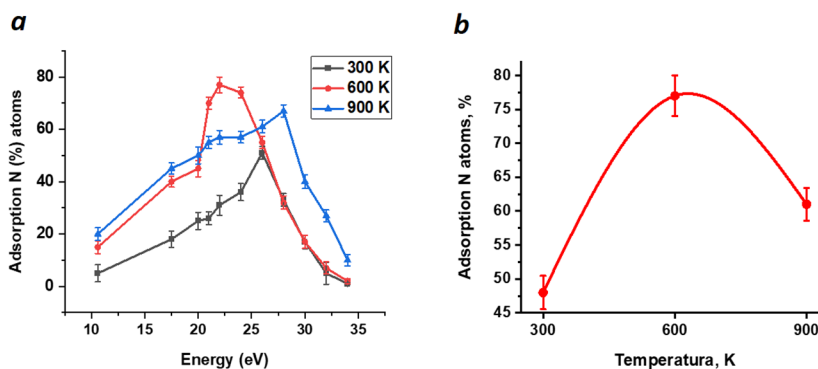


Figure 2. (a) Dependence of the number of adsorbed nitrogen (N) atoms on their kinetic energy, (b) The temperature dependence of the maximum adsorption index of nitrogen atoms.

That is, at temperatures of 300 K, 600 K and 900 K, the maximum adsorption index was equal to 48%, 77% and 61% (Fig.2b). The largest adsorption index is at 600 K, which is 1.52 and 1.19 times greater than at 300 K and 900 K. It can be seen from the results that the adsorption index did not increase linearly with increasing temperature. From the results, it is known that the temperature also affects the N adsorption process. As the velocity (i.e., kinetic energy) of N atoms falling on the DWNT(5,5)@(10,10) surface increased, the adsorption level also increased (from 0 eV to 22.50 eV), further increasing the velocity of N atoms led to a decrease in the amount of adsorption (about, 26.24 eV for 300 K, 22.50 eV for 600 K and 28.74 eV for 900 K). The results indicate that an additional elevation in energy (i.e., 33.15 eV) led to a decrease in the adsorption index to a value approaching 0% (Fig.2a).

The chemisorption of N atoms on DWNT relies on multiple factors, such as the curvature of the nanotube surface, the arrangement of the six-membered carbon rings, among others [29],[30]. Furthermore, the adsorption index of DWNT varies at different temperatures. Depending on their position (para, ortho, meta) within the hexagon cell of the CNT,

N atoms on the surface of CNT can depart from the surface due to the influence of temperature [31]. N atoms adsorbed on the DWNT surface are influenced by the arrival of other N atoms on the surface, leading to the formation of molecules through the Langmuir-Hinshelwood recombination mechanism (where two N atoms on the surface covalently bond to form a nitrogen molecule) or Eley-Rideal desorption mechanism on the surface due to the impact of incoming N atoms on the adsorbed N atom [32], [33]. The temperature range (i.e., 300–900 K) employed in this study altered the quantity of N atoms adsorbed on the surface.

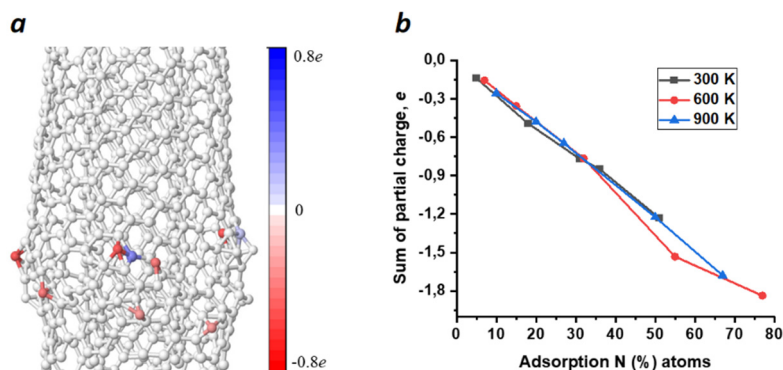


Figure 3. (a) N atoms chemisorbed onto DWNT(5,5)@(10,10) are introduced, and system atoms exhibit partial charges from $-0.8e$ to $+0.8e$, which range from red to blue is depicted by the color spectrum, which shows the transition from electron-rich regions to electron-poor regions, respectively, (b) The alteration in the partial charge of adsorbed N atoms in relation to temperature

In addition to these effects, in CNT, the carbon atom has a higher electronegativity value ($\chi=2.55$) compared to the N atom ($\chi=3.04$). Figure 3a shows the chemisorption process of N atoms on DWNT(5,5)@(10,10). Atoms in the system are depicted in blue with a positive charge and red with a negative charge, while uncharged (0) atoms are depicted in white. This difference in electronegativity results in interactions such as Coulomb forces between the CNT surface and N atoms. This, in turn, results in a relatively stronger interaction between N atoms and C atoms on the DWNT(5,5)@(10,10) surface, thereby leading to higher adsorption of N atoms on DWNT(5,5)@(10,10). Figure 3b illustrates that the partial charge increases with the rise in the adsorption index (%) of chemisorbed N atoms on DWNT(5,5)@(10,10).

Table 1. The variation in the partial charge of adsorbed nitrogen (N) atoms (%) is demonstrated as a function of temperature.

Adsorption N atoms, %	300 K		Adsorption N atoms, %	600 K		Adsorption N atoms, %	900 K	
	C	N		C	N		C	N
5	$0.14e$	$-0.14e$	7	$0.15e$	$-0.15e$	10	$0.25e$	$-0.25e$
18	$0.49e$	$-0.49e$	15	$0.35e$	$-0.35e$	20	$0.48e$	$-0.48e$
31	$0.76e$	$-0.76e$	32	$0.76e$	$-0.76e$	27	$0.65e$	$-0.65e$
36	$0.85e$	$-0.85e$	55	$1.53e$	$-1.53e$	50	$1.22e$	$-1.22e$
51	$1.23e$	$-1.23e$	77	$1.84e$	$-1.84e$	67	$1.67e$	$-1.67e$

As a result, the sum of maximum partial charges of C and N atoms appropriately $1.23e$ and $-1.23e$ (51 %) for 300 K, $1.84e$ and $-1.84e$ (77 %) for 600 K, $1.67e$ and $-1.67e$ (67 %) for 900 K which corresponds to the values of 5–77 % respectively (Table 1). This indicates that an increase in the concentration of N leads to an increase in negative (n-type) partial charges of the DWNT. This validates the outcomes achieved in earlier investigations [34].

Figure 4 shows the nitrogen adsorption coverage ($\rho\%=N_N/N_C$) and gravimetric density (wt%) of N atoms as a function of temperature. As can be seen from the figure, the ρ % (or, wt%) of N atoms at 300, 600 and 900 K is different, the maximum adsorption of N atoms on the surface at 300 K, 600 K and 900 K level 8 % (or 9.3 wt%), 12.1 % (or 12.4 wt%), 10.18% (or 10.6 wt%), respectively.

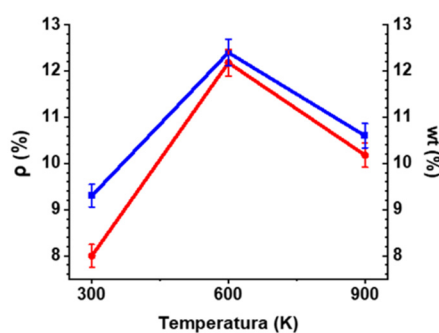


Figure 4. The gravimetric density of chemisorbed N atoms (right, blue) and the adsorption coverage (left, red) as a function of temperature

CONCLUSION

We can conclude that this molecular dynamics simulation has successfully visualized the N adsorption mechanism in DWNT(5,5)@(10,10). In this simulation the trend of N adsorbed in DWNT(5,5)@(10,10) is influenced by temperature factors. The N adsorption by DWNT(5,5)@(10,10) at lower temperatures such as at 300 K has a higher amount of N concentration than at higher temperatures (600 K and 900 K). As the temperature increases at a constant pressure, the amount of N that adsorbed will be decreases. While the trend of the amount of N absorbed will growth with increasing pressure at a constant temperature. The best result of gravimetric density 12.4 wt% (or 12.1% nitrogen concentration) that occurred at 1.94 MPa pressure with temperature (600 K) condition.

Acknowledgment

This research was carried out within the framework of the F-FA-2021-512 project, granted by the Agency for Innovative Development of the Republic of Uzbekistan. The simulations were performed using FISTUz cluster at the Institute of Ion-Plasma and Laser Technologies of the Academy of Sciences of Uzbekistan.

ORCID

©Ishmumin D. Yadgarov, <https://orcid.org/0000-0002-4808-2258>; ©Utkir B. Uljayev, <https://orcid.org/0009-0002-2564-5270>

REFERENCES

- [1] S. Iijima, "Carbon nanotubes: past, present, and future", *Phys. B Condens. Matter*, **323**(1-4), 1–5 (2002). [https://doi.org/10.1016/S0921-4526\(02\)00869-4](https://doi.org/10.1016/S0921-4526(02)00869-4)
- [2] M. Soto, et al., "Effect of interwall interaction on the electronic structure of double-walled carbon nanotubes", *Nanotechnology*, **26**(16), 165201 (2015). <https://doi.org/10.1088/0957-4484/26/16/165201>
- [3] Q. Wei, X. Tong, G. Zhang, J. Qiao, Q. Gong, and S. Sun, "Nitrogen-Doped Carbon Nanotube and Graphene Materials for Oxygen Reduction Reactions", *Catalysts*, **5**(3), 1574–1602 (2015). <https://doi.org/10.3390/catal5031574>
- [4] E.N. Nxumalo, and N.J. Coville, "Nitrogen Doped Carbon Nanotubes from Organometallic Compounds: A Review", *Materials*, **3**(3), 2141–2171 (2010). <https://doi.org/10.3390/ma3032141>
- [5] F. Shojaie, "N₂ adsorption on the inside and outside the single-walled carbon nanotubes by density functional theory study", *Pramana*, **90**(1), 4 (2018). <https://doi.org/10.1007/s12043-017-1498-5>
- [6] M. Jamshidi, M. Razmara, B. Nikfar, and M. Amiri, "First principles study of a heavily nitrogen-doped (10,0) carbon nanotube", *Phys. E Low-Dimens. Syst. Nanostructures*, **103**, 201–207 (2018). <https://doi.org/10.1016/j.physe.2018.06.003>
- [7] C. Zhao, Y. Lu, H. Liu, and L. Chen, "First-principles computational investigation of nitrogen-doped carbon nanotubes as anode materials for lithium-ion and potassium-ion batteries", *RSC Adv.* **9**(30), 17299–17307 (2019). <https://doi.org/10.1039/C9RA03235E>
- [8] S.-P. Ju, et al., "A molecular dynamics study of the mechanical properties of a double-walled carbon nanocoil", *Comput. Mater. Sci.* **82**, 92-99 (2014). <https://doi.org/10.1016/j.commatsci.2013.09.024>
- [9] V. Zólyomi, et al., "Intershell interaction in double walled carbon nanotubes: Charge transfer and orbital mixing", *Phys. Rev. B*, **77**(24), 245403 (2008). <https://doi.org/10.1103/PhysRevB.77.245403>
- [10] T. Koretsune, and S. Saito, "Electronic structures and three-dimensional effects of boron-doped carbon nanotubes", *Sci. Technol. Adv. Mater.* **9**(4), 044203 (2008). <https://doi.org/10.1088/1468-6996/9/4/044203>
- [11] K.-Y. Chun, H.S. Lee, and C.J. Lee, "Nitrogen doping effects on the structure behavior and the field emission performance of double-walled carbon nanotubes", *Carbon*, **47**(1), 169–177 (2009). <https://doi.org/10.1016/j.carbon.2008.09.047>
- [12] S.H. De Paoli Lacerda, J. Semberova, K. Holada, O. Simakova, S. Hudson, and J. Simak, "Carbon Nanotubes Activate Store-Operated Calcium Entry in Human Blood Platelets", *ACS Nano*, **5**(7), 5808–5813 (2011). <https://doi.org/10.1021/nn2015369>
- [13] H. Wu, D. Wexler, and H. Liu, "Effects of different palladium content loading on the hydrogen storage capacity of double-walled carbon nanotubes", *Int. J. Hydrog. Energy*, **37**(7), 5686–5690 (2012). <https://doi.org/10.1016/j.ijhydene.2011.12.120>
- [14] D. Xia et al., "Extracting the inner wall from nested double-walled carbon nanotube by platinum nanowire: molecular dynamics simulations", *RSC Adv.* **7**(63), 39480–39489 (2017). <https://doi.org/10.1039/C7RA07066G>
- [15] J.D. Correa, E. Florez, and M.E. Mora-Ramos, "Ab initio study of hydrogen chemisorption in nitrogen-doped carbon nanotubes", *Phys. Chem. Chem. Phys.* **18**(36), 25663–25670 (2016). <https://doi.org/10.1039/C6CP04531F>
- [16] H. Soleymanabadi, and J. Kakemam, "A DFT study of H₂ adsorption on functionalized carbon nanotubes", *Phys. E Low-Dimens. Syst. Nanostructures*, **54**, 115–117 (2013). <https://doi.org/10.1016/j.physe.2013.06.015>
- [17] R. Kronberg, H. Lappalainen, and K. Laasonen, "Hydrogen Adsorption on Defective Nitrogen-Doped Carbon Nanotubes Explained via Machine Learning Augmented DFT Calculations and Game-Theoretic Feature Attributions", *J. Phys. Chem. C*, **125**(29), 15918–15933 (2021). <https://doi.org/10.1021/acs.jpcc.1c03858>
- [18] Y. Fujimoto, and S. Saito, "Structure and stability of hydrogen atom adsorbed on nitrogen-doped carbon nanotubes", *J. Phys. Conf. Ser.* **302**, 012006 (2011). <https://doi.org/10.1088/1742-6596/302/1/012006>
- [19] M. Terrones, A. Jorio, M. Endo, A.M. Rao, Y.A. Kim, T. Hayashi, H. Terrones, et al., "New direction in nanotube science", *Mater. Today*, **7**(10), 30–45 (2004). [https://doi.org/10.1016/S1369-7021\(04\)00447-X](https://doi.org/10.1016/S1369-7021(04)00447-X)
- [20] M. Glerup, M. Castignolles, M. Holzinger, G. Hug, A. Loiseau, and P. Bernier, "Synthesis of highly nitrogen-doped multi-walled carbon nanotubes", *Chem. Commun.* **20**, 2542 (2003). <https://doi.org/10.1039/b303793b>
- [21] B.J. Alder, and T.E. Wainwright, "Phase Transition for a Hard Sphere System", *J. Chem. Phys.* **27**(5), 1208–1209 (1957). <https://doi.org/10.1063/1.1743957>
- [22] A.P. Thompson, H.M. Aktulga, R. Berger, D.S. Bolintineanu, W.M. Brown, P.S. Crozier, P.J. Veld, et al., "LAMMPS - a flexible simulation tool for particle-based materials modeling at the atomic, meso, and continuum scales", *Comput. Phys. Commun.* **271**, 108171 (2022). <https://doi.org/10.1016/j.cpc.2021.108171>
- [23] K. Chenoweth, A. C. T. Van Duin, and W. A. Goddard, "ReaxFF Reactive Force Field for Molecular Dynamics Simulations of Hydrocarbon Oxidation", *J. Phys. Chem. A*, vol. 112, no. 5, pp. 1040–1053, 2008, <https://doi.org/10.1021/jp709896w>

- [24] G. Chen, *et al.*, “Chemically Doped Double-Walled Carbon Nanotubes: Cylindrical Molecular Capacitors”, *Phys. Rev. Lett.* **90**(25), 257403 (2003). <https://doi.org/10.1103/PhysRevLett.90.257403>
- [25] H.J.C. Berendsen, J.P.M. Postma, W.F. Van Gunsteren, A. DiNola, and J.R. Haak, “Molecular dynamics with coupling to an external bath”, *J. Chem. Phys.* **81**(8), 3684–3690 (1984). <https://doi.org/10.1063/1.448118>
- [26] J. Sun, P. Liu, M. Wang, and J. Liu, “Molecular Dynamics Simulations of Melting Iron Nanoparticles with/without Defects Using a Reaxff Reactive Force Field”, *Sci. Rep.* **10**(1), 3408 (2020). <https://doi.org/10.1038/s41598-020-60416-5>
- [27] G. Bussi, D. Donadio, and M. Parrinello, “Canonical sampling through velocity rescaling”, *J. Chem. Phys.* **126**(1), 014101 (2007). <https://doi.org/10.1063/1.2408420>
- [28] D. Ugarte, A. Châtelain, and W.A. De Heer, “Nanocapillarity and Chemistry in Carbon Nanotubes”, *Science*, **274**(5294), 1897–1899 (1996). <https://doi.org/10.1126/science.274.5294.1897>
- [29] P. Ayala, A. Grüneis, T. Gemming, D. Grimm, C. Kramberger, M.H. Rummeli, F.L. Freire Jr., *et al.*, “Tailoring N-Doped Single and Double Wall Carbon Nanotubes from a Nondiluted Carbon/Nitrogen Feedstock”, *J. Phys. Chem. C*, **111**(7), 2879–2884 (2007). <https://doi.org/10.1021/jp0658288>
- [30] W. Su, X. Li, L. Li, D. Yang, F. Wang, X. Wei, W. Zhou, *et al.*, “Chirality-dependent electrical transport properties of carbon nanotubes obtained by experimental measurement”, *Nat. Commun.* **14**(1), 1672 (2023). <https://doi.org/10.1038/s41467-023-37443-7>
- [31] U. Khalilov, A. Bogaerts, B. Xu, T. Kato, T. Kaneko, and E. C. Neyts, “How the alignment of adsorbed ortho H pairs determines the onset of selective carbon nanotube etching”, *Nanoscale*, **9**(4), 1653–1661 (2017). <https://doi.org/10.1039/C6NR08005G>
- [32] X. Sha, B. Jackson, and D. Lemoine, “Quantum studies of Eley–Rideal reactions between H atoms on a graphite surface”, *J. Chem. Phys.* **116**(16), 7158–7169 (2002). <https://doi.org/10.1063/1.1463399>
- [33] T. Zecho, A. Güttler, X. Sha, D. Lemoine, B. Jackson, and J. Küppers, “Abstraction of D chemisorbed on graphite (0001) with gaseous H atoms”, *Chem. Phys. Lett.* **366**(1-2), 188–195 (2002). [https://doi.org/10.1016/S0009-2614\(02\)01573-7](https://doi.org/10.1016/S0009-2614(02)01573-7)
- [34] R. Czerw, M. Terrones, J.-C. Charlier, X. Blase, B. Foley, R. Kamalakaran, N. Grobert, *et al.*, “Identification of Electron Donor States in N-Doped Carbon Nanotubes”, *Nano Lett.* **1**(9), 457–460 (2001). <https://doi.org/10.1021/nl015549q>

АДСОРБЦІЯ АЗОТУ НА ДВОСТІННИХ ВУГЛЕЦЕВИХ НАНОТРУБКАХ ПРИ РІЗНИХ ТЕМПЕРАТУРАХ: МЕХАНІСТИЧНІ ДОСЛІДЖЕННЯ З МОДЕЛЮВАННЯ МОЛЕКУЛЯРНОЇ ДИНАМІКИ

Уткір Б. Уляєв, Шахнозаксон А. Мумінова, Ішмумін Д. Ядгаров

Інститут іонно-плазмових і лазерних технологій імені Арифова, Академії наук Узбекистану, Ташкент, 100125, Узбекистан
Вуглецеві нанотрубки, що адсорбують азот, привернули значну увагу в галузі матеріалознавства завдяки своїм унікальним властивостям і можливому застосуванню. Зокрема, адсорбовані азотом подвійні стінкові вуглецеві нанотрубки (DWNTs) можуть демонструвати широкий спектр регульованих електронних і оптоелектронних властивостей. У статті досліджується вплив різних температур (300, 600 і 900 K) DWNT на адсорбцію азоту за допомогою моделювання молекулярної динаміки з використанням потенціалу ReaxFF. Результати моделювання показують хорошу здатність DWNT зберігати азот, особливо при 600 K, досягаючи максимальної вагової щільності 12,4% мас. Це дослідження сприяє кращому розумінню механізмів адсорбції азоту на DWNT при різних температурах.

Ключові слова: двостінна вуглецева нанотрубка; адсорбція азоту; реактивна молекулярна динаміка

PROPERTIES OF SINGLE CRYSTAL SILICON DOPED WITH VANADIUM

 Khojakbar S. Daliev^a,  Zafarjon M. Khusanov^{b*}

^aBranch of the Federal State Budgetary Educational Institution of Higher Education “National Research University MPEI”, Tashkent, Uzbekistan

^bInstitute of Semiconductor Physics and Microelectronics at the National University of Uzbekistan
20 Yangi Almazar st., Tashkent, 100057, Uzbekistan

*Corresponding Author e-mail: zafarjon.xusanov@mail.ru

Received December 23, 2023; revised January 31, 2024; accepted February 2, 2024

The paper reports the sharp increase in resistivity and the conductivity change (type) in the single-crystal silicon sample doped with vanadium. The electrical and optical properties of single-crystalline silicon were determined Hall- and four-probe measurements and infrared (IR-) spectroscopy. Relative resistance, charge carrier concentration, mobility, and concentration of optically active oxygen and carbon in the samples were determined layer-by-layer. It is shown that in silicon samples doped with vanadium the concentration of optically active oxygen atoms tends to reduce.

Keywords: Silicon; Vanadium; Diffusion; Resistivity; Optically active; Oxygen; Carbon

PACS:78.30. Am

INTRODUCTION

The proposed technique of doping silicon with vanadium could possibly be used for the production of microcircuits, thus improving the physical parameters of the processed samples and ensuring production of sensitive diodes.

As is known, doping of silicon with impurity atoms that create deep levels leads to the formation of a defect structures in the silicon crystal lattice, and integrated circuits based on silicon doped with transition elements are traditionally characterized by robust long-term performance characteristics [1-2]. Transition elements embedded in silicon play a significant role by getting the outer electronic shells of impurity atoms and intrinsic atoms, and have high chemical activity. However, it was earlier mentioned that in silicon they are mostly in electrically inactive states [3-4]. However, the mechanisms of these physical phenomena, depending on the type of impurity atoms, environment, chemical composition and structure of these microformations, still remain unclear.

EXPERIMENTAL AND RESEARCH METHODS

The study shows that in the original single-crystalline silicon grown by the CZ- technique, the concentration of oxygen atoms was about $\sim 10^{18} \text{ cm}^{-3}$, while the concentration of carbon atoms approximately 10^{17} cm^{-3} , which were also in electrically inactive state. A series of analysis and studies of manufactured samples is shown in [4-5]. The authors compare various long-term scientific results, the molecular state of vanadium atoms in silicon and their interaction with growing layers.

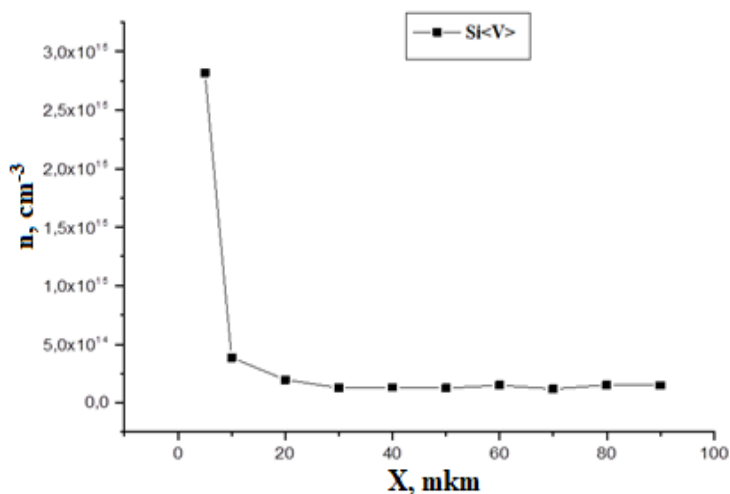


Figure 1. Dependence of charge carrier concentration layer-by-layer

Doping of silicon with vanadium impurity atoms was carried out by implementing the diffusion technique in unvacuumed ampoules at $T = 1200^{\circ} \text{C}$ for $t = 10$ hours and the deposition was induced from a layer of vanadium chloride

deposited on the surface of single-crystalline silicon. The maximum cooling rate of silicon samples after the diffusion of vanadium atoms was ensured by throwing quartz ampoules into coolant oil, the cooling rate of which $v_0 \approx 300$ K/s. Minimum cooling rate was $v_0 \approx 25$ K/s and was ensured after the electric furnace KSL-1075-1 has been turned off. As can be seen from Fig. 1, the charge carrier concentration (n) decreases depending on the penetration depth (x). The charge carrier concentration decreases across the depth of 20 μm from the sample surface, and then a stabilization of the charge carrier concentration is observed.

It was found that the doping Si with V at a diffusion temperature of $T_d=900-1000$ °C practically does not change the concentration of n-Si charge carriers.

Table 1. Reference Si sample

Si	Charge carrier concentration, n (cm^{-3})	Carriers mobility, μ (cm^2/Vs)	Specific resistance of samples, ρ ($\text{Ohm}\cdot\text{cm}$)	Conductivity type (type)
	$1.402 \cdot 10^{14}$	$9.855 \cdot 10^2$	$5.016\text{E} \cdot 10^1$	n

It is known that various high-temperature heat treatments (HHT) lead to changes in the defects structure of single-crystalline silicon. In this case, one can witness the process of assembly of various associated states of technological impurities (for example, oxygen atoms in silicon). Depending on the processing temperature, compounds of the SiO_x type are also formed on the silicon surface [5-6].

During the study, the results of the electrophysical parameters of doped silicon samples diffused for 10 hours at a constant temperature $T=1200$ °C are presented in Table 2.

Table 2. Electrophysical parameters of Si<V> diffusion samples

№	Thickness of the removed layer, X (mk)	Carrier mobility, μ (cm^2/Vs)	Specific resistance of samples, ρ ($\text{Ohm}\cdot\text{cm}$)	Conductivity type (type)
1	5	$3.852 \cdot 10^1$	$5.748 \cdot 10^1$	p
2	10	$3.869 \cdot 10^2$	$4.171 \cdot 10^1$	p
3	20	$7.881 \cdot 10^2$	$4.023 \cdot 10^1$	p
4	30	$8.839 \cdot 10^2$	$5.484 \cdot 10^1$	n
5	40	$8.798 \cdot 10^2$	$5.376 \cdot 10^1$	n
6	50	$8.597 \cdot 10^2$	$5.839 \cdot 10^1$	n
7	60	$8.311 \cdot 10^2$	$5.019 \cdot 10^1$	n
8	70	$9.676 \cdot 10^2$	$5.422 \cdot 10^1$	n
9	80	$8.921 \cdot 10^2$	$4.594 \cdot 10^1$	n
10	90	$8.707 \cdot 10^2$	$4.837 \cdot 10^1$	n

RESULTS AND DISCUSSION

The authors assume that the resistivity ρ of deep layers of the surface area of the resulting structure does not change sharply, and secondly, it is characterized by an almost flat distribution of resistivity ρ across the bulk of the silicon sample [7-8].

During the study, the resistivity of the starting samples was up to 50 $\text{Ohm}\cdot\text{cm}$, and the thickness of the mechanically polished samples was 1.5 mm. The concentration of the optically active oxygen atom is $N_0^{\text{opt}} \approx 9 \cdot 10^{17} \text{ cm}^{-3}$ and the carbon concentration $N_c^{\text{opt}} \approx 7.3 \cdot 10^{17} \text{ cm}^{-3}$, according to IR-absorption spectra at 1100 cm^{-1} (oxygen band area) and 610 cm^{-1} (carbon band area). Infrared absorption spectrum at 300 K according to a two-beam scheme, infrared spectra FSM-2201 operating in the range $370-7800 \text{ cm}^{-1}$ a spectrometer was used to determine the optically active oxygen (N_0^{opt}) carbon (N_c^{opt}) at room temperature [7-11]. IR-absorption spectra were measured for oxygen at 1106 cm^{-1} ($9.1 \mu\text{m}$) (Fig. 2b). For carbon, IR-absorption spectra were measured in the range $607 - 620 \text{ cm}^{-1}$ (Fig. 2a).

The concentration of optically active oxygen atoms and the concentration of optically active carbon atoms were analyzed using the following equations:

$$N_0^{\text{opt}} = 3.3 \cdot 10^{17} \cdot \frac{1}{d} \cdot \ln \frac{I}{I_0} \quad (1)$$

$$N_c^{\text{opt}} = 1.1 \cdot 10^{17} \cdot \frac{1}{d} \cdot \ln \frac{I}{I_0} \quad (2)$$

I and I_0 are intensities of incident and transmitted light, d is the thickness of the sample. 1- concentration of optically active oxygen was determined by the following equation:

1. $n\text{-Si}$ (control sample), $N_0^{\text{opt}} = 3.3 \cdot 10^{17} \cdot \frac{1}{d} \cdot \ln \frac{I}{I_0} = 9 \cdot 10^{17} \text{ cm}^{-3}$
2. $n\text{-Si}<V>$, $N_0^{\text{opt}} = 3.3 \cdot 10^{17} \cdot \frac{1}{d} \cdot \ln \frac{I}{I_0} = 8.3 \cdot 10^{17} \text{ cm}^{-3}$
3. $\Delta N_0^{\text{opt}} = N_0^{\text{opt}}(\text{control}) - N_0^{\text{opt}}(V) = 9 \cdot 10^{17} - 8.3 \cdot 10^{17} = 0.7 \cdot 10^{17} \text{ cm}^{-3}$.
4. $k = \frac{\Delta N_0^{\text{opt}}}{N_0^{\text{opt}}(\text{control})} \cdot 100 \%$

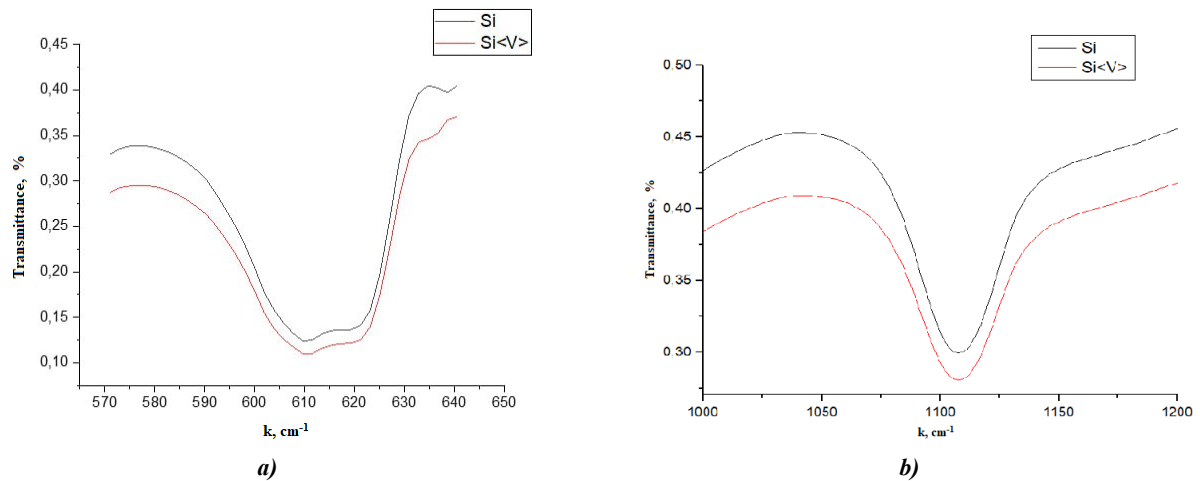


Figure 2. IR-absorption spectrum. a) N_c^{opt} , b) N_0^{opt} , 1 – high spectrum (n-Si) for the reference sample. 2 – for the lower spectrum (n-Si<V>)

Analysis of these results shows that in Si with *n*- and *p*-type vanadium, a decrease in the concentration of optically active oxygen by 8-10% was observed compared to reference samples that had undergone heat treatment under similar conditions. The IR-absorption spectra of optically active carbon at a wavelength of $\lambda=16.4 \mu\text{m}$ were also studied.

1. *n*-Si (control sample), $N_c^{opt} = 1.1 \cdot 10^{17} \cdot \frac{1}{d} \cdot \ln \frac{I}{I_0} = 7.3 \cdot 10^{17} \text{ cm}^{-3}$
2. *n*-Si<V>, $N_c^{opt} = 1.1 \cdot 10^{17} \cdot \frac{1}{d} \cdot \ln \frac{I}{I_0} = 7.1 \cdot 10^{17} \text{ cm}^{-3}$
3. $\Delta N_c^{opt} = N_c^{opt}(\text{control}) - N_c^{opt}(V) = 7.3 \cdot 10^{17} - 7.1 \cdot 10^{17} = 0.2 \cdot 10^{17} \text{ cm}^{-3}$.
4. $k = \frac{\Delta N_c^{opt}}{N_c^{opt}(\text{control})} \cdot 100 \%$

In reference samples and doped samples, a decrease in the concentration of optically active carbon by 2-3% was observed [12-16]. In particular, the results of measurements of IR-absorption spectra of starting silicon samples, of the doped silicon in the course of growth from solution and after various heat treatments show that the concentration of optically active oxygen in Si<V> and vanadium increase as a result high-temperature heat treatment of the sample.

CONCLUSIONS

Thus, it has been shown that doping Si with vanadium atoms leads to a decrease in the concentration of optically active oxygen N_0^{opt} by 8÷10 % depending on the concentration of introduced vanadium impurity atoms. The above proves that we are possibly seeing the interaction of vanadium atoms with oxygen atoms in the bulk of silicon. It has been established that preliminary heat treatments of starting silicon samples at $T = 1200^\circ\text{C}$ for $t = 12$ hours leads to the deposition of oxygen in parallel by forming SiO_2 molecules. In this case, the concentration of optically active carbon N_c^{opt} decreases by 2÷3 %. Additional V atoms in pre-heat-treated silicon led to a decrease in N_0^{opt} by 10÷15 %. This is due to the peculiarities of the interaction of V atoms with SiO_2 molecules. It is shown that *p*-Si <HT+V> samples also exhibit an increase in ρ after doping with vanadium atoms, but it is several times smaller compared to *p*-Si<V> samples.

It's worth mentioning that when exposed to IR-radiation (wavelength of $\lambda=16.4$ microns when silicon single crystals are transparent), absorption depends only on chemical composition, structure and oxygen concentration. In order to find out the clear mechanism of how vanadium atoms do influence the concentration and size of electroactive centers in silicon, as well as establishing the influence of boundary and surface states on the observed phenomena might require additional research into the subject.

Acknowledgment

The authors are grateful to the Director of the Research Institute of Semiconductor Physics and Microelectronics, Doctor of Physical and Mathematical Sciences, Prof. Sh.B. Utamuradova for assisting in conducting the experiments and discussing the results.

ORCID

✉ Khojakbar S. Daliev, <https://orcid.org/0000-0002-2164-6797>; ✉ Zafarjon M. Khusanov, <https://orcid.org/0009-0005-9420-8033>

REFERENCES

- [1] Kh.S. Daliev, Sh.B. Utamuradova, O.A. Bozorova, and Sh.Kh. Daliev, "Joint effect of Ni and Gf impurity atoms on the silicon solar cell photosensitivity," Applied Solar Energy (English translation of Geliotekhnika), **41**(1), 80–81 (2005). https://www.researchgate.net/publication/294234192_Joint_effect_of_Ni_and_Gf_impurity_atoms_on_the_silicon_solar_cell_photosensitivity

- [2] Sh.B. Utamuradova, Sh.Kh. Daliev, E.M. Naurzalieva, X.Yu. Utemuratova, "Investigation of defect formation in silicon doped with silver and gadolinium impurities by Raman scattering spectroscopy," *East Eur. J. Phys.*, (3), 430–433 (2023). <https://doi.org/10.26565/2312-4334-2023-3-47>
- [3] O. E. Sattarov, A. Mavlyanov and A. An, "Effect of Manganese Atoms on the Magnetic Properties of Silicon," *Surface Engineering and Applied Electrochemistry*, **59**(2), 216–219 (2023). <https://doi.org/10.3103/S106837552302014X>
- [4] Kh.S. Daliev, Sh.B. Utamuradova, O.A. Bozorova, and Sh.Kh. Daliev, "Joint influence of impurity atoms of nickel and hafnium on photosensitivity of silicon solar cells," *Geliotekhnika*, (1), 85–87 (2005).
- [5] Sh.B. Utamuradova, Kh.S. Daliev, E.K. Kalandarov, and Sh.Kh. Daliev, "Features of the behavior of lanthanum and hafnium atoms in silicon," *Technical Physics Letters*, **32**(6), 469–470 (2006). <https://doi.org/10.1134/S1063785006060034>
- [6] Sh.B. Utamuradova, A.V. Stanchik, and D.A. Rakhmanov, *East Eur. J. Phys.* 2, 201 (2023). <https://doi.org/10.26565/2312-4334-2023-2-21>
- [7] T.M. Razykov, J. Bekmirzoev, A. Bosio, B.A. Ergashev, D. Isakov, R. Khurramov, K.M. Kouchkarov, et al., "Structural and optical properties of Sb_xSe_y thin films obtained by chemical molecular beam deposition method from Sb and Se precursors," *Solar Energy*, **254**, 67–72 (2023). <https://doi.org/10.1016/j.solener.2023.03.010>
- [8] Sh.B. Utamuradova, Z.T. Azamatov, V.E. Gaponov, N.N. Bazarbaev, and A.B. Bakhromov, "Application of speckle interferometry for non-destructive testing of objects," *Applied Physics*, **4**, 115–120 (2023).
- [9] I. Sapaev, B. Sapaev, D. Abdullaev, J. Abdullayev, A. Umarov, R. Siddikov, A. Mamasoliev, et al., "Influence of the parameters to transition capacitance at NCDS-PSI heterostructure," *E3S Web of Conferences*, **383**, 04022 (2023). <https://doi.org/10.1051/e3sconf/202338304022>
- [10] K.P. Abdurakhmanov, Sh.B. Utamuradova, Kh.S. Daliev, N.Kh. Ochilova, and Z.O. Olimbekov, "Study of the interimpurity interaction in silicon doped with platinum and iron," *Applied Solar Energy*, **34**(2), 71–72 (1998).
- [11] Kh.S. Daliev, Sh.B. Utamuradova, I.Kh. Khamidzhonov, A.Zh. Akbarov, I.K. Mirzairova, and Zh. Akimova, "Thermally Induced Deep Centers in Silicon Doped with Europium or Lanthanum," *Inorganic Materials*, **37**, 436–438 (2001). <https://doi.org/10.1023/A:1017556212569>
- [12] S.I. Vlasov, and F.A. Saporov, "Effect of pressure on the electric properties of passivating coatings based on lead borosilicate glasses," *Surface Engineering and Applied Electrochemistry*, **47**(4), 338–339 (2011). <http://dx.doi.org/10.3103/2FS1068375511040156>
- [13] S.B. Utamuradova, Z.T. Azamatov, M.A. Yuldoshev, N.N. Bazarbayev, and A.B. Bakhromov, *East Eur. J. Phys.* 4, 147 (2023), <https://doi.org/10.26565/2312-4334-2023-4-15>
- [14] Sh.Kh. Daliev, and F.A. Saporov, "On the properties of the Si-SiO₂ transition layer in multilayer silicon structures", *East European Journal of Physics*, (4), 206–209 (2023). <https://doi.org/10.26565/2312-4334-2023-4-25>.
- [15] A. Yu. Lederman, R.A. Ayukhanov, R.M. Turmanova, A.K. Uteniyazov, and E.S. Esenbaeva, *Non-recombination injection mode, Semiconductor Physics, Quantum Electronics & Optoelectronics*, **24**(3) 248–254 (2021). <https://doi.org/10.15407/spqeo24.03.248>
- [16] Kh.S. Daliev, Sh.B. Utamuradova, O.A. Bozorova, and Sh.Kh. Daliev, Joint influence of impurity atoms of nickel and hafnium on photosensitivity of silicon solar cells. *Geliotekhnika*, (1), 85–87 (2005).

ВЛАСТИВОСТІ МОНОКРИСТАЛІЧНОГО КРЕМНІЮ, ЛЕГОВАНОГО ВАНАДІЄМ

Ходжакбар С. Далієв^а, Зафарджон М. Хусанов^б

^аФілія Федерального державного бюджетного навчального закладу вищої освіти «Національний дослідницький університет МПЕІ», м. Ташкент, Узбекистан

^бІнститут фізики напівпровідників та мікроелектроніки Національного університету Узбекистану
100057, Ташкент, Узбекистан, вул. Янги Алмазар, 20

У статті повідомляється про різке збільшення питомого опору та зміни (типу) провідності в зразку монокристалічного кремнію, легovanого ванадієм. Електричні та оптичні властивості монокристалічного кремнію були визначені вимірюваннями Холла та чотирьох зондів та інфрачервоною (ІЧ) спектроскопією. Відносний опір, концентрацію носіїв заряду, рухливість та концентрацію оптично активного кисню та вуглецю в зразках визначали пошарово. Показано, що в легованих ванадієм зразках кремнію концентрація оптично активних атомів кисню має тенденцію до зменшення.

Ключові слова: кремній; ванадій; дифузія; питомий опір; оптично активний; кисень; карбон

GROWING Sb_2Se_3 FILMS ENRICHED WITH SELENIUM USING CHEMICAL MOLECULAR BEAM DEPOSITION

 Takhirdjon M. Razikov,  Sultanpasha A. Muzafarova*,  Ruhiddin T. Yuldoshov*,
 Zafarjon M. Khusanov, Marg'uba K. Khusanova, Z.S. Kenzhaeva, B.V. Ibragimova

*Institute of Semiconductor Physics and Microelectronics at the National University of Uzbekistan,
20 Yangi Almazar St., Tashkent, 100057, Uzbekistan*

**Corresponding Author e-mail: samusu@rambler.ru; ruhiddin@yahoo.com*

Received January 2, 2024; revised January 22, 2024; accepted February 15, 2024

This study explores the growth of Sb_2Se_3 films on soda-lime glass (SLG) surfaces using the chemical molecular beam deposition (CMPD) method at a substrate temperature of 500°C. High-purity binary compounds, Sb_2Se_3 and Se, were employed as source materials for film deposition. Scanning electron microscopy (SEM) was employed to investigate the morphological characteristics of the Sb_2Se_3 films. Furthermore, the influence of temperature on the grain size and crystallographic orientation in selenium films was examined. Samples were obtained from a selenium source at temperatures of 370°C and 430°C. The results indicate that increasing the temperature of the selenium source results in the formation of larger grains and the presence of rod-shaped grains of Sb_2Se_3 aligned parallel to the substrate. A sample obtained at 370°C exhibited grains larger than 2 μm in size, evenly distributed across the substrate surface, indicating a uniform growth process. In contrast, when the temperature of the selenium source was raised to 430°C, considerably larger grains measuring approximately 4 μm were detected on the film surface substrate. X-ray diffraction analysis was conducted to gain insights into the crystalline phases and crystal structure of the Sb_2Se_3 films synthesized under different temperatures of the selenium source. The X-ray diffraction patterns displayed prominent peaks corresponding to the crystallographic planes (221) and (211), indicating the presence of strong crystalline phases. Additionally, peaks such as (020), (120), and (310) were observed in the X-ray patterns, further confirming the crystallinity of the films.

Keywords: *X-ray diffraction; Chemical molecular beam deposition; Sb_2Se_3 ; Selenium temperature*

PACS: 73.22

1. INTRODUCTION

Antimony selenide (Sb_2Se_3) has emerged as one of the most promising absorber materials for the development of next-generation thin-film solar cells, due to its outstanding photovoltaic performance. The remarkable properties of Sb_2Se_3 , including its simple crystal structure, substantial absorption coefficient exceeding 10^5 cm^{-1} , ideal band gap within the 1.1–1.3 eV range, and significant mobility, approximately $10 \text{ cm}^2\text{V}^{-1}\text{s}^{-1}$ [1], make it a highly attractive candidate for advanced thin-film solar cells. One distinct advantage of Sb_2Se_3 , compared to more established thin-film solar cells, specifically Copper Indium Gallium Selenide (CuInGaSe(S)_4 , referred to as CIGS) and Cadmium Telluride (CdTe), is its cost-effectiveness. Both antimony (Sb) and selenium (Se), the constituent elements of Sb_2Se_3 , are widely available and exhibit lower toxicity. As such, we can anticipate that Sb_2Se_3 technology will become a serious competitor in the mass production of thin-film photovoltaic modules. It has been discovered that [hk1]-oriented (vertically oriented) Sb_2Se_3 film is superior for efficient charge carrier transfer compared to the [hk0]-oriented Sb_2Se_3 compound film. However, controlling the orientation of the thin film remains a significant hurdle to further enhancing the efficiency of Sb_2Se_3 -based solar cells. It should be noted that during the synthesis of Sb_2Se_3 films via physical methods, a considerable amount of Se is lost due to film decomposition into Sb, Se, and SbSe. This results in the formation of Se vacancies, which subsequently increase the density of recombination centers in the films [2]. These changes have a negative impact on the optical and electrophysical properties of the solar cells. To mitigate this issue, researchers propose additional heat treatment in Se vapor. Zhiqiang Lee [2] has successfully produced thin film Sb_2Se_3 using a co-evaporation method of Sb_2Se_3 and Se [3, 4], whilst Shongalova [5] has introduced a method for creating Sb_2Se_3 films by sputtering, followed by "selenized" annealing in a H_2Se gas atmosphere. These innovative solutions illustrate the ongoing advancements in the field, paving the way for the full realization of Sb_2Se_3 potential in next-generation solar technology.

Sb_2Se_3 films are used various methods precipitation: thermal evaporation [6-7], gas transport evaporation [8, 9] method sublimation in a closed vacuum [10] and magnetron sputtering [11]. In this work, first time to grows films Sb_2Se_3 for solar cells by chemical molecular beam deposition (CMBD) method. In this study, we investigate the growth of Sb_2Se_3 films on SLG substrates using the CMBD method.

2. MATERIALS AND METHODS

Installed technological mode optimal grow Sb_2Se_3 films on surfaces SLG (soda- lime glass) by the method chemical molecular beam precipitation (Fig. 1). The experimental system was prepared by purging hydrogen to eliminate atmospheric pollutants. The SLG substrates with dimensions of $2.0 \times 2.0 \text{ cm}^2$ were used for film deposition. To obtain Sb_2Se_3 films with enriched selenium content and stoichiometric composition, the partial pressure of Se in the steam phase was adjusted during

the growth process. The substrate temperature was maintained at 500°C , while the temperatures of the source elements were varied within the ranges of 350°C to 430°C for Se and 700°C for Sb_2Se_3 . The growth rate was controlled between 0.1 to $1 \text{ \AA}/\text{sec}$, and a hydrogen flow rate of $\text{WH}_2 = 20 \text{ cm}^3/\text{min}$ was maintained.

Granules of Sb_2Se_3 and high-purity Se (99.999%) were utilized as the source materials. These compounds were placed in separate containers within the experimental setup. The morphological properties of the films were examined using a scanning electron microscope (SEM-EVO MA 10). The film compositions were determined by energy-dispersive elemental analysis (EDX) using an Oxford Instrument Aztec Energy Advanced X-act SDD detector. The crystal structure and phase composition were analyzed using X-ray diffraction (XRD) with a Panalytical Empyrean diffract meter, employing $\text{CuK}\alpha$ radiation ($\lambda = 1.5418 \text{ \AA}$) and 2θ measurements in the range of 20° to 80° with a step size of 0.01° . The phase composition analysis was conducted using the Joint Committee on Powder Diffraction Standards (JCPDS) database.

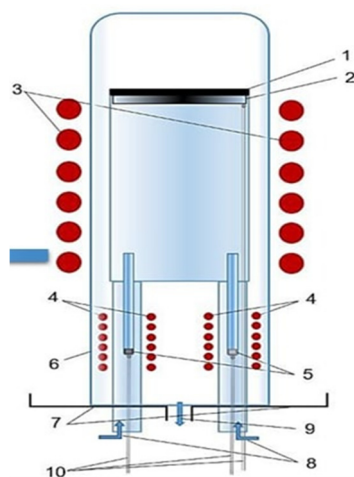


Figure 1. a) Schematic diagram of the system; b) Schematic image method chemical molecular beam deposition 1, 2 – substrate and its holder, 3- heater substrates, 4- heaters sources, 5- sources evaporated component (Sb_2Se_3 and Se), 6- hydrogen gas carriers (H_2), 7- flange holder, 8- hydrogen inlet, 9- hydrogen outlet, 10- thermocouple

3. RESULTS AND DISCUSSION

Morphological properties. The obtained SEM images revealed the morphological characteristics of the Sb_2Se_3 films, while the EDX analysis confirmed their elemental composition.

This study investigates the influence of temperature on grain size and crystallographic orientation in selenium films. A sample was obtained from a selenium source at temperatures of 370°C and 430°C . The characterization of the samples was performed using microscopy techniques, and the results were analyzed to understand the relationship between temperature and the observed grain size and crystallographic orientation. Our findings indicate that increasing the temperature of the selenium source leads to the formation of larger grains and the presence of rod-shaped grains of Sb_2Se_3 aligned parallel to the substrate. These observations are consistent with the collected data, which also revealed an increase in the peak texture coefficients ($hk0$) at the temperature of 430°C .

Upon analyzing the sample obtained at 370°C , grains larger than $2 \mu\text{m}$ in size were observed. These grains exhibited a uniform distribution across the substrate surface, indicating a uniform growth process. However, when the temperature of the selenium source was raised to 430°C , considerably larger grains measuring approximately $4 \mu\text{m}$ were detected on the film surface substrate. The increase in temperature led to the formation of larger grains, which can be attributed to enhanced diffusion and coalescence processes during film growth.

Furthermore, rod-shaped grains of Sb_2Se_3 were observed in the sample obtained at 430°C . These grains aligned themselves parallel to the substrate, as depicted in Figure 2. The formation of Sb_2Se_3 grains can be attributed to the reaction between antimony (Sb) impurities present in the selenium source and the substrate material. The alignment of these rod-shaped grains suggests an epitaxial growth mechanism on the substrate surface.

The XRD analysis revealed that the peak texture coefficients ($hk0$) began to exhibit an increase at the temperature of 430°C . This finding indicates a preferential crystallographic orientation in the film, which can be attributed to the growth conditions and the interaction between the deposited selenium and the substrate material. The increased peak texture coefficients further support the observed larger grain size and the presence of Sb_2Se_3 rod-shaped grains.

These observations are consistent with our data, as the presence of larger grains can positively impact the performance of solar cells by reducing recombination losses. Larger grains tend to have fewer defects along their boundaries, which can lead to improved efficiency in converting solar energy. In conclusion, our results demonstrate that temperature influences grain size and texture in the selenium film. The larger grain size observed at higher temperatures suggests the potential for enhanced solar cell performance.

Table 1 presents the chemical composition of the elements in the deposited Sb_2Se_3 films. The analysis using an energy dispersive elemental analyzer revealed that the Sb/Se atomic concentration ratio decreased as the selenium

temperature increased from 350°C to 430°C, approaching the stoichiometric composition of Sb/Se≈0.66. This indicates that the selenium content in the Sb₂Se₃ thin films increased with higher selenium flow. At a selenium source temperature of 350°C, the Sb₂Se₃ film was selenium-poor. However, at higher temperatures, the compound films approached a stoichiometric composition with an Sb/Se ratio of 0.68, which was achieved at a selenium source temperature of 430°C. It is evident that the temperature of the selenium source plays an important role in obtaining high-quality Sb₂Se₃ films.

Stoichiometric, vertically oriented Sb₂Se₃ grains larger than 4 μm were successfully obtained at a selenium temperature of 430°C, which are considered beneficial for charge carrier transport.

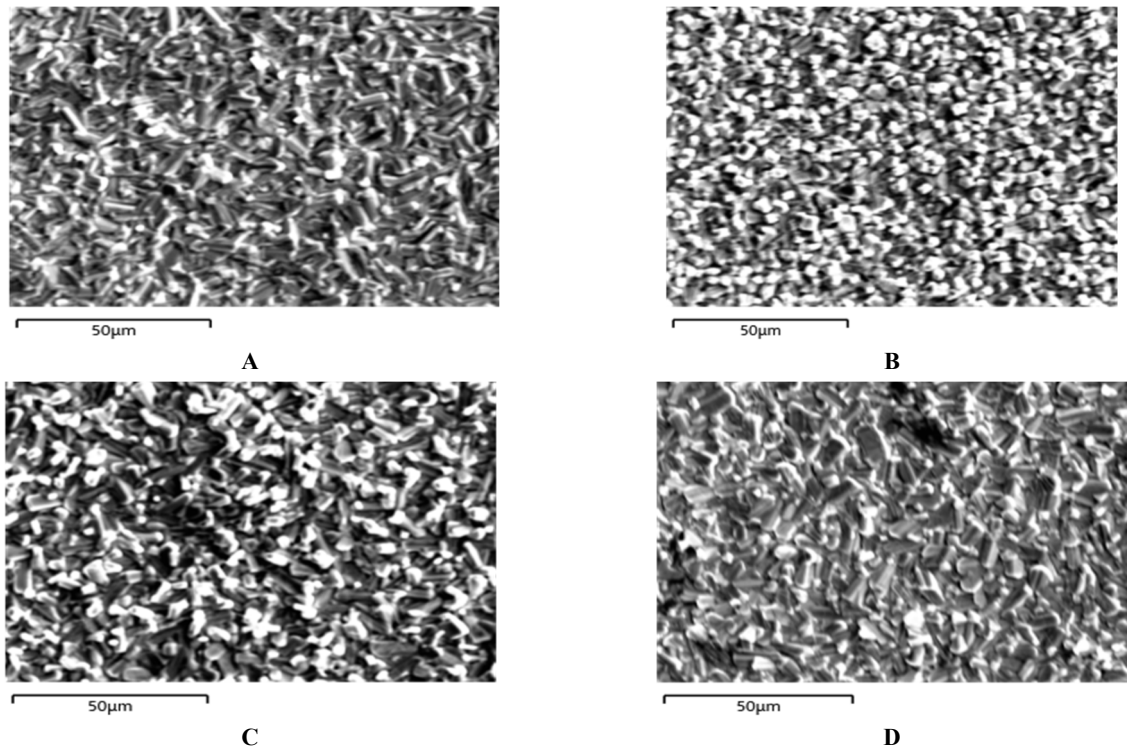


Figure 2. SEM images of Sb₂Se₃ films at different selenium temperatures: a) 350°C; b) 370°C; c) 400 °C; d) 430°C

It is worth noting that Sb₂Se₃ films exhibit p-type conductivity. However, some samples of Sb₂Se₃ may exhibit n-type conductivity due to the presence of Sb impurities. Additionally, the presence of (V_{Se}) defects can also contribute to n-type conductivity or act as donors [12].

Table 1. Chemical compound Sb₂Se₃ films at various temperatures selenium source

T _{Se} , (Temperatures of Selenium source °C)	T _{substrate} , °C	weight percentage, %		Atomic percentage, %		Sb/Se
		Sb	Se	Sb	Se	
350	500	53.3	46.7	0.43	0.59	0.74
370	500	52.6	47.4	0.43	0.60	0.72
400	500	51.8	48.2	0.42	0.61	0.70
430	500	51.2	48.8	0.42	0.618	0.68

The implications of the Sb/Se atomic concentration ratio approaching the stoichiometric composition in Sb₂Se₃ films are significant. The stoichiometric composition represents the ideal ratio of antimony (Sb) to selenium (Se) atoms in Sb₂Se₃. When the Sb/Se ratio approaches this stoichiometric composition, the film exhibits optimal electrical properties. This means that the film is more likely to have the desired characteristics for its intended applications, such as solar cells. Achieving the stoichiometric composition helps in attaining the desired electronic band structure and charge transport properties. Reduced Defects: Deviations from the stoichiometric composition can introduce defects in the crystal structure of the material. By approaching the stoichiometric composition, the number of defects, such as vacancies or impurities, can be minimized. Fewer defects lead to improved electrical and optical properties, as defects act as recombination centers for charge carriers, reducing their lifetime and overall device performance.

Structural properties of Sb₂Se₃ films. Figure 3 present the outcomes of the X-ray diffraction analysis, providing insights into the crystalline phases and crystal structure of the Sb₂Se₃ films synthesized under different temperatures of the selenium source. The X-ray patterns exhibit distinct features, with notable observations regarding the intensity variations of specific peaks in response to increasing temperature of the selenium source. The X-ray diffraction patterns display prominent peaks corresponding to the crystallographic planes (221) and (211), indicating the presence of strong crystalline

phases. Additionally, peaks such as (020), (120), and (310), are also obviously in the X-ray patterns. Notably, these peak intensities demonstrate a dependence on the temperature of the selenium source, with alterations observed as the temperature increases. The selenium source temperature of $T_{Se} = 370^\circ\text{C}$, the XRD analysis reveals the disappearance of weak peaks, including (020), (120), (310), (230), (240), (002), and (320), while the strong peaks (221) and (211) remain raised. This suggests a distinct influence of the temperature on the crystal structure, leading to the elimination of certain crystallographic planes at temperatures up to $T_{Se} = 370^\circ\text{C}$. Furthermore, a subsequent increase in temperature to $T_{Se} = 430^\circ\text{C}$ induces a decrease in the intensities of the (221) and (211) peaks, while the weak peaks (020), (120), (230), and (240) become significantly more pronounced. This temperature-dependent variation highlights the dynamic nature of the crystal structure and phase composition of the Sb₂Se₃ films. Moreover, an additional observation is made at $2\theta = 29.66^\circ$, where a low-intensity reflex is detected in correspondence to the (101) peak. This reflex indicates the formation of the Se phase, providing evidence of a distinct phase transition or phase presence within the Sb₂Se₃ films under the given experimental conditions. In summary, the XRD analysis of the Sb₂Se₃ films elucidated valuable information regarding their crystal structure and phase composition. The obtained results demonstrate the influence of the selenium source temperature on the intensities of specific peaks, emphasizing the temperature-dependent alterations in the crystal structure. Additionally, the identification of the Se phase further contributes to the understanding of the film's structural properties.

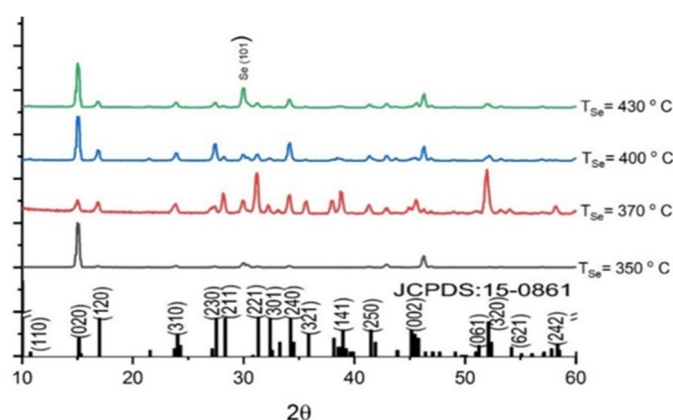


Figure 3. X-ray diffraction pattern of Sb₂Se₃ films at different temperatures of the selenium source

To quantitate the orientation of Sb₂Se₃ films, the texture coefficients (T_c) of diffraction peaks were calculated based on the following equation [13]:

$$T_c = \frac{I_{(hkl)}}{I_{0(hkl)}} \left/ \left(\frac{1}{N} \sum_{i=1}^N \frac{I_{(h_i k_i l_i)}}{I_{0(h_i k_i l_i)}} \right) \right. \quad (1)$$

The intensities of the diffraction peaks, denoted as $I_{(hkl)}$ and $I_{0(hkl)}$, respectively, correspond to the measured and standard X-ray diffraction patterns of Sb₂Se₃ (JCPDS 15-0861) for the crystallographic planes (hkl). The determination of the peak intensity is crucial for analyzing the crystal orientation and structural properties of the material under investigation. Notably, the texture coefficient, TK, associated with the diffraction peaks signifies the level of orientation prevalence along a specific direction. In the case of the examined samples, the high TK values observed for the diffraction peaks indicate a pronounced orientation in the corresponding direction. Interestingly, at a selenium source temperature of 370°C , the TC values for crystallographic planes (hk0) in our samples tend to decrease. This initial decrease suggests a deviation from the dominant orientation, possibly due to the effect of elevated temperature on the crystal lattice arrangement. However, as the temperature of the selenium source continues to rise 370°C , a subsequent increase in the TK values for the (hk0) planes is observed. The temperature of the selenium source plays a significant role in influencing the crystal orientation and can result in distinct variations in the diffraction patterns of Sb₂Se₃. Further investigation is necessary to comprehensively understand the underlying mechanisms behind these observed temperature-dependent changes in crystal orientation and their implications for the materials properties.

4. CONCLUSIONS

In this study, we investigated the effect of temperature on grain size and crystallographic orientation in selenium films. The results indicate that increasing the temperature of the selenium source leads to the formation of larger grains and the presence of rod-shaped grains of Sb₂Se₃ aligned parallel to the substrate. The observed grain sizes and crystallographic orientations are in line with the collected data, as evidenced by the increased peak texture coefficients at the temperature of 430°C . These findings contribute to a better understanding of the growth mechanisms and properties of selenium films, which can aid in the development of tailored thin film technologies for various applications. Further studies exploring the influence of other parameters on grain formation and crystallographic orientation are warranted to expand our knowledge in this field. At a selenium source temperature of 430°C , large rod-like grains can be observed on

the surface of the Sb_2Se_3 film. Sb_2Se_3 films Se -deficient at a selenium source temperature of 350°C . As the temperature of the selenium source increases, the composition of the Sb_2Se_3 film approaches stoichiometric.

Acknowledgment

The authors express their gratitude to Doctor of Physical and Mathematical Sciences, Professor T.M. Razikov for his assistance in conducting the experiments and discussing the results.

ORCID

- ✉ Takhirdjon M. Razikov, <https://orcid.org/0000-0001-9738-3308>;
- ✉ Zafarjon M. Khusanov, <https://orcid.org/0009-0005-9420-8033>
- ✉ Sultanpasha A. Muzafarova, <https://orcid.org/0000-0001-5491-7699>
- ✉ Ruhiddin T. Yuldoshov, <https://orcid.org/0000-0002-7886-1607>

REFERENCES

- [1] A. Mavlonov, T.M. Razykov, F. Raziq, J. Gan, J. Cantina, Yu. Kawano, T. Nishimura, et al., "A Review of Sb_2Se_3 Photovoltaic Absorber Materials and Thin-Film Solar Cells," *Solar Energy*, **201**, 227 (2020). <https://doi.org/10.1016/j.solener.2020.03.009>
- [2] Y. Zhao, S. Wang, and C. Li, "Regulating deposition kinetics via a novel additive-assisted chemical bath deposition technology enables fabrication of 10.57%-efficiency Sb_2Se_3 solar cells," *Energy Environ. Sci.* **15**, 5118-5128 (2022). <https://doi.org/10.1039/D2EE02261C>
- [3] C. Wang, S. Lu, S. Li, S. Wang, X. Lin, J. Zhang, R. Kondrotas, et al., "Efficiency improvement of flexible Sb_2Se_3 solar cells with non-toxic buffer layer via interface engineering," *Nano Energy*, **71**, 104577 (2020). <https://doi.org/10.1016/j.nanoen.2020.104577>
- [4] Y. Zhou, L. Wang, S. Chen, S. Qin, X. Liu, J. Chen, D.-J. Xue, et al., *Nature Photonics*, **9**(6), 409-415 (2018). <https://doi.org/10.1038/nphoton.2015.78>
- [5] A. Shongalova, M.R. Correia, J.P. Teixeira, J.P. Leitão, J.C. González, S. Ranjbar, S. Garud, et al., "Growth of Sb_2Se_3 thin films by selenization of RF sputtered binary precursors," *Sol. Energy Mater. Sol. Cells*, **187**, 219-226 (2018). <https://doi.org/10.1016/j.solmat.2018.08.003>
- [6] E.A. El-Sayad, "Compositional dependence of the optical properties of amorphous $\text{Sb}_2\text{Se}_3-x\text{S}_x$ thin films," *Journal of Non-Crystalline Solids*, **354**(32), 3806-3811 (2008). <https://doi.org/10.1016/j.jnoncrysol.2008.05.004>
- [7] R. Kondrotas, J. Zhang, C. Wang, and J. Tang, "Growth mechanism of Sb_2Se_3 thin films for photovoltaic application by vapor transport deposition," *Solar Energy Materials and Solar Cells*, **161**, 190-196 (2017). <https://doi.org/10.1016/j.solmat.2019.04.024>
- [8] X.X. Wen, C. Chen, S.C. Lu, K.H. Li, R. Kondrotas, Y. Zhao, W.H. Chen, et al., "Vapor transport deposition of antimony selenide thin film solar cells with 7.6% efficiency," *Nat. Commun.* **9**, 2179 (2018). <https://doi.org/10.1038/s41467-018-04634-6>
- [9] X.B. Hu, J.H. Tao, S.M. Chen, J.J. Xue, G.E. Weng, K. Jiang, Z.G. Hu, et al., "Improving the efficiency of Sb_2Se_3 thin-film solar cells by post annealing treatment in vacuum condition," *Sol. Energy Mater. Sol. Cells*, **187**, 170-175 (2018). <https://doi.org/10.1016/j.solmat.2018.08.006>
- [10] D.B. Li, X.X. Yin, C.R. Grice, L. Guan, Z.N. Song, C.L. Wang, C. Chen, et al., "Stable and efficient $\text{CdS}/\text{Sb}_2\text{Se}_3$ solar cells prepared by scalable close space sublimation," *Nano Energy*, **49**, 346-353 (2018). <https://doi.org/10.1016/j.nanoen.2018.04.044>
- [11] C.C. Yuan, X. Jin, G.S. Jiang, W.F. Liu, C.F. Zhu. " Sb_2Se_3 solar cells prepared with selenized dc-sputtered metallic precursors," *J. Mater. Sci: Mater. Electron.* **27**, 8906-8910 (2016). <https://doi.org/10.1007/s10854-016-4917-3>
- [12] S. Dias, B. Murali, and S.B. Krupanidhi, "Transport properties of solution processed $\text{Cu}_2\text{SnS}_3/\text{AlZnO}$ heterostructure for low-cost photovoltaics," *Sol. Energy Mater. Sol. Cells*, **143**, 152-158 (2015). <https://doi.org/10.1016/j.solmat.2015.06.046>
- [13] F.I. Mustafa, S. Gupta, N. Goyal, and S. Tripathi, "Thin Films. In: Non-Ideal p-n junction Diode of $\text{Sb}_{(x)}\text{Se}_{(1-x)}$ ($x=0.4, 0.5, 0.6, 0.7$) Thin Films," *AIP Conference Proceedings*, **1393**, 75-76 (2011). <https://doi.org/10.1063/1.3653616>

ВИРОЩУВАННЯ ПЛІВОК Sb_2Se_3 , ЗБАГАЧЕНИХ СЕЛЕНОМ, ЗА ДОПОМОГОЮ ХІМІЧНОГО МОЛЕКУЛЯРНОГО ОСАДЖЕННЯ

Тахирджон М. Разіков, Султанпаша А. Музафарова, Рухіддін Т. Юлдошов, Зафарджон М. Хусанов, Маргуба К. Хусанова, З.С. Кенжаєва, Б.В. Ібрагімова

Інститут фізики напівпровідників і мікроелектроніки Національного університету Узбекистану, 100057, Ташкент, Узбекистан, вул. Янги Алмазар, 20

У цьому дослідженні вивчено ріст плівок Sb_2Se_3 на поверхнях вапняно-натрієвого скла (SLG) за допомогою методу хімічного молекулярно-променевого осадження (СМРД) при температурі підкладки 500°C . Вихідними матеріалами для осадження плівок були використані високочисті бінарні сполуки Sb_2Se_3 та Se. Для дослідження морфологічних характеристик плівок Sb_2Se_3 використовували скануючу електронну мікроскопію (SEM). Крім того, було досліджено вплив температури на розмір зерен і кристалографічну орієнтацію в плівках селену. Зразки отримували з джерела селену при температурах 370°C і 430°C . Результати показують, що підвищення температури джерела селену призводить до утворення більших зерен і наявності стрижнеподібних зерен Sb_2Se_3 , розташованих паралельно підкладці. Зразок, отриманий при 370°C , показав зерна розміром понад 2 мкм, рівномірно розподілені по поверхні підкладки, що свідчить про рівномірний процес росту. Навпаки, коли температуру джерела селену підняли до 430°C , на поверхні плівки підкладки були виявлені значно більші зерна розміром приблизно 4 мкм. Рентгеноструктурний аналіз був проведений, щоб отримати уявлення про кристалічні фази та кристалічну структуру плівок Sb_2Se_3 , синтезованих за різних температур джерела селену. На рентгенівських дифракційних картинах відображені помітні піки, що відповідають кристалографічним площинам (221) і (211), що вказує на наявність сильних кристалічних фаз. Крім того, такі піки, як (020), (120) і (310), спостерігалися на рентгенівських картинах, що додатково підтверджує кристалічність плівок.

Ключові слова: рентгенівська дифракція; хімічне молекулярно-променево осадження; Sb_2Se_3 ; температура селену

STRUCTURAL PROPERTIES OF SILICON DOPED RARE EARTH ELEMENTS YTTERBIUM

 **Khodjakbar S. Daliev**^a,  **Sharifa B. Utamuradova**^b,  **Jonibek J. Khamdamov**^b,
 **Mansur B. Bekmuratov**^{c*}

^aBranch of the Federal State Budgetary Educational Institution of Higher Education “National Research University MPEI”,
1 Yogdu st., Tashkent, Uzbekistan

^bInstitute of Semiconductor Physics and Microelectronics at the National University of Uzbekistan,
20 Yangi Almazar st., Tashkent, 100057, Uzbekistan

^cNukus State Pedagogical Institute named after Ajiniyaz, Nukus, Uzbekistan

*Corresponding Author e-mail: mans-bek@mail.ru

Received January 1, 2024; revised January 27, 2024; accepted February 12

This paper presents the results of a study of the state of ytterbium atoms in silicon, carried out using the methods of Fourier transform infrared spectroscopy (IR) and Raman spectroscopy (RS). Silicon samples doped with ytterbium impurities were analyzed using FSM-2201 and SENTERRA II Bruker spectrometers. Registration and identification of both crystalline and amorphous phase components in the samples was carried out. The results of the study confirm that doping silicon with ytterbium impurities leads to a decrease in the concentration of optically active oxygen N_o^{opt} by 30-40%, depending on the concentration of the introduced impurities. It was also found that an increase in the number of defects leads to a broadening of the amorphous zone. It is assumed that similar dependencies exist for the Si-Yb system; however, to the best of our knowledge, similar results have not been reported previously. It is noted that the relative intensity of the three Raman bands in Si-Yb systems in the LTIOS (*The light and temperature induced ordered state*) state changes, and the relative intensity of Si-Si decreases. This indicates that pendant bonds are mainly formed by the breaking of Si-Si bonds. It was also observed that the light intensity causing this condition is far from that required for laser or solid phase crystallization. Using the Raman spectroscopy method, a structural transformation was discovered, expressed in a densely packed array of nanocrystals with a size of less than 11 lattice parameters. Small clusters were under strong internal stress (up to 3 GPa), which probably prevents the cluster size from increasing beyond the critical value for irreversible crystallization.

Key words: Silicon; Ytterbium; Rare Earth Elements; Raman; Diffusion; Thermal Coolant; Temperature

PACS: 33.20.Ea, 33.20.Fb

INTRODUCTION

In recent years, many scientists have shown significant interest in the interaction of rare earth metals (REMs) with a semiconductor surface, in particular, the Si surface [1–3]. This interest is caused by the following factors: 1) as a result of the high chemical activity of rare-earth metals, ordered films can be formed at the rare-earth metal–Si interface with specific physicochemical properties, such as high thermal stability, thermal conductivity and electrical conductivity. These films may be promising in terms of their applications in micro and nanoelectronics; 2) in some cases, a barrier (0.18 eV) is formed at the REM–Si interface [11], which in turn allows the use of such systems to create optoelectronic devices operating in the infrared region. Also interesting is the influence of the degree of filling of the 4f shell during the interaction of rare earth metals and silicon. Many studies have studied the processes of formation of REM–Si interference, including interfaces in Si-Yb structures [4,5]. However, in these works the stages of formation of silicides are not given. In this regard, divalent ytterbium, which is one of the components of these structures, is less chemically active than other rare-earth metals. Thus, we can assume that studying the structures will reveal some new fundamental features of the formation of Si-Yb interfaces. In addition, the Si-Yb system is interesting from a practical point of view, since silicide films are formed under certain conditions, and are promising for use in transistors based on the metal–oxide–semiconductor structure [6].

Amorphous semiconductors exhibit various metastable states under illumination [7-10], which results in a significant change in some properties of the films, which can negatively affect the performance and service life of the device. Therefore, the study of structural changes caused by illumination is of great interest for various technologies based on these silicide films. On the other hand, this should contribute to a better knowledge of the physics of amorphous semiconductors and the kinetics of their crystallization, which are fundamental to the above-mentioned technologies, which have not yet been fully studied. The most studied system is a-Si:H, for which two main metastable effects have been identified upon exposure to illumination. The first of these is the Wronski effect [7,8,10], in which light soaking of a-Si:H leads at relatively low concentrations (10^{16} – 10^{17} cm⁻³) to a medium gap state, associated with the formation of defects and breaking of bonds. Another registered metastable effect is structural transformation [9], and it has been proven that the optical and electrical properties of a-Si have undergone significant changes. These transformations disappear upon thermal annealing below 200°C.

The purpose of this work is to study Si<Yb> and nanofilms of Si-Yb structures. Structural changes were studied using Romanov and infrared spectroscopy.

Cite as: Kh.S. Daliev, Sh.B. Utamuradova, J.J. Khamdamov, M.B. Bekmuratov, East Eur. J. Phys. 1, 375 (2024), <https://doi.org/10.26565/2312-4334-2024-1-37>

© Kh.S. Daliev, Sh.B. Utamuradova, J.J. Khamdamov, M.B. Bekmuratov, 2024; CC BY 4.0 license

MATERIALS AND METHODS

Raman spectra were obtained using a SENTERRA II Bruker Raman spectrometer. This fully automated instrument combines excellent sensitivity and high resolution of 4.0 cm^{-1} . Senterra calibration was automatic and referenced to NIST acetaminophen and silica standards, resulting in wavelength accuracy of 0.2 cm^{-1} . The experiments were carried out with a laser with a wavelength $\lambda_0=532 \text{ nm}$, a maximum power $P_{\text{max}}=25 \text{ mW}$, an acquisition time of 100 s, and the addition of two spectra. This device allows you to obtain spectra in the range from 50 to 4265 cm^{-1} . The Raman spectra were specially processed to be able to compare intensity ratios between samples. Before normalizing the spectra to the peak at 522 cm^{-1} , which corresponded to the most intense peak in the spectral region $4265\text{-}50 \text{ cm}^{-1}$, we subtracted the baseline for each spectrum.

Raman spectra of samples (4 in total) were obtained at room temperature. The sample temperature was recorded with an accuracy of -60°C . The acquisition time for the Raman spectrum was about 120 s. The same laser beam that was used to measure Raman scattering was used to study structural changes. Measurements with increasing laser power density were carried out in order to determine the threshold above which irreversible changes occur. The sample temperature was increased by 20°C under the influence of a laser beam. This temperature increase was estimated using the Stokes/anti-Stokes intensity coefficient formula.

Fourier transform infrared (FTIR) spectroscopy is a powerful technique used to analyze the infrared spectrum of a sample. It provides information about the molecular vibrations of a substance, which allows the identification of functional groups and composition of the material.

n-Si samples with an initial resistivity from 0.3 to $100 \Omega \times \text{cm}$ were selected for the study. Before alloying, the samples were subjected to thorough acid-peroxide washing, and the oxide layers were removed from the surface of the samples using a HF solution. After thoroughly cleaning the surface of the samples, films of high-purity ytterbium impurities (99.999%) were deposited onto the clean Si surfaces using vacuum deposition. Vacuum conditions in the volume of the working chamber of the order of $10^{-7}\text{-}10^{-8}$ torr were provided by an oil-free vacuum pumping system.

Before diffusion annealing, the samples were placed in evacuated quartz ampoules. Doping of samples with Yb impurities was carried out by the diffusion method at a temperature of 1200°C for 40 hours, followed by rapid cooling. To study the interaction of impurity atoms in silicon, not only uniform doping of the material is necessary, but also a maximum concentration. In this regard, we took into account the optimal conditions for doping silicon with these impurity atoms.

RESULTS AND DISCUSSION

Infrared light passes through or reflects off the sample. Molecules in the sample absorb infrared photons, causing the bonds between atoms to vibrate. The transmitted light hits a detector, which records the light intensity depending on the wave number [20-23].

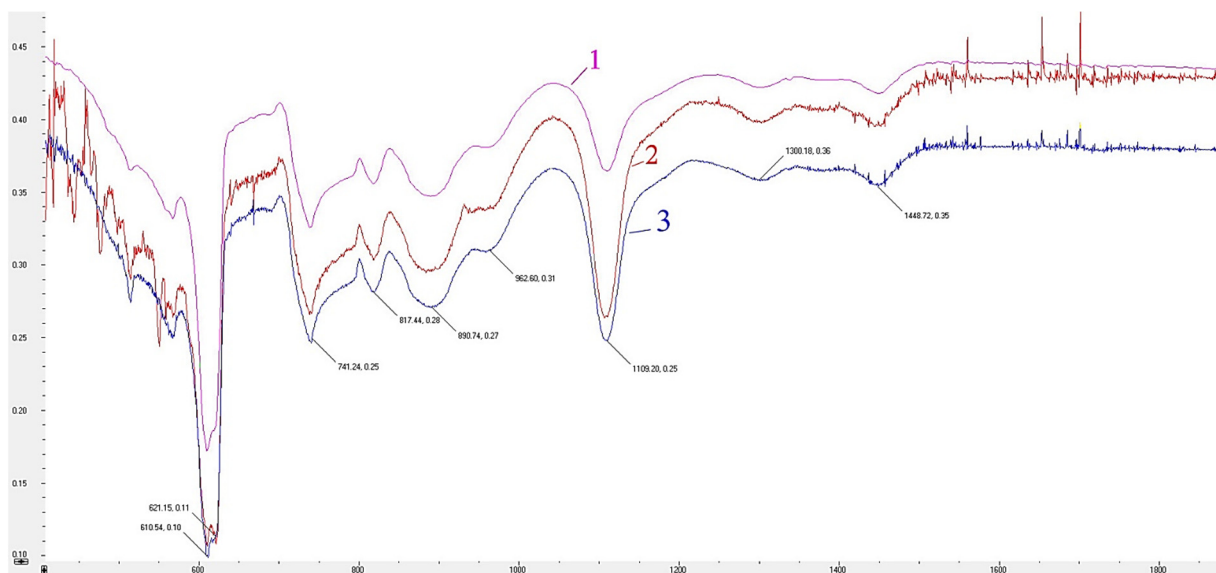


Figure 1. IR spectrum of n-type silicon doped with Yb impurities: 1 - IR spectrum of n-Si<Yb> samples, 2 - IR spectrum of Si original samples, 3 - IR spectrum of Si control samples

Comparing the results obtained, they show that the concentration of optically active oxygen N_0^{opt} decreases significantly after the diffusion of Yb impurities (Fig. 1).

The results show that doping silicon with ytterbium impurities reduces the concentration of optically active oxygen N_0^{opt} by 30-40%, depending on the concentration of the introduced impurities.

To determine the crystallite size using Raman scattering, the bands were selected in accordance with the modified length correlation [18,19]. The Raman intensity can be expressed as

$$I(\omega, L) \propto \int \exp\left(-\frac{q^2 L^2}{8}\right) \frac{d^3 q}{[\omega(q) - \omega]^2 + \left(\frac{\Gamma_0}{2}\right)^2} \quad (1)$$

where Γ_0 is the linewidth of the phonon peak of crystalline Si, $\omega(q)$ is the phonon dispersion law, the phonon wave vector q is expressed in units of $2\pi/a$, where a is the lattice parameter of crystalline Si, L is the diameter of the crystallites, expressed in units of the lattice parameter. For pure Si, the phonon dispersion equation can be approximated by the equation of the following expression:

$$\omega^2(q, T) = A(T) + [A^2(T) - B(T) \times (1 - \cos \pi q)]^{\frac{1}{2}} \quad (2)$$

A and B are determined from the phonon dispersion curve

$$A = \frac{(\omega_0(T) + \Delta\omega)^2}{2},$$

$$B = \frac{\frac{(\omega_0(T) + \Delta\omega)^4}{4} - \left(\frac{(\omega_1(T) + \Delta\omega)^2 - (\omega_0(T) + \Delta\omega)^2}{2}\right)^2}{2}, \quad (3)$$

where ω_0 and ω_1 are the phonon frequencies of the central ($q=0$) and outer zone ($q=1$), respectively, and $\Delta\omega$ is an additional parameter that we introduce to take into account the magnitude of the internal voltage. Initially, experimental LTIOS spectra in Si were fitted using equation (1) and assuming $\Delta\omega=0$ in equations (3). The change in ω_0 and Γ_0 with temperature changes were previously determined on a crystalline Si sample. The dependence of ω_1 on T was taken to be the same as ω_0 . We assume that the shift will occur due to the presence of internal tension and stress, which is not taken into account if $\Delta\omega=0$. The internal stress can be determined by the usual relationship given for crystalline Si [14]:

$$\Delta\omega(\text{cm}^{-1}) = 2.3\sigma \text{ (GPa)}, \quad (4)$$

It has previously been argued that the difference in Raman phonon bands between crystallites and nanocrystallites mainly concerns their passband, while the Raman frequencies are very similar, a statement supported by attributing the calculated transition to internal voltage [13]. IR (Fig. 1.) and Raman (Fig. 2.) spectra of Si and Si-Yb were obtained for use in the study. The Raman spectrum of amorphous layers consists of several broad bands reflecting a single phonon density of states. When the material is crystalline, the bands become narrower and distinct peaks appear. In the case of Si-Yb, three first-order Raman bands associated with Si-Si appear, and vibrations of the Si-Yb and Yb-Yb bonds also appear. The peak position and intensity of these bands depend on the composition, as well as on other factors, such as heating, etc., which in turn can contribute to a shift in the frequency of the peaks (Fig. 2.).

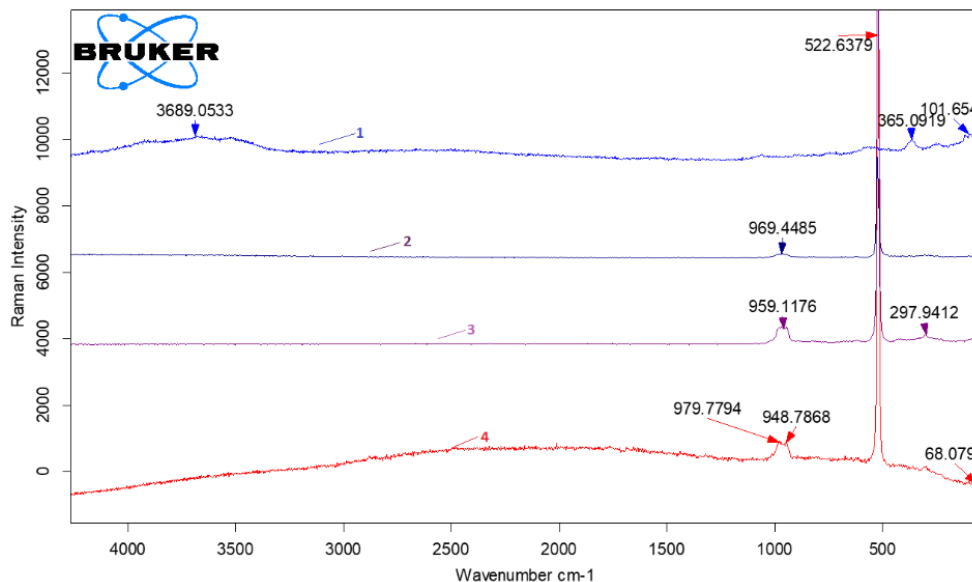


Figure 2. Raman spectrum. (1)-ytterbium (Yb); (2)-KEF-40 (initial); (3)-KEF-40-Si<Yb>; (4)-KEF-100-Si<Yb>

The laser beam and temperature induce an ordered state (hereafter referred to as LTIOS), which is monitored by the Raman spectrum. Further increase in temperature under the influence of light preserves the Raman signature of the nanocrystalline material.

As we already mentioned, LTIOS appears under the light exposure within a certain temperature range for various compositions of a-Si-Yb alloys. LTIOS is observed at significantly lower laser power densities than those required for laser crystallization.

The size of nanocrystals remains around 8 lattice parameters, reaching a maximum value of 11 lattice parameters. The amount of internal stress varies greatly. When $\Delta\omega$ is plotted as a function of T, it can be seen that the internal stress increases in the mid-temperature range and partially relaxes in the temperature range where the amorphous state is visible in the Raman spectra. The presence of large stresses should deform the crystallites, similar to the so-called paracrystallites, the existence of which has been reported by other authors in very thin a-Si layers [15,16]. On the other hand, the Raman spectrum of partially crystallized silicon is usually represented by two bands, one of which corresponds to the TO phonon of nanocrystals, which appears at a lower frequency than one of the large crystals (522 cm^{-1}) and the second, much wider, appearing at lower frequency (969 cm^{-1}) associated with the surrounding amorphous matrix. The volume fraction occupied by nanocrystalline nuclei (V_{nc}) is proportional to the Raman scattering intensity of the first order TO phonon band.

This can be estimated by the intensity of the TO phonon in the nanocrystalline state, normalized to the sum of the intensities of the TO phonon in the amorphous (969 cm^{-1}) and nanocrystalline state (522 cm^{-1}) where the coefficient of 0.88 is a correction due to the difference in the Raman cross sections of crystalline and amorphous Si [17].

$$V_{nc} = \frac{I_{nc}}{I_{nc} + 0.88I_a} \quad (5)$$

This means that the increase in the volume occupied by ordered Si does not arise due to the formation of large crystalline grains, but is a consequence of an increase in the number of crystallites of reduced size. This structure is characterized by tensile stress in grain boundaries, at which expansion of the bond length is energetically more favorable [18]. The activation energy for the transition from amorphous to nanocrystalline can be estimated at 0.15 eV. The size of the nuclei lies in the range of 8–11 lattice parameters, larger than the size of the threshold for the existence of a stable crystalline diamond-like lattice, which was estimated to be about 6 lattice parameters [18]. When the state of the highest order is reached, it is almost completely filled with crystalline grains. Since the grain size was about 8–11 lattice parameters, it is necessary to take into account a large number of nucleation centers. This large accumulation of nucleation may be due to defects in the amorphous material. This suggests that the existence of LTIOS is closely related to the structure of the amorphous layers and, therefore, defects in the amorphous layers may play an important role in this effect. It is also known that the kinetics of crystallization of amorphous Si strongly depends on its structural relaxation state [19]. The Raman spectrum of an amorphous semiconductor provides information about the state of structural relaxation. In particular, for amorphous Si, the TO-Raman bandwidth (969 cm^{-1}) is related to the distortion of the dihedral bond angle Dq which can be approximated by the following equation:

$$(\Gamma_{TO})^2 = 32^2 + (6.75Dq)^2 \quad (6)$$

It was found that an increase in the number of defects causes a broadening of the amorphous zone. Similar relationships should exist for Si-Yb, but to our knowledge they have not been previously reported. We noticed that the relative intensity of the three Raman bands in Si-Yb systems in the LTIOS state changes, the relative intensity of Si-Si decreases, which in turn indicates that pendant bonds are mainly formed as a result of the cleavage of the Si-Si bond.

CONCLUSION

The results of the study indicate that doping silicon with ytterbium impurities leads to a decrease in the concentration of optically active oxygen N_0^{opt} by 30-40%, depending on the concentration of the introduced impurities. A reversible ordered state was discovered in n-Si_{1-x}Y_{bx} ($0 < x < 0.38$) layers under the influence of a laser beam. The light intensity causing this condition was found to be far from that required for laser or solid-state crystallization. Using the Raman spectroscopy method, a structural transformation was revealed that manifests itself in a close-packed array of nanocrystals with a size of less than 11 lattice parameters. Small clusters were under strong internal stress (up to 3 GPa), which probably prevents the cluster size from increasing beyond the critical value for irreversible crystallization.

ORCID

© Khodjakbar S. Daliev, <https://orcid.org/0000-0002-2164-6797>; Sharifa B. Utamuradova, <https://orcid.org/0000-0002-1718-1122>
© Jonibek J. Khamdamov, <https://orcid.org/0000-0003-2728-3832>; © Mansur B. Bekmuratov, <https://orcid.org/0009-0006-3061-1568>

REFERENCES

- [1] S.B. Utamuradova, Kh.J. Matchonov, J.J. Khamdamov, and Kh.J. Utemuratova, "X-ray diffraction study of the phase state of silicon single crystals doped with manganese," *New Materials, Compounds and Applications*, 7(2), 93–99 (2023). http://jomardpublishing.com/UploadFiles/Files/journals/NMCA/v7n2/Utamuradova_et_al.pdf
- [2] N.V. Latukhina, and V.M. Lebedev, "Diffusion doping of silicon with rare earth elements," *Materials of electronic technology*, No.1, (2011). <https://www.rudmet.ru/journal/527/article/5458/>
- [3] Kh.S. Daliev, Sh.B. Utamuradova, Z.E. Bahronkulov, A.Kh. Khaitbaev, and J.J. Hamdamov, "Structure Determination and Defect Analysis n-Si<Lu>, p-Si<Lu> Raman Spectrometer Methods," *East Eur. J. Phys.* 4, 193 (2023). <https://doi.org/10.26565/2312-4334-2023-4-23>
- [4] Kh.S. Daliev, Z.E. Bahronkulov, and J.J. Hamdamov, "Investigation of the Magnetic Properties of Silicon Doped with Rare-Earth Elements," *East Eur. J. Phys.* 4, 167 (2023), <https://doi.org/10.26565/2312-4334-2023-4-18>

- [5] M.B. Gongalsky, N.V. Pervushin, D.E. Maksutova, U.A. Tsurikova, P.P. Putintsev, O.D. Gyuppenen, Y.V. Evstratova, et al., "Optical Monitoring of the Biodegradation of Porous and Solid Silicon Nanoparticles," *Nanomaterials*, **11**, 2167 (2021). <https://doi.org/10.3390/nano11092167>
- [6] C.-H. Shih, and S.-P. Yeh, "Device considerations and design optimizations for dopant segregated Schottky barrier MOSFETs," *Semicond. Sci. Technol.* **23**, 125033 (2008). <https://doi.org/10.1088/0268-1242/23/12/125033>
- [7] D.L. Staebler, and C.R. Wronski, "Reversible conductivity changes in discharge-produced amorphous Si," *Appl. Phys. Lett.* **31**, 292–294 (1977). <https://doi.org/10.1063/1.89674>
- [8] M.V. Kuz'min, M.A. Mittsev, and A.M. Mukhuchev, *Fizika Tverdogo Tela*, **57**(10), 2056–2060 (2015).
- [9] I. Abdulhalim, R. Beserman, and R. Weil, "Structural changes and crystallization of amorphous hydrogenated silicon generated by laser irradiation," *Phys. Rev. B*, **39**, 1081 (1989). <https://doi.org/10.1103/PhysRevB.39.1081>
- [10] M. Stutzmann, W.B. Jackson, and C.C. Tsai, "Light-induced metastable defects in hydrogenated amorphous silicon: A systematic study," *Phys. Rev. B*, **32**, 23 (1985). <https://doi.org/10.1103/PhysRevB.32.23>
- [11] H. Richter, Z. Wang, and L. Ley, "The one phonon Raman spectrum in microcrystalline silicon," *Solid State Commun.* **39**, 625–629 (1981). [https://doi.org/10.1016/0038-1098\(81\)90337-9](https://doi.org/10.1016/0038-1098(81)90337-9)
- [12] I.H. Campbell, and P.M. Fauchet, "The effects of microcrystal size and shape on the one phonon Raman spectra of crystalline semiconductors," *Solid State Commun.* **58**, 739–741 (1986). [https://doi.org/10.1016/0038-1098\(86\)90513-2](https://doi.org/10.1016/0038-1098(86)90513-2)
- [13] J. Jimenez, I. De Wolf, and J. P. Landesman, *Microprobe Characterization of Semiconductors*, Ch. 2. edited by J. Jimenez (Taylor, and Francis, New York, 2002).
- [14] J.E. Griffiths, G.P. Espinosa, J.P. Remeika, and J.C. Phillips, "Reversible quasicrystallization in GeSe₂ glass," *Phys. Rev. B*, **25**, 1272 (1982). <https://doi.org/10.1103/PhysRevB.25.1272>
- [15] P. Klebanski, S.R. Pillpot, D. Wolf, and H. Gleiter, "Thermodynamic Criterion for the Stability of Amorphous Intergranular Films in Covalent Materials," *Phys. Rev. Lett.* **77**, 2965 (1996). <https://doi.org/10.1103/PhysRevLett.77.2965>
- [16] S. Hazra, I. Sakata, M. Yamanaka, and E. Suzuki, "Formation of nanocrystallites governed by the initial stress in the ultrathin hydrogenated amorphous silicon films," *J. Appl. Phys.* **90**, 1067–1069 (2001). <https://doi.org/10.1063/1.1377299>
- [17] G.Z. Yue, J.D. Lorentzen, J. Lin, D.X. Hau, and Q. Wang, "Photoluminescence and Raman studies in thin-film materials: Transition from amorphous to microcrystalline silicon," *Appl. Phys. Lett.* **75**, 492–494 (1999). <https://doi.org/10.1063/1.124426>
- [18] S. Veprek, F.A. Sarott, and Z. Iqbal, "Effect of grain boundaries on the Raman spectra, optical absorption, and elastic light scattering in nanometer-sized crystalline silicon," *Phys. Rev. B*, **36**, 3344 (1987). <https://doi.org/10.1103/PhysRevB.36.3344>
- [19] M. Borowicz, W. Latek, A. Rzodkiewicz, A. Laszcz, Czerwinski, and J. Ratajczak, "Deep ultraviolet Raman investigation of silicon oxide: thin film on silicon substrate versus bulk material," *Advances in Natural Sciences: Nanoscience and Nanotechnology*, **3**, 045003 (2012). <https://doi.org/10.1088/2043-6262/4/045003>
- [20] P.A. Temple, and C.E. Hathaway, "Multiphonon Raman spectrum of silicon," *Physical Review B*, **7**(8), 3685–3697 (1973). <https://doi.org/10.1103/PhysRevB.7.3685>
- [21] A.G. Revesz, and H.L. Hughes, "The structural aspects of non-crystalline SiO₂ films on silicon: a review," *Journal of Non-Crystalline Solids*, **328**(1–3), 48–63 (2003). [https://doi.org/10.1016/S0022-3093\(03\)00467-8](https://doi.org/10.1016/S0022-3093(03)00467-8)
- [22] K.J. Kingma, and R.J. Hemley, "Raman spectroscopic study of microcrystalline silica," *American Mineralogist*, **79**(3–4), 269–273 (1994). https://pubs.geoscienceworld.org/msa/ammin/article-pdf/79/3-4/269/4209223/am79_269.pdf
- [23] G.E. Walrafen, Y.C. Chu, and M.S. Hokmabadi, "Raman spectroscopic investigation of irreversibly compacted vitreous silica," *The Journal of Chemical Physics*, **92**(12), 6987–7002 (1990). <https://doi.org/10.1063/1.458239>

СТРУКТУРНІ ВЛАСТИВОСТІ КРЕМНІЮ ЛЕГОВАНОГО РІДКІЗОЗЕМЕЛЬНИМ ЕЛЕМЕНТОМ ІТЕРБІЄМ

Ходжакбар С. Далієв^а, Шаріфа Б. Утамурадова^б, Джонібек Дж. Хамдамов^б, Мансур Б. Бекмуратов^с

^аФілія ФДБУ «Національний дослідницький університет МПЕІ», Йогду, 1, Ташкент, Узбекистан

^бІнститут фізики напівпровідників та мікроелектроніки Національного університету Узбекистану, 100057, Ташкент, Узбекистан, вул. Янги Алмазар, 20

^сДержавний педагогічний інститут імені Аджініязи, Нукус, Узбекистан

У даній роботі наведено результати дослідження стану атомів ітербію в кремнії, проведені методами інфрачервоної спектроскопії (ІЧ) та спектроскопії комбінаційного розсіювання (РС). Зразки кремнію, леговані домішками ітербію, аналізували за допомогою спектрометрів FSM-2201 та SENTERRA II Bruker. Проведено реєстрацію та ідентифікацію компонентів як кристалічної, так і аморфної фаз у зразках. Результати дослідження підтверджують, що легування кремнію домішками ітербію призводить до зниження концентрації оптично активного кисню N₂O^{opt} на 30–40 % залежно від концентрації введених домішок. Також встановлено, що збільшення кількості дефектів призводить до розширення аморфної зони. Припускається, що аналогічні залежності існують для системи Si-Yb; однак, наскільки нам відомо, подібні результати раніше не повідомлялися. Відзначено, що відносна інтенсивність трьох раманівських смуг у системах Si-Yb у стані LTIOS (The light and temperature induced ordered state) змінюється, а відносна інтенсивність Si-Si зменшується. Це вказує на те, що підвищені зв'язки в основному утворюються шляхом розриву зв'язків Si-Si. Було також помічено, що інтенсивність світла, яка викликає цей стан, далека від необхідної для лазерної або твердофазної кристалізації. За допомогою методу раманівської спектроскопії було виявлено структурне перетворення, виражене в щільно упакованому масиві нанокристалів з розміром менше 11 параметрів решітки. Невеликі кластери перебували під сильною внутрішньою напругою (до 3 ГПа), що, ймовірно, запобігає збільшенню розміру кластера понад критичне значення для необоротної кристалізації.

Ключові слова: кремній; ітербій; рідкоземельні елементи; Раманівські спектри; дифузія; теплоносій; температура

TRIBOLOGICAL PROPERTIES AT 20 AND 500°C OF TiN AND CrN CATHODIC ARC COATINGS DEPOSITED ON Ti-6Al-4V ALLOY

 Ilyia O. Klimenko^a,  Vitaliy A. Belous^a,  Viktoriya Ya. Podhurska^b,  Orest P. Ostash^b,
 Valeriy D. Ovcharenko^a,  Galyna N. Tolmachova^a,  Igor V. Kolodiy^a, Mykhailo G. Ishchenko^c,
Ivan M. Babayev^c,  Oleksandr S. Kuprin^a

^a National Science Center Kharkiv Institute of Physics and Technology, Kharkiv, Ukraine

^b Karpenko Physico-Mechanical Institute of the NAS of Ukraine, Lviv, Ukraine

^c JSC "Ukrainian Energy Machines", Kharkiv, Ukraine

*Corresponding Author e-mail: ilyaklimenko91@gmail.com

Received January 4, 2024; February 2, 2024; accepted February 18, 2024

Tribological properties of TiN and CrN coatings deposited by cathodic arc method at three different bias potentials -50, -150 and -300 V on Ti-6Al-4V alloy in pair with alumina have been investigated. X-ray diffraction analysis showed that single-phase textured cubic nitrides of TiN and CrN were formed in these coatings. It is shown that the friction coefficient of the coatings is practically equal to that established for the Ti6Al4V alloy, but the wear rate is more than an order of magnitude lower than for the titanium alloy substrate. Coatings deposited at a potential of -50 V show optimal tribological properties at temperatures 20 and 500°C. Friction coefficients for TiN coatings are 0.4-0.8 at 20°C and 0,75 at 500°C; for CrN coatings they are 0.5 at 20°C and 0,7 at 500°C. Wear rates for TiN coatings are $0.86 \cdot 10^{-5}$ MM³/HM at 20°C and $3.56 \cdot 10^{-5}$ MM³/HM at 500°C; for CrN coatings they are $1.43 \cdot 10^{-5}$ MM³/HM at 20°C and $7.13 \cdot 10^{-5}$ MM³/HM at 500°C.

Keywords: Titanium alloy; Cathodic arc deposition; Nitride coatings; Bias potential; Structure; Nanohardness; Friction coefficient; Wear

PACS: 61.46.-w; 62.20.Qp; 62-25.-g; 81.15.Cd

INTRODUCTION

One of the main factors determining the energy efficiency of nuclear and thermal power plants is the reliability of the steam turbine unit (STU) [1]. Ion-plasma surface modification and the use of protective coatings with high wear resistance can improve the reliability and longevity of titanium alloy components and extend the time between turbine overhauls. The high protective properties of TiN coatings deposited at elevated nitrogen pressure of 1...3 Pa allowed the selection of conditions for the synthesis of the optimal coating for the strengthening of steam turbine blades made of Ti-6Al-4V alloy [2]. The tribological properties of TiN and CrN coatings deposited by cathodic arc deposition have been extensively studied [3-7]. However, for specific technical applications of protective coatings, it is necessary to determine the influence of deposition process parameters on the wear resistance of the substrate-coating pair [8, 9]. One of the most important parameters in the cathodic arc coating process is the bias potential, which determines the energy of the deposited ions [10]. The ion energy determines the structure and properties of the coatings [11].

The aim of this work is to investigate the effect of deposition process parameters (bias potential) of protective nitride coatings TiN and CrN on the tribological properties of Ti-6Al-4V alloy.

EXPERIMENTAL DETAILS

Using a Bulat-6 type apparatus, the schematic of which is shown in Fig. 1, and two metal plasma sources, coatings were deposited on titanium alloy samples at a distance of 300 mm from the cathode. The cathodes were made of pure titanium (99.9%) and chromium (99.9%). The current of the vacuum arc discharge was 85 A for each cathode. The initial pressure in the vacuum chamber was 2×10^{-3} Pa. Before the deposition of the coating, the surface of the samples was subjected to sputtering with cathode material ions at a negative bias voltage of 1.2 kV. To improve the adhesion of the nitride layers, a thin metallic sublayer (titanium or chromium) of 0.1 μm thickness was deposited on the titanium alloy surface in vacuum (0.001 Pa) at a bias potential of -100 V. Negative bias potentials (U_b) of -50, -150 and -300 V were applied to the samples. The nitrogen pressure during the deposition of TiN and CrN coatings was 2 Pa. The temperature of the samples did not exceed 450°C. The thickness of the deposited coatings was 13-15 μm.

Deposited coatings were examined by X-ray diffraction using a DRON-UM1 diffractometer with filtered Cu-Kα radiation. To obtain a complete characterization of coatings, additional XRD tests were performed for the texture analysis and microstructural parameters estimation.

Texture study was carried out by analyzing the ratio of the integral intensities of the diffraction peaks according to [12]. The texture coefficient $TC_{(hkl)}$ was used to quantify the preferred orientations:

Cite as: I.O. Klimenko, V.A. Belous, V.Ya. Podhurska, O.P. Ostash, V.D. Ovcharenko, G.N. Tolmachova, I.V. Kolodiy, M.G. Ishchenko, I.M. Babayev, O.S. Kuprin, East Eur. J. Phys. 1, 380 (2024), <https://doi.org/10.26565/2312-4334-2024-1-38>

© I.O. Klimenko, V.A. Belous, V.Ya. Podhurska, O.P. Ostash, V.D. Ovcharenko, G.N. Tolmachova, I.V. Kolodiy, M.G. Ishchenko, I.M. Babayev, O.S. Kuprin, 2024; CC BY 4.0 license

$$TC_{(hkl)} = \frac{I_{(hkl)}/I_{0(hkl)}}{(1/N)[\sum N I_{(hkl)}/I_{0(hkl)}]} \tag{1}$$

where $TC_{(hkl)}$ – texture coefficient; $I_{(hkl)}$ – measured intensity of the peak (hkl) ; $I_{0(hkl)}$ – intensity of the peak (hkl) in randomly oriented sample (taken from ICDD PDF-2 database); N – number of analyzed diffraction peaks.

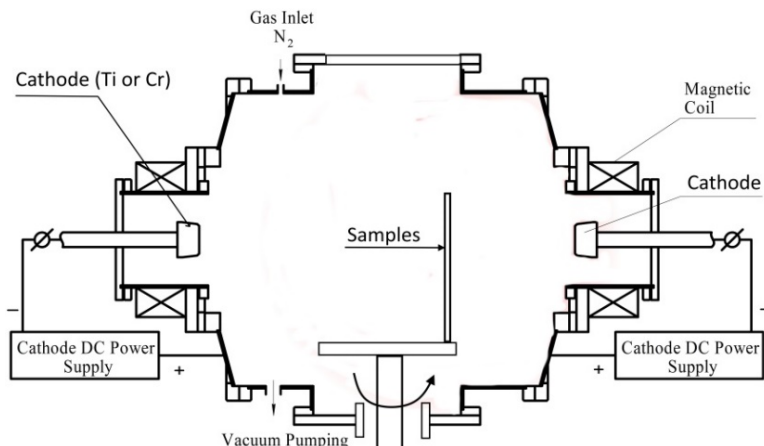


Figure 1. Scheme of the Bulat 6 type apparatus

Williamson-Hall method was applied for the estimation of microstructural parameters (crystallites size CSD and microstrains) of coatings:

$$\beta = \frac{\lambda}{D \cdot \cos(\theta)} + 4 \cdot \varepsilon \cdot \text{tg}(\theta), \tag{2}$$

де β – true physical broadening; λ – X-ray wavelength; D – crystallite size; θ – diffraction angle; ε – microstrains. The instrumental function was obtained from a reference sample of recrystallized silicon.

The mechanical properties of the coatings were investigated by nanoindentation methods using a device Nanoindenter G200 with a CSM module with Berkovich indenter at 300 nm indentation depth [13].

The wear tests were carried out using a reciprocating device consisting of a pair of coated plates (dimensions 20×36×3 mm) and a 10 mm diameter ball of alumina with a hardness of 19 GPa. The friction coefficient was determined at a temperature of 20°C and of 500°C for 30 minutes using a force of 2 N to press the ball against the sample. The wear of the coatings was evaluated using the "Calibre C-265" profilograph-profilometer to measure the area S of the wear track profile [14].

RESULTS AND DISCUSSION

The TiN and CrN coatings deposited on the titanium alloy are golden and gray in color, typical of the cathodic arc deposition method. XRD analysis revealed (Fig.2, Table 1) that both types of coatings are single phase and consists of strongly textured nitrides TiN and CrN, respectively, with preferred orientation of grains with crystallographic planes {111} parallel to the surface. The lattice parameters of both nitrides are significantly large then literature data ($a = 4.239 \text{ \AA}$ for TiN and $a = 4.148 \text{ \AA}$ for CrN). The fact of increased lattice parameters can be explained by the presence of residual stresses in the coatings.

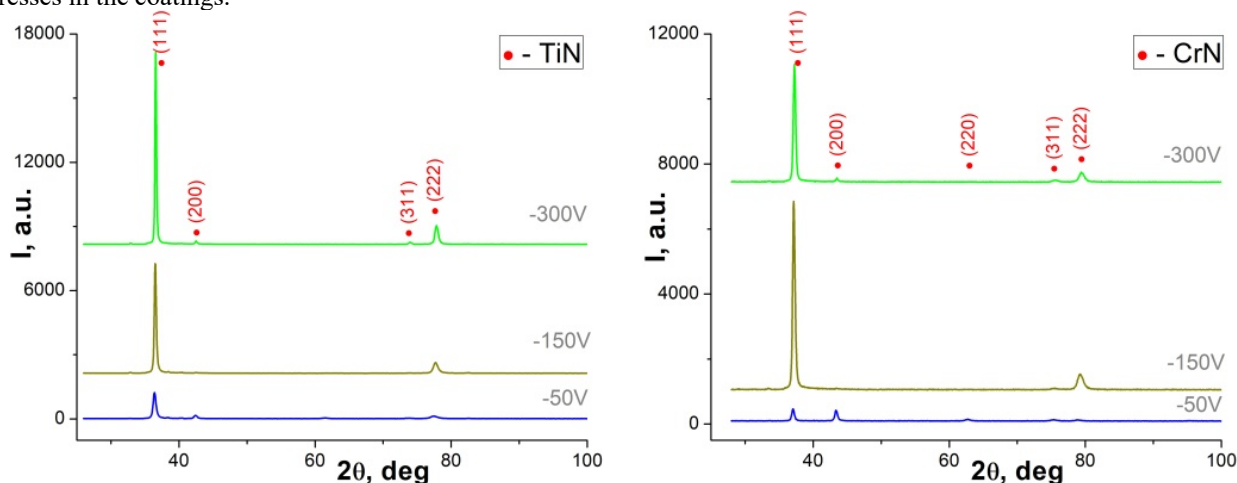


Figure 2. Diffraction patterns of Ti-6Al-4V samples with TiN (left) and CrN (right) coatings deposited at different substrate bias

Table 1. Phase composition and microstructural characteristics of investigated coatings

Coatings	U_b , V	Phase	Lattice parameter, Å	CSD size D, nm	Microstrains, ϵ	$T_{c(111)}$
TiN	-50	TiN	4.267	26.0	$4.2 \cdot 10^{-3}$	4.7
		Ti- α	a = 2.93; c = 4.68	-	-	-
	-150	TiN	4.256	49.0	$3.3 \cdot 10^{-3}$	6.0
		Ti- α	a = 2.93; c = 4.68	-	-	-
-300	TiN	4.250	92.8	$2.7 \cdot 10^{-3}$	5.7	
CrN	-50	CrN	4.181	35.4	$4.2 \cdot 10^{-3}$	2.0
	-150	CrN	4.186	36.5	$3.6 \cdot 10^{-3}$	6.0
	-300	CrN	4.177	35.8	$3.2 \cdot 10^{-3}$	5.5

An increase in the substrate bias potential U_b leads to monotonous decrease in the lattice parameter of TiN nitride (from a = 4.267 Å at $U_b = -50$ V to from a = 4.250 Å at $U_b = -300$ V). At the same time, crystallite size (CSD) increases considerably (from $D \approx 26$ nm to $D \approx 93$ nm) while the microstrains decrease. The magnitude of the bias potential also affects the texture of the TiN nitride: texture coefficient $T_{c(111)}$ increases with U_b increasing, but has maximum $T_{c(111)} = 6.0$ at -150 V.

The evolution of structural and microstructural parameters of CrN nitride with the change in bias potential is significantly different from the results obtained for TiN nitride. Thus, with the increase in the substrate bias the lattice parameter first increases, reaching a maximum a = 4.186 Å at -150 V, and then decreases down to a = 4.177 Å. Microstrains in CrN nitride slightly decrease with the increase in U_b potential (from $4.2 \cdot 10^{-3}$ to $3.2 \cdot 10^{-3}$), while the crystallites size doesn't depend on bias changes and equal $D \approx 36$ nm. More significantly, U_b potential affects the preferred orientation of CrN grains: it changes from weak texture with $T_{c(111)} = 2.0$ at $U_b = -50$ V to strong texture with $T_{c(111)} = 5.5$ at $U_b = -300$ V.

Friction coefficient measurement data as a function of test time and temperature, as well as wear track profilograms of the Ti6Al4V alloy with TiN and CrN coatings deposited at bias potentials of -50, 100 V and -50, -150 V, respectively, compared to the uncoated alloy are shown in Figure 3 and Figure 4.

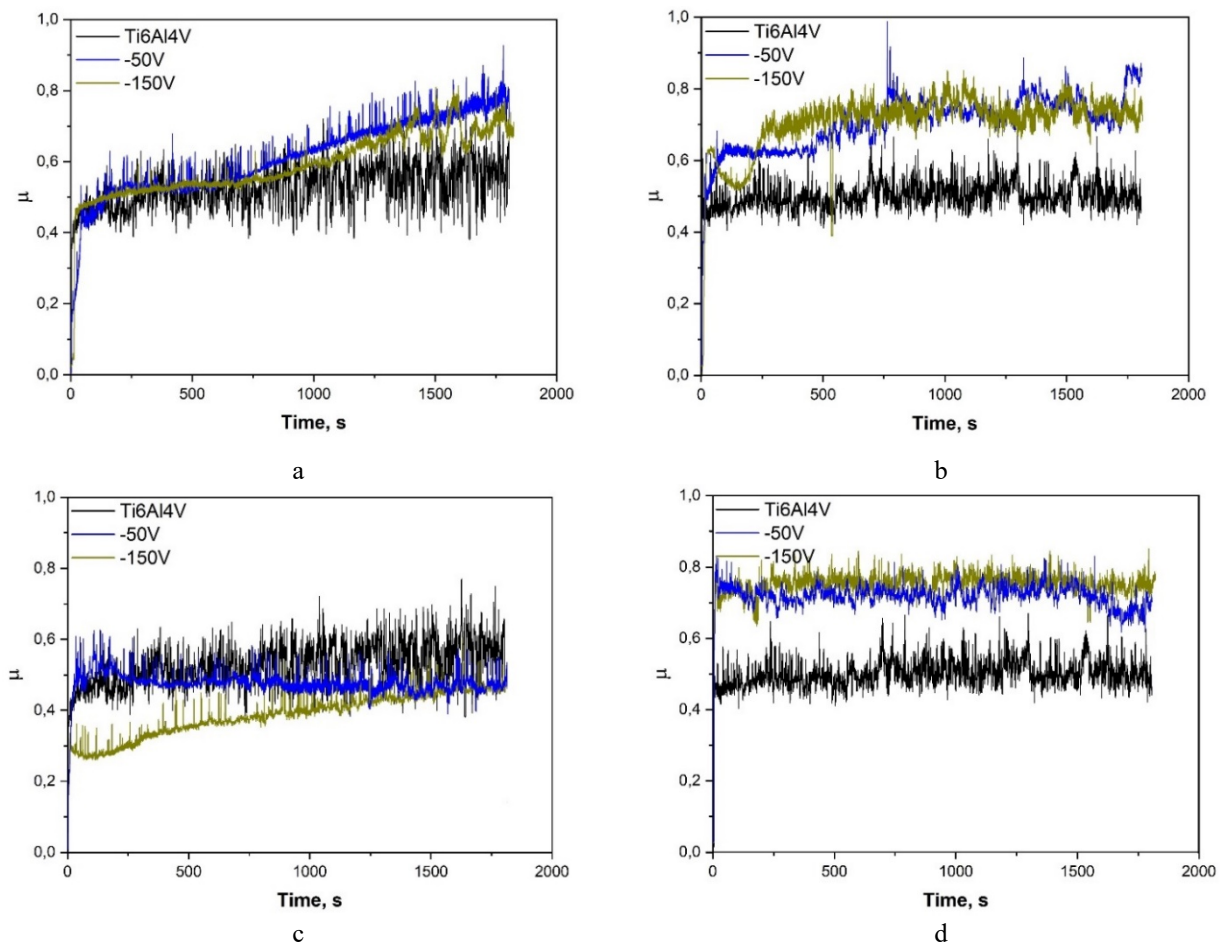


Figure 3. Friction coefficients of the Ti6Al4V with TiN (a, b) and CrN (c, d) coatings at temperatures 20°C (a, c) and 500°C (b, d).

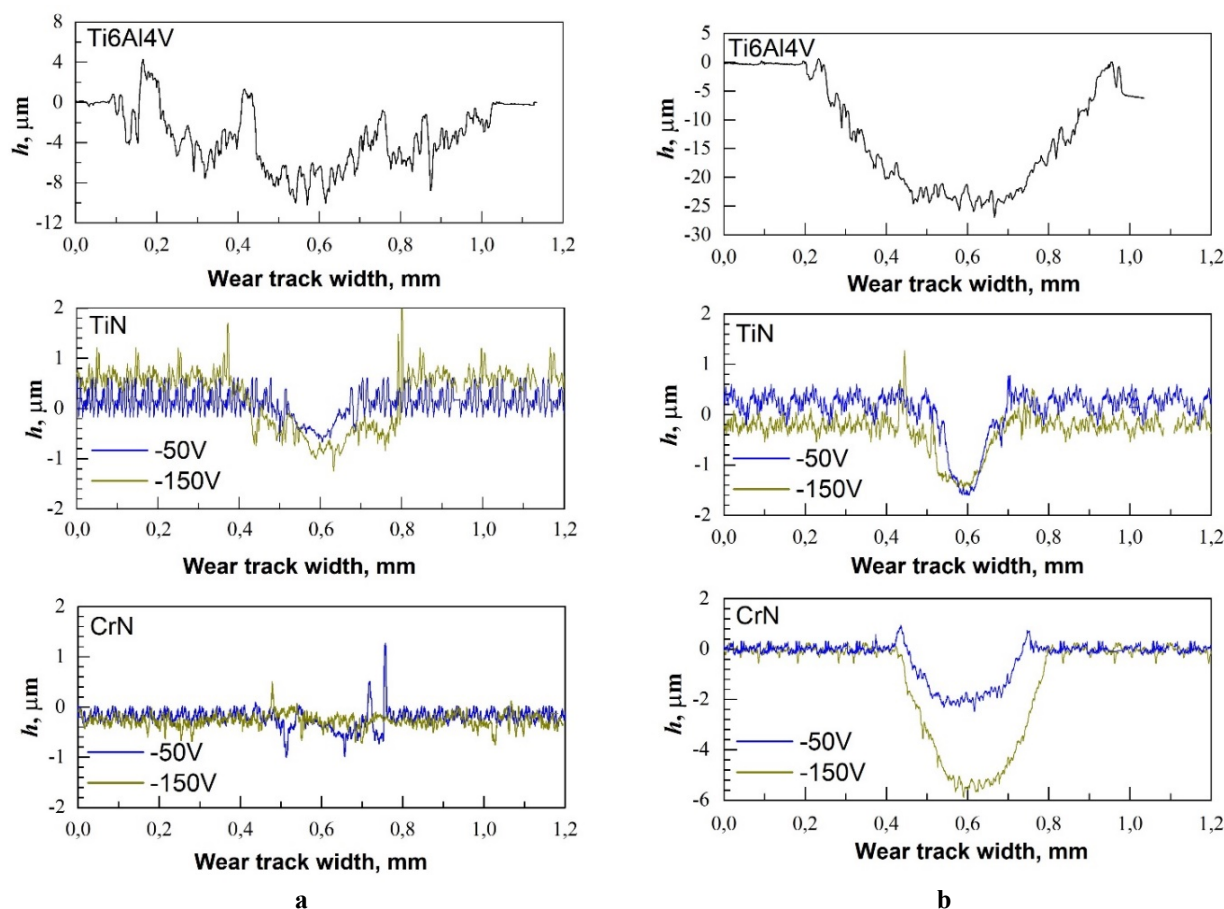


Figure 4. Wear profiles of the Ti6Al4V with TiN and CrN coatings at temperatures 20°C (a) and 500°C (b)

The initial nanohardness of the titanium alloy is 4 GPa, and the coefficient of friction remains constant at 0.55 throughout the test period at a temperature of 20 °C (Fig. 3 a). This value is very close to the literature values of $\mu = 0.55$ -0.6 for the Ti6Al4V alloy-alumina pair at a load of 2 N [15]. The wear intensity for the alloy in the initial state is $6.32 \times 10^{-4} \text{ mm}^3/\text{Nm}$, and the depth of the friction track reaches a maximum of 10 μm (Fig. 4a). At a test temperature of 500 °C, the friction coefficient increases to 0.6 and the wear rate to $1.87 \times 10^{-3} \text{ mm}^3 \text{ N/m}$ (Table 2).

The results of the mechanical property studies (nanohardness, Young's modulus, H^3/E^2 coefficient, friction coefficient, and wear rate) of the initial Ti6Al4V alloy and TiN and CrN coatings are presented in Table 2.

Table 2. Mechanical properties of Ti6Al4V alloy samples with TiN and CrN coatings.

Materials	Ub, V	H, GPa	E, GPa	H^3/E^2 , GPa	Friction coefficient, μ		Wear rate, $\times 10^{-5} \text{ mm}^3/\text{HM}$	
					20 °C	500 °C	20 °C	500 °C
Ti6Al4V	-	4	120	0.004	0.55	0.6	63.2	187
TiN	-50	24	437	0.072	0.5-0.8	0.75	0.86	3.56
	-150	30	470	0.122	0.4-0.8	-	2.73	-
	-300	25	428	0.085	0.4-0.7	-	2.83	-
CrN	-50	25	359	0.121	0.5	0.7	1.43	7.13
	-150	18	296	0.066	0.3-0.5	0.75	1.85	22.3
	-300	19	318	0.067	0.4-0.5	-	1.58	-

TiN coatings have a high nanohardness of 24-30 GPa. Titanium alloy with TiN coatings has a μ coefficient in the range of 0.4-0.8. Depending on the bias potential, there is a slight decrease in the μ coefficient for TiN coatings: at a potential of -50 V, it is 0.5-0.8, and at a potential of -300 V, it is 0.4-0.7. The wear rate of TiN coatings is more than an order of magnitude lower than that of the initial alloy (Table 2). The minimum wear rate of $8.61 \times 10^{-6} \text{ mm}^3/\text{Nm}$ is observed for coatings deposited at a bias potential of -50 V. An increase in the bias potential (-150 and -300 V) results in an increase in the wear rate, which is 2.73 - $2.83 \times 10^{-5} \text{ mm}^3/\text{Nm}$. The values obtained for the coefficient of friction and the wear rate are in the range of the known values for TiN coatings deposited by the cathodic arc method and alumina balls (0.58 and $6 \times 10^{-6} \text{ mm}^3/\text{Nm}$) [3]. Tests at a temperature of 500 °C were performed only on the TiN-coated sample (-50 and -150 V), which showed minimum wear at a temperature of 20 °C (Fig. 4 a, b). The coefficient of friction for the TiN coating remained at 0.75 at this temperature, and the wear rate increased slightly to $3.56 \times 10^{-5} \text{ mm}^3/\text{Nm}$.

The titanium alloy with CrN coatings shows a similar trend in the change of mechanical and tribological properties depending on the bias potential (Table 2). The nanohardness of CrN coatings decreases with increasing bias potential from 25 to 18-19 GPa. The coefficient of friction is 0.3-0.5 and weakly depends on the bias potential. CrN coatings applied at a bias potential of -50 V show the lowest wear rate ($1.43 \times 10^{-5} \text{ mm}^3/\text{Nm}$). Increasing the bias potential (-300 V) leads to a slight increase in the wear rate to $1.58 \times 10^{-5} \text{ mm}^3/\text{Nm}$. Tests at 500°C were performed on two samples with CrN coatings deposited at potentials of -50 and -150 V because the wear rates at room temperature were very similar in value (Fig. 4 a). These tests clearly showed a lower coefficient of friction and a significantly lower wear rate ($7.13 \times 10^{-5} \text{ mm}^3/\text{Nm}$) for the coating deposited at -50 V compared to the coating deposited at a bias potential of -150 V (Fig. 4 b), for which the wear rate is $2.23 \times 10^{-4} \text{ mm}^3/\text{Nm}$.

The correlation between the H^3/E^2 ratio [16] and the wear resistance of coatings was found only for chromium nitride coatings, confirming that the higher the ratio, the higher the wear resistance of the coating (Table 2). There is no such correlation for TiN coatings, which was also noted by the authors of [17].

It is interesting to note that the wear rate of the alumina counterbody paired with a titanium alloy does not depend on the test temperature and is at the level of $1.2 - 2.1 \times 10^{-3} \text{ mm}^3/\text{Nm}$. At the same time, this value is one order of magnitude lower for a pair with a TiN coating and is at the level of $1.31 \times 10^{-4} \text{ mm}^3/\text{Nm}$ at room temperature and increases slightly to $4.03 \times 10^{-4} \text{ mm}^3/\text{Nm}$ at a temperature of 500 °C. For CrN coatings, this value is even lower, $1.03 \times 10^{-5} \text{ mm}^3/\text{Nm}$ at room temperature, but increases to a value of $3.36 \times 10^{-4} \text{ mm}^3/\text{Nm}$ at 500°C, which is close to the wear rate in a pair with a TiN coating. This dependence of the wear rate of the Al_2O_3 ball on the test temperature and the material of the counterpart (plane) may be related to the peculiarities of the formation of abrasive particles and oxide layers in the contact zone. The wear pattern of the alloy, coatings and alumina ball corresponds to abrasive wear in general.

CONCLUSIONS

Titanium nitride and chromium nitride coatings were deposited on Ti-6Al-4V alloy by cathodic arc method at three different bias potentials -50, -150, and -300 V.

X-ray diffraction analysis has shown that single-phase textured cubic nitrides of TiN and CrN are formed in these coatings at bias potentials from -50 to -300 V. The level of microdeformations in the coatings decreases with increasing substrate potential.

TiN and CrN coatings have high nanohardness of 24-30 and 25-18 GPa, respectively. With an increase in the bias potential, the nanohardness of TiN coatings increases, while that of CrN coatings decreases.

The study of the tribological properties of the Ti6Al4V titanium alloy substrate and coatings at temperatures of 20 and 500°C in a pair with an Al_2O_3 ball showed that:

- for the Ti-6Al-4V alloy, the coefficient of friction is 0.55 and the wear rate is $6.32 \times 10^{-4} \text{ mm}^3/\text{Nm}$ at 20°C and 0.6 and the wear rate $1.87 \times 10^{-3} \text{ mm}^3/\text{Nm}$ at 500°C;

- TiN and CrN coatings deposited at a bias potential of -50 V have the lowest wear rate at 20°C: $8.61 \times 10^{-6} \text{ mm}^3/\text{Nm}$ and $1.43 \times 10^{-5} \text{ mm}^3/\text{Nm}$, respectively. The coefficient of friction is in the range of 0.4-0.8 for TiN coatings and 0.5 for CrN coatings. The wear rate at 500 °C for these coatings increases to $3.56 \times 10^{-5} \text{ mm}^3/\text{Nm}$ and $7.13 \times 10^{-5} \text{ mm}^3/\text{Nm}$, respectively, and the coefficient of friction increases to 0.75 and 0.7, respectively.

Thus, the research results indicate that TiN and CrN coatings can be used to increase the wear resistance of Ti6Al4V alloy in air at temperatures from 20 to 500 °C.

Acknowledgment

The work was financially supported by the National Academy of Science of Ukraine (program “Support of the development of main lines of scientific investigations” (KPKVK 6541230)).

ORCID

- Illya O. Klimenko, <https://orcid.org/0000-0001-9006-2261>; Vitaliy A. Belous, <https://orcid.org/0000-0002-9371-4138>
Viktoriya Ya. Podhurska, <https://orcid.org/0000-0002-8067-0180>; Orest P. Ostash, <https://orcid.org/0000-0001-6441-3830>
Valeriy D. Ovcharenko, <https://orcid.org/0000-0003-1169-6608>; Galyna N. Tolmachova, <https://orcid.org/0000-0002-0786-2979>
Igor V. Kolodiy, <https://orcid.org/0000-0001-8598-9732>; Oleksandr S. Kuprin, <https://orcid.org/0000-0003-4293-4197>

REFERENCES

- [1] R. Sherfedinov, M. Ishchenko, L. Slaston, and S. Alyokhina, *Academic Journal of Manufacturing Engineering*, **21**(1), 126 (2023). https://ajme.ro/PDF_AJME_2023_1/L16.pdf
- [2] V.A. Belous, V.N. Voeyvodin, V.M. Khoroshikh, G.I. Nosov, V.G. Marinin, S.A. Leonov, V.D. Ovcharenko, et al., *Sci. Innov.* **12**(4), 27 (2016). <http://dx.doi.org/10.15407/scinc12.04.027>
- [3] P. Panjan, A. Drnovšek, P. Terek, A. Miletić, M. Čekada, and M. Panjan, *Coatings*, **12**(3), 294 (2022). <https://doi.org/10.3390/coatings12030294>
- [4] A. Sayilan, N. Mary, D. Philippon, P. Steyer, and S. Descartes, *Surface and Coatings Technology*, **455**, 129228 (2023). <https://doi.org/10.1016/j.surfcoat.2023.129228>
- [5] S. Datta, M. Das, V.K. Balla, S. Bodhak, and V.K. Murugesan, *Surface and Coatings Technology*, **344**, 214 (2018). <https://doi.org/10.1016/j.surfcoat.2018.03.019>
- [6] D. Yonekura, J. Fujita, and K. Miki, *Surface and Coatings Technology*, **275**, 232 (2015). <https://doi.org/10.1016/j.surfcoat.2015.05.014>

- [7] J. Wu, M. Shen, W. Wang, Y. Cheng, and S. Zhu, *Surface and Coatings Technology*, **448**, 128924 (2022). <https://doi.org/10.1016/j.surfcoat.2022.128924>
- [8] M.M. Al-Asadi, and H.A. Al-Tameemi, *Tribol. Int.* **176**, 107919 (2022). <https://doi.org/10.1016/j.triboint.2022.107919>
- [9] J. Brezinova, J. Hasul, J. Brezina, P.O. Maruschak, and J. Vinas, *Materials Science*, **58**, 629 (2023). <https://doi.org/10.1007/s11003-023-00709-y>
- [10] A.I. Kalinichenko, E. Reshetnyak, V. Strel'nitskij, and G. Abadias, *Surface and Coatings Technology*, **391**, 125695 (2020). <https://doi.org/10.1016/j.surfcoat.2020.125695>
- [11] A.S. Kuprin, S.A. Leonov, V.D. Ovcharenko, E.N. Reshetnyak, V.A. Belous, R.L. Vasilenko, G.N. Tolmachova, et al., *Problems of Atomic Science and Technology*, **123**(5), 154 (2019). https://vant.kipt.kharkov.ua/ARTICLE/VANT_2019_5/article_2019_5_154.pdf
- [12] G.B. Harris, *Phil. Mag.* **43**, 113 (1951). <https://doi.org/10.1080/14786440108520972>
- [13] W.C. Oliver, and G.M. Pharr, *Journal of Materials Research*, **7**(6), 1564 (1992). <https://doi.org/10.1557/JMR.1992.1564>
- [14] V.Y. Podhurska, O.S. Kuprin, R.V. Chepil, O.P. Ostash, T.O. Prikhna, V.B. Sverdun, and M.O. Bortnytska, *Materials Science*, **59**, 10 (2023). <https://doi.org/10.1007/s11003-023-00737-8>
- [15] R.M. Oliveira, C.B. Mello, G. Silva, J.A.N. Gonçalves, M. Ueda, and L. Pichon, *Surface and Coatings Technology*, **205**, 111 (2011). <https://doi.org/10.1016/j.surfcoat.2011.03.029>
- [16] J. Musil, F. Kunc, H. Zeman, and H. Polakova, *Surface and Coatings Technology*, **154**(2-3), 304 (2002). [https://doi.org/10.1016/S0257-8972\(01\)01714-5](https://doi.org/10.1016/S0257-8972(01)01714-5)
- [17] X. Chen, Y. Du, and Y.-W. Chun, *Thin Solid Films*, **688**, 137265 (2019). <https://doi.org/10.1016/j.tsf.2019.04.040>

ТРИБОЛОГІЧНІ ВЛАСТИВОСТІ ПРИ ТЕМПЕРАТУРАХ 20 ТА 500°C КАТОДНО-ДУГОВИХ ПОКРИТТІВ TiN ТА CrN, ОСАДЖЕНИХ НА СПЛАВ Ti-6Al-4V

Ілля О. Клименко^a, Віталій А. Білоус^a, Вікторія Я. Подгурська^b, Орест П. Осташ^b, Валерій Д. Овчаренко^a, Галина М. Толмачова^a, Ігор В. Колодій^a, Михайло Г. Іщенко^c, Іван М. Бабаєв^c, Олександр С. Купрін^a

^a Національний науковий центр Харківський фізико-технічний інститут, Україна

^b Фізико-механічний інститут ім. Карпенка НАН України, Львів, Україна

^c ПАТ "Українські енергетичні машини", Харків, Україна

Були досліджені трибологічні властивості покриттів TiN та CrN, осаджених катодно-дуговим методом при трьох різних потенціалах зміщення -50, -150 і -300 В на сплав Ti-6Al-4V у парі з оксидом алюмінію. Рентгенівський аналіз показав, що у цих покриттях утворилися однофазні текстуровані кубічні нітриди TiN та CrN. Показано, що коефіцієнт тертя покриттів практично рівний тому, що відповідає для сплаву Ti6Al4V, але знос є більш ніж на порядок нижчим, ніж для підкладки з титанового сплаву. Покриття, осаджені при потенціалі -50 В, демонструють оптимальні трибологічні властивості при температурах 20 та 500 °С. Коефіцієнти тертя для покриттів TiN становлять 0,4-0,8 при 20°C та 0,75 при 500°C; для покриттів CrN - 0,5 при 20°C та 0,7 при 500°C. Знос для покриттів TiN становить $0,86 \cdot 10^{-5}$ мм³/Нм при 20°C та $3,56 \cdot 10^{-5}$ мм³/Нм при 500 °С; для покриттів CrN - $1,43 \cdot 10^{-5}$ мм³/Нм при 20°C та $7,13 \cdot 10^{-5}$ мм³/Нм при 500°C.

Ключові слова: Титановий сплав; катодно-дугове осадження; нітридні покриття; потенціал зміщення; структура; нанотвердість; коефіцієнт тертя; знос

STUDY OF THE CHARGE CARRIER COLLECTION COEFFICIENT OF SILICON *p-i-n* PHOTODIODES

✉ Mykola S. Kukurudziak^{a,b}, ✉ Eduard V. Maistruk^b

^a*Rhythm Optoelectronics Shareholding Company, Holovna str. 244, 58032, Chernivtsi, Ukraine*

^b*Yuriy Fedkovych Chernivtsi National University, Kotsyubyn'skogo str. 2, 58012, Chernivtsi, Ukraine*

E-mail: mykola.kukurudzyak@gmail.com

Received January 15, 2023; revised February 3, 2024; accepted February 23, 2024

The paper investigates the collection coefficient of minority charge carriers in silicon *p-i-n* photodiodes and the influence of certain technological factors on it. It has been found that the diffusion length of minority charge carriers and the resistivity of the material have a significant effect on the value of the collection coefficient, since the collection area of photogenerated charge carriers increases with increasing these parameters. It was also found that an effective method to increase the collection coefficient of photodiodes is to ensure that the thickness of the high-resistance region of the photodiode is equal to the sum of the diffusion length of minority charge carriers and the width of the space charge region. The effect of the concentration of dopants on the responsivity and collection coefficient is investigated. It was found that, in contrast to the calculated data, in which the collection coefficient increases with decreasing concentrations of phosphorus and boron, in the experimental data, with decreasing concentrations of impurities, the responsivity and, accordingly, the collection coefficient decrease due to a decrease in the degree of heterogenization and, as a result, a decrease in the width of the space charge region and the diffusion length of minority charge carriers.

Keywords: *Silicon; Photodiode; Responsivity; Charge carrier Collection coefficient; Barrier capacity*

PACS: 61.72. Ji, 61.72.Lk, 85.60.Dw

In semiconductor photovoltaic devices that convert radiation energy into electrical energy, it is necessary that most of the incident radiation is absorbed in the semiconductor volume, since radiation reflected from the surface or passed through the semiconductor is wasted. One of the types of interaction between radiation and a semiconductor that underlies the principle of operation of most photovoltaic devices is the generation of charge carriers under the action of photons. That is, if the structure with a *p-n* junction is exposed to radiation in the wavelength range corresponding to the intrinsic absorption in the semiconductor, then electron-hole pairs are generated in the semiconductor volume under the influence of radiation. If all the electron-hole pairs created by the radiation incident on the device are separated by the *p-n* junction field and create a current in the external circuit, the current conversion efficiency will be maximized. The efficiency of the radiation penetrating into the semiconductor is characterized by the charge carrier collection coefficient (γ), which is the ratio of the number of charge carriers separated by the *p-n* junction field to the number of photons penetrating the semiconductor (1):

$$\gamma = \frac{I_{sc}}{eN}, \quad (1)$$

where I_{sc} is the short-circuit current of the external circuit of the photodetector; e is the electron charge, N is the number of photons.

In this case, it is assumed that one photon creates one electron-hole pair in the semiconductor, i.e., the quantum yield of the photoconversion is equal to one. For an ideal photodetector, the collection coefficient is equal to one over the entire wavelength range to which a given semiconductor is sensitive. In real devices, due to various losses, it is less than unity; this difference is also caused by the fact that some of the carriers created by radiation recombine with each other or on impurity centers before reaching the *p-n* junction [1]. Carrier losses due to recombination depend on the structure of the photodetector, geometric thicknesses of the *n*- and *p*-regions, impurity concentration distribution in the *n*- and *p*-regions, diffusion lengths of non-basic charge carriers, etc. [2].

The responsivity and photocurrent of photodetectors, as their main parameters, are a function of the charge carrier collection coefficient. With the development of optoelectronics and photoelectronics, there is an increasing need to manufacture photodetectors with maximum responsivity and, accordingly, with the maximum collection coefficient. A review of scientific sources shows that many works have been devoted to the problems of ensuring high values of the collection coefficient in photodetectors with a *p-n* junction. For example, [3] shows that in organic photodetectors, an indium oxide and gold electrode with modified output operation acts as a resonator mirror, improving the collection coefficient and at the same time providing an extremely selective cathode, sharply suppressing the dark current. In [4], methods for improving the efficiency of photodetectors based on low-halide perovskite materials were investigated and it was shown that the best device characteristics were obtained by optimizing the thickness of the absorbing layer, doping, and defect density of the buffer and absorbing layers. However, it should be noted that the sources provide rather little information on methods for increasing the collection coefficient of photodetectors with a *p-i-n* structure, in particular silicon *p-i-n* photodiodes (PD).

However, a well-known method of increasing the collection coefficient of *p-i-n* photodiodes is the use of side illumination of the photodetector, which ensures the absorption of radiation in the high-resistance *i*-region bypassing the doped low-resistance *n*- and *p*-regions [5]. This is also possible with the use of mesa-structures [6, 7], but this method requires precise beam focusing and is not possible in the manufacture of large-area PDs. Another effective method of increasing the photosensitivity and collection coefficient is the use of anti-reflective coatings [8, 9]. A common method of increasing the collection coefficient is to ensure double passage of radiation through the thickness of the semiconductor, which is ensured by using a mirror (usually gold) layer on the back of the device, but this is possible at a high depth of radiation absorption and relatively small thickness of the devices [10]. The disadvantage of this method is the low adhesion of gold to silicon, which requires the use of adhesive layers, in particular, a chromium sublayer.

Taking into account the advantages of *p-i-n* PDs in speed, low barrier capacity, and photosensitivity over *p-n* PDs or other types of photodetectors, the establishment of methods to increase the charge carrier collection coefficient in this type of PD is an urgent scientific and technical task, which is the purpose of this article. In particular, we will investigate silicon PDs and pay special attention to the degree of doping of *n*- and *p*-regions of *p-i-n* PDs.

EXPERIMENTAL

The research was carried out in the manufacture of silicon four-element *p-i-n* PDs for operation at supply voltage $U_{bias} = 2$ V and operating wavelength $\lambda_{op} = 1.064$ μm . PDs were made on the basis of single-crystal dislocation-free *p*-type silicon with resistivity $\rho \approx 18\text{-}20$ $\text{k}\Omega\cdot\text{cm}$.

The samples were made by diffusion-planar technology according to the technological regimes given in [11]. The thickness of the crystals reached $X \approx 500\text{-}510$ μm .

The photodetector with a *p-i-n* structure consisted of two thin low-impedance n^+ - and p^+ -regions between which a long high-impedance layer depleted of free carriers was placed. On the reverse side of the crystal, a gold layer was formed with an adhesive sublayer of chromium. The thickness of the chromium sublayer reached 10 nm. The thickness of the n^+ -layer was $x_{n+p} \approx 4\text{-}5$ μm . The thickness of the p^+ -layer was $x_{p+p} \approx 1\text{-}2$ μm . Samples were made with different surface concentrations of phosphorus and boron (surface resistance R_S) of the n^+ - and p^+ -layers, respectively. The surface resistance of n^+ -layers reached the range $R_S \approx 2.1\text{-}8.1$ Ω/\square . The surface resistance of the p^+ -layers was in the range $R_S \approx 16\text{-}40$ Ω/\square . The surface resistance was measured by the four-probe method.

To determine the transmittance of the doped layers at λ_{op} at different concentrations of the impurity, the transmission spectra were measured. It should be noted that the transmission spectra were measured on silicon wafers of the same thickness with only n^+ - or p^+ -layers.

Investigation of the transmission spectra were performed using NIKOLET 6700 and SF-2000 spectrophotometers at room temperature, the total wavelength range was 0.2-26 μm .

The transmission spectra were used to theoretically determine the charge carrier collection coefficient and responsivity. The theoretical responsivity was compared with the experimentally obtained one with the same photodiode characteristics used in the calculations.

Monitoring of current monochromatic pulse responsivity (S_{pulse}) was carried out by method of comparing responsivity of the investigated PD with a reference photodiode certified by the respective metrological service of the company. Measurements were performed when illuminating the PD with a radiation flux of a power of not over $1 \cdot 10^3$ W; load resistance across the responsive element $R_l = 10$ $\text{k}\Omega$, at the bias voltages of $U_{bias} = 2$ V and pulse duration $\tau_i = 500$ ns.

CALCULATIONS

To be able to determine the charge carrier collection coefficient, it is necessary to determine what radiation intensity (I) (in absolute units) is absorbed in the semiconductor thickness equal to the sum of the width of the space charge region (W_i) and the diffusion length of the minority charge carriers (L_n), since the photogenerated charge carriers will be separated by the electric field in this region. A schematic diagram of a photodiode with its various layers is shown in Figure 1.

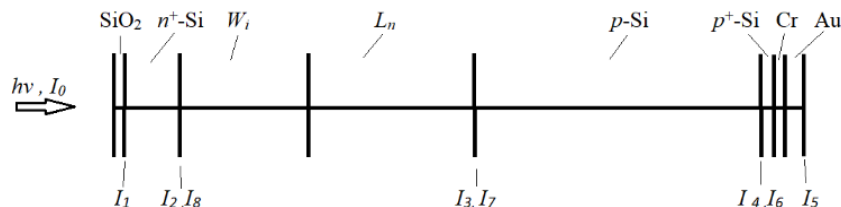


Figure 1. Layer-by-layer schematic representation of a *p-i-n* photodiode.

We determine the radiation intensities according to the Bouguer-Lambert-Beer law [12]:

$$I(x) = I_0[1 - R]e^{-\alpha x}, \quad (2)$$

where $I(x)$ is the intensity of light that has passed through a layer of substance with thickness of x , - the I_0 intensity of light at the entrance to the substance, R is the reflection coefficient, α is the absorption index.

First, it is necessary to determine the transmittance of the n^+ - and p^+ -layers (Figs. 2, 3).

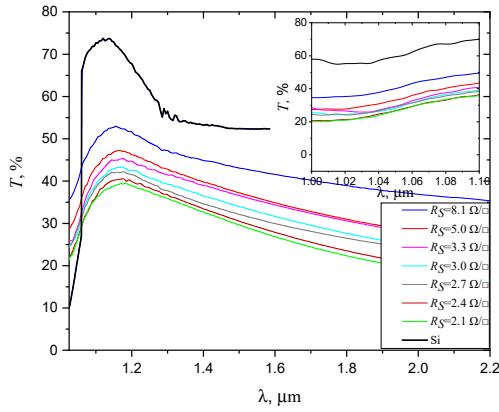


Figure 2. Transmittance of silicon substrates with n^+ -layer at different phosphorus concentrations

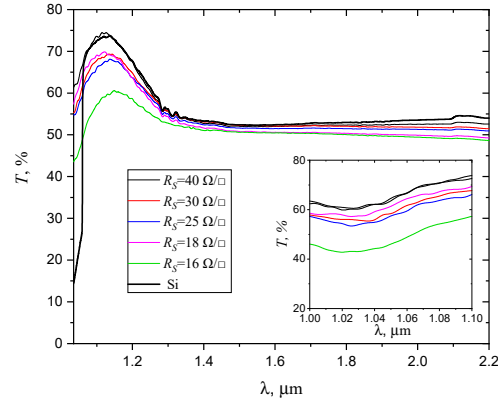


Figure 3. Transmittance of silicon substrates with p^+ -layer at different boron concentrations

In [11] and [13], we found that the optimal values of the surface resistance of phosphorus and boron are $R_S = 2.7 \Omega/\square$ and $R_S = 18 \Omega/\square$, respectively. We present the calculations of the charge collection coefficient at these values.

The surface of the PD receives radiation I_0 , the intensity of which, after passing through the anti-reflective coating, will be I_1 :

$$I_1 = I_0(1 - R), \tag{3}$$

where $R = 5\%$ [14].

In the n^+ -layer, determining the amount of absorbed radiation using the exponential Bouguer's law is a difficult technical task. Since this layer is unevenly doped, the degree of radiation absorption by this layer is determined experimentally by measuring the transmission spectrum. Figure 2 shows that at $R_S = 2.7 \Omega/\square$, the transmittance of the substrate decreases by 32% ($T_{n^+} \approx 32\%$ at λ_{op}) relative to the transmittance of silicon ($T_{Si} \approx 64\%$). That is, 32 % of the radiation was additionally absorbed by the n^+ -layer. Therefore, to determine the radiation intensity that will pass through this layer, the transmission coefficient of the n^+ -layer must be subtracted from the intensity found by the Bouguer's law. Accordingly, the radiation intensity that enters the spatial charge region is equal to I_2 :

$$I_2 = 0.68 \cdot I_1 e^{-\alpha \cdot x_{n^+ - p}}. \tag{4}$$

To determine the intensity of radiation absorbed in the thickness of a crystal equal to the sum of $W_i + L_n$, it is necessary to know their individual thicknesses. To determine the value of W_i and L_n of end products, it is necessary to know the resistivity of their high-resistance i -region, or the concentration of acceptors (N_A) in this region. The value of N_A can be determined by knowing the barrier capacity of responsive elements (C_{RE}). In the investigated case, the capacitance was measured at a bias voltage of $U_{bias} = 120$ V and reached $C_{RE} = 12.1$ pF. From the formula for the barrier capacitance [15], we can determine N_A :

$$C_{RE} = A_{RE} \left(\frac{\epsilon \epsilon_0 e N_A}{2(\phi_c - U_{bias})} \right)^{\frac{1}{2}}, \tag{5}$$

where A_{RE} is the area of responsive elements; ϵ , ϵ_0 are dielectric constants for silicon and vacuum, respectively; ϕ_c is contact potential difference.

In this case, $N_A \approx 1.4 \cdot 10^{12} \text{ cm}^{-3}$.

Next, it is necessary to determine the voltage at which the responsivity or dark current of the PD reaches saturation. In this case, we measured the dependence of pulsed monochromatic responsivity on voltage (Fig. 4). The saturation of the responsivity means that the sum of the width of the space charge region and the diffusion length of the minority charge carriers is equal to the thickness of the high-resistance region of the PD crystal, and further responsivity growth is not possible. At saturation, the value of $W_i + L_n$ is:

$$W_i + L_n = X - (x_{n^+ - p} + x_{p^+ - n}). \tag{6}$$

From Fig. 4, we can see that at $U_{bias} = 100$ V, the responsivity reaches saturation. Knowing N_A , it is possible to determine W_i from the formula (at $U_{bias} = 100$ V) [15]:

$$W_i = \left(\frac{2\epsilon \epsilon_0 (\phi_c - U_{bias})}{e N_A} \right)^{\frac{1}{2}}. \tag{7}$$

From formula (7) $W_i \approx 310 \mu\text{m}$, respectively, from formula (6) $L_n \approx 180 \mu\text{m}$.

Further, knowing N_A , we can determine the value of W_i at $U_{bias} = 2$ V from formula (7). After performing these calculations, you can see that at $U_{bias} = 2$ V the value of $W_i + L_n \approx 233 \mu\text{m}$.

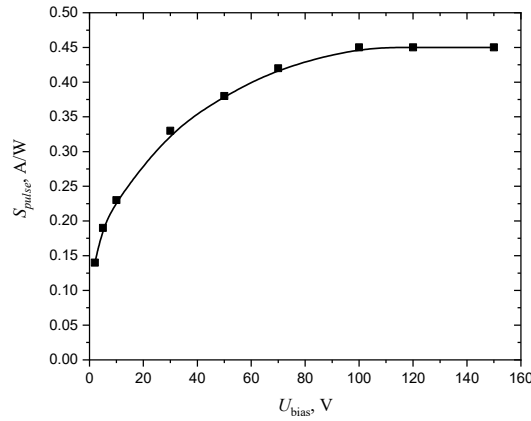


Figure 4. Dependence of the responsivity of the PD on the bias voltage.

Knowing these parameters, you can determine the radiation intensity that will be absorbed in this layer:

$$I_3 = I_2 e^{-\alpha(W_i+L_n)}. \tag{8}$$

Next, it is necessary to determine how much radiation intensity will be emitted in the «inactive» high-resistance region:

$$I_4 = I_3 e^{-\alpha(x-(W_i+L_n+x_{n+-p}+x_{p+-p}))}. \tag{9}$$

Next, it is necessary to determine how much the radiation flux will be attenuated after passing through the p^+ -layer and the adhesive sublayer of chromium. Figure 3 shows that the presence of a p^+ -layer on the surface of a silicon substrate with a $R_S = 18 \text{ k}\Omega/\square$ decreases the transmittance by 4 %. Therefore, by analogy with the n^+ -layer, it is necessary to subtract the following 4% from the radiation intensity found by the Bouguer's law. Also, in [10], we found that a 10 nm thick chromium film absorbs 4% ($T_{Cr} \approx 96\%$) of the radiation of the operating wavelength. Accordingly, the radiation intensity after passing through these layers will be:

$$I_5 = 0.96 \cdot T_{Cr} I_4 e^{-\alpha x_{p+-p}}. \tag{10}$$

The intensity of the radiation after reflection from the gold layer and passing through the adhesive layer of chromium and the p^+ -layer will gain value:

$$I_6 = 0.96 \cdot T_{Cr} R_{Au} I_5 e^{-\alpha x_{p+-p}}, \tag{11}$$

where R_{Au} is reflection coefficient of gold at λ_{op} is $R_{Au} = 98.3\%$ [16].

The intensity of radiation after passing through the «inactive» i -region after reflection from gold will reach:

$$I_7 = I_6 e^{-\alpha(x-(W_i+L_n+x_{n+-p}+x_{p+-p}))}. \tag{12}$$

The radiation intensity absorbed in the crystal layer W_i+L_n after reflection from the gold will reach:

$$I_8 = I_7 e^{-\alpha(W_i+L_n)}. \tag{13}$$

The collection coefficient of minority charge carriers will be determined by the formula [17]:

$$\gamma = 1 - e^{-\alpha x}. \tag{14}$$

Taking into account the change in radiation intensity, this formula will take the form:

$$\gamma_1 = I_3(1 - e^{-\alpha(W_i+L_n)}) \approx 0.106, \tag{15}$$

where γ_1 is coefficient of collection of minority charge carriers at the first passage through the crystal thickness.

$$\gamma_2 = I_8(1 - e^{-\alpha(W_i+L_n)}) \approx 0.042, \tag{16}$$

where γ_2 is coefficient of collection of minority charge carriers at the second passage through the crystal thickness.

The responsivity was determined using the formula [18]:

$$S_\lambda = (1 - R)TQ \sum \gamma \frac{\lambda_{op}}{1.24} \approx 0.12 \text{ A/W}, \tag{17}$$

where T is the transmission coefficient of the input window or optical filter (consider that $T = 100\%$); Q is the quantum output of the internal photoeffect (consider that $Q = 1$).

RESULTS OF THE RESEARCH AND THEIR DISCUSSION

The value of responsivity obtained by the calculated method correlates well with the experimental one, which reached $S_{pulse} = 0.12-0.14$ A/W.

As can be seen from the calculations, the charge carrier collection coefficient provided by the reflected radiation from the gold "mirror" is about 40 % of the collection coefficient provided by the first passage of radiation through the photodiode crystal or 28 % of the total collection coefficient. The decrease in this parameter is caused by the absorption of radiation by the semiconductor thickness, p^+ -layer, and chromium sublayer. It is possible to increase the collection coefficient by increasing the resistivity of the material, which will increase the W_i , and by increasing the L_n . This will ensure the expansion of the collection area of the charge carriers. To ensure the maximum values of these parameters, it is necessary to use silicon with high resistivity and lifetime of minority charge carriers and to use a technology that ensures minimal degradation of these characteristics during the production process, for example, it can be a mesa-technology [6, 7].

An effective method of γ of low-voltage PDs is to reduce the crystal thickness to minimize the area of the semiconductor in which there is no "charge carrier collection". In this case, the ideal PD is a crystal variant in which the W_i+L_n region covers the entire high-resistance region of the substrate. Such a case is provided in high-voltage photodiodes, but to realize it in low-voltage PDs, it is necessary to reduce the crystal thickness.

Thus, if we calculate the collection coefficient according to the methodology given in the previous section with the same initial data, but assuming that the crystal thickness is less by the value of:

$$X_1 = X - (W_i + L_n + x_{n+-p} + x_{p+-p}), \tag{18}$$

where X_1 is the thickness of the crystal region in which there is no charge carrier collection, $X_1 \approx 257$ μm .

We obtain that $\gamma_2 \approx 0.07$, which is about 66 % of the collection coefficient provided by the first passage of radiation through the photodiode crystal or 40 % of the total collection coefficient. With the obtained value of the collection coefficient, it will be possible to increase the responsivity of the product by about 16% and obtain $S_\lambda = 0.14$ A/W. In practice, a significant reduction in the substrate thickness is a difficult technological task due to the reduced mechanical strength of the wafers. However, it is possible by forming thinnings on the back side of the crystal by chemical-dynamic polishing [19] in a shape that corresponds to the responsive element, provided that the proper thickness of the crystal periphery is ensured, which will play the role of stiffeners [20]. The described thinning on the back side of the substrate can be seen in Figure 5.

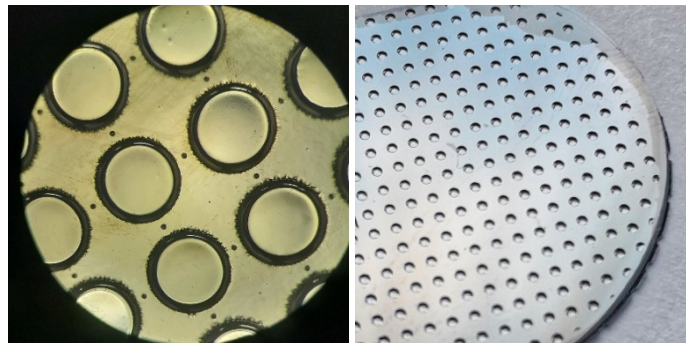


Figure 5. Etched thinning on the back side of the substrate

It should be noted that according to Figure 1, the transmittance of the substrates at different phosphorus concentrations differs, which may affect the final value of the collection coefficient and responsivity. Let's calculate these parameters according to the above methodology with the specified initial data, taking into account only the change in the transmittance of the n^+ -layer (Table 1).

Table 1. Calculations of the collection coefficient of minority charge carriers and responsivity at different phosphorus concentrations in the n^+ -layer

$R_S, \Omega/\square$	$T_{n^+}, \%$	$\sum \gamma, \text{ abs.}$	$S_\lambda, \text{ A/W}$	$S_\lambda, \text{ A/W } (U_{bias}=120 \text{ V}), \text{ exp.}$
8.1	45	0.16	0.13	0.42-0.43
5.0	37	0.152	0.124	0.42-0.44
3.3	34	0.151	0.122	0.45-0.47
3.0	33	0.149	0.121	0.46-0.47
2.7	32	0.148	0.12	0.46-0.47
2.4	31	0.147	0.119	0.4-0.41
2.1	31	0.147	0.119	0.38-0.4

As can be seen from Table 1, with increasing phosphorus concentration in the n^+ -layer, the transmittance of this region decreases. When the surface resistance value $R_S = 3.3 \Omega/\square$ is reached, the transmittance changes minimally and at $R_S = 2.4 \Omega/\square$ it does not decrease anymore. The same pattern was observed with the collection coefficient and

responsivity. From the calculations, we can see that the lowest value of R_S corresponds to the highest value of responsivity. But in practice, the situation is quite different. We measured the S_{pulse} at $U_{bias} = 120$ V at different R_S (Table 1, 5 column). We obtained the value of high-voltage responsivity to be able to estimate of this parameter in saturation, since at low voltages the responsivity may differ minimally.

As can be seen from the experimental data, there is no correlation between them and the calculations for the dependence of responsivity on phosphorus concentration, which is caused by the different degree of substrate gettering during phosphorus diffusion, respectively, at different duration of gettering, the diffusion length of minority charge carriers and resistivity differed, which was reflected in the responsivity values. The decrease in responsivity at $R_S = 2.1-2.4 \Omega/\square$ is caused by the formation of structural defects, in particular dislocations due to high phosphorus concentration, which in turn can reduce of the diffusion length of charge carriers due to their recombination on crystallographic defects (provided they are placed in the space charge region) [21]. Accordingly, in the methodology for calculating the collection coefficient, it is necessary to provide other initial data of the capacitance, resistivity, and diffusion length of minority charge carriers, which are characteristic of each case, since they completely depend on the degree of gettering. The absence of correlation between the calculations and the experiment is caused by the difference in these initial data

The same situation was observed in the case of the p^+ -layer, since, as can be seen from the Figure 2, with a decrease in the boron concentration in the p-layer, the transmittance of this layer increases, which should ensure an increase in the collection coefficient. However, in practice, with a decrease in boron concentration, a decrease in responsivity was observed due to a decrease in the degree of boron gettering on the back side of the substrate [13].

CONCLUSIONS

The influence of technological factors on the collection coefficient of minority charge carriers of silicon *p-i-n* photodiodes is investigated. The following conclusions have been made:

1. The width of the space charge region and the diffusion length of the minority charge carriers have a significant effect on the collection coefficient, since these two parameters form the region in which the photogenerated charge carriers "collect" and will be separated by the p-n junction.
2. The maximum value of the collection coefficient is possible when the thickness of the high-resistance region of the photodiode is equal to the sum of the diffusion length of the minority charge carriers and the width of the space charge region.
3. The degree of doping of the n^+ - and p^+ -regions affects the value of the collection coefficient, since the transmittance of these regions decreases with increasing concentration. However, it should be noted that with a decrease in the concentration of dopants and a decrease in the duration of diffusion processes, the degree of crystal volume gettering decreases, which negatively affects the diffusion length of minority charge carriers and the resistivity of silicon (the width of the space charge region).
4. With an increase in the phosphorus concentration and with an increase in the duration of the gettering, there is a slight decrease in the responsivity and, accordingly, the collection coefficient due to the formation of structural defects on the surface of the substrate, which results in the recombination of photogenerated charge carriers on crystallographic defects. The optimum value of the surface resistance of the n-layer after phosphorus diffusion to ensure the maximum collection coefficient and responsivity is $R_S = 2.7-3.0 \Omega/\square$.

ORCID

Mykola S. Kukurudziak, <https://orcid.org/0000-0002-0059-1387>; Eduard V. Maistruk, <https://orcid.org/0000-0002-9025-6485>

REFERENCES

- [1] C.M. Proctor, M. Kuik, and T.Q. Nguyen, *Progress in Polymer Science*, **38**(12), 1941 (2013). <https://doi.org/10.1016/j.progpolymsci.2013.08.008>
- [2] B. Yang, F. Zhang, J. Chen, S. Yang, X. Xia, T. Pullerits, and K. Han, *Advanced Materials*, **29**(40), 1703758 (2017). <https://doi.org/10.1002/adma.201703758>
- [3] A. Yazmaciyan, P. Meredith and A. Armin, *Advanced Optical Materials*, **7**(8), 1801543 (2019). <https://doi.org/10.1002/adom.201801543>
- [4] S. Singh, S. Kumar and M. Deo, *Opt. Quant. Electron.*, **55**, 846 (2023). <https://doi.org/10.1007/s11082-023-05127-7>
- [5] S. Zie, *Physics of semiconductor devices*, (Mir, Moscow, 1984). (in Russian).
- [6] M.S. Kukurudziak, and E.V. Maistruk, *Semicond. Sci. Technol.* **38**, 085007 (2023). <https://doi.org/10.1088/1361-6641/acdf14>
- [7] K.O. Boltar, I. V. Chinareva, A.A. Lopukhin and N.I. Yakovleva, *Appl. Phys.* **5**, 10 (2013).
- [8] S. Zhang, Y. Yao, and D. Hu, *Energies*, **12**(6), 1168 (2019). <https://doi.org/10.3390/en12061168>
- [9] S.B. Khan, S. Irfan, Z. Zhuanghao, and S.L. Lee, *Materials*, **12**(9), 1483 (2019). <https://doi.org/10.3390/ma12091483>
- [10] M.S. Kukurudziak and E.V. Maistruk, in: *Fifteenth International Conference on Correlation Optics, 121261V* (SPIE, Chernivtsi, 2021). <https://doi.org/10.1117/12.2616170>
- [11] M.S. Kukurudziak, *Semiconductor Physics, Quantum Electronics & Optoelectronics*, **25**(4), 385 (2022). <https://doi.org/10.15407/spqeo25.04.385>
- [12] A.V. Igo, *Optics and Spectroscopy*, **128**, 1125-1130 (2020). <https://doi.org/10.1134/S0030400X20080135>
- [13] M.S. Kukurudziak, and E.V. Maistruk, in: *2022 IEEE 3rd KhPI Week on Advanced Technology (KhPIWeek)* (IEEE, Kharkiv, 2022), pp. 1-6. <https://doi.org/10.1109/KhPIWeek57572.2022.9916420>

- [14] M.S. Kukurudziak, East Eur. J. Phys. 2, 311 (2023), <https://doi.org/10.26565/2312-4334-2023-2-36>
- [15] N. M. Tugov, B.A. Glebov, and N. A. Charykov, *Semiconductor devices: Textbook for universities*, edited by V.A. Labuntsov, (Energoatomizdat, Moscow, 1990). (in Russian)
- [16] N.I. Koshkin, and M.G. Shirkevich, *Handbook of Elementary Physics*, (State Publishing House of Physical and Mathematical Literature, Moscow, 1962). (in Russian)
- [17] L.K. Buzanova, and A.Y. Gliberman, *Semiconductor photodetectors* (Energia, Moscow, 1976). (in Russian)
- [18] A.V. Fedorenko, Technology and design in electronic equipment, 17(3–4), 17 (2020).
<https://doi.org/10.15222/TKEA2020.3-4.17> (in Ukrainian)
- [19] M.S. Kukurudziak, Surface Chemistry, Physics and Technology, 14(1), 42 (2023). <https://doi.org/10.15407/hftp14.01.042> (in Ukrainian)
- [20] A.A. Ascheulov, Y.G. Dobrovolsky and V.M. Godovanyuk. Scientific Bulletin of Chernivtsi University, 32, 135-142 (1998).
- [21] K. Ravey, *Defects and impurities in semiconductor silicon*, (Trans.), edited by G.N. Gorina, (Mir, Moscow, 1984). (in Russian).

ДОСЛІДЖЕННЯ КОЕФІЦІЄНТА ЗБИРАННЯ НОСІЇВ ЗАРЯДУ КРЕМНІЄВИХ *p-i-n* ФОТОДІОДІВ†

Микола С. Кукурудзяк^{a,b}, Едуард В. Майструк^b

^aАТ «Центральне конструкторське бюро Ритм», 58032, м. Чернівці, вул. Головна, 244, Україна

^bЧернівецький національний університет імені Юрія Федьковича, 58002, м. Чернівці, вул. Коцюбинського, 2, Україна

В статті досліджено коефіцієнт збирання неосновних носіїв заряду кремнієвих *p-i-n* фотодіодів та вплив на нього окремих технологічних чинників. Встановлено, що значний вплив на значення коефіцієнта збирання має дифузійна довжина неосновних носіїв заряду та питомий опір матеріалу, оскільки при збільшенні даних параметрів зростає область збирання фотогенерованих носіїв заряду. Також встановлено, що ефективним методом підвищення коефіцієнта збирання фотодіодів є забезпечення товщини високоомної області фотодіода рівною сумі дифузійної довжини неосновних носіїв заряду та ширини області просторового заряду. Досліджено вплив концентрації легуючих домішок на значення чутливості та коефіцієнта збирання. Встановлено, що на відміну від розрахункових даних, в яких коефіцієнт збирання зростає при зниженні концентрації фосфору та бору, в експериментальних даних, при зниженні концентрації домішок, чутливість, а відповідно і коефіцієнт збирання зменшуються внаслідок зниження міри гетерування та, як наслідок, зниження ширини області просторового заряду та дифузійної довжини неосновних носіїв заряду.

Ключові слова: кремній; фотодіод; чутливість; коефіцієнт збирання носіїв заряду; бар'єрна ємність

SINGLE AND MULTIPHOTON OPTICAL TRANSITIONS IN ATOMICALLY THIN LAYERS OF TRANSITION METAL DICHALCOGENIDES

✉ **Rustam Y. Rasulov**^a, ✉ **Voxob R. Rasulov**^{a*}, **Kamolakhon K. Urinova**^b,
 ✉ **Makhliyo A. Mamatova**^a, ✉ **Bakhodir B. Akhmedov**^a

^a Fergana State University, Fergana, Uzbekistan

^b Kokand State pedagogical Institute, Kokand, Uzbekistan

*Corresponding Author e-mail: vrrasulov83@gmail.com

Received January 3, 2024; revised February 7, 2024; accepted February 17, 2024

This study explores the optical properties of monolayers from transition metal dichalcogenides (TMDs), materials that have gained attention post-graphene discovery for their unique electronic and optical characteristics. We analyze the crystal structure, Brillouin zones, and electronic band structures of TMD monolayers, laying the foundation to understand their diverse optical phenomena. Special emphasis is placed on the energy spectrum across valleys and the use of an effective Hamiltonian for parallel spin bands. We investigate interband optical transitions, including single-, two-, and three-photon processes, developing equations to calculate transition probabilities that take into account polarization, light frequency, and temperature. Our theoretical analysis, rooted in quantum mechanics, sheds light on the matrix elements that dictate these transitions, underscoring the impact of complex compositions on the optical behavior of TMD monolayers. This work not only advances our understanding of TMD optical properties but also highlights their potential for optoelectronic applications, marking a significant contribution to the field of semiconductor physics.

Keywords: Polarized photon; Matrix element; Optical transitions; Two-Band approximation; Current carriers; Electron Hamiltonian; Momentum operator; Spin states

PACS: 71.20. – b, 71.28. + d

INTRODUCTION

The discovery of a method for producing graphene [1] sparked significant interest in the exploration of various two-dimensional (2D) atomic layers of transition metal dichalcogenides (TMDs), which exhibit unique physical properties. Transition metal dichalcogenides are a class of chemical compounds denoted by the formula MX_2 , where M represents a transition metal (e.g., Mo, W) and X denotes a chalcogen (e.g., S, Se) [2-5].

In recent years, two-dimensional (2D) structures such as graphene, monolayers of transition metal dichalcogenides (TMDs), monolayers of hexagonal boron nitride, and van der Waals heterostructures based on them have occupied a special place in the field of semiconductor nanosystems [3,4]. The most widely studied representatives among TMDs include MoS_2 , $MoSe_2$, WS_2 , and WSe_2 monolayers [5-7]. These two-dimensional systems are actively investigated both experimentally and theoretically. It's noteworthy that the boundaries of the hexagonal Brillouin zone are delineated at the K_{\pm} points. In such scenarios, under the dipole approximation, σ^+ or σ^- polarized light is selectively absorbed in the K_+ or K_- valleys, respectively [6].

Currently, numerous studies focus on the diverse structures of metal dichalcogenides [6]. However, the optical properties of samples with intricate structures remain insufficiently explored. In light of this, the theoretical investigation of single- and multiphoton absorption in monolayers of metal dichalcogenides becomes paramount. This involves a detailed examination of the matrix elements of optical transitions, which constitutes the core subject of this work. Such analysis is crucial for understanding the complex optical behaviors of these materials.

BASIC PROPERTIES OF TMD MONOLAYERS

Fig. 1a,b schematically illustrates the crystal structure and atomic arrangement within TMD monolayers. The monomolecular layer, characterized by the D_{3h} point group, features a horizontal mirror plane that intersects the metal atom layer. The unit cell comprises a metal atom flanked by two chalcogen atoms, positioned in planes above and below the metal plane, respectively. The Brillouin zone is depicted as a regular hexagon (Fig. 1c). The correct exclusion zones at the K_{\pm} points are identified by the time-reversal symmetry between them. Near these points, the electron dispersion in both the valence and conduction bands exhibits a parabolic shape (Fig. 1d). It is important to note that at the K_{\pm} points, the band splitting due to spin-orbit coupling vanishes, leading to degeneracy. This symmetry, under the time-reversal operator, allows for the association of states with opposite spins in different valleys.

As a result, we derive the effective Hamiltonian matrix for the K_+ point, which is a 2×2 matrix describing the states with parallel spins in the conduction and valence bands for spin projection $s = +1/2$ near this point [6], i.e.

$$H_+ = \begin{pmatrix} E_g/2 & \gamma(k_x - ik_y) \\ \gamma(k_x + ik_y) & -E_g/2 \end{pmatrix}. \quad (1)$$

Here, $k_{\perp} = (k_x, k_y)$ represents the two-dimensional wave vector relative to the γ point in the Brillouin zone, and K_+ signifies a parameter proportional to the interband matrix element of the momentum operator. E_g denotes the band gap. For spin levels within the same valley ($s = -1/2$), the band gap E_g transforms to $E_{g+\Delta}$, where Δ is the sum of the spin-orbit coupling induced energy splittings in the conduction and valence bands. It is important to note that the band gap widths in structures based on molybdenum and tungsten exhibit quantitative differences [5-8]. The effective Hamiltonian for the K_- valley is obtained by the substitution in expression (1) from $k_x \pm ik_y \rightarrow k_x \mp ik_y$ [1]. The energy spectrum of an electron, as described by Hamiltonian (1), is given by the following expression, which is also referred to as the Dirac-like energy spectrum [8]:

$$\varepsilon_{\lambda,k} = \lambda\varepsilon_k, \varepsilon_k = \sqrt{(E_g/2)^2 + \gamma^2 k_{\perp}^2}, \quad (2)$$

where $\tau = +$ corresponds to the conduction band, while $\tau = -$ denotes the valence band. The distinction in band gaps, denoted as $E_{\pm}(\vec{k}_{\perp})$, leads to variations in the energy spectrum, which are depicted in Fig. 1. This figure illustrates how the energy spectrum varies with different band gap values (Fig. 1a) and electron effective masses (Fig. 1b) [5-10]. The diverse band gaps and effective masses across different materials result in significant differences in their electronic properties, as visually represented in these figures.

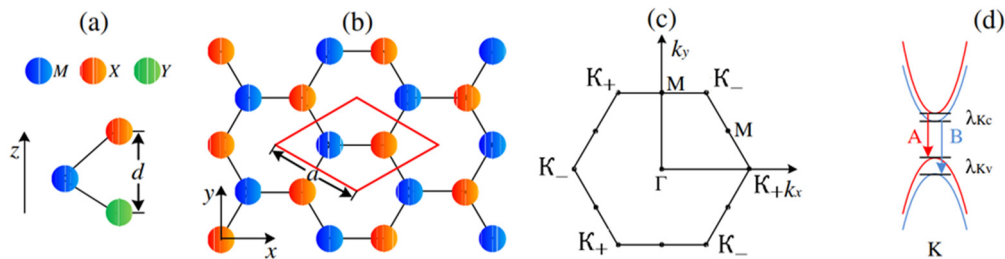


Figure 1. (a) is an MX_2 schematic representation of the monolayer crystal structure of TMD described by the chemical formula. Blue spheres - metal atoms (M), yellow - chalcogen (X), (b) - arrangement of atoms, (c) two-dimensional Brillouin zone, (d) K_{\pm} image of the energy spectrum near points corresponding to the Brillouin zone and the usual rules for choosing radiation for falls. Here λ_{Kc} and λ_{Kv} are the widths of the spin-orbit bands separating the conduction band and valence band, respectively.

In many instances, to streamline the calculations, the energy spectrum of charge carriers for very small magnitudes of the wave vector (k) can be approximated as follows:

$$\varepsilon_k \approx \frac{E_g}{2} + \frac{\hbar^2 k_{\perp}^2}{2m^*}, \quad (3)$$

where $m^* = E_g/(2v_0^2)$ is expressed as effective mass, $v_0 = \gamma/\hbar$ quantity per unit speed.

Literature sources, including [4], present varying numerical values for the effective mass of electrons and the band gap in monolayers of metal dichalcogenides. Consequently, Figure 1 illustrates the energy spectra of charge carriers for diverse values of the aforementioned band parameters: it showcases how the energy spectrum's band gap varies with a specific effective mass, alongside the results plotted against the two-dimensional wave vector. Meanwhile, Figure 2 displays the energy spectrum as a function of the effective mass and two-dimensional wave vector, with the band gap held constant.

COMPONENT MATRIX ELEMENTS OF INTERBAND OPTICAL TRANSITIONS

The coefficient of linear-circular dichroism, indicative of the probabilities of optical transitions, is determined by the underlying matrix elements. These elements facilitate a quantum mechanical analysis of such transitions. Moving forward, we will conduct a detailed examination of the matrix elements associated with single- and multiphoton optical transitions, aiming to deepen our understanding of these processes.

Interband single-photon optical transitions. This optical transitions in monolayers of metal dichalcogenides are influenced by the polarization vector \vec{e} of light, its frequency, and the temperature of the sample. Assuming the effect of coherent saturation is negligible, the probability of these optical transitions between the conduction (C) and valence (V) bands can be expressed as:

$$W_{C,V}^{(1)} = \frac{2\pi}{\hbar} \left(\frac{eA_0}{c\hbar} \right)^2 \times \sum_{\vec{k}} (f(E_-) - f(E_+)) |(\vec{e} \cdot \vec{p})_{cV}|^2 \delta(E_+ - E_- - \hbar\omega) \quad (4)$$

is calculated by the expression, here where $(\vec{e} \cdot \vec{p})_{cV}$ -pulse operator and the interband matrix element of the scalar product of the polarization vector of polarized light, the remaining quantities are well-known quantities. (1) the eigenfunctions of

the Hamiltonian, i.e., the propagation coefficient of the wave functions of current carriers [10] is determined as noted in the work, and if we pay attention to the fact that the operator \vec{k} impulse is the first-order derivative obtained from relation (1) according to wave vector, then $(\vec{e} \cdot \vec{p})_{cV}$ the matrix element of the operator of single-photon interband optical transitions will be noted in the following form

$$\langle c | \vec{e} \cdot \vec{p} | V \rangle = \frac{m_0}{\hbar} \left\langle c \left| e_x \frac{\partial H_+}{\partial k_x} + e_y \frac{\partial H_+}{\partial k_y} \right| V \right\rangle = \frac{m_0}{\hbar} \frac{\gamma}{2\varepsilon(\vec{k})} \left\{ e_- [\tilde{E}_g + E(\vec{k}_\perp)] - \frac{k_\perp^2}{k_\perp^2} [-\tilde{E}_g + E(\vec{k}_\perp)] e_+ \right\}. \quad (5)$$

Here $p_0 = \frac{m_0 \gamma}{\hbar}$, $k_\perp^2 = k_x^2 + k_y^2$, $e_\pm = (e_x \pm i e_y)$. (Diagonal) matrix element of the pulse operator corresponding to single-band networks and single-photon optical transitions:

$$p_{cc} = -p_{vv} = \vec{e} \cdot \vec{p}_{cc} = 4 \frac{m_0 \gamma^2}{\hbar} \frac{\vec{e}_\perp \cdot \vec{k}_\perp}{\sqrt{E_g^2 + 4\gamma^2 k_\perp^2}} = 4 p_0 \gamma \frac{\vec{e}_\perp \cdot \vec{k}_\perp}{\sqrt{E_g^2 + 4\gamma^2 k_\perp^2}} \quad (6)$$

is recorded on the form. If we neglect the contribution of the coherent saturation effect, then the squared modulus of the composite matrix element will be written as

$$|M_{cV}^{(1)}(\vec{k})|^2 = \left(\frac{eA_0}{\hbar c} \right)^2 p_0^2 \frac{E_g^2 + 2\gamma^2 k_\perp^2}{E_g^2 + 4\gamma^2 k_\perp^2} \left[e_\perp^2 - 2 \frac{\gamma^2 k^2}{E_g^2 + 2\gamma^2 k_\perp^2} (e_x^2 - e_y^2) \right], \quad (7)$$

Interband two-photon optical transitions. In the general case, two-photon interband optical transitions occur in two stages: at the first stage - interband single-photon optical transitions, then intraband single-photon optical transitions (and vice versa at the second stage) [12]. Then the matrix element of the two-photon optical transition has the form

$$M_{cV}^{(2)}(\vec{k}_\perp, \vec{e}) = \left(\frac{eA_0}{m_0 c} \right)^2 \left\{ \frac{(\vec{e} \cdot \vec{p})_{cc} (\vec{e} \cdot \vec{p})_{cV}}{E_c(\vec{k}_\perp) - E_V(\vec{k}_\perp) - \hbar\omega} - \frac{(\vec{e} \cdot \vec{p})_{cV} (\vec{e} \cdot \vec{p})_{VV}}{\hbar\omega} \right\}, \quad (8)$$

If we take into account the law of conservation of energy for a given optical transition, then

$$M_{cV}^{(2)}(\vec{k}_\perp, \vec{e}) = \left(\frac{eA_0}{m_0 c} \right)^2 \frac{(\vec{e} \cdot \vec{p})_{cc} - (\vec{e} \cdot \vec{p})_{VV}}{\hbar\omega} (\vec{e} \cdot \vec{p})_{cV}. \quad (9)$$

Since the energy spectra of current carriers in the conduction band and valence band differ from each other in sign, the relation $(\vec{e} \cdot \vec{p})_{cc} = -(\vec{e} \cdot \vec{p})_{VV}$ is appropriate. Expression (9) takes into account $E_c(\vec{k}_\perp) - E_V(\vec{k}_\perp) - N\hbar\omega = 0$ relationships associated with N photon absorption of polarized light (from this relationship we obtain $k_\perp(\omega) = [(N\hbar\omega)^2 - E_g^2]^{1/2} / (2\gamma)$ expressions. Thus, $M_{cV}^{(2)}(\vec{k}_\perp, \vec{e})$ is determined by the relation

$$\frac{p_{cV}}{\hbar\omega} (p_{cc} - p_{vv}) = \frac{4}{\hbar\omega} \frac{\gamma p_0^2}{\sqrt{E_g^2 + 4\gamma^2 k_\perp^2}} \left(T_+^2 e_- - T_-^2 e_+ \frac{k_\perp^2}{k_\perp^2} \right) (e_+ \cdot k_- + e_- \cdot k_+), \quad (10)$$

where $T_\pm^2 = \left[(E_g^2 + 4\gamma^2 k_\perp^2)^{\frac{1}{2}} \pm E_g \right] / \left[2(E_g^2 + 4\gamma^2 k_\perp^2)^{\frac{1}{2}} \right]$, also here the squared modulus of the value $M_{cV}^{(2)}(\vec{k}_\perp, \vec{e})$ is determined by the expression

$$\left(\frac{4}{\hbar\omega} p_0 \gamma \frac{p_0}{\sqrt{E_g^2 + 4\gamma^2 k_\perp^2}} \right)^2 (\Re_{cV}^{(1)} + \Re_{cV}^{(2)} + \Re_{cV}^{(3)}), \quad (11)$$

where,

$$\Re_{cV}^{(1)} = 4T_-^4 k_\perp^2 e_\perp^2 (2e_x k_x + e_y k_y)^2, \quad \Re_{cV}^{(3)} = 4T_+^4 e_\perp^2 (e_x k_x + e_y k_y)^2,$$

$$\Re_{cV}^{(2)} = 8 \cdot T_+^2 \cdot (T_-^2 / k_\perp^2) \cdot [(k_x + k_y)e_x - (k_x k_y)e_y] \cdot [(k_x - k_y)e_x + (k_x + k_y)e_y] \cdot (e_y k_y + e_x k_x)^2.$$

Interband three-photon optical transitions. Now optical transitions involving three photons from the valence band to the conduction band (interband) occur according to the following scheme

$$(V, \vec{k}_\perp) \rightarrow (V, \vec{k}_\perp) \rightarrow (V, \vec{k}_\perp) \rightarrow (c, \vec{k}_\perp), \quad (V, \vec{k}_\perp) \rightarrow (V, \vec{k}_\perp) \rightarrow (c, \vec{k}_\perp) \rightarrow (c, \vec{k}_\perp), \\ (V, \vec{k}_\perp) \rightarrow (c, \vec{k}_\perp) \rightarrow (c, \vec{k}_\perp) \rightarrow (c, \vec{k}_\perp), \quad (V, \vec{k}_\perp) \rightarrow (c, \vec{k}_\perp) \rightarrow (V, \vec{k}_\perp) \rightarrow (c, \vec{k}_\perp).$$

Then the matrix element of interband three-photon optical transitions is represented as

$$M_{cV}^{(3)}(\vec{k}_\perp, \vec{e}) = \frac{(\vec{e} \cdot \vec{p})_{cV}}{4(\hbar\omega)^2} \{2[(\vec{e} \cdot \vec{p})_{cc}^2 + (\vec{e} \cdot \vec{p})_{VV}^2] - 4(\vec{e} \cdot \vec{p})_{cc}(\vec{e} \cdot \vec{p})_{VV} - (\vec{e} \cdot \vec{p})_{cV}(\vec{e} \cdot \vec{p})_{Vc}\}.$$

Then the square of the modulus of the two-photon optical transition ($|M_{cV}^{(3)}(\vec{k}_\perp, \vec{e})|^2$):

$$|M_{cV}^{(3)}(\vec{k}_\perp, \vec{e})|^2 = \left(\frac{eA_0}{m_0c}\right)^6 \frac{\gamma^6 m_0^6}{16\hbar^6 (\hbar\omega)^4 k_\perp^2 (E_g^2 + 4\gamma^2 k_\perp^2)^2} (\mathfrak{R}_{41} + \mathfrak{R}_{42} \mathfrak{R}_{43}). \quad (12)$$

here,

$$\mathfrak{R}_{41} = \left(T_-^2 k_\perp^4 e_\perp^2 - 2\left((e_x^2 - e_y^2)(k_x^2 - k_y^2) + 4k_x k_y e_x e_y\right) k_\perp^2 T_+^2\right) (E_g^2 + 4\gamma^2 k_\perp^2) T_-^2,$$

$$\mathfrak{R}_{42} = \left(T_+^4 (4\gamma^2 k_\perp^2 + E_g^2) e_\perp^2 - 128\gamma^2 (e_x^2 k_x^2 + k_y^2 e_y^2) - 256\gamma^2 k_x k_y e_x e_y\right) k_\perp^4,$$

$$\mathfrak{R}_{43} = \left[T_-^4 k_\perp^2 e_\perp^2 - 2T_+^2 T_-^2 k_\perp^2 \left((e_x^2 - e_y^2)(k_x^2 - k_y^2) + 4k_x k_y e_x e_y\right) + T_+^4 k_\perp^4 e_\perp^2\right].$$

CONCLUSIONS

Through this analysis, we have derived matrix element expressions for single-, two-, and three-photon optical transitions between the spin states of the conduction and valence bands. These expressions enable the classification of optical transitions based on the angle between the polarization vectors and wave vectors of the charge carriers, as well as on the band parameters specific to monolayers of transition metal dichalcogenides. Furthermore, they allow for the determination of the spectral and temperature dependences of the coefficients for single- and multi-photon interband absorption of light and linear-circular dichroism. These aspects will be thoroughly investigated in subsequent work.

The theory of nonlinear absorption of polarized radiation in two-dimensional, atomically thin layers of transition metal dichalcogenides has been advanced. It is important to highlight that excluding the effects of coherent saturation from the analysis of interband single-photon absorption of polarized radiation [11] reveals that linear-circular dichroism does not manifest in atomically thin metal dichalcogenides. This observation is attributed to the fact that, under these conditions, the probabilities of single-photon optical transitions are independent of the polarization states of light.

ORCID

✉ Rustam Y. Rasulov, <https://orcid.org/0000-0002-5512-0654>; ✉ Voxob R. Rasulov, <https://orcid.org/0000-0001-5255-5612>
 ✉ Bakhodir B. Akhmedov, <https://orcid.org/0000-0003-4894-3588>; ✉ Makhliyo A. Mamatova <https://orcid.org/0000-0001-6980-9877>

REFERENCES

- [1] K.S. Novoselov, A.K. Geim, S.V. Morozov, D.E. Jiang, Y. Zhang, S.V. Dubonos, I.V. Grigorieva, and A.A. Firsov, “Electric field effect in atomically thin carbon films,” *science*, **306**(5696), 666-669 (2004). <https://doi.org/10.1126/science.1102896>
- [2] N. Huo, Y. Yang, Y.N. Wu, X.G. Zhang, S.T. Pantelides, and G. Konstantatos, “High carrier mobility in monolayer CVD-grown MoS₂ through phonon suppression,” *Nanoscale*, **10**(31), 15071-15077 (2018). <https://doi.org/10.1039/C8NR04416C>
- [3] A. Taffelli, S. Dirè, A. Quaranta, and L. Pancheri, “MoS₂ based photodetectors: a review,” *Sensors*, **21**(8), 2758 (2021). <https://doi.org/10.3390/s21082758>
- [4] G.H. Shin, C. Park, K.J. Lee, H.J. Jin, and S.Y. Choi, “Ultrasensitive phototransistor based on WSe₂-MoS₂ van der Waals heterojunction,” *Nano Letters*, **20**(8), 5741-5748 (2020). <https://doi.org/10.1021/acs.nanolett.0c01460>
- [5] T. Wang, F. Zheng, G. Tang, J. Cao, P. You, J. Zhao, and F. Yan, “2D WSe₂ flakes for synergistic modulation of grain growth and charge transfer in tin-based perovskite solar cells,” *Advanced Science*, **8**(11), 2004315 (2021). <https://doi.org/10.1002/advs.202004315>
- [6] S.H. Su, W.T. Hsu, C.L. Hsu, C.H. Chen, M.H. Chiu, Y.C. Lin, W.-H. Chang, al., “Controllable synthesis of band-gap-tunable and monolayer transition-metal dichalcogenide alloys,” *Frontiers in Energy Research*, **2**, 104870 (2014). <https://doi.org/10.3389/fenrg.2014.00027>
- [7] C. Ernan-des, L. Khalil, H. Almabrouk, D. Pierucci, B. Zheng, J. Avila, P. Dudin, et al., “Indirect to direct band gap crossover in two-dimensional WS₂(1-x)Se_{2x} alloys,” *npj 2D Mater. Appl.* **5**(1), 7 (2021). <https://doi.org/10.1038/s41699-020-00187-9>
- [8] E.L. Ivchenko, *Optical Spectroscopy of Semiconductor Nanostructures*, (Alpha Science International Ltd., Harrow, UK, 2005).
- [9] R.Y. Rasulov, V.R. Rasulov, N.Z. Mamadaliyeva, and R.R. Sultanov, “Subbarrier and Overbarrier Electron Transfer through Multilayer Semiconductor Structures,” *Russian Physics Journal*, **63**, 537-546 (2020). <https://doi.org/10.1007/s11182-020-02067-7>
- [10] M.M. Glazov, *Electron and Nuclear Spin Dynamics in Semiconductor Nanostructures*, (Oxford University Press, Oxford, 2018). <https://doi.org/10.13140/RG.2.2.18718.56640>
- [11] V.R. Rasulov, R.Ya. Rasulov, and I. Eshboltaev, “Linearly and circular dichroism in a semiconductor with a complex valence band with allowance for four-photon absorption of light,” *Physics of the Solid State*, **59**(3), 463-468 (2017). <https://doi.org/10.1134/S1063783417030283>
- [12] R. Rasulov, V. Rasulov, and I. Eshboltaev, “On the Theory of the Ballistic Linear Photovoltaic Effect in Semiconductors of Tetrahedral Symmetry Under Two-Photon Absorption,” *Russian Physics Journal*, **59**, 92-98 (2016). <https://doi.org/10.1007/s11182-016-0742-7>

ОДНО-ТА БАГАТОФОТОННІ ОПТИЧНІ ПЕРЕХОДИ В АТОМНО ТОНКИХ ШАРАХ ДИХАЛЬКОГЕНІДІВ ПЕРЕХІДНИХ МЕТАЛІВ**Рустам Я. Расулов^a, Вокхоб Р. Расулов^a, Камолахон К. Урінова^b, Махліс А. Маматова^a, Баходір Б. Ахмедов^a**^a *Ферганський державний університет, Фергана, Узбекистан*^b *Кокандський державний педагогічний інститут, Коканд, Узбекистан*

У статті обговорюється виробництво та властивості двовимірних атомних шарів дихалькогенідів перехідних металів (ТМД) з акцентом на оптичних властивостях моношарів. Він починається зі вступу до відкриття методів виробництва графену та подальшого інтересу до ТМД. Деталізовано основні властивості моношарів ТМД, їх кристалічну структуру та зону Бріллюена. У статті досліджено енергетичний спектр електронів у різних долинах та ефективний гамільтоніан, що описує стани в паралельних спінових зонах. Обговорення поширюється на матричні елементи міжзонних оптичних переходів, включаючи одно-, дво- та трифотонні переходи. Наведено рівняння для розрахунку ймовірностей оптичних переходів, включаючи такі фактори, як вектор поляризації, частота світла та температура зразка. Викладено теоретичний аналіз складових матричних елементів для цих переходів, наголошуючи на квантово-механічних аспектах. Стаття сприяє дослідженню оптичної поведінки моношарів дихалькогенідів перехідних металів (ТМД), зокрема в структурах складного складу.

Ключові слова: *поляризований фотон; матричний елемент; оптичні переходи; двозонне наближення; носії струму; електронний Гамільтоніан; оператор імпульсу; спінові стани*

THERMOGRAPHIC METHOD OF ACTIVATED CARBON PACKING QUALITY DIAGNOSTICS IN NPP AIR FILTERS

 Mykola Azarenkov^{a,b},  Volodymyr Lytvynenko^{c*},  Ivan Kolenov^{c,d},  Oleksii Haluza^{e,f},
 Anatoly Chupikov^a,  Volodymyr Sokolenko^a,  Olena Roskoshna^a,
 Mariya Kanishcheva^a,  Valeriy Shatov^c

^a National Science Center "Kharkiv Institute of Physics and Technology", 1, Akademichna St., Kharkiv, 61108, Ukraine

^b V.N. Karazin Kharkiv National University, sq. Svobody, 4, Kharkiv, 61022, Ukraine

^c Institute of Electrophysics & Radiation Technologies of NAS of Ukraine, 28, Chernyshevsky St., Kharkiv, 61002, Ukraine

^d O.Ya. Usikov Institute for Radiophysics and Electronics of NAS of Ukraine, 12, Ac. Proskura St., Kharkiv, 61085, Ukraine

^e National Technical University "Kharkiv polytechnic institute", 2, Kyrpychova St., Kharkiv, 61002, Ukraine

^f Kharkiv National University of Radio Electronics, 14, Nauky Ave., Kharkiv, 61166, Ukraine

*Corresponding Author e-mail: vvlytvynenko@ukr.net

Received November 1, 2023; revised December 7, 2023; accepted December 12, 2023

The work is devoted to the tasks of safe operation of nuclear power plants, namely the prevention of inert radioactive gases, iodine, and its compounds from entering the air. The latter is particularly dangerous because it can accumulate in the human body. One of the methods of air purification is the use of air filters filled with activated carbon granules that have undergone preliminary treatment of thermal expansion and impregnation. At the same time, there is a problem with evaluating the change in local aerodynamic resistance as a result of the shape change of granules and their compaction when activated carbon is filled into the filter. For this purpose, the model that calculates the spatial field of movement of ventilation gases through a chamber that simulates an adsorber of the AU-1500 type filled with carbon granules was created. To verify the model, it was necessary to develop approaches to the assessment of the topology of the intergranular space and to draw up ideas about the possible inhomogeneities of such topology due to inhomogeneities in the compaction of granules during backfilling and vibration effects during operation. Therefore, an experimental model based on the assumption that air passage channels are spatially contiguous with electric current passage channels if a potential difference is applied to the "input-output" sections was proposed. Clusters of areas with heterogeneous packing by measuring the temperature distribution, which is released in the form of Joule heat were identified. Correlations between the characteristics of the spread of temperature fields and modes of current trans-mission have been established. It is shown that the obtained experimental data correlate with theoretical calculations of the flow of ventilation gases. The created set of methods allows optimization of the aerodynamic characteristics of the filter to improve their functional properties.

Keywords: Thermography; Air filters; Active carbon; Air flow; Current distribution

PACS: 87.63.Hg, 81.05.U.

INTRODUCTION

The development of technology, industry, and energy security is a key factor in raising people's living standards [1-3]. A lot of attention is paid to the prevention of environmental pollution and, a large number of effective technologies have been developed to reduce the level of pollution, including from industrial enterprises. Thus, one of the components of any industrial enterprise is such engineering structures as ventilation systems, which ensure the necessary sanitary standards in production premises, labor protection, and compliance with the norms of emissions into the environment [3-7]. Particular attention is paid to ventilation systems as the main source of emissions harmful to human health and the environment, industrial waste generated in the chemical, mining, construction, and energy industries, including nuclear [3].

The operation of nuclear power plants is necessarily associated with the need to control emissions and filter radioactive gases. Gaseous isotopes formed by nuclear reactions penetrate through imperfect seals and lead to increased radiation background in the working premises, the danger of which is that radioactive substances can penetrate the human body via the respiratory organs. Since it is impossible to avoid the release of radioactive gases in the first circuit with their subsequent entry into the working premises and then into the environment, iodine, and aerosol filters are used at the stations, which reduce the radiation load by several orders of magnitude. One of the ways iodine enters the coolant and its further spread is the destruction of the shells of heat-dissipating elements due to the manufacturing defects that develop as a result of the passage of high-energy particles, which causes local heating along the track and, as a result, delamination of the material [8, 9]. It is worth noting that even in the conditions of a cold shutdown of NPP power units, due to the fission of ²³⁵U, iodine isotopes are released and penetrate through discontinuities in the shells of nuclear fuel elements into the coolant and then into the environment. Also, the problem of identifying iodine compounds at the NPP, which was in a long-term shutdown is extremely non-trivial. In addition, the peculiarities of the distribution of the mentioned compounds in the conditions of an unprecedentedly long-term shutdown are almost unexplored. Problems

of identification of accumulated radionuclides in nuclear energy materials are solved by various methods, among which the most precise are nuclear physical ones [10].

A particular problem is cleaning air flows from radioactive fission products of fuel elements during nuclear power plants (NPP) operation. The main gaseous radioactive components in the air at NPP are isotopes of xenon and krypton, as well as radioactive iodine vapor [11-13]. The ^{131}I isotope (half-life 8.5 days) is particularly dangerous due to its ability to accumulate in the human body. Also, the permissible rate of volumetric activity of iodine in the air of premises of NPP with constant presence of personnel is $2 \cdot 10^{-12}$ Ci/l, and when air is released into the atmosphere at 1 operating unit of NPP – $2 \cdot 10^{-4}$ Ci/day [11]. One of the ways to clean the air from gaseous compounds of radioactive iodine is to trap them with sorption-filtering materials. In air emissions from nuclear reactors, radioactive iodine is contained in the form of aero-sols and gaseous compounds: vapors of molecular iodine (I_2), hydrogen iodide (HI), iodates, and various organic compounds, in particular, methyl iodide (CH_3I) [12-13]. In modern technology, to purify gases from radioactive iodine, various filtering and sorbing materials are used that are capable of capturing aero-dispersed and gaseous products of radioactive iodine. To capture iodine radionuclides in ventilation air flows at nuclear power plants, sorption bulk filters based on active carbons impregnated with various compounds are mainly used: iodides of various metals (K, Al, Zn, Pb, Sn, Ti, Ba); organic substances (derivatives of amines, phenol); silver and its compounds, as well as their mixtures [11-13].

One of the urgent tasks is to improve the operational properties of NPP sorption filters, in particular, the quality of filtration and increase the working life. Optimizing the operation of a ventilation system consists of finding a compromise between the cross-section of passage through the sorption material, sorption efficiency, and traction force of the blower. Many works are devoted to this issue [3, 14-19]. One of the ways to improve the above properties is to increase the uniformity of filling the filter layer (activated carbon granules) into the adsorber, which leads to a more uniform distribution of gas flow throughout the volume of the sorbent, more uniform wear, and, accordingly, an increase in service life. Therefore, to control the uniformity of the backfill of activated carbon granules, a simple method of non-destructive express testing is required. This work proposes a thermographic method for visualizing inhomogeneities in the backfill of activated carbon granules. The method is based on the assumption that the channels for the passage of air are spatially adjacent to the channels for the passage of electric current if a potential difference is applied to the "input-output" sections. Clusters of areas with inhomogeneous packing can be identified by measuring the distribution of the temperature released in the form of Joule heat. Next, we consider the research methods used in this work.

METHODS OF THEORETICAL AND EXPERIMENTAL RESEARCH

To evaluate the capabilities of the proposed thermographic method for diagnosing the quality of the packaging of activated carbon granules and its influence on the distribution of airflow passing through it, computer modeling and comparison of 2 processes in the filter were carried out: 1) distribution of airflow in a carbon filter with homogeneous and non-uniform packaging of granules, 2) distribution of current density and temperature in a carbon filter with homogeneous and non-uniform packing of granules. Next, we will consider the theoretical basis for calculating airflow through a porous medium.

Method for calculating airflow through a sorbent layer

The sorbent layer is a bath (basket) filled with activated carbon granules. In this work, activated carbon granules were used in the form of cylinders with a diameter of 4 mm and a length of 4-8 mm.

To select the correct mathematical airflow model, it is necessary to predict its nature (laminar or turbulent). To predict the nature of the airflow, a dimensionless value is used - the Reynolds number (Re). Re is the ratio of the inertial forces to the viscous force [20]. If $Re < Re_{cr}$ then the flow is laminar, but if $Re > Re_{cr}$ then the flow becomes turbulent. The Re_{cr} threshold value depends on the flow geometry. For a porous medium consisting of porous granules it is equal to:

$$Re = \frac{\rho v_s D_p}{(1-\varepsilon)\mu}, \quad (1)$$

where ρ is the airflow density, v_s is the superficial velocity (the ratio of the volumetric flow rate of the phase to the cross-sectional area), D_p is the cylinder diameter, μ is the dynamic viscosity of the flow, ε is the porosity of the granule.

The main characteristics of the porous medium state are the porosity ε_p and the permeability k . When calculating the porosity of a packed medium, the porosity of granules can be neglected and only the intergranular space can be taken into account [21, 22]:

$$\varepsilon_p = \frac{A}{(D_v/D_p)^n} + B, \quad (2)$$

where for cylindrical granules $A = 0.9198$, $B = 0.3414$, $n = 2$, D_v is the filter diameter, D_p is the granule diameter. Work [18] provides formulas for calculating the porosity of packages for granules of various shapes. The formula for estimating the permeability of a porous medium is as follows [23]:

$$k = \varphi_s^2 \frac{\varepsilon_p^2 D_p^2}{180(1-\varepsilon_p)^2}, \quad (3)$$

where φ_s is a parameter that takes into account the geometry of the granules.

The concept of the above characteristics and parameters was formulated by Henry Darcy. Darcy's experiments [20] showed that the total flow rate is directly proportional to the total pressure drop divided by the flow viscosity and the permeability of the medium. Darcy's law is widely used for laminar flow, i.e. in cases where $Re < 2000$. In our case, $Re = 3500$, i.e. the flow is turbulent. The equations used for transient and turbulent flow are derived from the basic Darcy equations. This work uses the Brinkman equation [24], which is widely used to analyze transitional flow in porous bulk media. The dependent variables in the Brinkman equations are Darcy's velocity and pressure. Flow in porous media is determined by a combination of the continuity equation and the momentum equation, which together form the Brinkmann equations:

$$\frac{\partial}{\partial t}(\varepsilon_p \rho) + \nabla \cdot (\rho \mathbf{u}) = Q_m, \tag{4}$$

$$\frac{\rho}{\varepsilon_p} \left(\frac{\partial \mathbf{u}}{\partial t} + \frac{1}{\varepsilon_p} (\mathbf{u} \cdot \nabla) \mathbf{u} \right) = -\nabla p + \nabla \cdot \left[\frac{1}{\varepsilon_p} \left\{ \mu (\nabla \mathbf{u} + (\nabla \mathbf{u})^T) - \frac{2}{3} \mu (\nabla \cdot \mathbf{u}) \mathbf{I} \right\} \right] - \left(\frac{\mu}{\kappa} + \frac{Q_m}{\varepsilon_p^2} \right) \mathbf{u} + \mathbf{F}, \tag{5}$$

where μ is the dynamic viscosity of the liquid, \mathbf{u} is the velocity vector, ρ is the flow density, p is pressure, ε_p is porosity, κ is the permeability of the porous medium, Q_m is the flow rate. To take into account the influence of gravity and other volumetric forces, the term \mathbf{F} is introduced.

Figure 1 shows the filter model, which was used to simulate the airflow through the sorbent layer.

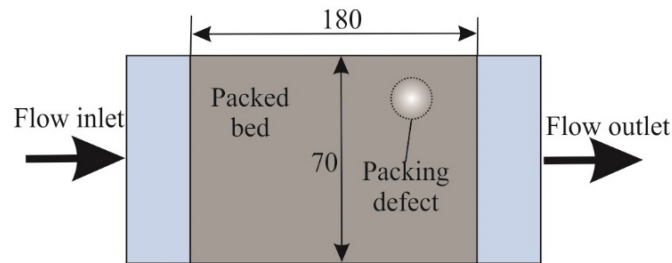


Figure 1. Schematic representation of the filter.

The model filter is a cylinder pipe with a diameter of 70 mm and a height of 240 mm. The flow inlet and outlet are at the beginning and at the end of pipe. Activated carbon granules are located in the middle part of the pipe. The layer thickness is 180 mm. The porosity and permeability calculated using formulas (2) and (3) were 0.3414 and $1.67 \cdot 10^{-8} \text{ m}^2$, respectively. Next, we will consider a method for calculating the distributions of current densities and the release of Joule heat in the sorbent layer.

Method for calculating the distribution of current densities and the release of Joule heat in the sorbent layer

When considering heat transfer in a porous medium at the microscopic level, two heat transfer equations can be established: for the solid and liquid phases. For undeformed stationary solids, the heat transfer equation has the form:

$$\rho C_p \frac{\partial T}{\partial t} - \nabla \cdot (k \nabla T) = \mathbf{J} \cdot \mathbf{E}, \tag{6}$$

where ρ is the density, C_p is the specific heat capacity at constant stress, T is the absolute temperature, the term $\mathbf{J} \cdot \mathbf{E}$ characterizes resistive heating (ohmic heating) due to the electric current, where \mathbf{J} is the current density and \mathbf{E} is the voltage electric field. This term also takes into account electromagnetic surface losses as a heat source.

Figure 2 shows the model according to which the current density and temperature distributions were calculated.

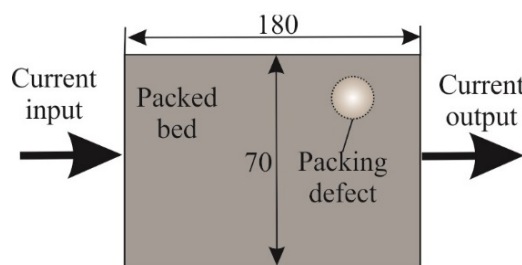


Figure 2. Scheme of passing current through the sorbent layer.

To visualize the distribution of airflow passing through the filter between the upper and lower parts of the sorbent, a potential difference is applied. Since both the distribution of airflow velocity and the distribution of current density are related to the quality of packaging (density) of the sorbent, these two parameters must correlate with each other. The correlation should also be displayed on sorbent thermograms and characterize the airflow distribution in the filter.

An experimental method for identifying inhomogeneity in AC granules packing in air filters.

For the experiment, a specialized cylindrical flask was constructed, shown in Figure 3a. Activated carbon granules 4 were poured into flask 3, transparent to IR radiation. Next, the compaction procedure and fixation with covers 2 and 5 were carried out. At the same time, denser packing was ensured in the area of lid 5. The current was passed through contacts 1 and 6. Diameter d and height h of the layer of packaged activated carbon were 70 mm and 180 mm, respectively.

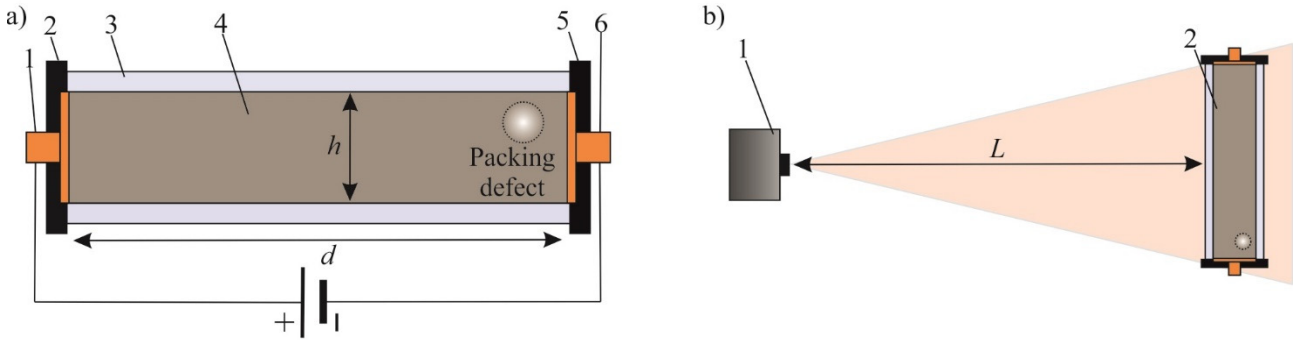


Figure 3. Schematic representation of the object under study (a): 1 – + power supply, 2 and 5 – covers, 3 – transparent flask for IR, 4 – activated carbon granules, 6 – – power supply. Experiment scheme (b): 1 – thermal imager, 2 – the object under study

The experimental scheme is shown in Figure 3b. The relative position of the thermal imager (1) and the sample (2) is shown in Figure 3b. A direct current was passed through the volume with activated carbon granules. As the volume warmed up, thermograms were recorded using a Fluke Ti31I thermal imager. Next, we consider the simulation and experimental results.

SIMULATION AND EXPERIMENTAL RESULTS.

To qualitatively illustrate the flow distribution in a layer of activated carbon, two packaging options were considered: 1) uniform packaging of activated carbon granules, and 2) non-uniform packaging with the decreased density of granules at the top right corner. The calculation results are shown in Figure 4.

Figure 4 shows that in the case of a homogeneous backfill, the flow is uniformly distributed over the entire cross-section of the filter. In the case of non-uniform packaging (Figure 4b), the airflow velocity is higher through an area of lower density and lower through the adjacent filter areas, which should lead to faster filter wear and deterioration in filtration quality. Next, we will consider the results of calculations with current passing through filters.

Two cases with uniform and non-uniform packaging of activated carbon granules in the filter were also considered. In the case of uniform packaging, the electrical conductivity is the same throughout the entire cross-section of the filter. A decrease in packaging density should lead to a decrease in electrical conductivity due to a decrease in the number of contacts between granules. Therefore, in the second case is with gradually decreased conductivity in the top right corner, according to the same law as the packing density of activated carbon granules. The calculation results are shown in Figure 5.

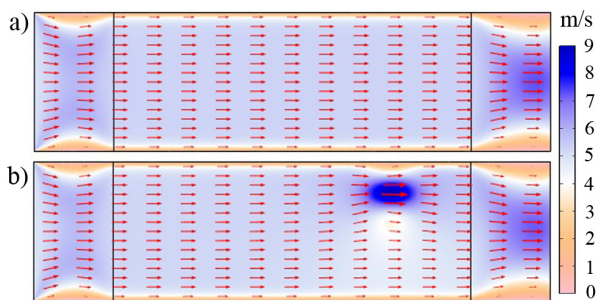


Figure 4. Results of modeling air flow with a uniform distribution of activated carbon granules (a) and with a non-uniform distribution of granules (b)

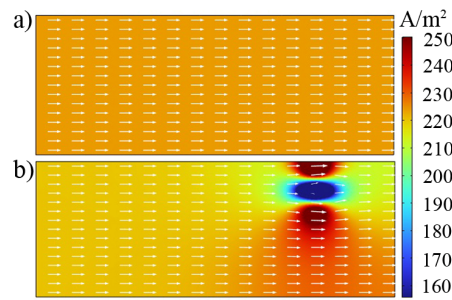


Figure 5. Results of modeling the current density distribution with a uniform distribution of activated carbon granules (a) and with a non-uniform distribution of granules (b)

Figure 5 shows that the current density decreased in the region with lower electrical resistance. Figure 6 shows the calculated thermograms of sections with a uniform distribution of granules (a) and with a reduced density of granules in the top right corner (b).

One can see from the figure that a region with a lower density will have a lower temperature compared to a denser packing. The low temperature around the perimeter of the sample is associated with heat exchange with the environment. Next, we consider the results of experimental studies.

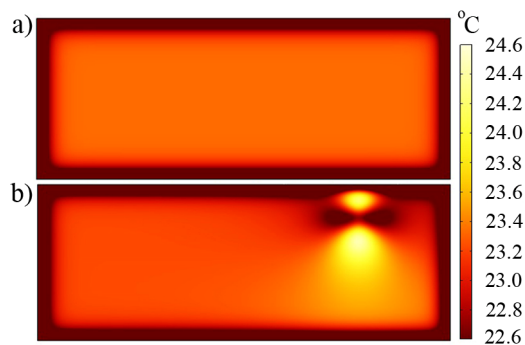


Figure 6. Results of modeling the temperature distribution in a filter with a uniform distribution of activated carbon granules (a) and in a filter with a non-uniform distribution of granules (b).

Figure 7a shows a thermogram of a flask filled with active carbon granules. Also, Fig. 7b shows temperature distribution profiles along lines C1 and C2 for better clarity.

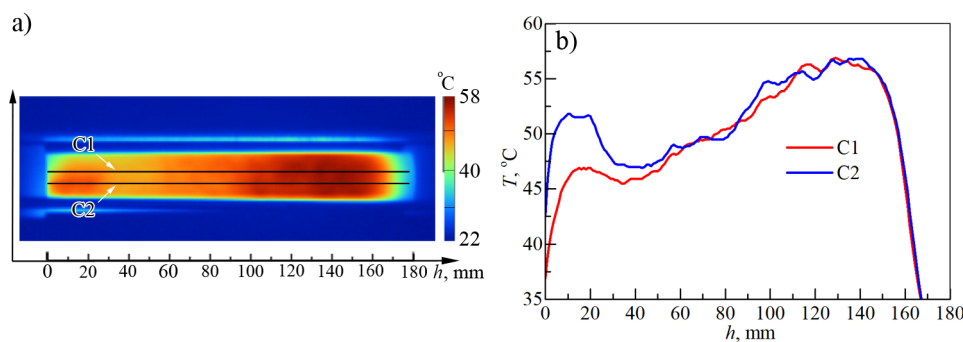


Figure 7. Thermogram of a flask filled with active carbon granules (a) and temperature distribution profiles along sections C1 and C2 (b)

One can see from the above thermogram, that a higher temperature is observed near one of the lids (where a denser package was created). At the same time, the heterogeneity of heating of the internal area is 4-10 °C (Fig. 7b). It is clear from the thermogram that a smaller contact area between the granules entails an increase in electrical resistance and a decrease in current density in these areas, as a result, these areas on the thermogram are colder. Closer contact of granules leads to a decrease in electrical resistance, an increase in current density, and heating of the sorbent area. Consequently, the greater the heating of the sorbent area, the less airflow this area can allow, which leads to uneven wear of the sorbent.

We will also consider thermograms depending on the heating time. Figure 8 shows thermograms taken at regular intervals (20 seconds).

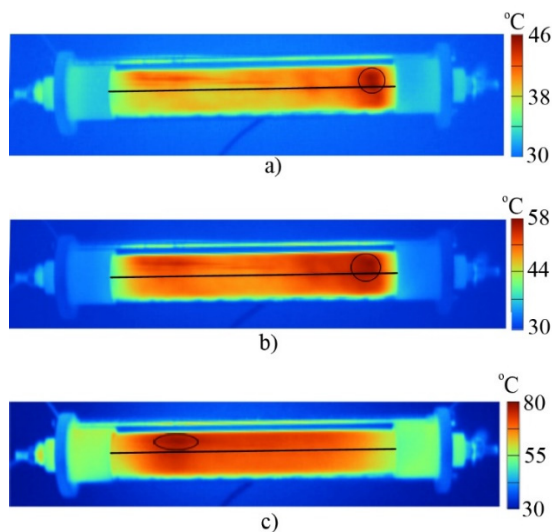


Figure 8. Experimental thermograms of the sample taken at time intervals of 20 seconds (a), 40 seconds (b), and 60 seconds (c)

It is clear from the figures that more heated regions in the samples can be identified (indicated by circles and ellipses), which indicates a higher current density in this region and, accordingly, a higher packing density. In Figure 8(a) and 8(b), the hotter region corresponds to the denser region. For better visualization of the temperature distribution, graphs of

temperature versus coordinate h were plotted (Figure 8). The sections are shown as solid lines in Figure 8 and were made in the center of the cylinders.

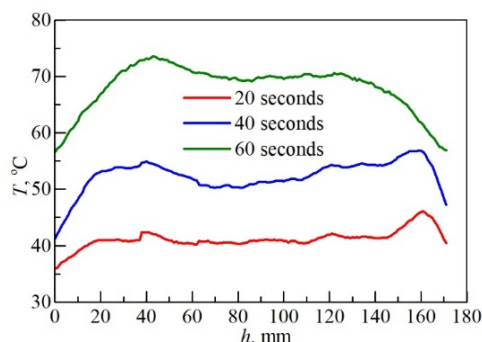


Figure 9. Temperature distributions in selected sample cross-sections for different heating times

Figure 9 shows that there is local temperature inhomogeneity at a length of 40 mm in all dependences. Local temperature inhomogeneity, corresponding to the created packing defect, is present at 160 mm when the sample is heated for 20 and 40 seconds. When heated for 60 seconds, this heterogeneity is not distinguishable, apparently due to a greater temperature gradient between the center of the sample and the body. It is worth noting that all graphs have a local minimum in the center. The temperature inhomogeneities described above are associated with the quality of packing of activated carbon granules and, as shown above, a higher temperature can characterize a denser packaging.

CONCLUSIONS

The work assessed the possibility of thermographic control of the uniformity of the packaging of activated carbon granules in the filter. The correlation between the distributions of gas flow, current density, and temperature is theoretically shown and experimentally confirmed. Thus, more air flows through a less dense area of the package, but a lower current density can flow, resulting in less heating.

The possibility of identifying areas with non-uniform packaging of activated carbon granules has been experimentally confirmed. It was found that the duration of heating affects the resolution of the method: prolonged heating leads to a decrease in the contrast of these areas.

The approach proposed in the work can be used to debug and control the process of packaging activated carbon granules in a filter, which will improve their performance characteristics. At the same time, the method has ample opportunities for further development.

Acknowledgements

The research presented in this article was financially supported by the Ukrainian government budget program «Government support for priority scientific research and scientific & technical (experimental) developments» (budget financial Code 6541230) and Simons Foundation Program: Presidential Discretionary-Ukraine Support Grants, Award No 1030287.

ORCID

- Mykola Azarenkov, <https://orcid.org/0000-0002-8628-9014>; Volodymyr Lytvynenko, <https://orcid.org/0000-0003-4850-2555>
 Ivan Kolenov, <https://orcid.org/0000-0002-1741-5195>; Oleksii Haluza, <https://orcid.org/0000-0003-3809-149X>
 Anatoly Chupikov, <https://orcid.org/0009-0002-7712-4194>; Volodymyr Sokolenko, <https://orcid.org/0000-0003-1821-4042>
 Olena Roskoshna, <https://orcid.org/0009-0006-4016-5071>; Mariya Kanishcheva, <https://orcid.org/0009-0002-3094-7628>
 Valeriy Shatov, <https://orcid.org/0009-0007-6908-0490>

REFERENCES

- [1] S. Gössling, C. Meyer-Habighorst, and A. Humpe, "A global review of marine air pollution policies, their scope and effectiveness." *Ocean Coast. Manag.* **212**, 105824 (2021). <https://doi.org/10.1016/j.ocecoaman.2021.105824>
- [2] H. Chen, B.G. Oliver, A. Pant, A. Olivera, P. Poronnik, C.A. Pollock, and S. Saad, "Effects of air pollution on human health – Mechanistic evidence suggested by in vitro and in vivo modelling," *Environ. Res.* **212** Part C, 113378 (2022). <https://doi.org/10.1016/j.envres.2022.113378>
- [3] L. Blankenship, and R. Mokaya, "Modulating the porosity of carbons for improved adsorption of hydrogen, carbon dioxide, and methane: a review," *Mater. Adv.* **3**(4), 1905-1930 (2022). <https://doi.org/10.1039/D1MA00911G>
- [4] A. Roy, C. Mishra, and N. Solanki, "A review of general and modern methods of air purification," *J. Therm. Eng.* **5**, 22-28 (2018). <http://dx.doi.org/10.18186/thermal.529054>
- [5] G. Peters, R. Andrew, J. Canadell, S. Fuss, R. Jackson, J.I. Korsbakken, C. Le Quéré, and N. Nakicenovic, "Key indicators to track current progress and future ambition of the Paris Agreement," *Nat. Clim. Change* **7**, 118-122 (2017). <https://doi.org/10.1038/nclimate3202>
- [6] C. Lin, R. He, and W. Liu, "Considering multiple factors to forecast CO2 emissions: a hybrid multivariable forecasting and genetic programming approach," *Energies* **11**, 3432 (2018). <http://dx.doi.org/10.3390/en11123432>
- [7] A.M.F. Mohammed, I.A. Saleh, Y.H. Ibrahim, and N.R.G. Mohamed, "Theory and technology of air filtration: review," *Material Sci & Eng.* **6**(1), 6-12 (2022). <https://medcraveonline.com/MSEIJ/MSEIJ-06-00173.pdf>

- [8] A.Yu. Didyk, V.I. Slisenko, P.A. Selishchev, and A.Yu. Lyashenko, "Change in sample surface area during formation of cylindrical tracks as a result of high-energy heavy-ion irradiation," *Metallofiz. Noveishie Tekhnol.* **32(3)**, 357–363 (2010).
- [9] V.I. Slisenko, O.E. Zoteev, O.A. Vasylykevych, V.O. Zoteev, and V.V. Krotenko, "The Dynamics of Crystal Lattice of Solid Solutions Based on Zirconium Dioxide," *J. Phys. Stud.* **25(4)**, 4601-1-4601-6 (2021). <https://doi.org/10.30970/jps.25.4601>
- [10] V.A. Zheltonozhsky, D.E. Myznikov, V.I. Slisenko, M.V. Zheltonozhskaya, and A.P. Chernyaev, "Determination of the long-lived ¹⁰Be in construction materials of nuclear power plants using photoactivation method," *J. Environ. Radioact.* **227**, 106509 (2021). <https://doi.org/10.1016/j.jenvrad.2020.106509>
- [11] Strategy for the management and disposal of used nuclear fuel and high-level radioactive waste. U.S. Department of Energy, Washington DC, (2013).
- [12] S.U. Nandanwar, K. Coldsnow, V. Utgikar, P. Sabharwall, and D.E. Aston, "Capture of harmful radioactive contaminants from off-gas stream using porous solid sorbents for clean environment – A review," *Chem. Eng. J.* **306**, 369-381 (2016). <https://doi.org/10.1016/j.cej.2016.07.073>
- [13] B. Riley, J. Vienna, J. McCloy, and J. Jerden, "Materials and processes for the effective capture and immobilization of radioiodine: A review," *J. Nucl. Mater.* **470**, 307-326 (2016). <https://doi.org/10.1016/j.jnucmat.2015.11.038>
- [14] M. Yadollahi, H. Hamadi, and V. Nobakht, "Capture of iodine in solution and vapor phases by newly synthesized and characterized encapsulated Cu₂O nanoparticles into the TMU-17-NH₂ MOF," *J. Hazard. Mater.* **399**, 122872 (2020). <https://doi.org/10.1016/j.jhazmat.2020.122872>
- [15] J. Zhou, S. Hao, and Y. Zhang, "Study on adsorption performance of coal based activated carbon to radioactive iodine and stable iodine," *Ann. Nucl. Energy* **72**, 237-241 (2014). <https://doi.org/10.1016/j.anucene.2014.05.028>
- [16] H. Zhu, B. Wang, W. Zhu, T. Duan, G. He, Y. Wei, D. Sun, and J. Zhou, "Space and structure activation of collagen fiber for high efficient capture iodine in off-gas," *Colloids Surf. A: Physicochem. Eng.* **617**, 126389 (2021). <https://doi.org/10.1016/j.colsurfa.2021.126389>
- [17] A. Belyaeva, A.A. Galuza, V.F. Klepikov, V.V. Litvinenko, A.G. Ponomarev, M.A. Sagajdachny, K.A. Slatin, et al., "Spectral ellipsometric complex for early diagnostics of metall and alloy transformations," *Probl. At. Sci. Technol.* **2(60)**, 191-197 (2009). https://vant.kipt.kharkov.ua/ARTICLE/VANT_2009_2/article_2009_2_191.pdf (in Russian)
- [18] A.I. Belyaeva, A.A. Galuza, I.V. Kolenov, and A.A. Savchenko, "Multipurpose optical setup for studying radiation-induced transformations of metals and alloys surface," *PAST*, **2(90)**, 174-179 (2014). https://vant.kipt.kharkov.ua/ARTICLE/VANT_2014_2/article_2014_2_174.pdf
- [19] E.M. Prohorenko, V.F. Klepikov, V.V. Lytvynenko, N.I. Bazaleev, T.G. Prohorenko, and A.I. Morozov, "Application of IR-radiometric diagnostic for control of vacuum connections of electrophysical installation," *Probl. At. Sci. Technol.* **1(113)**, 212-217 (2018). https://vant.kipt.kharkov.ua/ARTICLE/VANT_2018_1/article_2018_1_212.pdf
- [20] V. Pozzobon, J. Colin, and P. Perre, "Hydrodynamics of a packed bed of non-spherical poly-disperse particles: A fully virtual approach validated by experiments," *Chem. Eng. J.* **354**, 126-136 (2018), <https://doi.org/10.1016/j.cej.2018.07.214>
- [21] A.S. Pushnov, "Calculation of average bed porosity," *Chem. Petrol. Eng.* **42**, 14–17 (2006). <https://doi.org/10.1007/s10556-006-0045-x>
- [22] W. Zhang, K.E. Thompson, A.H. Reed, and L. Beenken, "Relationship between packing structure and porosity in fixed beds of equilateral cylindrical particles," *Chem. Eng. Sci.* **61(24)**, 8060-8074 (2006). <https://doi.org/10.1016/j.ces.2006.09.036>
- [23] R. Chhabra, and M.G. Basavaraj, editors, *Coulson and Richardson's Chemical Engineering Volume 2a: Particulate Systems and Particle Technology*, (Butterworth-Heinemann, 2019).
- [24] F.J. Valdes-Parada, J.A. Ochoa-Tapia, and J. Alvarez-Ramirez, "On the effective viscosity for the Darcy–Brinkman equation," *Physica A*, **385(1)**, 69-79 (2007). <https://doi.org/10.1016/j.physa.2007.06.012>

ТЕРМОГРАФІЧНИЙ МЕТОД ДІАГНОСТИКИ ЩІЛЬНОСТІ ЗАСІПКИ АКТИВОВАНОГО ВУГІЛЛЯ В ПОВІТРЯНИХ ФІЛЬТРАХ АЕС

Микола Азаренков^{a,b}, Володимир Литвиненко^c, Іван Коленов^{c,d}, Олексій Галуза^{c,f}, Анатолій Чупіков^a, Володимир Соколенко^a, Олена Роскошна^a, Марія Канишева^a, Валерій Шатов^c

^a Національний науковий центр "Харківський фізико-технічний інститут", вул. Академічна 1, Харків, 61108, Україна

^b Харківський національний університет імені В.Н. Каразіна, майдан Свободи 4, Харків, 61022, Україна

^c Інститут електрофізики і радіаційних технологій НАН України, вул. Чернишевська 28, Харків, 61002, Україна

^d Інститут радіофізики та електроніки ім. О.Я. Усикова НАН України, вул. Академіка Проскури 12, Харків, 61085, Україна

^e Національний технічний університет "Харківський політехнічний інститут", вул. Кирпичова 2, Харків, 61002, Україна

^f Харківський національний університет радіоелектроніки, пр. Науки 14, Харків, 61166, Україна

Робота присвячена задачам безпечної експлуатації атомних електростанцій, а саме запобіганню потрапляння в повітря інертних радіоактивних газів, йоду та його сполук. Останній особливо небезпечний, оскільки може накопичуватися в організмі людини. Одним із способів очищення повітря є використання повітряних фільтрів, наповнених гранулами активованого вугілля, які пройшли попередню обробку термічного розширення та імпрегування. Водночас виникає проблема оцінки зміни локального аеродинамічного опору внаслідок зміни форми гранул та їх ущільнення при засипці активованого вугілля у фільтр. Для цього створено модель, що розраховує просторове поле руху вентиляційних газів через камеру, що імітує адсорбер типу АУ-1500, наповнений гранулами активованого вугілля. Для верифікації моделі необхідно було розробити підходи до оцінки топології міжзернового простору та сформулювати уявлення про можливі неоднорідності такої топології через неоднорідності ущільнення гранул під час засипки та вібраційних впливів під час експлуатації. Тому була запропонована експериментальна модель, заснована на припущенні, що повітряні канали просторово суміжні з каналами проходження електричного струму, якщо різниця потенціалів прикладена до ділянок «вхід-вихід». Кластери областей з неоднорідною упаковкою шляхом вимірювання розподілу температури, яка виділяється у вигляді джоулева тепла, були виявлені. Встановлено кореляції між характеристиками поширення температурних полів і режимами пропускання струму. Показано, що отримані експериментальні дані корелюють з теоретичними розрахунками потоку вентиляційних газів. Створений комплекс методів дозволяє оптимізувати аеродинамічні характеристики фільтрів для покращення їх функціональних властивостей.

Keywords: термографія; повітряні фільтри; активоване вугілля; потік повітря; розподіл струму

IDENTIFICATION OF HEAVY METAL POLLUTION SOURCES ON THE TERRITORY ADJACENT TO THE NSC OF “KHARKIV INSTITUTE OF PHYSICS & TECHNOLOGY” BY PMF METHOD

 **Maryna F. Kozhevnikova***,  **Volodymyr V. Levenets**,  **Oleksii Yu. Lonin**,
 **Oleksandr P. Omelnik**,  **Andriy O. Shchur**

NSC “Kharkiv Institute of Physics & Technology” NASU,
1, Academichna str., 61108, Kharkiv, Ukraine

*Corresponding Author e-mail: marko@kipt.kharkov.ua

Received November 7, 2023; revised January 25, 2024; accepted January 30, 2024

In this paper the content of heavy metals at the territory of Pyatihatki settlement, where the National Scientific Center Kharkiv Institute of Physics & Technology (NSC KIPT) is located. The nuclear-physical methods were used to determine the content of chemical elements in the soil samples taken in 30 points at the territory of Pyatihatki settlement in 2011-2021. The elemental analysis was carried out on the analytical nuclear-physical complex "Sokol". The methods, based on registration of characteristic X-ray radiation of atoms and γ -radiation of nuclei excited by accelerated protons, were used. After the measurements completion, the data arrays on the content of 15 chemical elements (N, Na, S, Cl, K, Ca, Ti, Mn, Fe, Cu, Zn, Zr, Br, Sr, Pb) in the soil samples were obtained. The data arrays processing was carried out using the EPA (Environmental Protection Agency) PMF v3.0.2.2.2 software based on the application of the PMF (Positive matrix factorisation) algorithm. ArcView 3.2a was chosen as the basic software product for the analysis of spatial distribution of the major polluting chemical elements. As a result of the performed work, the pollution sources, which have an impact on the territory near the NSC KIPT, have been identified. The source of the soil pollution is the autostrades, among which the road around the city Kharkiv stands out, where an increase in the content of Pb, Sr, Zr, Cr and Cu was detected. A source of chromium contamination, located presumably to the north-east of Pyatihatki settlement, was identified. The analyses of the obtained data showed that the PMF method allows to identify the factors that affect the soil contamination, and to determine the presumptive sources of pollution with the help of wind rose.

Keywords: Heavy metals; Elemental analysis; Characteristic X-ray radiation; Positive matrix factorization; Method of principal component analysis (PCA)

PACS: 89.60.Gg, 89.60-k

INTRODUCTION

A serious environmental problem over the last century has been the intensive development of industry and transport complex, which are the most powerful sources of biosphere pollution. The soil is a poorly migrating medium, which is exposed to heavy metal pollution every day. According to WHO, up to 95% of heavy metals together with the products of plant and animal origin enter the human body through the trophic chains [1].

The soil protection from the pollution is an important problem, since any harmful compounds in the soil, sooner or later, get into the human body. First, there is a constant washing out of contaminants into open water bodies and ground waters, which can be used by people for drinking and other needs. Second, these contaminants from the soil moisture, groundwater and open water bodies get into the organisms of animals and plants that use this water, and then through the food chains again get into the human body. Third, many compounds that are harmful to the human body have the ability to accumulate in tissues, and, above all, in bones [1].

The heavy metals and their compounds form a significant group of toxins, which makes the anthropogenic impact on the ecological structure of the environment and on the humans themselves. First of all, those metals that are most widely and in significant amounts used in human production activities and, as a result of their accumulation in the external environment, pose a serious danger in respect to their biological activity and toxic properties, are of interest. They include Pb, Hg, Cd, Zn, Bi, Co, Ni, Cu, Sn, Sb, V, Mn, Cr, Mo and As.

Table 1 presents the hazard classes of chemical pollutants [2].

Table 1. Hazard classes of chemical pollutants

Class	Elements
1	As, Cd, Hg, Pb, Zn, F, 3,4- benzo(a)pyrene
2	B, Co, Ni, Mo, Cu, Sb, Cr
3	Ba, V, W, Mn, Sr

The soil contamination with heavy metals has different sources: metalworking industry waste; industrial emissions; fuel combustion products; automobile exhaust gases; agricultural chemicals.

The heavy metal distribution on the soil surface is determined by many factors. It depends on peculiarities of the pollution sources, meteorological features of the region, geochemical factors and landscape conditions in general.

From the historical point of view, an interest in this problem appeared when studying the soil fertility, as long as the elements such as Fe, Mn, Cu, Zn, Mo and Co are very important for the plant life and, consequently, for the animals and humans. They are known as microelements because they are required by plants in small quantities. All the microelements can make a negative effect on the plants if the concentration of their available forms exceeds certain limits. Table 2 presents the data on the effects of heavy metal concentrations on plants [3].

Table 2. Effect of toxic concentrations of some heavy metals on plants

Element	Concentration in soil, mg/kg	Plant response to the increased concentrations of heavy metals
Pb	100-500	Inhibition of respiration and suppression of photosynthesis process; sometimes an increase of cadmium content and a decrease of zinc, calcium, phosphorus, sulphur supply; decrease in the crop yield; deterioration of the plant products quality. External symptoms are the appearance of dark green leaves, curling of old leaves, stunted foliage.
Cd	1-13	Disruption of enzyme activity, processes of transpiration and fixation of CO ₂ ; retardation of photosynthesis, inhibition of biological recovery of NO ₂ to NO; difficulty in the supply and metabolism of a number of nutrition elements in plants. External symptoms: growth retardation, root system damage, leaf chlorosis.
Zn	140-250	Chlorosis of young leaves.
Cr	200-500	Deterioration of plant growth and development, wilting of the plant above-ground parts, root system damage, chlorosis of young leaves, sharp decrease in the content of most essential macro- and microelements (K, P, Fe, Mn, Cu, B, etc.) in plants.
Ni	30-100	Suppression of photosynthesis and transpiration processes, appearance of chlorosis signs.

Vehicle gases exhaust, wastewater irrigation, wastes, residues and emissions from the operation of mines and industrial sites, application of phosphorus and organic fertilizers, use of pesticides, etc. have resulted in an increase of heavy metal concentrations in soil.

As long as the heavy metals are firmly bound to the soil constituents and are difficult to access, their negative impact on the soil and environment will be insignificant. However, if the soil conditions allow heavy metals to pass into the soil solution, there is a direct danger of soil contamination, and there is a probability of their penetration into the plants, as well as into the organism of humans and animals that consume these plants. The danger of soil and plant contamination depends on: the type of plants; forms of chemical compounds in the soil; presence of the elements that counteract the influence of heavy metals and substances that form complex compounds with them; the adsorption and desorption processes; the amount of available forms of these metals in soil and the soil-climatic conditions. Thus, the negative influence of heavy metals depends, in essence, on their mobility, i.e. solubility.

The content of Pb in soil usually ranges from 0.1 to 20 mg/kg. Pb from the soils enters plants and accumulates in them. Pb adversely affects the biological activity in soil, inhibiting the enzyme activity by reducing the intensity of carbon dioxide release and the number of microorganisms. Pb also has the ability to be transmitted through food chains, accumulating in plant, animal and human tissues. The lead dust is deposited on the soil surface, adsorbed by organic matter, moves along the profile with the soil solutions, but is carried outside the soil profile in small quantities.

Zn content in soil varies from 10 to 800 mg/kg, but most often it is 30-50 mg/kg. The accumulation of Zn excessive amount negatively affects most of the soil processes: it causes changes in physical and physicochemical properties of soil, reduces its biological activity. Zn suppresses the vital activity of microorganisms, thus disturbing the processes of organic matter formation in soils.

Zn and Cu are less toxic than the above-mentioned heavy metals, but their excessive amount in the metallurgical industry wastes pollutes the soil and inhibits the growth of microorganisms, reduces the enzymatic activity of soils, reduces the plant yield [4].

It should be noted, that the toxicity of heavy metals increases with their combined effect when they act together on the living organisms in the soil. Since the heavy metals are usually found in various combinations both in the fuel combustion products and the metallurgical industry emissions, their effect on the environment surrounding the sources of pollution can be stronger than inferred from the concentration of individual elements.

SUBJECT OF STUDY AND INPUT DATA

The sources of harmful emissions can be located not only in megalopolises, but also in small settlements engaged in knowledge-intensive production, such as Pyatihatki settlement (Fig. 1), where NSC KIPT is located. As a part of the study of the impact of such an enterprise on the environment by nuclear-physical methods, the content of chemical elements in the soil samples, which were taken at 30 points in Pyatihatki in 2011-2021, was determined.



Figure 1. Placement of observation points in the 5-km zone of NSC KIPT

The samples were prepared according to the standard technology. The measurements were performed on the analytical nuclear-physical complex "Sokol" of NSC KIPT [5]. The methods based on the registration of the characteristic X-ray radiation of atoms (it is method 1) and γ -radiation of nuclei excited by accelerated protons (it is method 2) were used. The elements with an order number of 16 and higher were determined by method 1, and the elements with an order number lower than 16 were determined by method 2. The spectra were measured at the proton beam energy of 1.7 MeV, the current of 20...50 nA, and the proton charge on the target of 100...150 μ C. The radiation was registered by Si (Li) and Ge (Li) detectors. After the measurements, the data arrays on the elemental content in the soil were obtained. In the range of elements from N to Pb, 15 elements (N, Na, S, Cl, Cl, K, Ca, Ca, Ti, Mn, Fe, Cu, Zn, Zr, Br, Sr, Pb) were selected for further processing.

Using the EPA PMF v3.0.2.2 programme [6], the concentrations of these chemical elements and the calculation errors were investigated.

ArcView 3.2a package was chosen as the basic software product for the spatial distribution analysis of the main polluting chemical elements [7].

ArcView is a geographic information system that is designed to display, edit, spatially analyze, search, and manage geospatial data. This software tool was developed by ESRI (Environmental Systems Research Institute).

The tools of geoprocessing and analysis by ArcView package allow performing complex spatial operations on geographic data such as creating buffer zones around the map objects, clipping, sectioning, merging themes_and data assigning by location.

ANALYSIS METHODS

Many practical methods of environmental monitoring require the use of complex non-trivial computational methods implemented by software. To determine the characteristics and location of the pollution sources, the method, called Receptor Modeling in the scientific literature, has been proposed [8, 9]. Its fundamental principles are the mass conservation and mass balance. The input data are the constituent chemical components contained as elemental concentrations in a large number of samples. The basic mass balance equation for m chemical components in n samples from the contribution from p independent sources can be represented as follows:

$$x_{ij} = \sum_p g_{ip} f_{pj} + e_{ij}, \quad (1)$$

where x_{ij} is the measured concentration of j -th compound in i -th sample, f_{pj} is the concentration of j -th compound in the material emitted by p -th source (source profile), g_{ip} is the contribution of p -th source to the i -th sample, e_{ij} is the fraction of measurements that cannot be fitted by the model. The decomposition of the x_{ij} matrix in the form (1) represents it by the principal components (PCA - Principal Component Analysis) e.g. g_{ip} , in this case, is the score matrix, f_{pj} is the the loadings matrix, e_{ij} is the matrix of residuals. In general, the task is to determine the number of principal components, which is equal to the rank of the x_{ij} matrix. When the PCA method is used to divide the data into meaningful components, it is often referred to as the factor analysis. The PCA method can be interpreted as projecting the data onto a subspace of lower dimensionality. The resulting residuals of e_{ij} are treated as noise with no meaningful information.

Two computational algorithms UNMIX and PMF have been proposed to determine the composition of sources and the contribution of each of them to the sample with the recorded data [10]. UNMIX is based on eigenvalue analysis. The UNMIX model is a new type of multivariate receptor model based on the PCA method. As for the PMF (Positive matrix factorization) algorithm, it differs significantly from other factor analysis methods. All the other methods use

singular matrix decomposition. PMF is to use the least squares method to minimize the objective function, which has the form:

$$Q = \sum_{j=1}^n \sum_{i=1}^m \left(\frac{x_{ij} - \sum_{p=1}^P g_{ip} f_{pj}}{s_{ij}} \right)^2, \tag{2}$$

where s_{ij} is the error estimate of the j -th chemical component measured in the i -th sample. The problem is to minimise the Q function with respect to g_{ip} and f_{pj} subject to the constraints for these variables, which take into account their non-negativity. That is, the source profiles and their contributions to the samples are chosen so as to minimise the sum of all residuals e_{ij} .

To analyse the soil data PMF v3.0.2.2.2 programme was used. Preliminary data, obtained using the programme, can be refined. Two additional algorithms are used for this purpose. The first of them, Bootstrap Runs, randomly selects the non-overlapping blocks of samples, thereby revealing new input data. The second algorithm F_{peak} , uses a rotation transformation for the matrices G and F ($G^* = GT$ and $F^* = FT^{-1}$), so that the contribution of the most significant factors is increased and that of the less significant factors is decreased. It should be noted that the solution of the problem, which is defined by expression (1) is not unambiguous, and the result depends on the qualification and subjective perceptions of the researcher.

RESULTS OF THE RESERCH

An input matrix of 30x10x8 (30 is the number of sampling points, 10 years is sampling period, 8 is the number of chemical elements) was used. The following chemical elements were selected to analyse the pollution source: Ti, Zr, Pb, Mn, Sr, Cu, Cr, Zn. The PMF programme was run with the following parameters: number of iterations – 20; number of factors – 4; starting point for each iteration – 25. As a result of the PMF v3.0.2.2 programme operation, the presumptive sources of pollution were obtained, which are presented in Table 3.

Table 3. Sources of pollution

Factor	Dominant elements	Name
1	Titanium, Zirconium, Plumbum	Ti+Zr+Pb
2	Manganese, Strontium	Mn+Sr
3	Copper	Cu
4	Chromium	Cr

For further operation, the spatial distribution analysis of the main polluting chemical elements at the territory of Pyatihatki settlement was carried out by Arc View software in order to define how the environmental situation has changed judging by the presence of some heavy metals such as Pb, Sr, Cr, Cu and Zr for the period 2011-2021.

When comparing the concentrations of Pb (hazard class 1) in the soil samples during 2011-2021 (Fig. 2), a slight increase in its content near autostrades was detected, which did not exceed the maximum permissible concentration (less than 32 mg/kg) [11, 12].

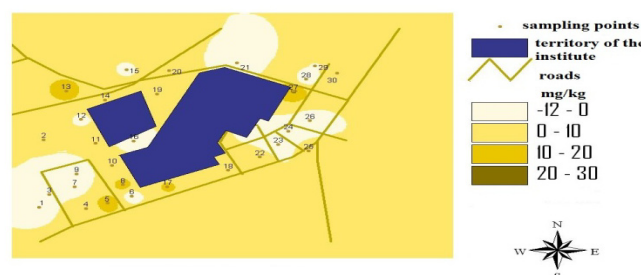


Figure 2. Pb Accumulation 2011-2021 in Pyatihatki settlement

When comparing the concentrations of Sr (hazard class 3) in the soil samples for 2011-2021 (Fig. 3), a slight increase in its content near autostrades, which did not exceed the background concentration (less than 350 mg/kg) was detected.

When studying the accumulation of Cr (hazard class 2) in the soil samples 2011-2021 (Fig. 4), its increase was detected in the eastern part of Pyatihatki settlement. The Cr factor as a source of pollution was detected using the programme PMF v3.0.2.2.2. The 2017 samples were a major contributor to this factor: points 1, 3, 5, 6, 7, 12, 15, 16, 17, 19, 30 showed significant concentrations of chromium, indicating the need for research and action; and points 9 and 20 showing threshold concentrations indicating the need for urgent soil cleanup measures. Such concentrations of chromium in soil cause deterioration of plant growth and development, wilting of the plant above-ground parts, root

system damage, chlorosis of young leaves, and a sharp decrease in the content of most essential macro- and microelements (K, P, Fe, Mn, Cu, B, etc.) in plants. When the wind rose was overlaid on the 2017 chromium map, the source of chromium was observed in the north-east direction. In the 2021 samples, the contribution of Cr was insignificant and did not exceed the maximum permissible concentration (less than 100 mg/kg).

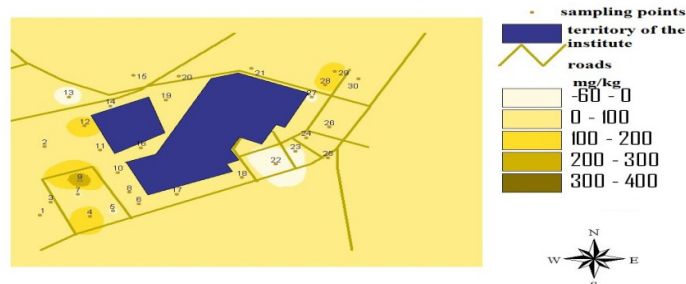


Figure 3. Sr Accumulation 2011-2021 in Pyatihatki settlement

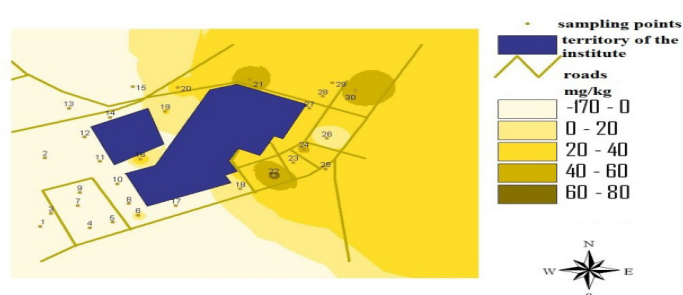


Figure 4. Cr Accumulation 2011-2021 in Pyatihatki settlement

When studying the accumulation of Zr in the 2011-2021 soil samples (Fig. 5), a slight increase in its content near autostrades was detected, which did not exceed the background concentration (200 mg/kg).

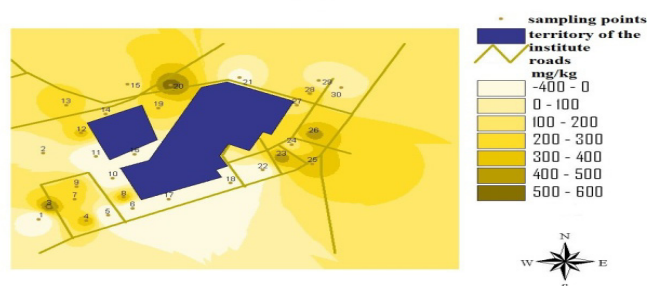


Figure 5. Zr Accumulation 2011-2021 in Pyatihatki settlement

When studying the accumulation of Cu (hazard class 2) in the 2011-2021 soil samples (Fig. 6), a slight increase in its content near autostrades was detected, which did not exceed the maximum permissible concentration (less than 55 mg/kg).

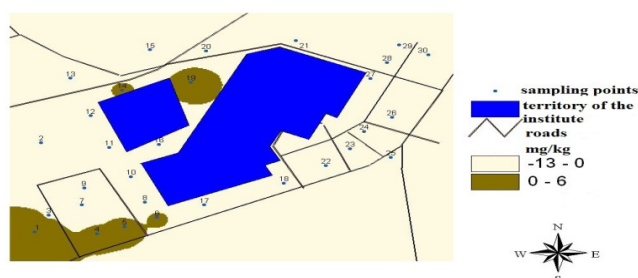


Figure 6. Cu accumulation for 2011-2021

CONCLUSIONS

The nuclear-physical methods were used to determine the content of chemical elements in the soil samples taken in 30 points at the territory of Pyatihatki settlement in 2011-2021. After the measurements completion, the data arrays on the content of elements in the soil were obtained.

For the analysis of the obtained data EPA PMF v3.0.2.2.2 software was used. When studying by PMF method the data on heavy metals concentration in the soil samples for 2011-2021, the sources of pollution, which had an impact on the territory near NSC KIPT, were identified. The sources of the soil pollution are autostrades (especially the road around the city Kharkiv, where an increase in the content of Pb, Sr, Zr, Cr and Cu was identified. A source of chromium contamination, which is located presumably to the north-east of Pyatihatki settlement, has been detected.

Thus, it can be concluded that the PMF method allows to identify the factors that influence soil contamination and to determine the presumptive sources of contamination by the use of the wind rose.

ORCID

- 📄 Maryna F. Kozhevnikova, <https://orcid.org/0000-0003-2464-3847>; 📄 Volodymyr V. Levenets, <https://orcid.org/0000-0002-6439-0576>
📄 Oleksii Yu. Lonin, <https://orcid.org/0000-0002-5386-3825>; 📄 Oleksandr P. Omelnik, <https://orcid.org/0000-0003-2467-3632>
📄 Andriy O. Shchur, <https://orcid.org/0000-0002-6619-4069>

REFERENCES

- [1] V.P. Seredina, *Загрязнение почв: учебное пособие [Soil Pollution: A Study Guide]*, (TSU Publishing House, 2015), pp. 346. (in Russian)
- [2] I.N. Bezcopylny, "Some methodological approaches to studying the impact of environmental factors on public health in the area of the territorial-industrial complex", *Hygienic sanitation*, **11**, 24–27 (1984). (in Russian)
- [3] B.A. Yagodin, *Агрохимия [Agrochemistry]*, (Agropromizdat, 1989), pp. 639. (in Russian)
- [4] Yu.A. Israel, I.K. Gasilina, and F.Ya. Rovinsky, *Мониторинг загрязнения природной среды [Monitoring of environmental pollution]*, (Gidrometeoizdat, Leningrad, 1978), pp. 560. (in Russian)
- [5] V.N. Bondarenko, L.S. Glazunov, et al., "Analytical installation for nuclear physics analysis methods", *Scientific statements. Series: Physics. Belgorod State University*, **2(15)**, 86–92 (2001). (in Russian)
- [6] *EPA Positive Matrix Factorization (PMF) 3.0 Fundamentals & User Guide*, (U.S. Environmental Protection Agency, 2008), pp. 81. <https://nepis.epa.gov/Exe/ZyPDF.cgi/P100GDUM.PDF?DockKey=P100GDUM.PDF>
- [7] T. Ormsby, *Extending ArcView GIS: with Network Analyst, Spatial Analyst and 3D Analyst*, (ESRI Press, 1999), pp. 527.
- [8] P.K. Hopke, "Application of receptor modeling methods", *Journal of Chemometrics*, **17**, 255–265 (2003). <https://doi.org/10.5094/APR.2011.016>
- [9] M.F. Kozhevnikova, V.V. Levenets, and I.L. Rolik, "The Pollution Source Identification: Computational Approach", *PAST*, **6(76)**, 149-156 (2011). https://vant.kipt.kharkov.ua/ARTICLE/VANT_2011_6/article_2011_6_149.pdf (in Russian)
- [10] E. Kim, T.V. Larson, P.K. Hopke, C. Slaughter, L.E. Sheppard, and C. Claiborn, "Source identification of PM2.5 in an arid Northwest U.S. City by positive matrix factorization", *Atmospheric Research*, **66(4)**, 291–305 (2003). [http://dx.doi.org/10.1016/S0169-8095\(03\)00025-5](http://dx.doi.org/10.1016/S0169-8095(03)00025-5)
- [11] *Гігієнічні регламенти допустимого вмісту хімічних речовин у ґрунті. Наказ Міністерства охорони здоров'я України № 1595 [Hygienic regulations on the permissible content of chemical substances in the soil. Order of the Ministry of Health of Ukraine No. 1595]*, (2020). <https://zakon.rada.gov.ua/laws/show/z0722-20#Text> (in Ukrainian)
- [12] S.M. Ryzhuk, M.V. Lisovy, and D.M. Bentsarovsky, *Методика агрохімічної паспортизації земель сільськогосподарського призначення [Methodology of agrochemical certification of agricultural lands]*, (Kyiv, 2003), pp. 64. (in Ukrainian)

ВИЯВЛЕННЯ ДЖЕРЕЛА ЗАБРУДНЕННЯ ВАЖКИМИ МЕТАЛАМИ НА ТЕРИТОРІЇ, ЩО ПРИЛЯГАЄ ДО ННЦ «ХАРКІВСЬКИЙ ФІЗИКО-ТЕХНІЧНИЙ ІНСТИТУТ», МЕТОДОМ РМФ

Марина Ф. Кожевнікова, Володимир В. Левенець, Олексій Ю. Лонін, Олександр П. Омельник, Андрій О. Щур
Національний науковий центр «Харківський фізико-технічний інститут», НАНУ

вул. Академічна, 1, 61108, Харків, Україна

У роботі досліджено вміст важких металів біля пос. П'ятихатки, де знаходиться Національний науковий центр Харківський фізико-технічний інститут (ННЦ ХФТІ). Ядерно-фізичними методами визначено вміст хімічних елементів у пробах ґрунту, які були взяті у 30 точках на території сел. П'ятихатки у 2011-2021рр. Елементний аналіз виконано на аналітичному ядерно-фізичному комплексі «Сокіл». Використані методи, що ґрунтуються на реєстрації характеристичного рентгенівського випромінювання атомів та γ -випромінювання ядер, що збуджуються прискореними протонами. Після проведення вимірювань отримані масиви даних щодо вмісту 15 хімічних елементів (N, Na, S, Cl, K, Ca, Ti, Mn, Fe, Cu, Zn, Zr, Br, Sr, Pb) у пробах ґрунту. Обробка масивів даних проводилася з використанням програми EPA PMF v3.0.2.2, заснованої на застосуванні алгоритму РМФ (Positive matrix factorization – позитивне матричне розкладання). Як базовий програмний продукт для просторового аналізу розподілу основних забруднюючих хімічних елементів, вибрано пакет ArcView 3.2a. В результаті виконаної роботи виявлено джерела забруднення, які мають вплив на територію біля ННЦ ХФТІ. Джерелом забруднення ґрунту є автомобільні дороги (особливо окружна дорога міста Харкова), де виявлено збільшення вмісту Pb, Sr, Zr, Cr та Cu. Виявлено джерело забруднення хромом, який розташований приблизно на північний схід від сел. П'ятихатки. Таким чином, можна зробити висновок, що метод РМФ дозволяє виявити фактори, що впливають на забруднення ґрунту, та визначити за допомогою троянди вітрів передбачувані джерела забруднення.

Ключові слова: важкі метали; елементний аналіз; характеристичне рентгенівське випромінювання; позитивне матричне розкладання; метод основних компонентів(РСА)